Freie Universität Berlin Institut für Chemie und Biochemie
und
Fritz-Haber Institut der Max-Planck Gesellschaft

Adsorption und Funktionalisierung von Graphen auf Metalloberflächen

Dissertation

zur Erlangung des akademischen Grades des Doktors der Naturwissenschaften (Dr. rer. nat.)

eingereicht im Fachbereich Biologie, Chemie, Pharmazie der Freien Universität Berlin

vorgelegt von

Stefan Böttcher

aus Berlin

2014

Probleme kann man niemals mit der selben Denkweise lösen, durch die Sie entstanden sind.

- Albert Einstein

Die vorliegende Arbeit wurde im Zeitraum von Januar 2011 bis August 2014, am Fritz-Haber Institut der Max-Planck Gesellschaft unter der Betreuung von Prof. Dr. Karsten Horn angefertigt.

1. Gutachter: Prof. Dr. Karsten Horn

2. Gutachter: Prof. Dr. Thomas Risse

Disputation am 3. November 2014

Hiermit erkläre ich an Eides statt, dass ich die vorliegende Arbeit eigenständig und ohne unerlaubte Hilfsmittel angefertigt habe.

Berlin, d.

Für Kati

Zusammenfassung

Die vorliegende Arbeit beschäftigt sich mit dem Einfluss molekular und atomarer Adsorbate auf Graphen/Ni(111) und Graphen/Ir(111), zum Zwecke einer chemischen Funktionalisierung des Graphens. Der Begriff Funktionalisierung bezieht sich in diesem Zusammenhang auf die Nutzbarmachung bereits vorhandener Eigenschaften des Graphens, dem Einbau chemischer Gruppen in dessen Struktur und dessen Funktionalisierung durch Variation des unterliegenden Substrates. Diese drei Wege der Funktionalisierung werden durch die Adsorption von Wasser und Ammoniak, die Photolyse von Vorläufer-Molekülen mit anschließender Oxidation und durch das Einbringen einer künstlichen, einatomigen Mangan-Schicht in dem Raum zwischen Graphen und seinem Substrat erzeugt. Die im folgenden beschriebenen Resultate der Funktionalisierung wurden mit den Methoden der Photoemissions Spektroskopie der Kern- und Valenz-Zustände, der Röntgen-Nahkanten-Absorptions-Spektroskopie und der Rastertunnelmikroskopie untersucht.

Die Adsorption von Wasser und Ammoniak kann durch die einzigartige elektro-nische Struktur des Graphens, nicht nur im Adsorbat sondern auch im Graphen selbst nachgewiesen werden. Im Zuge dieser schwachen und reversiblen Adsorption ist es möglich, mittels der elementspezifischen Röntgenabsorption die Ausbildung neuer, unbesetzter Kohlenstoff-Zustände im Graphen-Substrat nachzuweisen, welche vom Adsorbat induziert wurden. Diese schwache, chemische Bindung ist nur durch die sehr deutliche elektronische Struktur der monoatomaren Graphen-Schicht zu ermitteln. Die Ausbildung dieser neuen Zustände hängt dabei von der Wechselwirkungsstärke des Adsorbates in Graphene/Ni(111) und Graphen/Ir(111) ab und lässt einen Rückschluss auf die unterschiedliche Wechselwirkungsstärke der Graphen-Schicht zu ihrem jeweiligen Substrat zu.

Eine Funktionalisierung durch den Einbau einer neuen chemischen Gruppe in die Graphenstruktur konnte durch eine Oxidation mittels Photolyse von NO_2 und SO_2, herbeigeführt werden. Durch die Bestrahlung dieser adsorbierten Moleküle mit harter UV und Röntgenstrahlung ist es möglich, die Graphen-Schicht, mittels der bei der Photolyse entstehenden Sauerstoffatome, zu oxidieren. Die Oxidierung erfolgt chemisch selektiv zugunsten der epoxidischen Oxidphase, lokal selektiv zum Adsorptionsort und unter der Erzeugung einer geringen Zahl von Defektstellen. Diese Oxidations-Reaktion ist thermisch vollständig reversibel.

Mittels Interkalation einer Monolage von Mangan zwischen die Graphen-Schicht und das Ir(111) Substrat ist es gelungen, die Eigenschaften von Graphen nicht nur punktuell, sondern auf der gesamten Fläche des Graphens zu verändern. Im vorliegenden Fall ist es möglich, eine erhebliche Anisotropie in der elektronischen Struktur und eine starke Erhöhung der Oberflächen-Rauigkeit zu erzeugen. Dabei bleiben wesentliche strukturelle und elektronische Eigenschaften, d.h. die Hybridisierung der Kohlenstoff-Atome und die lineare Dispersion des Graphen π-Bandes um den Dirac Punkt, erhalten.

Abstract

The aim of this work is to study the influence of molecular and atomic adsorbates on graphene/Ni(111) and graphene/Ir(111), towards a chemical functionalization of graphene. Functionalization means here to access and modify properties of graphene, to introduce new properties into graphene by adding new chemical components into the graphene lattice, or to vary the properties of graphene by modifying its substrate. These three pathways of functionalization are studied in the context of water and ammonia adsorption, the photolysis and subsequent oxidation from photolysis of adsorbed molecules, and by introducing a single atomic layer of manganese between graphene and its substrate. The observations and results presented below are observed by means of core level and valence band photoemission spectroscopy, near edge x-ray absorption fine structure spectroscopy, and scanning tunneling microscopy.

The adsorption of water and ammonia can be detected due to the unique electronic structure of graphene, not only on the adsorbate states but also from the substrate level modification. Due to the weak and reversible adsorption, new adsorbate-induced unoccupied electronic states are observed in graphene, using element-specific x-ray absorption spectroscopy. This weak chemical bond between the adsorbate and graphene is only detectable due to the distinct electronic structure of the single atomic graphene layer. The spectral manifestation of these induced electronic states depends on the interaction strength of the adsorbate to the graphene/metal system and permits to estimate its strength.

The incorporation of novel functional groups is achieved by adsorption and photolysis of NO_2 and SO_2 on graphene/Ir(111). The photolysis of these adsorbates leads to the formation of oxygen atoms on the surface, able to selectively oxidize graphene towards the epoxidic oxygen phase, locally restricted to the adsorption site and under the formation of only a small number of defects. The resulting graphene oxide layer is hence of high quality and is thermally completely reversible towards a high quality graphene layer.

By means of intercalation of manganese between graphene and the Ir(111) substrate, graphene can be functionalized not only locally, such as by oxidation, but by affecting the entire graphene layer. The intercalation process of manganese is observed at room temperature and the intercalation of manganese leads to the formation of a strong anisotropy in the electronic structure of graphene and to an enhanced surface roughness. However, many unique properties, such as the hybridization and the linear dispersion of the graphene π-band, stay intact.

Contents

Part I.

Introduction

1. Motivation

The concept of chemical functionalization is a term well known to modern applied chemistry. To a chemists this term means the introduction of a chemical species into a molecule, in order to fulfil a special task. Such a task can be the protection of a reactive chemical group during a chemical syntheses, for example, forcing the chemical reaction into a desired direction. Another form of functionalization is the introduction of a chemical group into a molecule itself, in order to form a reaction centre for a desired chemical reaction or to change its properties, such as its solubility or secondary and tertiary structure.

The term of functionalization applied to surface science is in this concept limited because a surface is a different reaction partner than another molecule. However, this circumstance allows to extend the concept of functionalization much wider and requires, hence, a slightly extended definition has been adapted for surface science. Hence, the chemical functionalization of a surface may be defined as the addition of a chemical species to the surface, in order to introduce a desired property, or to make a property of the surface accessible.

The present work attempts to study such a chemical functionalization of a solid surface, applied to a material which is not only highly suitable for the studies presented here, but also technologically highly relevant for the intended functionalization. This material is graphene.

Graphene is the ultimate two-dimensional material that exists. When, in 2004, the isolation of a single layer of graphite on silicon oxide was reported to have an astonishing high charge carrier mobility [1], this gave rise to an extraordinary scientific interest in this particular material [2, 3]. Since then, many thousands of publications have appeared, revealing and predicting graphene's properties, aiming on possible technological graphene-based applications [3]. The chemical functionalization is a suitable tool for the tuning of graphene's properties. Graphene alone does not exist as suggested for any two-dimensional material by Landau [4]. Hence graphene is always adsorbed on a surface, and often on metal surfaces, as used in this work. This adsorption may change the electronic structure of graphene, but also offers the possibility to access special properties of graphene and to tune them. In the following, three distinct forms of functionalization will be applied to graphene, in order to modify and reveal the properties and functionalities of graphene.

The first main topic is the interaction of graphene with adsorbed polar molecules, water and ammonia. If these molecules adsorb non-dissociatively, it is possible to study their interaction with graphene. In particular, the well defined electronic structure of graphene allows to detect the interaction by changes that appear in the electronic structure of graphene, to an extent that is rarely observed in surface science.

The next topic is the introduction of a chemical group into the graphene lattice. This is chosen to be the oxidation, which we achieve by photolysis of precursor molecules, such as NO_2 and SO_2, and fluorination from photolysis of PF_3. The chemical modification leads to the appearance of a tuneable band gap, especially important for graphene applied in electronic devices.

The last topic is the modification of graphene by the variation of the substrate. To this purpose we introduce a metal monolayer, namely manganese, into the space between graphene and its substrate. This procedure will be shown to modify the electronic and structural properties of the complete graphene layer, systematically and symmetrically across the entire graphene surface.

The present work is structured as follows. In Chapter 2 of Part I, a general introduction into the field of graphene, its crystallographic and electronic properties and its adsorption on substrates will be given. In particular the two systems used in this work will be presented in detail: graphene/Ni(111) and graphene/Ir(111). A short description of the interaction classification between graphene and its environment is given. In Part II, Chapter 3 provides an overview about some necessary formalisms for the surface physics discussed here. Chapters 4 and 5 provide an overview about the experimental methods and procedures, as well as of the experimental equipment and preparation. Part III presents the results: First, experiments on the adsorption of water and ammonia on graphene/Ni(111) and graphene/Ir(111) are presented in Chapter 6 and evaluated in terms of the possibility to detect the adsorbate interaction with the substrate, by a spectroscopic fingerprint. Chapter 7 presents experiment on the incorporation of additional chemical groups into graphene, namely the photolysis-induced oxidation and fluorination of graphene/Ir(111) from adsorbed molecules. Chapter 8 presents a study of the morphology and electronic properties of an artificial manganese layer intercalated in the space between graphene and Ir(111). In Part IV, general conclusions will be drawn from these experiments. In Part V, supplementary information will be given.

2. Graphene

2.1. Graphene: The Ultimate 2D Material

Carbon is a substance essential for life on earth. It is the building block of all life-based organic materials such DNA, proteins, carbohydrates and many more. It is also the building block for a tremendous variety of organic substances such as hydrocarbons and related products such as plastics, chemicals, pharmaceuticals and many more. The reason for this variety is its ability to exist in different bonding situations. Carbon has four valence electrons: two $2s$ and two $2p$ electrons. Its valence shell is hence exactly half occupied. It has the ability to rearrange its valence electrons in different, so-called hybridization states: a tetragonal sp^3 state, where all four bonds are in a degenerate state. Another state is the trigonal planar sp^2 one, where three of the four valence electrons are distributed in a plane and the last electron populates an orbital perpendicular to this plane. At last, there is the possibility to mix only the s and one p orbital into an sp hybridization state where two of the three p-orbitals are unaffected. These three basic building blocks can exist isolated or in combination. sp^3 hybridized carbon atoms form diamond and alkanes, where the carbon atoms (and their bonding partners) are arranged in a tetrahedral symmetry. The sp^2 state allows to form double bonds which are stronger, shorter and undergo chemical reactions more easy, when isolated. However, in a closed system of sp^2-bonded carbon atoms they can be chemically highly stable, such as in the cyclic systems, e.g. in benzene. They form the group of the alkenes and the graphite solid phase. The alkines are triple-bonded sp carbon atoms, such as the simplest, the acetylene molecule.

All commonly known solid forms of carbon consist either of sp^3 (diamond) or sp^2 (graphite) carbon atoms. Diamond is an insulator. The stacked graphite crystal however exhibit a conductance in its plane of hexagonally arranged carbon atoms due to the double bonds, which form an extended system of overlapping p_z orbitals in the plane. This is known as a delocalized π-system of double bonds. When a single layer of graphite is now extracted one arrives (in theory) at a perfect two-dimensional, single atomic crystal of carbon atoms; all electronically linked by their planar sp^2 bonds and the overlap of the p_z orbitals of every carbon atom. This building block has been treated very early in computational physics and chemistry by Wallace [5], who used it to calculate the electronic

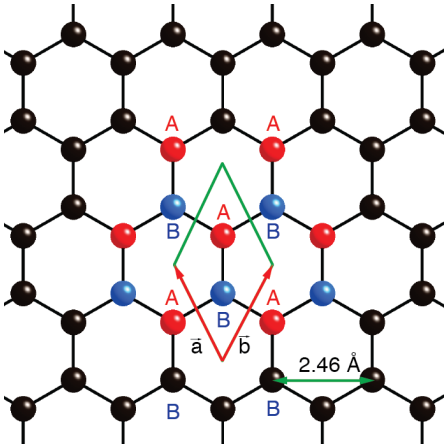

Figure 2.1. – Crystallographic structure of free-standing graphene. The unit cell of graphene (green rhombus) is a two atomic basis of the graphene lattice, set up by the two lattice vectors $\vec{a}$ and $\vec{b}$. It contains the by symmetry unique carbon atoms A and B. The unit cell length is 2.46Å.

band structure of a monolayer of graphite for the purpose of understanding the properties of graphite. Such a two-dimensional layer of carbon atoms is called graphene. It is beside the common allotropes, such as diamond and graphite, one of the novel carbon allotropes, that has been discovered at the end of the last century: The zero dimensional fullerenes in 1985 [6] and one-dimensional carbon nanotubes in 1991 [7].

Graphene, first isolated in 2004 by Geim and Novoselov [1, 8] is a carbon allotrope formed of sp^2 hybridized carbon atoms in a hexagonal lattice. A schematic representation of the crystallographic structure is presented in Figure 2.1. The hexagonally arranged carbon atoms, often referred to as the honeycomb lattice, are arranged in a unit cell containing two carbon atoms A and B. The unit cell has to contain two carbon atoms, since the carbon hexagon is empty and two trigonally coordinated carbon atoms are hence needed to set up the graphene lattice, containing two sublattices A and B. However, it is not possible to distinguish between the two sublattices other than by definition of A and B. This circumstance has a direct consequence on the electronic structure, as it will be presented below.

Such an arrangement of atoms in a two-dimensional lattice of carbon atoms exhibits special properties. In the literature, public and scientific, graphene is often named for its outstanding mechanical stability [3], for example by its enormous Young's modulus (elastic modulus) of 1 TPa [9]. A consequence of the dense lattice is also the fact that graphene is impermeable to most gases [10], which could be important in hydrogen storage, for example [11, 12]. Graphene further shows a high thermal conductivity of 3000 W/mK [13] and an astonishingly high charge carrier mobility of $2.5 \cdot 10^5$ cm^2/Vs [14], which makes it a possible candidate for fast electronic devices. A mechanism that multiplies charge

carriers in graphene after a photo-excitation process has recently been discussed, which may be of importance in fabricating efficient solar cells [15]. The latter examples are not only a consequence of the atomic lattice, but also of the electronic structure of graphene.

2.2. The Electronic Structure of Graphene

2.2.1. Introduction

The formation of the electronic structure of solids will not be derived here in detail. The interested reader is kindly refereed to the common physics textbooks such as the book by Ashcroft and Mermin [16] or Roald Hoffman's "A Chemists Guide to Bonding in Extended Structures" [17–19], for a more "chemical" derivation of the electronic band structure. What should be noted here is that the electronic band structure can be derived from the physicist's view, using wave functions and the Schrödinger equation (SEQ), but also from the atomic and molecular orbitals that the chemist uses. Both approaches are equally correct, however, a different terminology is used. Hence, both approaches have influenced the nomenclature of the electronic structure of graphene. For example, the electronic bands of graphene, as described below, are named after their "chemist's" origins, the π and σ molecular orbitals and bonds of aromatic systems.

2.2.2. Free-Standing Graphene

The electronic structure of graphene's valence band was published as early as 1947 [5]. The properties described in Section 2.1 and in this section are a direct consequence of the crystallographic structure of graphene with its two-atomic basis. Due to the trigonal real space lattice of the carbon hexagons one arrives at a hexagonal Brillouin zone, set up by the reciprocal lattice vectors $\vec{k}_a$ and $\vec{k}_b$. The reciprocal lattice also exhibits a trigonal symmetry as the real space lattice. This means, that at the corners of the Brillouin zone, the K points, are distinguishable by their symmetry and are therefore named K and K'. A direct consequence of this purely symmetric necessity is, as we will see, the linear dispersion of the electronic π-band at the K points near the Fermi level. The valence band electronic structure of free-standing graphene, obtained from a DFT calculation performed by the present author in his masters thesis [20], is presented in Figure 2.2. The representation in reciprocal space shows the energy vs. electron in-plane momentum, unfolded along the high symmetry direction $\Gamma \rightarrow \mathrm{M} \rightarrow \mathrm{K} - \Gamma$ of the Brillouin zone. The electronic structure is built from four occupied bands, namely the σ_1-, σ_2-, σ_3- and the π-band. The unoccupied bands are named π^* and σ^*, according to the molecular orbitals of aromatic systems, e.g. benzene. The σ_1- and π-bands exhibit an s-band character, σ_2 and σ_3 have p-band character. σ_1 originates from the totally symmetric (s-like) orbital of

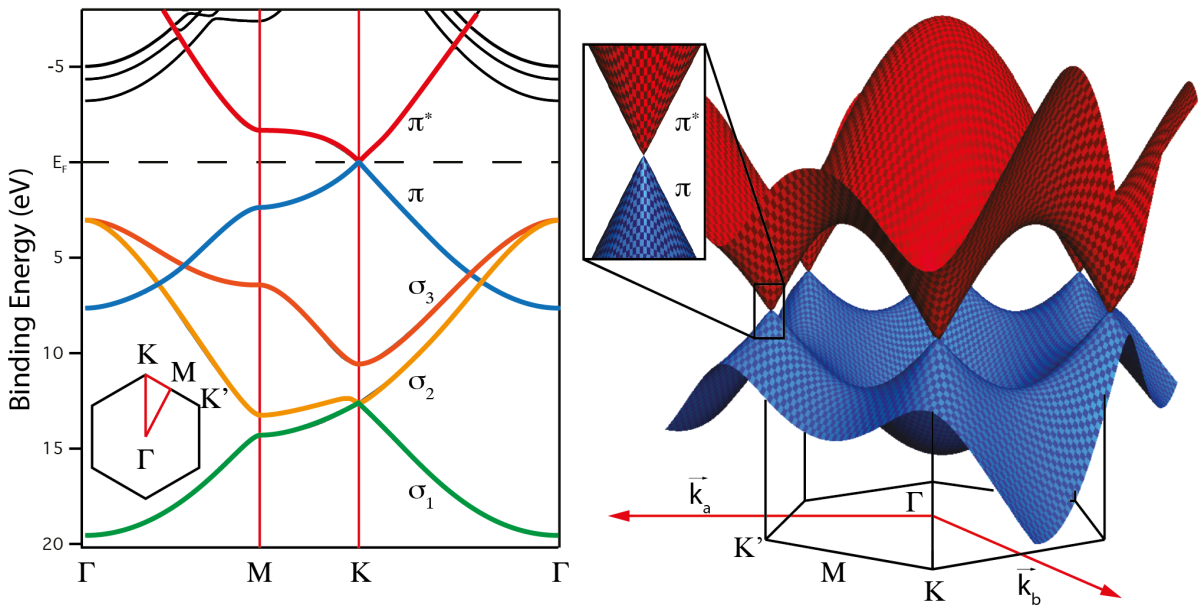

Figure 2.2. – **Left:** Electronic band structure of graphene as derived from DFT calculations by the present author in his masters thesis [20]. The high symmetry points of the Brillouin zone are labeled. **Right:** Three dimensional representation of the π and π^* band in blue and red, respectively. The dispersion is derived from a tight binding calculation, taken from ref. [21]

the sp^2 configuration. Its band dispersion can be explained within the model of a chain of hydrogen atoms [17–19]. The π-band originates from the p_z orbitals, which have D_{3h} symmetry with respect to the carbon atoms, where they are located. This band also exhibits an s-band character. The minimum of the graphene π-band is found at an energy of 7.6 eV. σ_2 and σ_3 behave p-like, since the orbitals are the in-plane orbitals of an sp^2 hybridized carbon atom. They have nodal planes perpendicular to the graphene plane. Their energy maximum is found at a binding energy of 3 eV. Note that the hybrid or local orbital representation of the sp^2 state is not sufficient for the derivation of the band structure by Hofmann [19], since in this case at the Γ point only two bands would be present (one from the π orbital and one triply degenerate sp orbital). The hybrid or local orbitals of the sp^2 configuration are unitary transformations of the so-called canonical orbitals from *ab-initio* solutions. However this artificial (because empirical) degeneracy of the electronic states of the sp^2 hybridized carbon atoms would produce an error in this particular case, if they are used to explain the electronic structure of graphene.

The unique property of graphene's band structure is found at the K and K' point of the hexagonal Brillouin zone. The π-band intersects the Fermi level with a linear dispersion and without the opening of a band gap. The two branches of the π-band do not show avoided crossing as in other materials, since they originate from the two, by

symmetry different, K points, K and K'. This linear dispersion is a direct consequence of the population of the π-band (or the p_z-orbitals, forming the π-band). Since the valence shell is exactly half occupied, the π-band is also, meaning the π-band is filled exactly up to the crossing point of the graphene π-bands at the K point, where the linear dispersion is observed. The quantum mechanical description of these electrons at the Fermi level is given by a Dirac equation.

Considering the tight binding derivation of the π-band dispersion from Castro-Neto [22], the energy relation with respect to the electron momentum at the K point (here defined as $\vec{k} = \vec{K} + \vec{q}$) is found to be

$$E_{\pm}(\vec{q}) \approx \pm\nu_F|\vec{q}| + O[(q/K)^2], \tag{2.1}$$

with $\nu_F \approx 1 \cdot 10^6\, m/s$ [5]. This is in contrast to the usual case of an electron dispersion, where $E(\vec{q}) = q^2/2m$ and the Fermi velocity is a function of the particle mass m and the electron momentum $\vec{k}$; $\nu = k/m = \sqrt{2E/m}$. In graphene, where the band dispersion around the K point can be approximated by a linear dispersion, the Fermi velocity is a constant, which cannot be described by the Schrödinger equation. However, it is possible to write this in a two-dimensional Dirac equation

$$-i\nu_F\vec{\sigma}\cdot\nabla\psi(\vec{r}) = E\psi(\vec{r}). \tag{2.2}$$

The particles (the electrons) described in this way are hence called Dirac Fermions. The three-dimensional representation (the dispersion in E_B vs. k_x, k_y) of this point is called the Dirac cone, due to its conical shape (see the inset of Figure 2.2) and the touching point of the π- and π^*-band at the K point is called the Dirac point with its energy E_D [23].

2.2.3. Graphene on Metal Substrates

Graphene as studied and used as a substrate in the present work is grown on metal substrates. The huge variety of graphene on metallic substrates can be treated in two different groups: strong or weak interaction with the substrate, and graphene on surfaces, which match the graphene lattice constant and those who do not. These two general properties of the graphene-metal interfaces are not necessarily linked. Common examples (further discussed in this section) are graphene on Ni(111) and Cu(111). Both are lattice matched (omitting a discrepancy of about 1%) but the interaction is strongly different for both systems. The other case is graphene adsorbed on Ir(111) or Ru(0001), which are both lattice mismatched systems and also exhibit very different bonding situations: weak for Ir(111) and strong for Ru(0001). A graphical summary can be found in Figure 2.3. The determination of the adsorption strength is typically achieved by (either) comparing a) the energy shift of the carbon $1s$ core level component with respect to graphite or by comparing two graphene/metal systems, b) the appearance of a Dirac cone or a band gap

in general and c) the shift of the Fermi level and the corresponding shift of the valence band and the Dirac point to higher (or lower) binding energies. In this section, a general view on the different adsorption properties will be given and the systems under investigation are presented in detail. We will start with a short historic literature overview, followed by the description of the two model examples graphene/Ni(111) and graphene/Ir(111).

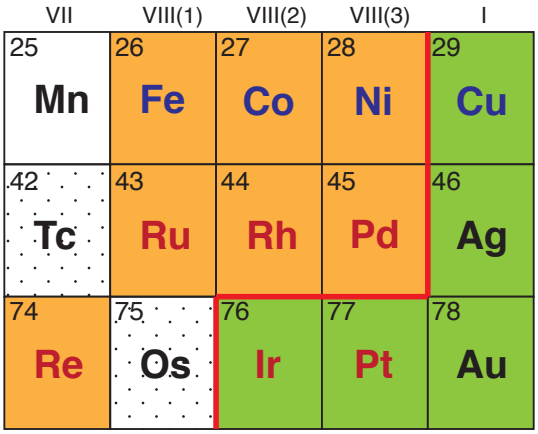

Figure 2.3. – A summary of the transition metals of column 6 to 11 (IUPAC) or side column VII to I (traditional). The orange highlighted elements represent strongly interacting graphene, the green highlighted elements represent weakly interacting graphene. Blue labeled elements are lattice matched systems, red labeled elements are lattice mismatched systems. The dotted elements have not been studied and Mn is part of this thesis.

Some widely discussed examples of graphene adsorbed on *d* metals are presented in Table 2.1 with references and *interaction strengths* or *bonding strength* assumed by the graphene community (see for example [24, 25]). These classifications are insufficient, as I will describe on the next pages. For now, the introduction shall contain these classification, since they still used by the community and found in the literature. I will define the term *interaction strength* before discussing the two main graphene/metal system on this thesis, graphene/Ni(111) and graphene/Ir(111), in order to use it in an appropriate way.

The preparation of graphene on metals is relatively easy and is achieved by physical or chemical vapour deposition from hydrocarbon gases on the hot metal surface. This method was used very early for graphene (then called monolayer-graphite, MG) on Ni(111) starting from 1983 [26–28]. Even earlier, carbide phases, which we know to be graphene today, were already reported in the 1960's and 1970's, e.g. on platinum [29, 30] or in a combined study on Ru(0001) and Rh(111) [31]. These early "graphene" structures were obtained by annealing and segregation of carbon from the bulk to the surface during the cleaning process. The story of graphene on metal substrates therefore starts much earlier than 2004, when Geim and Novoselov reported the preparation of a single layer of

graphene on SiO_2 [1], a paper that started the general interest in this field. Until that time, the interesting properties were not observed. Ref. [24] gives an excellent overview on the graphene/metal literature until 2008.

The properties of graphene/metal systems vary strongly with the crystallographic structure and the strength of chemical interaction. It is not possible to estimate the electronic properties or the binding situation from the crystallographic structure or vice versa. However, some general trends may be seen in the literature [32, 33].

Metal	Reference	Adsorption	Surface Reconstruction	a_{hex}[Å] (Mismatch in%)
Nickel	[26–28, 34, 35]	Strong	(111)	2.49 (1.2%)
Cobalt	[36]	Strong	(111)[a]	2.50 (1.6%)
Rhodium	[37, 38]	Strong	(111)	2.69 (9.5%)
Ruthenium	[39–41]	Strong	(0001)	2.71 (9.8%)
Platinum	[29, 30, 42]	Weak	(111)	2.77 (11.2%)
Iridium	[43, 44]	Weak	(111)	2.72 (9.6%)

Table 2.1. – Selection of graphene on *d*-metal surfaces. Representative literature, assumed adsorption strength classification, surface lattice constants and amount lattice mismatch. The lattice constants are extracted from [24]. [a]The *fcc* phase Co(111) is grown on the W(110) surface.

Graphene Intercalation Substrates

Another possibility to obtain graphene on (artificial) metal-like surfaces is the method of intercalation. For a review of this method, see the book by Dresselhaus and Dresselhaus from 1981 [45]. In this method, also applicable to graphene on various surfaces, a new metal is brought into the space between the first graphene/graphite layer and the underlying surface. This happens in general by deposition of a specified amount of a metal (for example one monolayer) on the graphene surface, followed by subsequent heating, such that the deposited metal film floats underneath the surface and forms a closed layer (or flat cluster for submonolayer deposition) in the interface between graphene and the substrate. This technique is not only applicable to metals but also to nonmetallic substrates (see for example ref. [46]) and intercalating materials [47]. A list of references is given in Table 2.2. This method allows access to structures that are difficult or impossible to produce on single crystals. One example is graphene on gold. The preparation of graphene/Au(111) directly has not yet been achieved, since the catalytic activity of gold is too low to induce hydrocarbon decomposition. On the other hand, the low sublimation point of gold

Compound	Reference	Doping	Substrates
Gold	[46, 48–50]	Weak	Ni,Ir,SiC
Iron	[59, 60]	Strong (n-type)	Ni,Ru
Cesium	[61]	Strong (n-type)	Ir
Nickel	[58, 60]	Strong (n-type)	Ir,Ru
Oxygen	[47, 62]	weak (p-type)	Ir
Fluorine	[63]	strong (p-type)	SiC
Hydrogen	[63, 64]	strong (p-type)	SiC

Table 2.2. – Selection of graphene intercalation compounds. Representative literature, strength and type of the electron doping, surface lattice constants and lattice mismatch.

limits the temperature that can be reached for hydrocarbons to decompose. It is, however, possible to intercalate one monolayer of gold underneath graphene/Ni(111) [48, 49] or Ir(111) [50, 51]. Another example is the formation of graphene on Cu(111). The preparation of this industrially highly important graphene/metal system [3, 52, 53], is difficult under UHV conditions, since it requires a high partial pressures [54]. Graphene on copper can, however, easily be achieved by intercalation of copper between graphene/Ni(111) [55] or graphene/Ir(111) [56].

The structure of the intercalation compounds is determined by the lattice constants of their intercalate and the metal substrate. In case of Ni(111), most of the period III transition metals grow epitaxially and follow the lattice constant of the substrate, since the natural lattice constants of Ni and these metals are almost equal. On Ir(111), however, the lattice constants differ, but the newly formed intercalated layers grow with the same lattice constant as the substrate. This means that elements like copper [56], cobalt [57], nickel [58] or, as it will be examined in this work, manganese occur in an artificially stretched lattice on graphene/Ir(111).

On the Term Interaction Strength

A major part of this thesis deals with the interaction of molecules with graphene-metal systems and the description of the graphene/metal systems itself. The classification of the bonding strength, in terms of energy/mole or atom, often fails when discussing the bond of graphene to a substrate or, as we will show in this work, the adsorption strength of a molecule to graphene. For an appropriate description of the bonding interaction the term of *interaction strength* has to be defined. In order to motivate this definition, we will anticipate some information, which will be explained in the corresponding chapter below.

Common classifications of adsorption are physisorption and chemisorption (see chapter 3). Physisorption is defined as a weak interaction with no charge transfer. Instead, fluctuating dipoles on the molecule are established, which lead to an attractive force between the molecules and the surface. On the other hand, chemisorption is defined as an exchange of electrons between two partners, e.g. an adsorbate and a substrate. This correlates with the formation of new electronic states between the two bonding partners, i.e. molecular orbitals or so-called "hybrid states". The chemisorption bond strength, is on the order of a few electron volts per molecule, whereas physisorption is usually considered for bonding stengths up to 500 meV.

Graphene/metals systems cannot easily be classified within the above definitions. There are problems in the theoretical description of bonding (see discussion below), and in the experimental determination of adsorption energies for graphene on metals, e.g. by thermal desorption spectroscopy.

The graphene/metal systems have so far been classified in "weakly" and "strongly" bonded systems [24, 25, 32], based on of several criteria: the binding energy of the C 1s core level, the formation of a band gap at the K point or a shift of the Fermi level with respect to the valence band structure of graphene. Graphene/Ni(111) has been classified as strongly bonded graphene because of a shift of the C 1s core level line and the valence bands as well as by the appearance of a band gap in the π-band at the K point. The existence of hybrid electronic states between graphene and the metal were shown experimentally with NEXAFS [25], as well as theoretically [65–67]. On the other hand theoretical calculations have not been able to verify the expected strong adsorption energy [65, 68], sometimes even predicting an instability of this system [69]. With the introduction of the Van-der-Waals corrected DFT functionals [70, 71], the results have become more reasonable, i.e. they predict a bonding situation. However, the calculated binding energies are still extremely weak (150 meV/atom) [72, 73].

Systems such as graphene/Ir(111) have been classified to be weakly interacting systems [24, 32], from the criteria given above. Current state-of-the-art calculations predict graphene/Ir(111) to be bonded with an average energy of 60 meV/C-atom [44]. The lack of a band gap in the π-band at the K point would support this assumption because the

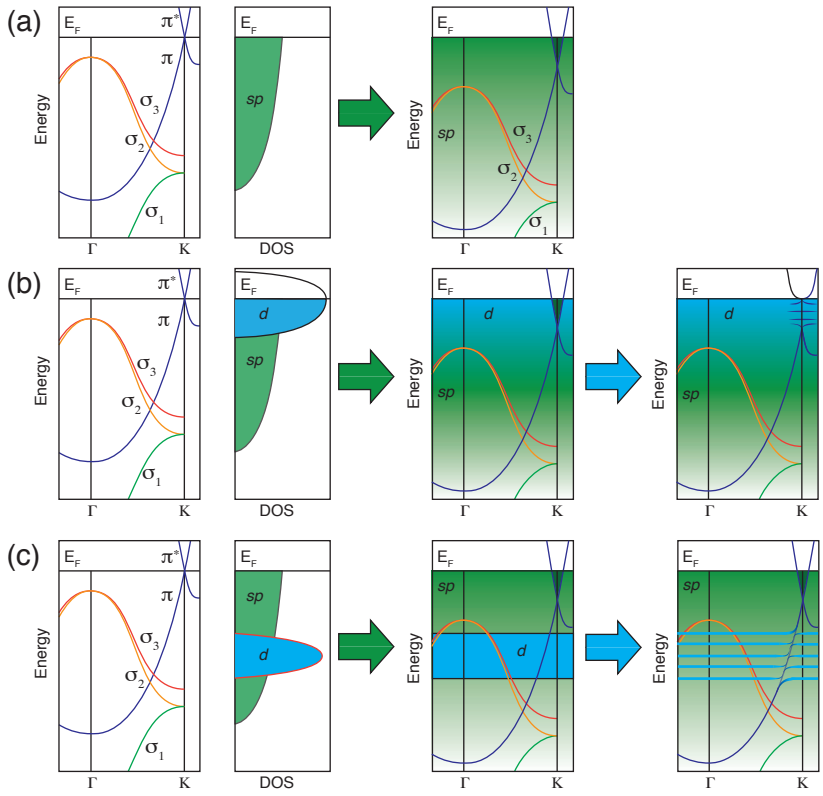

Figure 2.4. – Schematic picture of band gap formation in graphene/Ni(111) for *sp* metals (a) open shell *d*-metals (b) and closed shell *d*-metals (c). The initial doping is caused by the contact with the metal surface's *sp*-states. The metal *d*-states may interact with the graphene π-band by avoided crossing. The open-shell metal nickel has in addition partly filled electronic *d* states at the Fermi level. These interact with the π-band and form avoided crossing gaps ("hybridization gaps"). This figure is drawn after reference [33].

formation of a gap is often interpreted as a sign for a chemical interaction, due to the symmetry breaking of the graphene when bonded to the substrate. However, the same calculations also show, that in certain areas on the surface, new electronic hybrid states are present with a considerable charge transfer [44, 74].

In all these examples, the binding energy seems to be an insufficient quantity to classify the bond between the graphene layer and the metal because the appearance of a chemical bond does apparently not coincide with a larger binding energy, as for example observed from DFT calculations. Therefore, we will use the term *interaction strength* to describe the modification in the electronic structure, without implying a strong magnitude of net binding energy. The reason for this definition can be found in a recent publication by Voloshina et al. [33] that intends to classify the interaction of graphene and a metal substrate in a general scheme. Consider Figure 2.4 for illustration. Graphene adsorbed on various metals is here separated into three classes: Graphene on *sp* metals (a), graphene

on open shell d-metals (such as nickel or cobalt) (b), and graphene on closed shell d-metals (such as Cu) (c). In this model, the contact of the graphene layer to any metal results in a shift of the Fermi level relative to graphene as defined by the metal substrate (here for example n-doping). Secondly, shifted graphene bands interact with the d-states of the metal substrate. If the conditions for gap formation, according to avoided crossing, occurs, gaps are formed at the intersection of the corresponding metal d-band and the graphene π-band. This can happen around the Fermi level for open shell systems (b) or far below E_F for closed shell systems (c). The important observation in this model is that the interaction happens in the occupied states which do, hence, not contribute to the binding energy of the complex, even though they form *hybrid states*. This is a similar picture to the formation of a bond in O_2 or N_2, where the deep $2s$ states of both atoms form a bonding and antibonding molecular orbital, which is fully occupied and has hence no contribution to the binding energy of the system. The bonding interaction is gained by different population of the HOMO and LUMO of the molecule. The only exception in the graphene/metal scheme described above is found in the systems with open electron shells: nickel has states close to the Fermi level and an interaction of the π-band with these states may form an empty antibonding state above E_F. In this model, these states are responsible for the chemical interaction. They form such "chemically active" states which then contribute to the chemical bond of graphene to the metal and possibly even to adsorbates on graphene/metal systems [75]. Since we still deal with electronic bands, and only a small fraction of the band may be unoccupied above E_F, the total contribution to the adsorption energy of the graphene/metal system may still be small compared to the Van-der-Waals contribution to the adsorption energy.

The *interaction strength* in the context of this thesis is the classification of the electronic interaction of graphene to the metal, that needs not to be strong in terms of adsorption or binding energy (for the reason described above), but may be strong (or weak) in terms of the amount of modification of the electronic structure, such as gap or *hybrid state* formation. We will also see that for the discussion of adsorbates on graphene, the existence of such states (however possibly occupied on both, the bonding and antibonding part) is enough to allow a chemical interaction between graphene and adsorbates, that shall hence be designated by the same term of *interaction strength*. The lack of a clear connection between the bonding strength and the modification of the electronic structure is unsatisfactory, but represents to the best of my knowledge the state of the art of theory and experiment as far as graphene-metal interaction is concerned.

Graphene/Ni(111)

Graphene on the (111) surface of nickel is one of the most intensely studied graphene/metal systems in the recent years [24]. The origin of this interest is the crystallographic struc-

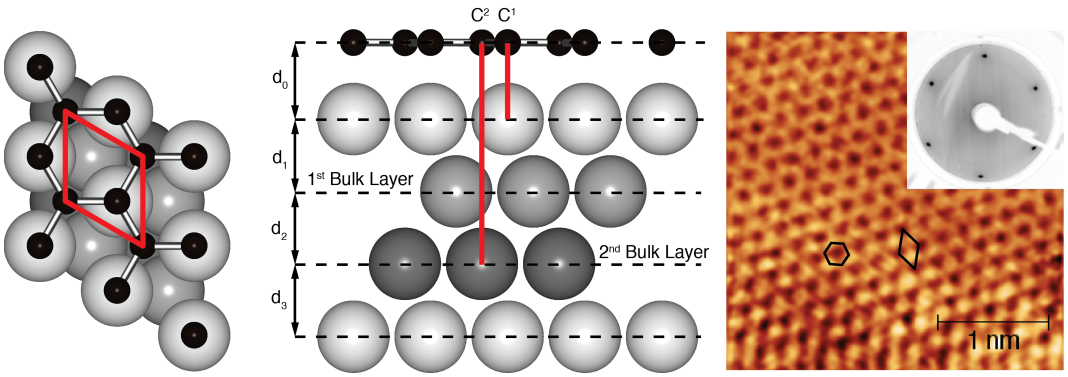

Figure 2.5. – Schematic representation of the graphene/Ni(111) system and STM image of graphene/Ni(111)/W(110). The crystallographic structure presented here is the so-called *top-fcc* configuration, with one carbon atom on top of a surface nickel atom and one above the *fcc* hollow site (on top of the second bulk layer nickel atom). The two carbon atoms of the graphene unit cell are now distinguishable (C^1 and C^2). The right panel shows an STM picture of graphene prepared on a thick Ni(111) film on W(110) with an inset of the corresponding LEED image, acquired by the present author. The hexagon shows the graphene honeycomb lattice and the rhombus represents the surface unit cell.

ture that shows an almost perfect flat adsorption of graphene on Ni(111) [25]. It is hence discussed, together with other lattice matched system such as graphene/Cu(111) as a basis for a large scale production of graphene by growth and transfer [52, 76].

Due to a combination of the electronic and crystallographic structure described below, this system has been predicted to work as a spin filter by Karpan *et al.* [66, 67]. They predicted that the ferromagnetic nickel substrate would inject minority charge carriers with higher efficiency, due to the fact that, at the K point, only the electronic states of the minority spin charge carriers of the nickel substrate exist at the Fermi level. This is also the only location in reciprocal space where graphene shows electronic states (see Figure 2.2). An appropriate stack of multilayered graphene on Ni(111) would transmit mainly minority spin electrons through a graphene stack, while inhibiting the transmission of the majority spin electrons. This has led to experiments aimed at obtaining multilayered and well ordered graphene on Ni(111), with limited success [77] because the results did not match with the predictions by Karpan *et al.*. The stacked graphene layers are found to be twisted with respect to each other, which will inhibit the proposed electron transport mechanism [77]. So the spin filter effect action in a real device may actually be difficult to realize.

The crystallographic structure of graphene adsorbed on *fcc* Ni(111) surface is shown in Figure 2.5. This structure is based on a DFT calculation of the present author, performed in his master's thesis [20]. Identical results have been published in ref. [78]. The graphene

lattice and the (111) surface of nickel show a structure whose lattice constants differ by 1.2% ($a_{\mathrm{hex}}^{\mathrm{Ni}} = \sqrt{2}a_{\mathrm{fcc}}^{\mathrm{Ni}} = 2.49\,\text{Å}$ and $a_{\mathrm{hex}}^{\mathrm{Gr}} = 2.46\,\text{Å}$). The result is a structure of both materials with no evidence of lattice mismatch and where the unit cell of free-standing graphene is equal to the unit cell of graphene/Ni(111). The structure presented in Figure 2.5 is the so-called *top-fcc* configuration, one carbon atom being located directly on top of a surface Ni atom. The second carbon atom of the unit cell is located on top of the Ni atom of the second atomic layer from the top; this crystallographic hollow site is the *fcc* hollow site. In this structure, the two carbon atoms of the graphene unit cell are no longer equivalent, which leads to a broken symmetry, affecting the crystallographic as well as electronic structure. While Rosei et al. [26] proposed that an *fcc-hcp* configuration (with both carbon atoms on hollow sites) is present, Gamo *et al.* later concluded that the configuration presented here is more reasonable [28]. Note that the opposite orientation, with the second carbon atom on the *hcp* hollow site (the *top-hcp* configuration), is energetically and electronically not distinguishable from the *top-fcc* configuration, because of the bond that is formed between graphene and the metal. The electronic states described below form mainly between the surface nickel atoms and the graphene layer; the hollow position of the second carbon atom is not of importance for the formation of the bonds discussed below [65]. The graphene-nickel distance is reported to be 2.1 Å [79], in agreement with theoretical predictions on the same order [78, 80, 81]. The theoretical values for the interatomic distances and energies exhibit large differences, depending on the functional (LDA or GGA [81]) and the basis set used in the calculations, especially if dispersion interactions, i.e. Van-der-Waals interactions, are taken into account [81]. The structure shown in Figure 2.5 represents the generally agreed ground state structure as proposed in the literature [65]. Other structures, such as the so-called *bridge* configuration, have been proposed as well [72, 73, 81]. In this configuration, the surface unit cell of graphene is shifted by half a unit cell along the $\langle 110 \rangle$ direction of the Ni(111) surface. This means that the C-C bond is located on top of the surface nickel atom. However, it has recently been shown by statistically evaluated STM measurements that indeed the *top-fcc* structure with $\approx 65\,\%$ is the most apparent, among the appearance of the *top-hcp* (18%) and *bridge* (22%) structures [72].

The electronic structure of graphene on Ni(111) is strongly affected compared to that of free-standing graphene (see figure Figure 2.6). The figure contains an ARPES intensity map $I(E_B, k_x, k_y)$ unfolded along the high symmetry directions $\Gamma \rightarrow \mathrm{M} \rightarrow \mathrm{K} \rightarrow \Gamma$ of the Brillouin zone in false colour, superimposed by a DFT band structure calculation. Both measurement and calculation were performed by the present author during his master thesis (for details, see caption). A photoemission measurement of this structure (monolayer graphite adsorbed on nickel) was published as early as 1994 [27]. The electronic bands of graphene are affected through the contact of the graphene layer with the metal surface,

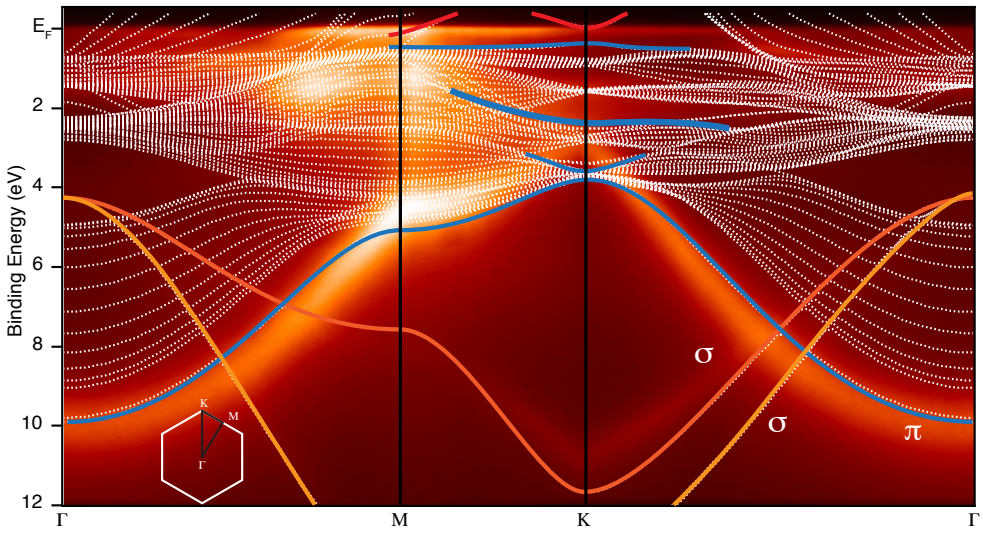

Figure 2.6. – Band map of Graphene/Ni(111) in the high symmetry directions $\Gamma \rightarrow \mathrm{M} \rightarrow \mathrm{K} \rightarrow \Gamma$ of the hexagonal Brillouin zone. The photoemission spectrum in the background is extracted from a 3D dataset of PE intensity $I(E_B, k_x, k_x)$. The spectrum is superimposed by a DFT calculation of graphene Ni(111) performed with VASP and the GGA functional PBE. Both measurement and calculation were performed by the present author in his masters thesis [20]. For simplicity, only the minority spin states are plotted. The former graphene π-band and the new carbon/nickel hybrid states are highlighted in blue, the graphene σ-bands are marked in orange as in Figure 2.2.

and the interaction leads to avoided crossings between the nickel $3d$ valence bands and the graphene π-band. The amount of doping from the metal contact can be read from the rigid shift of the graphene σ-bands. Since these bands originate from in-plane orbitals, they do not interact with the Ni $3d$ bands. The rigid shift of the bottom of the σ band compared to free-standing graphene is 1 eV, caused by an electron transfer from the nickel surface into the graphene layer and is hence a shift of the Fermi energy with respect to graphene. The valence band structure as well as the carbon $1s$ core level are shifted by a similar amount. Due to the interaction of the graphene π-band with the nickel states, this electronic band is shifted by 1 eV in addition to the rigid shift, by a total shift of 2 eV, as determined from the bottom of the π-band at the Γ point. The bands around the K point of graphene and Ni(111) match in energy, momentum and the crystallographic structure of graphene and nickel matches in real space. Hence, these bands show avoided crossings and the π-band dispersion reaches an energy of $E_B \approx 3$ eV at the K point. The Dirac cone is destroyed due to a mixing of graphene and nickel surface electronic states. Bertoni *et al.* [65] first described the electronic origin of this state mixing and interpreted their findings as the formation of interface states (similar to surface states). The term *interface states* may be misleading, since these electronic states describe chemical bonds, including nickel d-states, rather than what is usually considered to be an *interface* or *surface* state.

State	E_B maj. [eV]	E_B min. [eV]	type	location
I_1	3.27	2.93	bonding between C2 and top-Ni $3d$ states	K-point
I_2	2.28	1.93	bonding between C1 and top-Ni Ni $3d$ states	K-point
I_3	0.28	-0,16	antibonding between C2 and top-Ni Ni $3d$ states	K-point
I_4	-0.12	-0.55	antibonding between C1 and top-Ni Ni $3d$ states)	K-point
I_5	-3.20	-3.32	bonding between C1/C2 and top-Ni $3d$ and ferromagnetic Ni $4s$ and $4p$ states	M-point

Table 2.3. – List of majority and minority spin hybrid states of the graphene/Ni(111) electronic structure. The DFT derived energies are taken from Voloshina *et al.* [78], which are VdW corrected results, similar to the results from Bertoni *et al.*. The type is an interpretation of the electron density distribution as a chemical bond orbital picture according to [65, 78].

The term *hybrid states* may therefore be more appropriate. According to the nomenclature of Bertoni *et al.* [65], there are five *hybrid* or *interface* states (for each spin) with both graphene π- and Ni $3d$-character, called I_1 to I_5. An electron density plot of these states is presented in Figure 2.7, taken from ref. [65]. In the following, the nomenclature of *hybrid state* will be used to describe these electronic states, consistent with the existing literature [78]. The *hybrid states* are presented in Table 2.3. Their energies vary in the range of ± 300 meV, depending on the functionals used in the calculations. The values presented here are taken from [78]. Comparable values obtained from different functionals and/or parameters used can be found in [65, 81].

This mixing of electronic states represents what was generally assumed to be a strong bonding between graphene and the group VIII-metals Fe, Co and Ni. However, current theoretical considerations suggest that the overall binding energy per carbon atom is surprisingly small (about 150 meV/C-atom, see for example a recent study in [72]) when considering the huge changes in the electronic structure. For comparison, note that the interaction calculated for graphene/Ir(111) is on the order of 60 meV/C-atom, averaged over the whole supercell. This may be explained by a model proposed by Voloshina and Dedkov [33], as presented in Section 2.2.3. The hybridization observed in the electronic structure of graphene/Ni(111) is strong and a small part of the formed *hybrid states* may be located in the unoccupied states, which means that a chemical bond is formed. How-

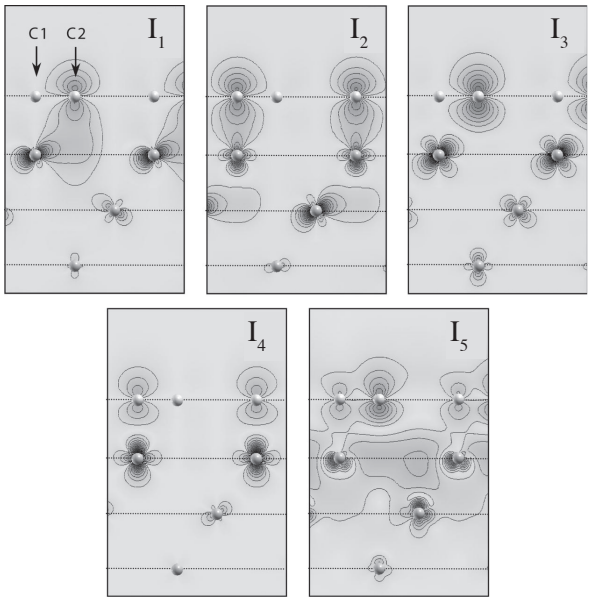

Figure 2.7. – **Upper panel:** Electron density plot of the interface (hybrid) states I_1 (a) to I_5 (d) The grey levels are proportional to the electron density $r[\rho r]^{1/2}$. The figure is kindly provided by C. Bertoni. Reprinted figure with permission from [65] http://doi.org/10.1103/PhysRevB.71.075402. Copyright (2005) by the American Physical Society.

ever, the contribution to the net binding energy may be small. After the doping, the electronic bands around the K-point match in energy, momentum and real space and hence, do not cross and form the described *hybrid states*. They exhibit at least 3 avoided crossings (consider the π-band and three Ni $3d$ states with out-of-plane character).

The classification of a strong interaction is still valid for graphene/Ni(111) within the concept of *interaction strength*. However, the net binding energy is small; the formation of hybrid states, the fact that some of these states are close to the Fermi level and in some cases even in the unoccupied states, and the fact that a considerable extra shift of the graphene π-band is observed leads to a classification of a strong (electronic) interaction.

An entirely different interpretation of the electronic structure of graphene/Ni(111) has been presented by Varykhalov *et al.* [82], who recently suggested that the Dirac cone in graphene/Ni(111) is still intact. The authors observed in a high resolution ARPES study, identical band structures as presented in Figure 2.6; however, they interpreted these in terms of hybridization occuring below E_F but exclusively above the Dirac point of the graphene band structure. An almost conical structure was presented by the authors at a binding energy of almost 3 eV. This conical structure was interpreted to be the remaining Dirac cone of graphene. However, several aspects of this interpretation suggest that indeed

the model presented above is correct. The most important argument is that the assumed shift of the Dirac point of the graphene π-band at the K-point and the bottom of the π-band at the Γ point shows a difference of $\approx 1\,\mathrm{eV}$. Secondly, the conical structure exhibits no linear dispersion but a sharp flattening of the bands above the intersection, which is in contrast to other experiments where the graphene π-band has been shifted by doping (e.g. in refs. [61, 83]).

Graphene/Ir(111)

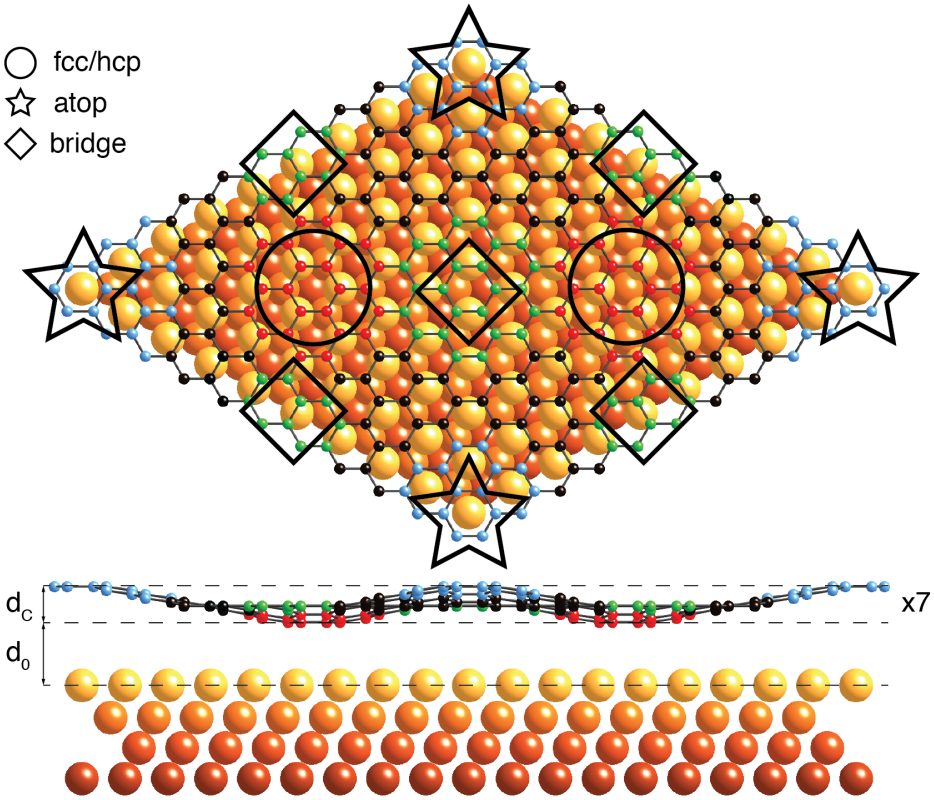

Figure 2.8. – Schematic representation of the crystallographic structure of graphene/Ir(111). The surface unit cell is a supercell consisting of (9×9) Ir(111) and (10×10) graphene unit cells. The result is a moiré structure with different adsorption configurations: The circles represent the *fcc* and *hcp* adsorption sites, where one surface Ir atom and the *fcc* or *hcp* hollow site is occupied by a carbon atom. The stars shows the *atop* sites, where both carbon atoms occupy both hollow sites (and form a ring around the surface Ir atom). The diamonds show the intermediate configuration of the *bridge* site, where the carbon bond is centred over a surface Ir atom. The side view shows the surface corrugation of 0.3 Å of the graphene overlayer exaggerated by 7 for presentation.

After having discussed an electronically strongly interacting system, another substrate which exhibits a weaker interaction is necessary for a comparison of the effects of adsorbates as presented in this work. Graphene/Cu(111) is not a suitable system since its preparation is difficult for in-situ experiments [54]. Graphene/Ir(111), on the other hand, is a good system because it also exhibits a weak interaction and is rather simple to prepare with a high quality and low number of defects in its atomic structure, such as point defects or rotated domains.

The crystallographic structure of graphene adsorbed on Ir(111) is presented in Figure 2.8. The structure is dominated by the difference in the lattice constants of the

Ir(111) surface and the graphene unit cell. Ir(111) has a surface lattice constant of 2.72 Å that has a 10% relative difference to the graphene lattice constant of 2.46Å. This results in a supercell of (9×9) Ir(111) and (10×10) graphene unit cells, which form a so-called moiré pattern. These graphene superstructures exhibit several different adsorption sites as also found on other surfaces, such as rhodium [38, 60] or ruthenium [39], and in general when the lattice constants between graphene and the surface do not match. The unit cell contains two areas where the crystallographic structure of graphene/Ir(111) is similar to the *top-fcc/hcp* structure of graphene Ni(111): in the areas marked by a circle, one carbon atom is situated on top of a surface Ir atom, and the second carbon atom is located above the *fcc* or *hcp* hollow site, respectively. These areas are also referred to as the *hollow* sites of the supercell, a term that will be used later when discussing possible adsorption sites on graphene/Ir(111). The corners of the supercell show a structure where both carbon atoms occupy the hollow sites of the (111) surface. These regions are called *atop* sites. Located between the *top-fcc/hcp* and the *atop* sites are the so-called *bridge* positions with the carbon-carbon bond centre located on top of a surface Ir atom. The supercell of graphene/Ir(111) not only shows a moiré pattern from the geometrical point of view, but also exhibits a systematic corrugation related to the atomic structure. The *atop* sites have a larger distance d_0 to the Ir(111) surface (3.58 Å) than the *fcc* (3.27 Å) and *hcp* (3.28 Å) sites, respectively, where the *fcc* site is the closest to the surface, and the bridging positions have intermediate distances of 3.32 Å. These values are taken from [74], obtained from DFT calculations including the Grimme D2 dispersion interaction correction [71]. The corrugation d_c between the *atop* and *fcc/hcp* sites is found to be on the order of 0.3 Å, obtained experimentally via STM and AFM measurements [74, 84] as well as theoretically [44, 74]. The corrugation is modulated by the chemical interaction between the different adsorption sites of graphene/Ir(111). The *top-fcc* and *top-hcp* sites of graphene/Ir(111) exhibit a picture similar to the *hybrid states* of graphene/Ni(111) in DFT calculations [44, 74]; however, they are only found in these *hollow* sites of the graphene/Ir(111) supercell. The *atop* sites, on the other hand, do not show any sizeable hybrid state formation in DFT calculations since the distance is larger and comparable to other system that exhibit a weak or no electronic interaction between graphene and the surface such as graphene/Au(111)/Ni(111) [85] or graphene/Al(111)/Ni(111) [80]. One result of the structural modulation is the fact that graphene/Ir(111) has areas of different chemical activity (I abbreviate this as *activated areas*). These areas are the discussed *hollow* sites (*top-fcc* and *top-hcp*) where *hybrid states* are formed between the graphene layer and the surface [32, 44]. Adsorbates appear to bond most likely on the hollow sites of the graphene/Ir(111) unit cell [74, 84, 86].

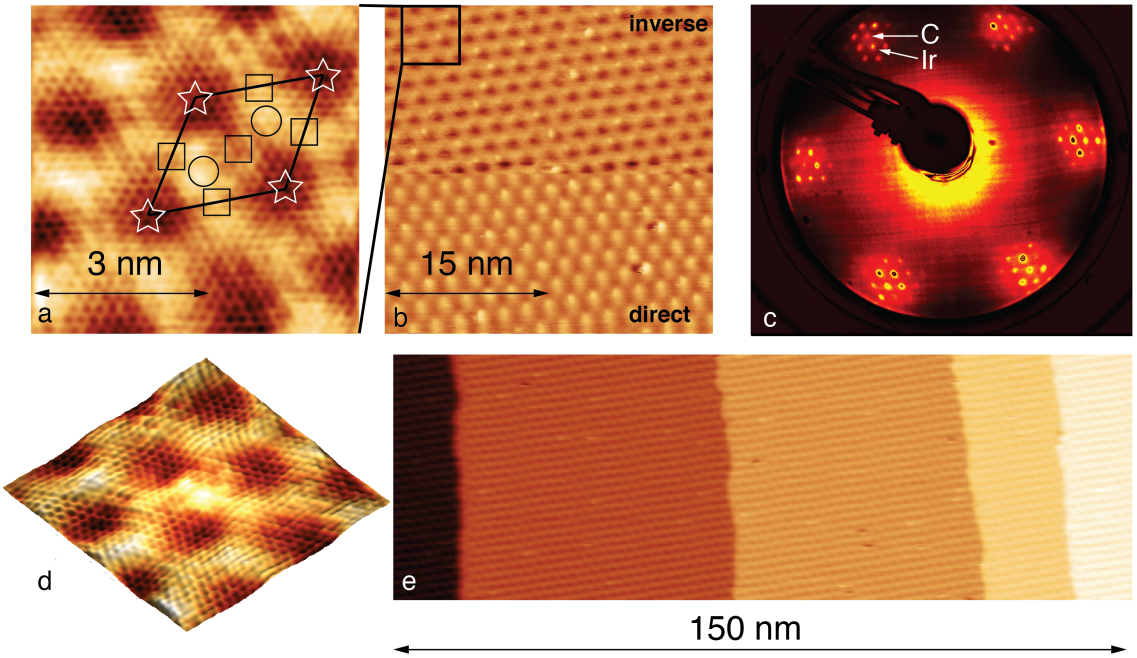

Figure 2.9. – Structural data from graphene/Ir(111) obtained by STM and LEED experiments performed by the present author. a) and d) show a closeup on the graphene/Ir(111) supercell with atomic resolution. These figures have been filtered by FFT in order to enhance the atomic structure for presentation. The markers correspond to the classification of the adsorption sites from Figure 2.8. b) presents a switching from inverse to direct contrast, achieven by a switch in the tunneling bias from $U_T = 400\,\mathrm{mV}$ to $U_T = 800\,\mathrm{mV}$ at $I_T = 0.3\,\mathrm{nA}$. c) represents a typical LEED image of the graphene/Ir(111) surface diffraction at $E = 95\,\mathrm{eV}$. The unit cells of graphene and Ir(111) show individual diffraction spots, as marked in the image. The additional diffraction spots are due to the supercell. e) is a large scale STM image over and and several atomic steps. The graphene layer completely covers the surface.

Figure 2.9 shows our structural investigations from STM and LEED experiments. The images a) and d) show a closeup of the surface with atomic resolution in false colour and 3D, respectively. Markers for the *atop*, *top-fcc/hcp* and *bridge* sites are as in Figure 2.8. The STM image is displayed in the so-called *inverse* contrast. The high *atop* sites appear as dark areas, whereas the deeper *top-fcc/hcp* sites are imaged as bright areas. In case of electronically homogeneous surfaces, the intensity of the tunneling current (and hence the intensity of the false colour representation) often correlates with the actual height of the surface structures. Considering the fact that not the actual height but the local density of states is measured, the inverse contrast must be attributed to an electronic effect. The inverse contrast, first observed by Coraux *et al.* [87], together with the first description of the moiré supercell, was later assigned to *hybrid states* that form in the vicinity of the *top-fcc/hcp* sites of graphene/Ir(111) [74]. In this reference, Voloshina *et al.* observed a

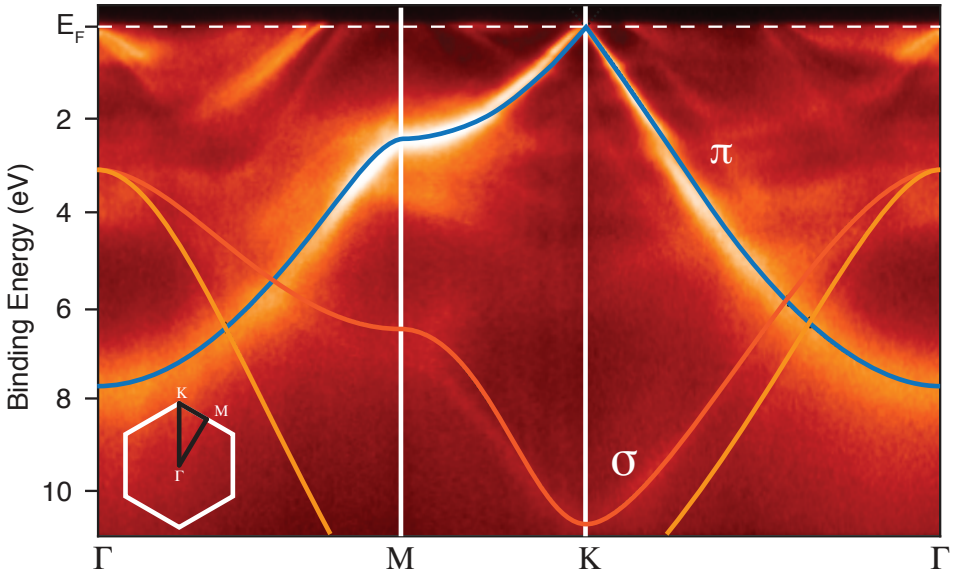

Figure 2.10. – Photoemission intensity map $I(E_B, k_x, k_y)$ of graphene/Ir(111) unfolded along the high symmetry directions $\Gamma \rightarrow \mathrm{M} \rightarrow \mathrm{K} \rightarrow \Gamma$. The superimposed DFT calculation is for comparison with free-standing graphene from Figure 2.2. It is obtained for free-standing graphene, from a slab calculation using the GGA functional PBE [88] and a plane wave basis set [89] calculated with the VASP code [90]. This measurement and calculation was performed by the present author within his master's thesis.

frequency shift in an AFM measurement in the same areas, and interpreted their findings as the atomic force response to the tip caused by the enhanced chemical adsorption character in the *hollow* sited as found by Busse *et al.* [44]. Depending on the tunneling bias voltage (and the tip conditions), the inverse contrast can be switched to direct contrast. This switching is shown in Figure 2.9 b), where a manual switching from $U_T = 400\,\mathrm{mV}$ to $U_T = 800\,\mathrm{mV}$ at $I_T = 0.3\,\mathrm{nA}$ was performed in the middle of the image to invert the contrast. These values differ slightly from the literature values [74], which can be explained by a different tip condition. In the present case, the tunneling electrons reached with a bias voltage of 400 mV originate mainly from the hybrid states of the *hollow* sites of the graphene/Ir(111) supercell and dominate the tip height measurement (in constant current mode), displayed in the false colour representation. The moiré superstructure manifests itself in a LEED pattern as shown in Figure 2.9. Both individual sublattices of graphene and Ir(111) show individual diffraction spots as marked. The moiré supercell induces the appearance of the additional spots around the substrate diffraction spots as a result of the superposition of the two reciprocal lattice vectors of graphene $\vec{k}_{Gr}$ and the smaller lattice vector of the graphene/Ir(111) supercell $\vec{k}_{Gr/Ir}$.

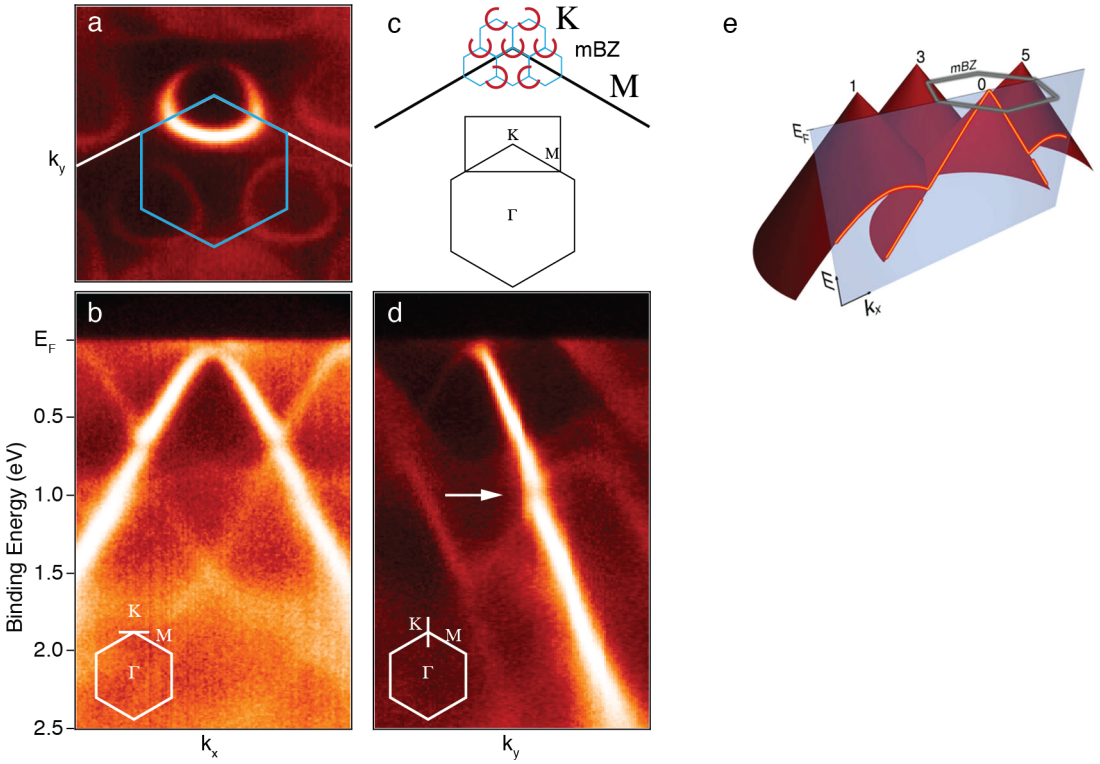

Figure 2.11. – Closeup of photoemission map I_{E_B,k_x,k_y} of graphene/Ir(111) around the K point (top) of the Brillouin zone. a) shows a constant energy map $I(k_x, k_y)$ around $E_B \approx 500\,\text{meV}$ around the position of the K-point, b) and d) present the photoemission maps $I(E_B, k_x)$ and $I(E_B, k_y)$, respectively. c) is a schematic representation of the K point with sketches of the Dirac and replica cones, related to the mini-Brillouin zones. e) is an illustration of the replica cones and the intersection with the original Dirac cone, taken from [43] with kind permission from M. Kralj. Reprinted with permission from [43] http://doi.org/10.1103/PhysRevLett.102.056808. Copyright (2009) by the American Physical Society.

The "chemical modulation" of graphene/Ir(111) [44] has almost no influence on the electronic band structure of graphene. Figure 2.10 shows a photoemission intensity map $I(E_B, k_x, k_y)$ of graphene/Ir(111) unfolded along the high symmetry directions $\Gamma \rightarrow \text{M} \rightarrow \text{K} \rightarrow \Gamma$ of the hexagonal Brillouin zone in false colour; overlaid are bands from a DFT calculation of a free-standing graphene layer performed by the present author in his master's thesis (for details of the calculation, see caption). A very good match is found; only a small p-doping is observed, which shifts the Dirac point slightly into the unoccupied electronic states. In the vicinity of the Dirac point, no Ir bands appear that could interact with the graphene π-band. Therefore, no evidence of a gap formation such as in graphene/Ni(111) is observed. The superstructure of the moiré unit cell, on the other hand, does have an influence. Figure 2.10 shows the electronic structure with respect to the unit cell of graphene. The actual Brillouin zone of graphene/Ir(111) is smaller (mini-

Brillouin zone, mBZ) and the broken symmetry induces the appearance of back-folded replica bands. These replica bands, first reported by Pletikosić and coworkers [43], appear at the K points of the large graphene Brillouin zone. Figure 2.11 shows a closeup of the photoemission intensity maps around the upper lying K point. Figure 2.11 a) shows a constant energy map $I(k_x, k_y)$ around $E_B \approx 500\,\text{meV}$ around the position of the K point, b) and d) present the photoemission maps $I(E_B, k_x)$ and $I(E_B, k_y)$, respectively. c) is a schematic representation of the K point of the Brillouin zone with sketches of the Dirac and replica cone, related to the mini-Brillouin zones. e) is an illustration of the replica cones and the intersection with the original Dirac cone, taken from [43]. At an energy of $E_B = 500\,\text{meV}$, the cut through the Dirac cone is not perfectly circular, the trigonal symmetry of the substrate being still visible; it becomes more circular at lower binding energies. At a photon energy of 65 eV the upper part of the cone is not visible (the so-called "dark corridor"). This is a final state effect of the photoemission process where the photoelectrons with $\vec{k}$ vector along the direction $\text{K} \rightarrow \text{M}$ in the second Brillouin zone interfere negatively, which causes a reduction in photoemission intensity at this point. It has, however, been shown that choosing a specific photon energy, will close the "dark corridor" [91]. The replica bands are located at the corresponding corners of the mini-Brillouin zone of the graphene/Ir(111) supercell, where the basis of the two reciprocal lattice vectors match. The positions are reached by going along the reciprocal lattice vectors $\vec{k}_{Gr}$, from $\Gamma \rightarrow \text{K}$ and then from $\text{K} \rightarrow \text{K}_{\text{replica}}$ with $\vec{k}_{Gr/Ir}$. At the crossing points of the original and back-folded band, a small band gap appears due to an avoided crossing, which is possible due to the symmetry breaking that also causes the replica bands to appear. The arrow marks the low energy mini-gap around 1 eV in Figure 2.11 d) in direction $\Gamma \rightarrow \text{K}$. Another mini-gap appears around 2.5 eV.

The theoretical and experimental observations, presented above, show that graphene/Ir(111) can be classified as a weakly interacting system; however, some interaction is present. The formation of "hybrid states" is present, which may allow experimental access to the observation of these states. On the other hand, the number of these states has to be lower compared to graphene/Ni(111) because they probably only form in the *hollow* sites of the graphene/Ir(111) supercell. It is even possible that the missing electronic interaction close to E_F, such as found for graphene/Ni(111), even leads to a smaller strength of interaction, for example fewer available empty states.

The two structures described in this section, graphene/Ni(111) and graphene/Ir(111) will serve as the substrates for the studies towards a chemical modification of graphene. The adsorption experiments of Chapter 6 were carried out on both substrates for comparison. The chemical reaction and intercalation experiments of Chapter 7 and 8 are performed on graphene/Ir(111) only, since the evaluation of these experiments requires the appearance of a Dirac cone, as we will show.

2.2.4. Comparison of graphene on Ni(111) and Ir(111)

The two graphene/metal system described above, graphene/Ni(111) and graphene/Ir(111), are good examples for the classification as "strongly" and "weakly" interacting systems. This classification considers the change in the electronic structure of the graphene layer compared to the free-standing phase, the formation of hybridized electronic states between graphene and the metal and the accessibility of these states in experiments. In the absence of an easily accessible quantity, such as the binding energy between the graphene layer and the substrate, the classification only works for one system relative to the other. Following this argument, the two systems can be described as strongly interacting in the case of graphene/Ni(111) and weakly interacting in the case of graphene/Ir(111).

The electronic and crystallographic structure is different for both systems. Graphene/Ni(111) shows an almost perfectly planar graphene layer with a unit cell of the same size as free-standing graphene. The electronic structure is heavily disturbed by the band interaction of the nickel $3d$ and graphene π-bands. The Dirac cone, is destroyed due to the band interaction and replaced by *hybrid states* that form laterally uniformly distributed chemical bonds between graphene and the nickel substrate.

Graphene/Ir(111), on the other hand, exhibits a large supercell due to the lattice mismatch of graphene and the Ir(111) lattice constants, that gives rise to a moiré structure and a height modulation between the different adsorption sites of the unit cell. The height modulation is driven by a different chemical interaction between graphene and the different adsorption sites within the graphene/Ir(111) moiré supercell. The electronic structure is only weakly affected. The Dirac-cone is preserved with only a slight p-doping. No hybridization between Ir $5d$ and graphene π-band is present due to the absence of Ir $5d$ states in the vicinity of the Dirac cone.

However, graphene/Ir(111) shows a noticeable chemical interaction between graphene and the Ir(111) surface in the *hollow* sites of the moiré cell [44]. These hybrid states are not equally distributed over the surface, such as in graphene/Ni(111), but localized in the *hollow* sites of the supercell. The formation of hybrid states as such is, however, a similarity between graphene/Ni(111) and graphene/Ir(111), that has the potential to make these two structures a well comparable system in terms of *interaction strength*. The number of these hybrid states on the surface is limited by the *hollow* sites of graphene/Ir(111) and the amount of the manifestation of these hybrid states is likely to be weaker, because of the larger distance between graphene and the Ir(111) substrate, compared to graphene/Ni(111). We will see that the hybrid states are relevant for the adsorption of molecules on graphene and both the number of hybrid states and their manifestation will be shown to determine the strength of the adsorption.

3. Adsorbates

3.1. Introduction

The present section intends to give an overview of the terminology used to describe adsorption on surfaces. It also provides insight into some experiments to understand the energetics and kinetics of adsorbates on surfaces. First, a general description about the energy regimes of the bonds of adsorbates to a surface will be given, followed by a quick overview about the growth mechanisms and methods to determine desorption enthalpies from kinetic experiments. A good introduction into this field of surface physics can be found in refs . [92–94] and references therein.

3.2. Adsorbates on Surfaces

The adsorption of molecules on a surface can exhibit different types of interaction. The weakest among those is the *Van-der-Waals* (VdW) interaction. This type of adsorption is driven by fluctuating dipoles that form spontaneously in the electron distribution cloud around a molecule. The dipole formed on one molecule can then induce an image dipole on its bonding counterpart, i.e. another molecule or a metal surface. The strength of such a bond is weak, on the order of up to 500 meV or 50 kJ/mol, since no electrons are shared between the bonding partners. The VdW interaction is a diffuse interaction, in contrast to, for example, the directed hydrogen bond, such as found in water which exhibits a fixed dipole. The strength of the VdW interaction, i.e. the spontaneous dipole moment p_A, depends strongly on the distance of the two bonding partners r, the polarizability α of the molecule and the spontaneous dipole of its counterpart p_B:

$$p_A \propto \alpha p_B \cdot r^{-3}. \tag{3.1}$$

Since p_A is acting on p_B and vice versa, the VdW interaction scales to the power of r^{-6} for two individual molecules and decreases quickly for larger distances. A description of the potential energy curve was given by Lennard-Jones [95] as

$$V = 4\epsilon \left[\left(\frac{\sigma}{r}\right)^{12} - \left(\frac{\sigma}{r}\right)^{6} \right] = \epsilon \left[\left(\frac{r_m}{r}\right)^{12} - 2\left(\frac{r_m}{r}\right)^{6} \right], \tag{3.2}$$

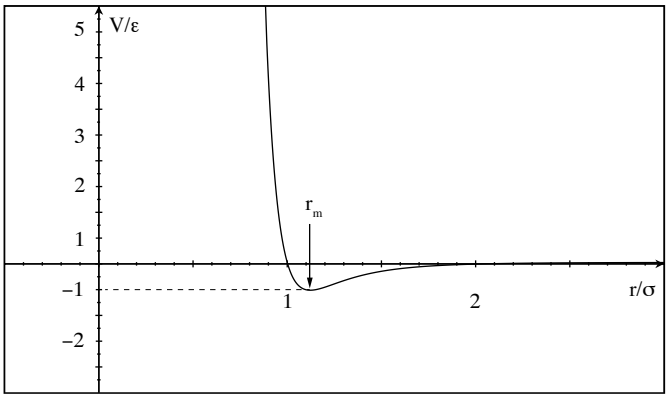

Figure 3.1. – Illustration of the [12,6] Lennard-Jones Potential with indicated minimum energy distance $r_m = 2^{\frac{1}{6}}\sigma$.

where ϵ is the depth of the potential well, i.e. the attractive interaction, σ is the finite distance for which the particle-particle potential is zero and r is the distance between the bonding partners. The second formalism is a representation of the Lennard-Jones potential with the minimum energy distance $r_m = 2^{\frac{1}{6}}\sigma$. The corresponding plot of a Lennard-Jones potential is shown in Figure 3.1. The first term with a r^{-12} dependence is the Pauli repulsion that comes into play for very short interatomic distances. The situation is slightly different for adsorption on a metal surface: The spontaneous dipole of the molecule p_A leads to an image dipole of the same size as p_A inside the metal. Hence the interaction depends only on the distance as r^{-3}. This allows VdW interactions to extend much further away from a metal surface, compared to the case of two interacting molecules. Bringing an adsorbate to the surface will induce VdW interactions in a range of typically 3 Å. In this distance to a surface (r_m), the potential energy surface exhibits a "physisorption minimum". The better an adsorbate is polarizable, the stronger the VdW interaction can get. This is especially true for large atoms, where the outermost electron shell is less strongly bound to the core than for small atoms. However, also delocalized systems, such as π-systems can interact relatively strongly via VdW interactions. Physisorbed species on surfaces are usually relatively mobile due to the weak interaction and large distances. In heterogeneous catalysis, physisorption generally is a precursor state prior to chemisorption where directional bonds can be formed from a molecule adsorbed in the physisorption minimum.

Real chemical bonds, formed between an adsorbate and the surface, are called chemisorption bonds. The description is similar to the bond of two atoms in order to form a molecule, where one partner of the bond is the adsorbate and the other part of the bond is a localized or delocalized electronic state of the surface. In case of a transition metal, this

could be a d orbital of the metal surface; in the case of graphene, we will see that this can also be a hybrid state of graphene π- and substrate d-states. The formalism is similar to the formation of a bond between atoms and will hence just be given very briefly here. The bond between the adsorbate and the metal shall be described by the Hamiltonian H where the solution is a linear combination of the wave functions ψ of the metal (m) and adsorbate (a) electronic states and the corresponding orbital coefficients c.

$$\psi = c_m\psi_m + c_a\psi_a \tag{3.3}$$

In order to simplify the solution of the SEQ, we define the following terms.

$$E_m = \int \psi_m^* H \psi_m dr, \tag{3.4}$$

$$E_m = \int \psi_a^* H \psi_a dr \tag{3.5}$$

and

$$-V = E_m = \int \psi_m^* H \psi_a dr = E_m = \int \psi_a^* H \psi_m dr. \tag{3.6}$$

The direct overlap integral S will be neglected for now.

$$S = \int \psi_m^* \psi_a dr = 0. \tag{3.7}$$

The SEQ then reads

$$H(c_m\psi_m + c_a\psi_a) = E(c_m\psi_m + c_a\psi_a), \tag{3.8}$$

the orbital coefficients c can be obtained by multiplying from the left with ψ_a^* and ψ_m^*, respectively, and integrating. This gives

$$\int \psi_a^* H \psi dr = c_m E_m - c_a V = E(c_m + S c_a). \tag{3.9}$$

The exact solution of the orbital coefficient is not of interest here. To obtain a solution, the determinant coefficient matrix has to vanish, i.e.

$$\begin{vmatrix} E - E_a & V - ES \\ V - ES & E - E_m \end{vmatrix} = 0. \tag{3.10}$$

Remembering that $S \approx 0$, the solution is found to be

$$E_{1,2} = \frac{E_a + E_m}{2} \pm \sqrt{\left(\frac{E_a + E_m}{2}\right)^2 + V^2} = \frac{E_a + E_m}{2} \pm \Delta, \tag{3.11}$$

where $E = \frac{E_a + E_m}{2}$ is the average energy of the newly formed state plus or minus a splitting of Δ, with 2Δ as the total splitting between the two states. We have obtained a solution of a positive and negative linear combination of the two individual electronic states of the

adsorbate and the metal surface and hence the formation of a bonding and anti-bonding electronic state between the surface and the adsorbate.

For a more realistic description of the adsorption complex (it may be seen as a big molecule), the band character of the electronic states of the substrate has to be taken into account. The energy state of the adsorbate (E_a) is a localized electronic state with an infinitely small width (like a δ-function). The metal electronic d states have a narrow energy width around E_m. The metal sp bands give rise to a constant shift and to a broadening of the density of states of the bonding and antibonding "orbitals" of the adsorption complex.

Since we deal here with real chemical bonds, e.g. an electron transfer between the bonding partners and the formation of new electronic states, the bonding distances are shorter and the binding energies are larger compared to physisorption. The binding energy may even be strong enough to loosen the bonds within the adsorbate itself, giving rise to the possibility of dissociative adsorption. The electrons of the surface d states are shared between the unoccupied states of the adsorbate molecule, which typically weakens the bond inside the adsorbate. This also leads to a lower activation energy for dissociation. The formation of ammonia from N_2 and H_2 is a famous example of this concept (see for example: Ertl, *Reactions at Solid Surfaces* 2010 [96]).

So far, the terms of physisorption and chemisorption have been discussed individually. However, these two concepts are linked. Prior to chemisorption, any adsorbate will go through the physisorption minimum of potential energy surface before actually binding to the substrate.

A less trivial observation is the formation of bonds and the corresponding rearrangement of adsorbate and substrate electronic states, without the formation of a *strong* bond measured in quantity of kJ/mol or eV/atom. The adsorption of N_2 on Ni(110) [97, 98] is a good example. Here, the adsorption of N_2 leads to the appearance of new hybrid states between the adsorbate and the surface in an energy range that is typically considered to be physisorption (e.g. 0.4 eV [98]). Upon adsorption, a surface chemical bond is formed that heavily changes the appearance of the intramolecular orbitals but is still weak. Nilsson *et al.* [98] showed that the molecular orbitals of the adsorbate are rearranged and redistributed over the molecule in a way that the HOMO and LUMO of N_2 partly survive, and in addition new hybrid states (located mostly on the adsorbate molecule) that participate in the bond are formed. On the other hand, this formation of hybrid state also causes the σ-bond (the N-N single bond) to change drastically, which introduces a repulsive force into the system and weakens the adsorption strength to the substrate.

What should be concluded from this is that the magnitude of adsorption energy does not necessarily cause or exclude the formation of interatomic electronic states. A chemical bond can be formed by electron exchange but is not necessarily linked to a large binding

energy. We will see that, for the discussion of water and ammonia adsorbed on graphene, this is of importance.

3.3. Adsorption and Desorption Kinetics

Several factors influence the adsorption and desorption of a molecule or an atom on a surface, i.e. the environment (e.g. temperature) as well as the adsorbate and the surface properties. Consider a molecule that is moving towards a surface: Its kinetic energy has to be transformed into heat or another energy carrier, e.g. electron-hole pairs, in order to prevent reflection. Then the molecule has to find a position where the environment is suitable for adsorption: a place has to be vacant and supply the electronic environment for physisorption or chemisorption. If a molecule finally sticks to the surface, its remaining internal energy has to be transferred in order to prevent immediate desorption. These considerations already show the complexity of an adsorption process, neglecting the fact that the experimental detection of adsorption also affects the adsorption (and desorption) probability, i.e. by photon-induced desorption.

Approximations are hence needed to simplify the problem and find models that may explain the experimental observations. This section intends to give an overview about simple formalisms of adsorption and desorption kinetics in order to examine the experiments presented below.

A very simple model assumes that an adsorbate stays on a surface whenever it impinges on an empty site on the surface. This model is due to Langmuir and connects the dose of a molecule (in the unit Langmuir L, being $1 \cdot 10^{-6}$ Torr·s or $1.33 \cdot 10^{-6}$ mbar·s) with the coverage on the surface. In this model it is also assumed that the molecule does not desorb again. Even though this is a strong simplification, it offers the possibility to quantify the amount of adsorbates on a surface relative to another dose, even if not every molecule sticks on the surface, assuming that the sticking probability (or better coefficient) is constant for different coverages.

The adsorption rate based on the Langmuir model can be written as the change of the surface coverage Θ over time:

$$\frac{d\Theta}{dt} = S\frac{dN}{dt} = S\frac{p}{\sqrt{2\pi m k_b T}}. \tag{3.12}$$

Here, N is the number of molecules that hit the surface, which can be derived from the pressure p, the mass m and the temperature T. In this formula, a term is included which is called the sticking coefficient S that is assumed to be 1 in the Langmuir model. However, the sticking coefficient can be obtained in the form

$$S_0 = (1-\Theta)^n = c(1-\Theta)^n \cdot e^{-\frac{E_a}{k_B T}}. \tag{3.13}$$

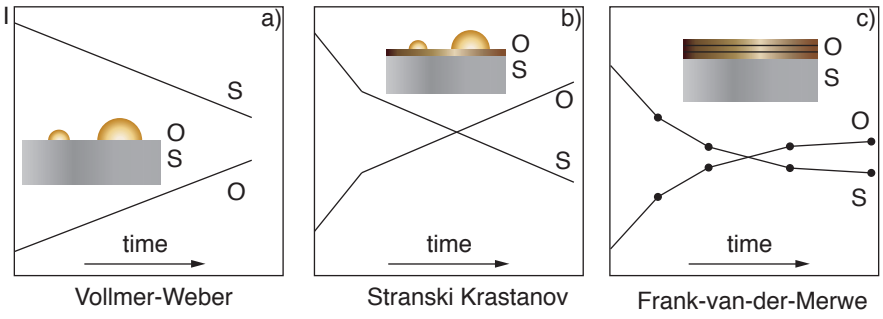

Figure 3.2. – Schematic growth plots for Volmer-Weber growth (a) Stranski-Krastanov growth (b) and Frank-van-der-Merve growth (c). These representations are adopted from ref. [101] and illustrate the growth by Auger emission spectroscopy of deposited metal films.

S_0 is the sticking coefficient of the clean surface, n is the order of the adsorption kinetics and c relates the sticking coefficient S_0 to the activation energy distribution of the adsorption energy E_a. For the latter this takes into account that a molecule "bounces" back if it cannot get rid of its kinetic energy, even if it is adsorbed at first. The order n takes into account that the adsorption actually has to find an adsorption site (for the order $n = 1$) or it may undergo a surface reaction, such as dissociation (in this case $n = 2$). For the latter, two dissociation products have to find an adsorption site after the break-up, which influences the adsorption probability hence in a quadratic dependence.

Note that this model is very simple and does not take into account that, for example, physisorption states act as a precursor, which does affect the sticking coefficient with surface coverage. An example for a change of the sticking probability for different surface coverages can be found in ref. [99] for the adsorption of N_2 on tungsten.

The growth of adsorbate layers on a surface is not only characterized by the amount of adsorbates that stick to it in a specific time interval, but also on the kind of stacking on the surface. Several growth modes have been observed and a good overview can be found in refs. [100–102]. Figure 3.2 summarizes the growth modes, visualized and described in these early references by the method Auger electron spectroscopy of the growing films. The growth measured can proceed in several ways:

a) **Volmer-Weber** (VM) growth describes a growth mechanism of small particles sticking to each other, forming small clusters that grow on the surface. The particles grow with subsequent dose of adsorbates on the surface. This mode is possible when the lateral interactions between the adsorbates (cohesion) are stronger than the bond to the substrate for example (adhesion).

b) **Stranski-Krastanov** (SK) growth is similar to VM growth, but prior to cluster growth, the formation of one (or several) closed monolayer occurs. The crystallites

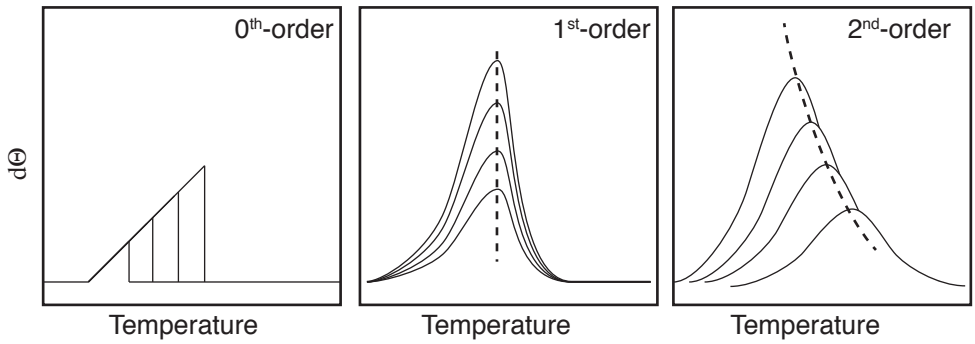

Figure 3.3. – Idealised representation of 0^{th}-, 1^{st} and 2^{nd}-order desorption kinetics for different amounts of adsorbed molecules.

for the cluster growth are formed on top of this monolayer of the adsorbate. It is assumed that lattice distortions of lattice mismatched systems lead to the transition from a two-dimensional layer growth to cluster growth after one or several monolayers.

c) **Frank-van-der-Merwe** (FM) growth is the opposite to the VM growth. Here only monolayers are formed layer by layer. This mode requires the lateral interaction (cohesion) to be weaker than the adhesion to the substrate.

All these growth modes require the possibility for the adsorbates to diffuse on the surface to some extent. The diffusion can occur in a physisorption state or if the remaining energy after the adsorption process is still high enough to overcome the diffusion barrier. If this is not possible, the atoms stick where they are and form clusters, without prior diffusion [102, 103].

The desorption process is basically the reverse process of adsorption. If the molecules desorb individually (neglecting the lateral interactions), the Langmuir model is an appropriate approximation. The desorption rate gan be given in analogy to eq. 3.12 as the *Wigner-Polany* equation:

$$-\frac{d\Theta}{dt} = \nu\Theta^n \cdot e^{-\frac{E_d}{RT}}. \tag{3.14}$$

Here, E_d is the activation energy of the desorption, Θ is the coverage to the order of n and ν is a frequency factor that takes into account that not all molecules desorb but an "attempt" frequency is needed for the desorption. This frequency is usually on the order of a typical vibrational frequency for a molecule adsorbed on a surface of $\nu \approx 10^{13}\, s^{-1}$.

This desorption formalism is the basis for a simple but effective technique, called thermal desorption spectroscopy (TDS). Here a specified amount of surface coverage (defined by the dose of the adsorbate to the adsorbate to the surface) is desorbed by heating up a surface with a constant heating rate. The amount of desorbed molecules is measured as a rise of partial pressure, ideally recorded with a mass spectrometer set at the characteristic

mass of the adsorbate. In a TDS experiment it is crucial to know the order of desorption because it determines the kind of analysis one has to carry out. Possible orders are (see also Figure 3.3):

- **0^{th}-order:** Here the desorption rate is limited by the area of desorption. It also means that the number of desorbing molecules has to be larger than the number of desorbing sites. In this case, TDS shows a series of spectra for different coverages, where the maximum desorption rate scales with the amount of molecules to be desorbed.

- **pseudo-0^{th}-order:** The spectra of such a kinetic order are equal to 0^{th}-order but the reason for such a mechanism is different. Here, much stronger cohesion forces are present than adsorption to the substrate, which have to be broken before desorption. Water on graphite is an example for such an mechanism [104]. The desorption enthalpy in this particular case is determined by the sublimation enthalpy of the intermolecular hydrogen-bonds, a quantity that is close to the desorption enthalpy of ice.

- **1^{st}-order**: Here the temperature maximum and the position of the desorption peak are independent of the coverage, since the desorption happens where there is a place for desorption, neither limited by a small desorption area nor by a reaction prior to desorption.

- **2^{nd}-order and higher**: If higher orders are present, this means that a reaction has to take place prior to the desorption. This can be a recombination reaction of dissociated molecules or products from heterogeneous catalysis. Orders higher than two are rare since the order explicitly describes the number of participants in one elementary step of the reaction (not from the reaction series). In the corresponding desorption spectra for different coverages, the maximum desorption rate scales logarithmically with the amount of molecules to be desorbed.

The TDS spectra can be interpreted in different ways. Often one is interested in the activation energy of the desorption E_d. The simplest method is the Redhead method [105] for 1^{st}-order desorption kinetics, given as:

$$E_d = RT_{max}\left[\ln\left(\frac{v_1 \cdot T_{max}}{\beta}\right) - \ln\left(\frac{E_d}{RT_{max}}\right)\right]. \tag{3.15}$$

In this approach, the last term can be approximated by a constant of 3.64 with an error of less than 1.5% for $10^8 < v_1/\beta < 10^{13}K^{-1}$.

For 0^{th}- and 2^{nd}-order, an Arrhenius plot of $\ln(d\Theta_{max})$ vs. T^{-1} for different coverages yields E_d as the slope of the Arrhenius plot:

$$\ln\left(\frac{dp}{dt}\right) = \ln\left(\frac{v_n}{\beta}\right) - \frac{E_{des}}{RT}, \tag{3.16}$$

In practice the desorption is automatized by a programmed heating of the sample, to ensure a constant and linear temperature rise. The method is then called temperature programmed desorption (TPD) spectroscopy. This method is used in Chapter 6 to the study of water and ammonia adsorbed on graphene/Ni(111) and Ir(111).

Part II.

Experimental Background

4. Spectroscopy and Microscopy

4.1. Photoelectron Spectroscopy

4.1.1. Basic Theory of Photoemission

This chapter will provide an insight into the basic theory of photoemission, as used for the spectroscopic analysis of the system studied described above. It will begin with a phenomenological approach to the photoelectric effect as used for photoelectron spectroscopy and will later provide a simple mathematical derivation of the physical process. In addition the experimental setup and the basic analysis of the spectra will be described in order to provide a basis for the understanding of the results shown in this work.

Photoelectron spectroscopy (PES) is a material-sensitive probe of the electronic structure of matter. It measures electrons which have been emitted from matter and are analyzed by their velocity and emission direction (and possibly also by their spin). The physical effect of this technique is the photoelectric effect, discovered by Hertz in 1885 [106] and later explained by Einstein [107]. It describes the process of the emission of an electron (from this point on called *photo*electron), after the matter has been irradiated by light. The energy of the photon of the monochromatic light is transferred to the electron, giving it the ability to leave the potential of the atom core. The resulting velocity of the electron is a direct probe of the energetic situation of the electron within the atom, meaning the binding energy which kept the electron attached to the atomic core. This effect can be described by a simple formula:

$$E_{kin} = h\nu - E_B - \Phi. \tag{4.1}$$

E_{kin} represents the kinetic energy of the electron leaving the matter. $h\nu$ is the energy of the photon which is used to excite the electron, E_B is the binding energy and is, in case of a solid, the energy difference of the electron to the highest occupied electronic state, e.g. the Fermi level (or the valence band maximum in semiconductors). Φ is a material-specific constant, called the work function. The work function represents the energy which is needed for the electron to leave the remaining attractive field of matter towards the vacuum. It consists of the chemical potential of the bulk material (in case of solids) and the dipole barrier at the surface.

The kinetic energy of the electron represents the velocity of the emitted electron and is, as equation 4.1 shows, a direct probe of the binding energy. Hence it is possible to analyze the emitted electrons by their velocity to get an energy spectrum of the electronic structure. This is only an approximation because the creation of a hole state in the solid affects the observed binding energy. For electrons close to the highest occupied electronic state, it turns out that in some cases such energy spectra are very close to the electronic ground state band structure of a solid, which can then be studied in great detail.

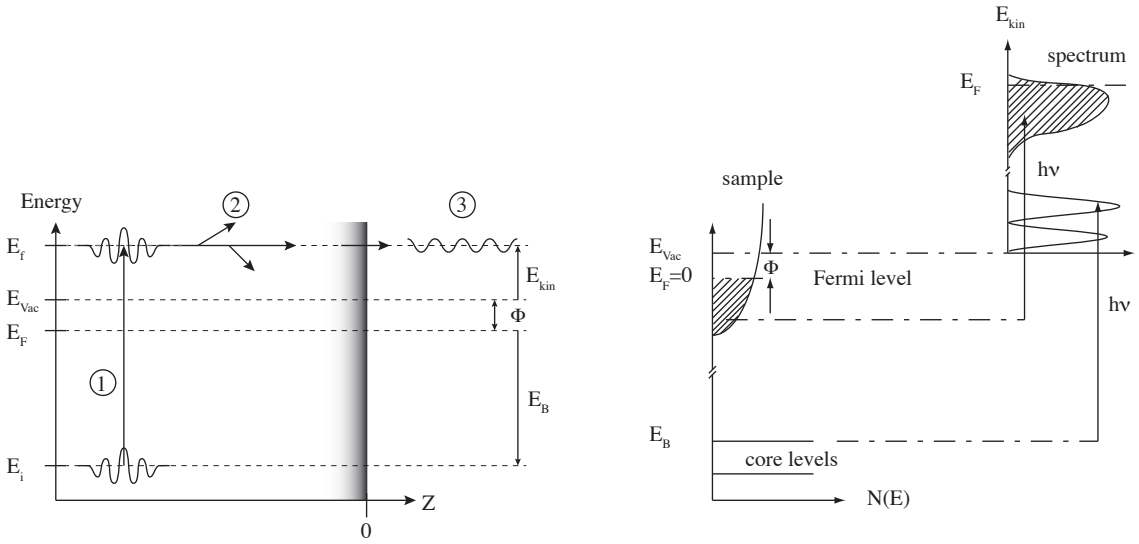

Figure 4.1. – **Left:** Schematic diagram of the photoemission process as described by the three step model. ① is the optical transition from an initial wavefunction with energy E_i into a final state with energy E_f. ② is the propagation towards the surface. The electron can undergo elastic and inelastic scattering. ③ is the escape from the solid into the vacuum with energy E_{kin}. This drawing is adopted from [108]. **Right:** Schematic energy diagram of the photoelectron spectrum. The binding energy E_B is transferred into the energy E_{kin} according to the energy conservation law in equation 4.1.

Before considering the mathematical basis of the photoemission process, a simplified schematic picture of the electron behaviour during the excitation is often used: the three-step-model. This model describes the photoemission process from a metal substrate divided into three hypothetical steps; it is often used in textbooks, even though it has been shown in the early days of this technique that this is a rough approximation, and the one step model, while being much more complex, is the correct one [109–111].

1. **The excitation process** is the first step in this model. The electron (inside an *initial* state) is excited by a photon of proper energy into an unoccupied (*final*) state, given by the matrix element in equation 4.2. This excited state consist now of an electron and a hole at the former electron position.

2. **The propagation** of the electron to the metal surface is the second step in this model. The electron might undergo scattering processes during its propagation to the surface. This is partly responsible for the asymmetry of electronic core level lines. Mathematically speaking, the electron wavefunction is affected by a complex component of the wave vector which results in a damping of the wave function.

3. **The escape of the electron** is the last and final step of this process. In this stage the out-of-plane momentum of the electron is affected by the attarcting surface potential of the solid. This leads to a major change in the out-of-plane momentum and to a challenging task if this momentum is of interest. The in-plane momentum of the electron is, however, unaffected in this process and can be analyzed in order to obtain information about the two dimensional electronic band structure of a solid surface. The out of plane component can, however, be calculated in addition by assuming a free electron final state.

Figure 4.1 illustrates the three-step model of electron excitation during the photoemission process. At this point it may be stated again that the real process of photoemission does not contain three distinguishable steps but is rather an instantaneous process of only one step [109–111]. However, in order to understand the different influences on the photoelectron, it serves very well.

The photoemission process is a complex mechanism, since electrons are not isolated in a solid but part of a many-body system. However, starting with a single particle picture is a good approximation for resolving the basis of the process. The many-body influence will be briefly introduced at the end of this part. Electronic states in solid mater are quantum states. Hence, quantum mechanics must to be used to describe the process. An optical excitation, as it takes place in the first hypothetical step of the photoemission process, is typically expressed by *Fermi's Golden Rule*, as derived by first order perturbation theory. In case of photoemission, the photoemission current J_κ is expressed by the transition of an electron from its ground state wave function Ψ_i into a final state wave function Ψ_f

$$J_\kappa(\hbar\omega) = \frac{2\pi}{\hbar} \sum_s |\langle \Psi_f^{\kappa,s} | \Delta | \Psi_i \rangle|^2 \delta(\epsilon_\kappa - \epsilon_s - \hbar\omega). \tag{4.2}$$

Here, κ is the momentum of the photoelectron and $\Psi_{i/f}$ are the initial and final state wave functions, respectively. The transitions are taken into account for all possible excitations, presented by their quantum numbers s. $\epsilon_\kappa = E_{kin} = \hbar^2\kappa^2/2m_e$ is the kinetic energy of the electron with momentum κ, and ϵ_s is the energy of such a quantum state s. $\hbar\omega$ is the energy of the light. The delta function δ represents the energy conservation and relates the measured kinetic energy of the photoelectrons to the binding energy of the electrons in the solid. Δ is the perturbed Hamiltonian of the excited system, as derived from the

unperturbed Hamiltonian as

$$\hat{H}_0 = \frac{\hat{p}^2}{2m_e} + eV(\hat{r}), \tag{4.3}$$

including the transformation of the momentum operator

$$\hat{p} \rightarrow \hat{p} - \frac{e}{c}\vec{A}. \tag{4.4}$$

$\vec{A}$ is the vector potential of the electromagnetic field of light, acting on the system during the excitation process. For a one-electron system, the Hamiltonian is given as

$$\begin{aligned} \hat{H} &= \frac{1}{2m_e}\left[\hat{p} - \frac{e}{c}\vec{A}\right]^2 + eV(\hat{r}) \\ &= \frac{p^2}{2m_e} + \frac{e}{2m_e c}(\vec{A}\cdot\hat{p} + \hat{p}\cdot\vec{A}) + \frac{e^2}{2m_e c^2}\vec{A}^{\,2} + eV(\hat{r}) \\ &= \hat{H}_0 + \hat{H}_{PE}. \end{aligned} \tag{4.5}$$

From equation 4.3 the perturbation operator of the photoemission process can be obtained:

$$\hat{H}_{PE} = \frac{e}{2m_e c}(\vec{A}\cdot\hat{p} + \hat{p}\cdot\vec{A}) + \frac{e^2}{2m_e c^2}\vec{A}^2. \tag{4.6}$$

At this stage some simple approximations are introduced to go on further with the interpretation. The quadratic term A^2 can be neglected since it represents only large intensity photoemission, which are for example present in laser PES. Further we can make use of the Coulomb gauge with the relation $[\vec{p}, \vec{A}] = -i\hbar\nabla\cdot\vec{A} = 0$. This brings equation 4.6 to a much simpler form:

$$\hat{H}_{PE} = \frac{e}{2m_e c}\vec{A}\cdot\hat{p}. \tag{4.7}$$

4.1.2. Photoemission from Core Level States

A major part of the results presented in this work deals with (soft) x-ray photoelectron spectroscopy. Since the binding energy of the inner shell core levels of light elements fits into this energy range, it provides a useful technique to determine the electronic structure of solids and/or adsorbates in the system of interest. Hence a quick look at the photoemission from strongly bound states is required. For such a case a single electron picture is sufficient to describe the physical process of photoemission.

The wave functions of the initial and final electronic state can be written as the product of the single electron orbitals $\phi_{i,k}$ and $\phi_{f,k}$ multiplied by their orbital coefficient C and the electron wave function $\Psi_i^k(N-1)$ and $\Psi_f^k(N-1)$ for the remaining $(N-1)$ electron system:

$$\Psi_i(N) = C\phi_{i,k}\Psi_i^k(N-1) \tag{4.8}$$

and

$$\Psi_f(N) = C\phi_{f,k}\Psi_f^k(N-1). \tag{4.9}$$

For simplicity, the orbitals of the initial and final state are assumed to be identical before and after the excitation. This is known as the *frozen orbital approximation* and thus the integral in equation 4.2 can be rewritten as:

$$\langle \Psi_f | \Delta | \Psi_i \rangle = \langle \phi_{f,E_{kin}} | \Delta | \phi_{i,\kappa} \rangle \langle \Psi_f^k(N-1) | \Psi_i^k(N-1) \rangle, \tag{4.10}$$

with $\Psi_f^k(N-1) \approx \Psi_i^k(N-1)$. The transition matrix element in this approach is a simple one-electron element. The reader can convince himself easily that, based on this equation, the measured binding energy from eq. 4.1, $E_{B,\kappa} = -\epsilon_\kappa$, is the negative Hartree-Fock energy of the orbital κ (see eq. 4.2), also called as *Koopmans binding energy*.

This simplistic model can be the basis for the interpretation of core level photoemission for chemical fingerprinting of common elements. Assuming that the photoemission probes approximately the orbital and the orbital-energy of the *initial* state, due to the frozen orbital approximation, we can compare the electron binding energy upon changes of the chemical environment. This gives the possibility to assign changes in the binding energy of a core level state due to changes in the Fermi level (e.g. doping) or due to changes in the chemical environment of the probed matter (e.g. chemical shift).

However, this model is very simple, reality is more complex and therefore this theory has to be developed a bit further. Spectroscopy often reveals the case that the orbitals are not frozen but undergo relaxation and correlation during photoionization, leading to additional shifts and line shape changes of the spectroscopic lines. One part is the contraction of the orbital due to the core-hole and polarisation screening-induced charge transfer, which can be seen as relaxation. A second part is the electron-electron correlation which is, however, in most cases only of minor importance. The *Koopmans binding energy* therefore has to be corrected towards $E_{B,\kappa} = -\epsilon_\kappa + \Delta\epsilon_{relax}(+\Delta\epsilon_{correlation})$.

Another common approach is the so-called *sudden approximation*, which takes into account the existence of several possible final states. It is therefore capable of explaining spectroscopic features such as satellite lines. This approximation can be included in eq. 4.10 by summing up over all possible transitions in all possible final states:

$$\sum_s c_s = \sum_s \langle \Psi_{f,s}^k(N-1) | \Psi_i^k(N-1) \rangle \tag{4.11}$$

where $|c_s|^2$ is the probability that the excitation leaves the system in the excited state s.

4.1.3. Photoemission from Valence States

The energy region of photoelectrons of low binding energy (roughly 0-20 eV) reflects the electronic states of the valence region. This region does not exclusively contain localized electronic states such as the core levels. This would only be true for atoms and molecules.

If extended periodic systems are under investigation, the electronic structure shows delocalized electronic states, known as bands. The excitation process is more complicated to describe as for the core level states. Since the excited photoelectrons do not end up located in a specific orbital, but in a delocalized conduction band, the corresponding final state is a sum over all possible final states. Moreover, the periodic nature of the crystal lattice requires more restrictions in the mathematical description. First, the basic photoemission theory will be extended to photoemission in delocalized and periodic systems and also within the *sudden approximation*. Then, a quick look into many body physics will be provided to completely derive the final formula describing the observable of photoemission.

Up to equation 4.7 the transition matrix element contains the unperturbed Hamiltonian and the perturbation from the electric field of light and the transition probability is restricted to energy conservation. Now, the perturbation potential $V_{int} = \hat{H}_{PE}$ will be extended to periodic systems. The transition probability is now written as

$$P_{fi} \propto |\langle \Psi_f^{(N)} | V_{int} | \Psi_i^{(N)} \rangle|^2 \delta(E_f^{(N)} - E_i^{(N)} - \hbar\omega). \tag{4.12}$$

$\Psi_{f,i}^{(N)}$ are the N-electron wave functions and the δ-function conserves the energy upon the optical transition from an initial state $E_i^{(N)}$ to a final state $E_f^{(N)}$ through light of energy $\hbar\omega$. At this stage, second quantization is introduced where V_{int} is written as

$$V_{int} = \sum_{\mu,\nu,\vec{k},\vec{k\prime}} M_{\nu\mu}(\vec{k},\vec{k\prime}) c_\nu^\dagger(\vec{k}) c_\mu(\vec{k\prime}), \tag{4.13}$$

with the matrix element of the optical transition defined by

$$M_{\nu\mu}(\vec{k},\vec{k\prime}) = \langle \phi_\nu^{\vec{k}} | V_{int} | \phi_\mu^{\vec{k\prime}} \rangle. \tag{4.14}$$

$c_\nu^\dagger(\vec{k})$ and $c_\mu(\vec{k\prime})$ are the fermionic creation and annihilation operators for an electron described by Bloch waves $\phi_\mu^{\vec{k}} = u_{\mu,\vec{k}} \cdot e^{(-i\vec{k}\cdot\vec{r})}$ in a band μ (in this case no longer a simple orbital) having a vector $\vec{k}$ and an energy $\epsilon_{\mu\vec{k}}$. Again, the vector potential of monochromatic light with wave vector $\vec{q}$ with the spatial dependence $\vec{A}(\vec{r}) = \vec{A}_0 \cdot e^{(\vec{q}\cdot\vec{r})}$ transfers the matrix element into

$$\begin{aligned} M_{\nu\mu}(\vec{k},\vec{k\prime}) &= \frac{e}{im} \int d^3r u_{\nu\vec{k}}^*(\vec{r}) e^{(-i\vec{k}\cdot\vec{r})} \vec{A}_0 \cdot e^{(\vec{q}\cdot\vec{r})} \cdot \vec{\nabla} u_{\mu\vec{k\prime}}(\vec{r}) e^{(i\vec{k\prime}\cdot\vec{r})} \\ &= \frac{e}{im} \int d^3r e^{-i(\vec{k}-\vec{k\prime}-\vec{q})\cdot\vec{r}} u_{\nu\vec{k}}^*(\vec{r}) \vec{A}_0 \cdot (\vec{\nabla} + i\vec{k\prime}) u_{\mu\vec{k\prime}}(\vec{r}). \end{aligned} \tag{4.15}$$

The integration is defined for the whole space but since periodic systems are investigated, the translation symmetry of the Bravais lattice can be taken into account via the relation

$u_{\mu\vec{k}\prime}(\vec{r}) = u_{\mu\vec{k}\prime}(\vec{r}+\vec{R})$, where $\vec{R}$ is the Bravais lattice vector, leading to

$$\begin{aligned} M_{\nu\mu}(\vec{k},\vec{k}\prime) &= \frac{e}{im}\sum_{\vec{R}}\int_{unit} d^3r e^{-i(\vec{k}-\vec{k}\prime-\vec{q})\cdot(\vec{r}+\vec{R})} u^*_{\nu\vec{k}}(\vec{r})\vec{A}_0\cdot(\vec{\nabla}+i\vec{k}\prime)u_{\mu\vec{k}\prime}(\vec{r}) \\ &= \frac{e}{im}\underbrace{\sum_{\vec{R}} e^{-i(\vec{k}-\vec{k}\prime-\vec{q})\cdot\vec{R}}}_{N\delta_{\vec{k}-\vec{k}\prime-\vec{q},\vec{G}}}\int_{unit} d^3r e^{-i(\vec{k}-\vec{k}\prime-\vec{q})\cdot\vec{r}} u^*_{\nu\vec{k}}(\vec{r})\vec{A}_0\cdot(\vec{\nabla}+i\vec{k}\prime)u_{\mu\vec{k}\prime}(\vec{r}) \\ &= N\delta_{\vec{k}-\vec{k}\prime-\vec{q},\vec{G}}\int_{unit} d^3r e^{-i(\vec{k}-\vec{k}\prime-\vec{q})\cdot\vec{r}} u^*_{\nu\vec{k}}(\vec{r})\vec{A}_0\cdot(\vec{\nabla}+i\vec{k}\prime)u_{\mu\vec{k}\prime}(\vec{r}) \\ &= N\delta_{\vec{k}-\vec{k}\prime-\vec{q},\vec{G}}\,\tilde{M}_{\nu\mu}(\vec{k},\vec{k}\prime). \end{aligned} \tag{4.16}$$

The last line of equation 4.16 now contains the information of the lattice periodicity. The integration is performed over the unit cell, multiplied by the number of unit cells N to be considered. The delta function again provides momentum conservation and the lattice vector is explicitly taken into account via $\vec{G}$.

In summary the transition matrix element has been extended towards periodic systems via the introduction of the lattice periodicity $\vec{G}$ of the Bravais lattice. This means that the photoelectron of a momentum $\vec{k}$ is equal to a photoelectron of the neighbouring (reciprocal) unit cell if the difference in their momenta is given by $\vec{G}$. It also means that one only has to consider the reduced (back-folded) Brillouin zone for the electronic structure of the valence region. The equations also show that the matrix element M can easily be transformed into its periodic equivalent $\tilde{M}$, just by summing up over all unit cells.

At this point the *sudden approximation* is introduced: If the photoelectron of momentum $\vec{k}_f$ has enough energy $\epsilon_{\alpha\vec{k}}$, then it immediately decouples from the remaining $(N-1)$ electron system and can be described by the wave function $\Psi^{(N-1)}_{f,s}$, where s accounts for the existence of different excited states. Bringing this information together, the remaining $(N-1)$ electron system has an energy $E^{(N)}_{f,s} \cong E^{(N-1)}_{f,s} + \epsilon_{\alpha\vec{k}}$. The final state expression may now be written as the sum over all possible excited states s from the product of the the annihilation operator $c^\dagger_\alpha$ times the $(N-1)$ electron wave function: $|\Psi_f\rangle \simeq \sum_s c^\dagger_\alpha(\vec{k}_f)|\Psi^{(N-1)}_{f,s}\rangle$. The photoemission transition probability in the solid is then derived as

$$\begin{aligned} P_{if} \propto& \sum_{s,\alpha}\sum_{\mu,\nu,\vec{k},\vec{G}} |\tilde{M}(\vec{k},\vec{k}-\vec{q}-\vec{G})|^2 |\langle\Psi^{(N-1)}_{f,s}|c_\alpha(\vec{k})c^\dagger_\nu(\vec{k})c_\mu(\vec{k},\vec{k}-\vec{q}-\vec{G})|\Psi^{(N-1)}_i\rangle|^2 \\ &\times\delta(E^{(N)}_{f,s}-E^{(N)}_i-\hbar\omega) \\ \propto& \sum_{\mu,\nu,\vec{G}} |\tilde{M}(\vec{k},\vec{k}-\vec{q}-\vec{G})|^2 \sum_s |\langle\Psi^{(N-1)}_{f,s}|c_\mu(\vec{k},\vec{k}-\vec{q}-\vec{G})|\Psi^{(N-1)}_i\rangle|^2 \\ &\times\delta(E^{(N)}_{f,s}-E^{(N)}_i-\hbar\omega) \end{aligned} \tag{4.17}$$

The second line was obtained by using the commutation relation for the fermionic operators $[c_\alpha(\vec{k}_f), c^\dagger_\mu(\vec{k})] = \delta_{\vec{k}_f,\vec{k}}\delta_{\alpha,\nu}$ and the fact that $c_\alpha(\vec{k})$ annihilates an electron above E_F after the excitation by the photon with $\hbar\omega$. Since this does not take place we can write $c_\alpha(\vec{k})|\Psi_i^{(N)}\rangle = 0$. As a consequence, the one-electron states $\phi_\nu^{\vec{k}}$ and $\phi_\mu^{\vec{k}}$ are directly involved in the transition, which will be of importance for the discussion of many-body effects.

The δ-function describes the energy conservation of the measured electron kinetic energy ϵ_{kin} to the initial state binding energy. We have already introduced the *sudden approximation*, hence the energy situation can be described as $E_f^{(N)} \simeq E_f^{(N-1)} + \epsilon_{\nu\vec{k}}$. We may introduce the chemical potential $\mu = E^{(N)} - E^{(N-1)}$ and the energy of the many body excitation in the solid left in the excited state s, $\epsilon_s = E_f^{(N)} - E_i^{(N)}$, an expression which can be seen as the excitation's "binding energy". At last we may define the kinetic energy of the photoelectron as $\epsilon_{kin} = \epsilon_{\nu\vec{k}} - \mu$. We can obtain the δ-function as

$$\delta(E_{f,s}^{(N)} - E_i^{(N)} - \hbar\omega) = \delta(\epsilon_{kin} - \epsilon_s - \hbar\omega). \tag{4.18}$$

Now we arrive at the expression for the photoemission intensity, for the first step of the photoemission process. The PE intensity for a photoelectron with momentum $\vec{k}_f$ (approximately, see below) and kinetic energy (binding energy) ϵ_{kin} is proportional to the transition probability of the optical transition (taking the Fermi-Dirac distribution N_F into account, since we only probe occupied states):

$$\begin{aligned} I(\epsilon_{kin}, \vec{k}_f) \propto & \sum_{\mu\nu\vec{G}} |M_{\mu\nu}(\vec{k}_f, \vec{k}_f - \vec{q} - \vec{G})|^2 \cdot N_F(\hbar\omega - \epsilon_{kin}) \\ & \sum_s |\langle\Psi_{f,s}^{(N-1)}|c_\mu(\vec{k}_f, \vec{k}_f - \vec{q} - \vec{G})|\Psi_i^{(N)}\rangle|^2 \delta(\epsilon_{kin} - \epsilon_s - \hbar\omega). \end{aligned} \tag{4.19}$$

Since ARPES is usually performed with low excitation energies, the escape depth is small. Hence the second step will lead to only minor distractions in the photoemission process by scattering in the bulk layer. However, the behaviour of the photoelectron when escaping the surface itself, is of importance. Due to refraction, the momentum of the photoelectron is affected. Figure 4.2 illustrates the problem. The surface potential acts on the photoelectron, lowering the kinetic energy ϵ_{kin} by the amount of the work function Φ into $\epsilon_{kin}^{vac} = E_{kin}$; hence, the out-of-plane momentum $\vec{k}_\perp$ or $\vec{k}_z$ is not conserved. However, the in-plane momenta $\vec{k}_\parallel$ are conserved, which allows us to calculate from the emission angle of the photoelectron the in-plane momentum according to

$$\vec{k}_{\parallel,x} = \sqrt{\frac{2m}{\hbar}}\sqrt{\epsilon_{kin}^{vac}}\sin\Theta\cos\beta. \tag{4.20}$$

The second component $\vec{k}_{\parallel,y}$ is observed in our experiment by variation of the angle β (see Figure 4.3). The out-of-plane momentum is not of interest for the work presented in this

thesis. However, it may be noted that such a component might be computed assuming a free electron final state.

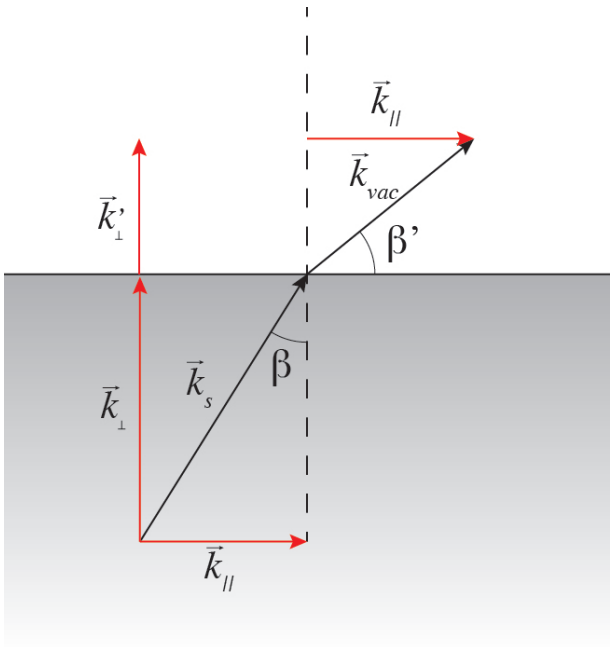

Figure 4.2. – Electron refraction from a solid into the vacuum. The out-of-plane momentum of the electron is affected by the dipole barrier and the attractive field of the surface during its escape. The electron momenta parallel to the surface are not affected and are conserved during photoemission.

We have derived an expression to describe core level and valence band photoemission intensity and the necessary assumptions to evaluate the experimental data. However, the electrons have so far been assumed as isolated and not interacting with the system apart from the crystal potential. Reality is much more complicated since the real measured quantity is not the ground state electronic band structure but the so called *spectral function*. This contains many body aspects and will now be briefly described.

Basic Formalism of Many Body Physics and the Spectral Function

In photoemission, a common approximation is to treat the measured spectra as the ground state band structure of an electron with momentum $\vec{k}$. To some extent this is a good approximation. However, in reality the spectral function $A(\vec{k},\omega)$, of momentum $\vec{k}$ and energy (frequency) ω from the excited system is probed, which will be shown very briefly in this section. The spectral function can derived as [112]

$$A(\vec{k},\omega) = -\frac{1}{\pi}\frac{|\Im\mathrm{m}\Sigma(\vec{k},\omega)|}{\Big[\omega - \epsilon(\vec{k}) - \Re\mathrm{e}\Sigma(\vec{k},\omega)\Big]^2 + \Big[\Im\mathrm{m}\Sigma(\vec{k},\omega)\Big]^2}. \tag{4.21}$$

In this equation, the so-called self energy Σ relates the bare band dispersion $\epsilon(\vec{k})$, with the lifetime of the excitation $\Im\mathrm{m}\Sigma(\tilde{\mathrm{k}},\omega)$ and the band renormalization $\Re\mathrm{e}\Sigma(\tilde{\mathrm{k}},\omega)$ to the spectral function.

$A(\vec{k},\omega)$ is derived from the imaginary part of the so called retarded Green's function:

$$A(\vec{k},\omega) = -\frac{1}{\pi}\Im\mathrm{m}G^R(\vec{k},\omega) \tag{4.22}$$

The concept of the Green's function, e.g. the probability to find the electron with $\vec{k}_1$ at $t = 0$ in $\vec{k}_2$ at time t, is a widely used tool, for example to describe many body effects in photoelectron spectroscopy. After photo-excitation, the hole is not located in a specific state, but in a continuum of valence band states. The hole can move; this representation has already been introduced in eq. 4.17 by the existence of several final states s. The Green's function (or in this particular case the ground state Green's function) applied to photoemission yields an expression

$$G^0(\vec{k},\omega) = \int d\omega' \left[\frac{A^+(\vec{k},\omega')}{\omega - \omega' - \mu + i\eta} + \frac{A^-(\vec{k},\omega')}{\omega - \omega' - \mu - i\eta}\right], \tag{4.23}$$

where A^+ and A^- are the spectral functions, responsible for inverse and normal photoemission, denoting an $(N+1)$ and $(N-1)$ electron system respectively, and μ is the chemical potential. Here, only A^- is of importance since A^+ is responsible for inverse photoemission. The interested reader may consider the common textbooks for a deeper understanding. We will restrict ourselves to the result: The Green's function can be obtained as

$$G^0(\vec{k},\omega) = G^R(\vec{k},\omega) = \frac{1}{\omega - (\epsilon(\vec{k} - \mu) + i\eta)} \tag{4.24}$$

The imaginary part is a δ like function $i\eta = \delta(\omega - (\epsilon(\vec{k}) - \mu)) = A^0(\vec{k},\omega)$, which is an expression similar to the *Koopmans binding energy*. We end up with an expression for the photoemission intensity, containing now also many-body interactions, which enable us to describe also observations not restricted to the ground state band structure.

$$\begin{aligned} I(\epsilon_{kin},\vec{k}_f) \propto \sum_{i,f} & -\frac{1}{\pi}\frac{|\Im\mathrm{m}\Sigma\vec{k},\omega|}{\left[\omega - \epsilon(\vec{k}) - \Re\mathrm{e}\Sigma(\vec{k},\omega)\right]^2 + \left[\Im\mathrm{m}\Sigma(\vec{k},\omega)\right]^2} \\ & \times \frac{|\tilde{M}_{i,f}|^2}{(k_{i,\perp}^{(1)} - k_{f,\perp}^{(1)})^2 (k_{f,\perp}^{(2)})^2}\delta(\vec{k}_{i||} - \vec{k}_{i||} + \vec{G})\delta(\vec{k}_i - \vec{k}_i + \vec{G}) \\ & \times \delta(\epsilon_f - \epsilon_i - h\nu)\delta(E - E_f + \phi) \cdot N_F(\hbar\omega - \epsilon_{kin}). \end{aligned} \tag{4.25}$$

For a deeper understanding, the interested reader may inspect the textbooks of Hüfner [113], Ibach [114] or Kevan [115], as well as references [83,112,116,117] and the references therein.

4.1.4. Instrumentation and Data Analysis

The Hemispherical Analyzer Phoibos 100/150

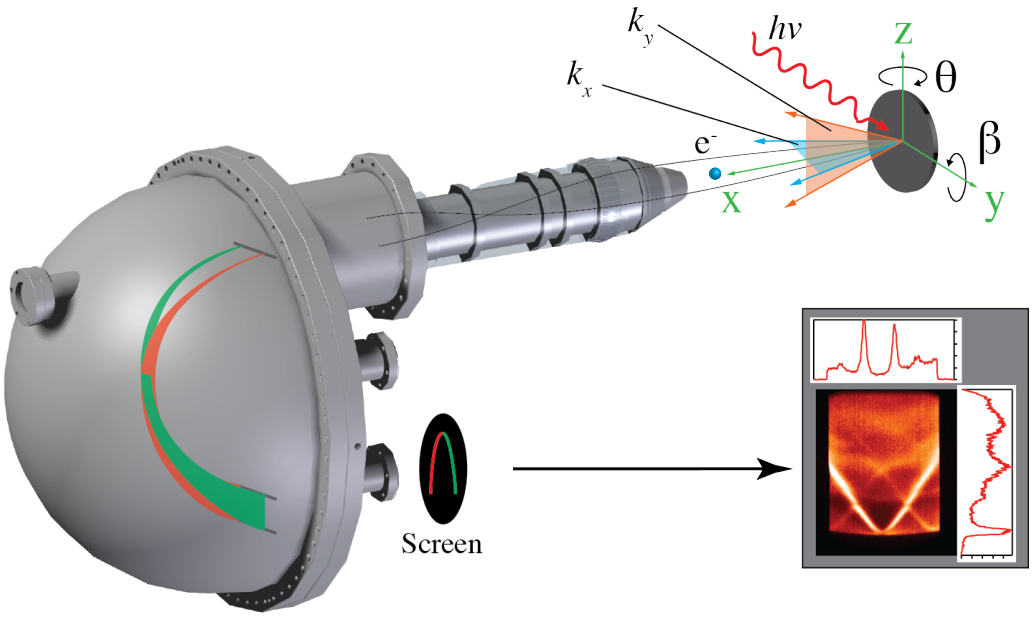

Figure 4.3. – 3D Model of the analyzer and sample geometry alignment. The electrons, ejected from the surface contain two in plane momenta, representing their k_x and k_y components according to their emission angles β and θ, respectively. The lens system guides the electrons into the energy analyzer (hemispheres), where the trajectory of the electrons (depending on the lens mode) preserves the spectroscopic information of the electron emission angle. The electron signal is amplified and projected on a screen. Here, the spectroscopic signal is recorded with a CCD camera from a phosphorous screen and displayed on a computer. The model of the Phoibos 150 is kindly provided by Jörg Oschmann with permission from SPECS GmbH.

The analysis and detection of the photoelectrons was performed with a SPECS Phoibos 100 hemispherical analyzer, produced by SPECS Surface Nanoanalysis GmbH. Such analyzer type, among others, is able to analyze emitted photoelectrons according to their kinetic energy and their emission direction. Figure 4.3 shows a schematic drawing of such an analyzer. It consists of a lens system, entrance and exit slits, two hemispheres and a detector section.

The lens system is responsible for guiding the photoelectrons into the analyzer. They can be focussed in different ways. Mainly two modes are used for photoelectron spectroscopy: The *high magnification mode* and the *angular dispersion* mode:

- The *high magnification* mode guides all electrons within a small region of the sample, independent of their emission angle, into the detector. Therefore, the electrons only

pass the hemisphere section on one horizontal trajectory and can only be analyzed by their kinetic energy. This mode is therefore used for spectroscopy of localized states, such as core levels, since it need not to contain any dispersion information of the electrons. The alignment of the analyzer with the sample and beam position is also done in this mode.

- The *angular dispersion* mode, on the other hand, guides the electrons through the lens system in a way that the information of the emission angle and hence the in-plane momentum of the emitted electrons is conserved, according to the green and red trajectories, labeled in the hemisphere section of Figure 4.3. The direct relation between the angular dispersion of the photoelectrons and the in-plane momentum of the photoelectron is given in eq. 4.20.

Located between the lens and the hemispheres is the entrance slit. This slit is used to exclusively detect photoelectrons in a single plane, meaning a specific horizontal emission angle (see Figure 4.3, the in-plane emission of electrons from the sample is marked as a blue triangle). This is necessary when angular-resolved lens modes are used. Open slits on the other hand can be used for core level data, since no angular information is needed. The slit can be curved or straight if the focussing of the electrons on the entrance slit is small enough. This is indeed true for the high magnification mode. However, in this work only curved slits are used to ensure the energy relation between the center and the edge regions detector, where the photoelectrons are detected.

Potentials of opposite polarities are applied to the hemispheres. The inner hemisphere has a positive potential, attracting the photoelectrons; the outer hemisphere has a negative potential, repulsing the electrons. Electrons of high kinetic energy will be repulsed less from the hemispheres and the trajectory will be closer to the outer hemisphere. They will reach the detector at its lower end. Electrons of low kinetic energy, on the other hand, are repulsed more strongly and their trajectory will be along the inner hemisphere. Choosing the potential of the two hemispheres properly will yield a specific energy window through which selected electrons can travel without hitting the walls or the sides of the exit slit. Due to the spherical character, also the angular information of the incoming electrons is conserved during this kinetic energy analysis process. However, the electron paths are distorted, which requires a correction (see end of this section).

The last part of the analyzer is the detector section. It contains of an electron multiplier, a phosphorous screen and a CCD camera. The electrons which leave the hemisphere through the exit slit, are accelerated into the multi-channel plate (MCP). The MCP multiplies the signal of every electron by creating secondary electrons from electron impact. The increased electron flux is afterwards accelerated onto a phosphorous screen, which images the enhanced electron signal. The image on this screen is recorded by a CCD camera and saved as a picture in the data acquisition software.

Software for Photoemission and -absorption Data Acquisition

The data acquisition software is based on a software package as LabView program written by Eli Rotenberg and Aaron Bostwick at the Advanced Light Source at Lawrence Berkeley National Lab, Berkeley USA. The software enables control over the measurement routines as well as the stepper motors and peripheral instruments, such as the CCD data acquisition camera.

Two measurement modes are used: *fixed* and *swept* mode. The *fixed* mode acquires a picture which is taken from the phosphorous screen on the detector. The energy window and the pass energy of the hemispherical analyzer are kept fixed, which means that a specific angle vs. energy photoemission image is acquired. This mode can be used for the acquisition of valence band data in the angular-resolved modes of the analyzer, but also a specific core level photoemission line can be detected. It is, however, limited to the fact, that in this case the photoemission structure of interest has to be displayed on the phosphorous screen. The phosphorous screen has a limited "energy" size. This implies typically a large pass energy to permit the photoemission to be fully visible. This necessity reduces the spectral resolution due to the limited number of MCP channels and pixels on the CCD camera. The spectra are integrated over time and saved as a picture in the *fits* file format. It is further possible to repeat a certain number of spectra and save the data in a 3D block containing several spectra with $I(E_{kin}, k)$ versus time or versus different experimental geometries, as for example the flipping angle β, resulting in $I(E_{kin}, k_x, k_y)$. The *swept* mode represents a measurement technique where a small pass energy window is swept over a certain range of the electron's kinetic energy. This mode has some advantages over the *fixed mode*, since photoemission structures larger than the pass energy window can be detected, increasing the spectral resolution. The spectra are saved normalized to the number of iterations. The final spectrum A_n is acquired from the single sweeps a_n according to

$$A_n = \frac{\sum a_n}{n}, \tag{4.26}$$

which means the spectra are normalized to the number of scans at the end. Typically, core level data are acquired in this mode but it is in principle possible to use every lens mode in this mode. In our experiments, the valence band region is not taken with this technique but with a different kind of *swept* mode. In order to reduce the effect of regions of different imaging efficiency on the detector, the valence band photoelectron spectra in angular resolved mode are acquired in a way that the complete displayed picture is shifted over the whole detector (see Figure 4.4). This is called *dithered image* and provides a homogeneous photoemission intensity, ruling out darker corridors and spots on the detector screen and MCP. The single spectra are finally combined into one picture with respect to the Fermi level. However, due to the fact that the photoemission spectra are

distorted by the hemispherical and slit system, an intrinsic trapezoid correction has to applied to every so called *dither-step*, as explained earlier.

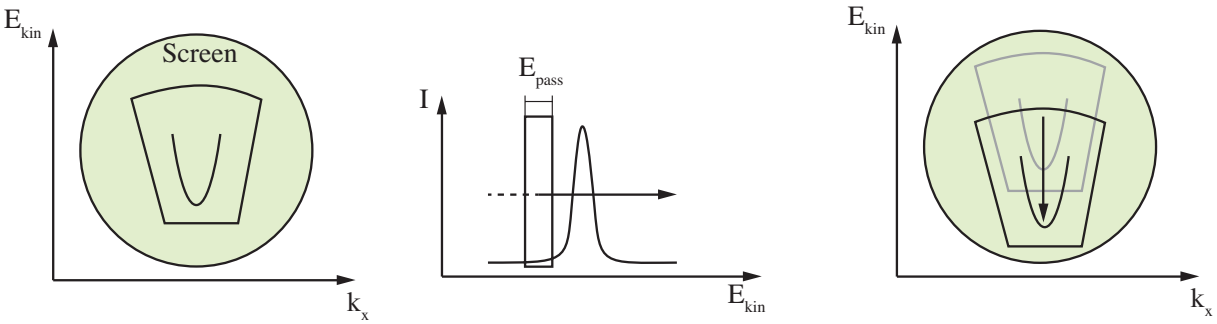

Figure 4.4. – *Fixed* (left) and sweeping imaging modes *swept* (centre) and *dithered* (right) of the data acquisition software.

The Trapezoid and Dispersion Correction for Angular Resolved Lens Modes

The hemispherical analyzer and the slit system lead to a distortion in the image of the photoemission lines on the detector screen. First of all, the hemisphere does not reproduce the incoming electron coordinate directly but towards lower kinetic energies the image is contracted, yielding of the image in a trapezoid shape, such that the horizontal coordinate for low kinetic energies is smaller compared to high kinetic energies. This is an effect of the electron optics. Secondly, the straight entrance slit is reproduced for the same reason as a curved image. This can be directly observed in the raw data as a curved Fermi level. Hence, the data has to be corrected. In case of ARPES data acquired in the dithered swept mode, the trapezoidal correction has to be applied during the measurement after every image step, to ensure the correct combination of the single dither steps. The procedure is an iterative correction, applied first to the trapezoidal distortion. A trapezoid is aligned along the edges of the image (these edges are the reproduction of the entrance slit, distorted by the hemispheres). The trapezoid is then stretched into a rectangular shape. Afterwards, the Fermi level has to be corrected. The straight entrance slit image becomes a ring segment. Hence the Fermi level can be fitted and the fit can then be used to correct the photoemission image collected from the screen. Due to software restrictions, one correction affects the other. Hence, both corrections have to be applied alternatingly, starting with the trapezoidal correction, and repeated until the dispersion of the photoemission lines is correct.

4.2. X-Ray Absorption Spectroscopy

4.2.1. Basics of X-Ray Absorption Spectroscopy

X-ray absorption spectroscopy uses the same effect of photo excitation as photoemission spectroscopy. However, the electrons are not ejected from the solid but are only excited into an unoccupied electronic state. The measured quantity are fluorescence photons or, more commonly, emitted electrons from various decay channels, which fill the created hole after electron excitation. Such a decay channel is the Auger process for example. This method provides a quantity which is directly proportional to the density of the unoccupied atomic or molecular energy states. Hence, this method is an ideal complementary probe together with the photoemission spectroscopy, which gives information about the occupied states.

In the following the basic formalism of x-ray absorption process is presented, and in the next section applied to the special case of near edge x-ray absorption fine structure spectroscopy (NEXAFS). A detailed description can be found in the textbook by Stöhr "NEXAFS Spectroscopy" [118]. A schematical description of the Auger decay process is presented in Figure 4.5. When light of the exact energy between the bound state (e.g. a $1s$ state) and an unoccupied state is applied ($\hbar\omega = E_B$), electrons are excited into the latter. The resulting electron-hole pair (or exciton) relaxes, which releases the excitation energy. This relaxation can occur in various ways. The exciton can recombine, emitting exactly the amount of incorporated energy. This would lead to x-ray emission, which can be detected in x-ray emission spectroscopy. The electron hole in the core state can also be filled by an electron originating from another filled state. Such an event releases, in particular cases, enough energy to emit an electron or a photon of an intermediate energy. The emitted electrons are called Auger electrons and can be detected in an electron collector.

The theoretical description starts with Fermi's golden rule for optical transitions. The transition probability $P_{i,f}$ is given as

$$P_{i,f} = \frac{2\pi}{\hbar} |\langle \Psi_f | \hat{V} | \Psi_i \rangle|^2 \, \delta_f(E). \tag{4.27}$$

$\Psi_{i/f}$ are the initial and final state, respectively. $\delta_f(E)$ forces energy conservation criterium and $\hat{V}$ is the perturbation potential of the incident light. Starting from the transition probability, the x-ray absorption cross section σ_x can be derived from the ratio between transition probability and photon flux:

$$\sigma_x = \frac{P_{i,f}}{F_{\mathrm{ph}}} \tag{4.28}$$

In order to obtain a complete expression for this ratio, a detailed look on the properties of the light is necessary: The excitation of the inner shell electrons is produced by light,

represented by an electromagnetic wave of electric field $\vec{E}$ and vector-field $\vec{A}$. They transform into each other as

$$E = -\frac{1}{c}\frac{\delta \vec{A}}{\delta t}, \tag{4.29}$$

where $\vec{A}$ is given as a plane wave:

$$A = \vec{e}\,\frac{A_0}{2}\left(e^{i(\vec{k}\cdot\vec{x}-\omega t)} + e^{-i(\vec{k}\cdot\vec{x}-\omega t)}\right). \tag{4.30}$$

$\vec{E}$ and $\vec{A}$ are collinear in space and the magnitudes are related by $E_0 = A_0\frac{\omega}{c}$. The number of photons per unit time and and area defines the photon flux:

$$F_{ph} = \frac{A_0^2\omega}{8\pi\hbar c} = \frac{E_0^2 c}{8\pi\hbar\omega} \tag{4.31}$$

The transition probability $P_{i,f}$ can now be further evaluated. The expression for the perturbation term depends on the electric field of the light, given by its vector potential. For the same reason as in eq. 4.7, we only take into account the electric field of light within the Coulomb gauge:

$$\hat{V} = V(t) = \frac{e}{2m_e c}\vec{A}\cdot\hat{p}. \tag{4.32}$$

Using the information and derivations given so far, the transition probability can be written as

$$P_{i,f} = \frac{\pi e^2}{2\hbar m^2 c^2}\; A_0^2|\langle f|e^{i\vec{k}\cdot\vec{x}}\cdot\vec{e}\cdot\vec{p}|i\rangle|^2\delta_f(E). \tag{4.33}$$

This equation can be further simplified by using the dipole approximation $\vec{k}\cdot\vec{x} \ll 1$ or expressed as $|\vec{x}| \ll \lambda/2\pi$. This means $e^{i\vec{k}\cdot\vec{x}} \approx 1$, due to the fact that the wavelength of the excitation is larger than the extension of the core shell. The final expression for the x-ray absorption cross section is then given as:

$$\sigma_x = \frac{4\pi^2}{m^2}\frac{e^2}{c}\frac{1}{\omega}|\langle f|\vec{e}\cdot\vec{p}|i\rangle|^2\;\delta_f(E). \tag{4.34}$$

4.2.2. Near Edge X-Ray Absorption Fine-Structure Spectroscopy

The near edge of the the x-ray absorption spectrum describes an energy range of approx. 20-30 eV, beginning from the first measured transition, named as *absorption edge* or *absorption threshold*. This energy region reflects the low energy unoccupied states of a system. From eq. 4.33, the transition matrix element only acts between states of the same element, otherwise the overlap of the wave functions is zero. Hence, this spectroscopic method is element-specific and the measured spectrum can be approximated by the element-specific projected density of states. This fact makes this method an excellent probe in particular for *low Z* (low mass) elements of the second period of the

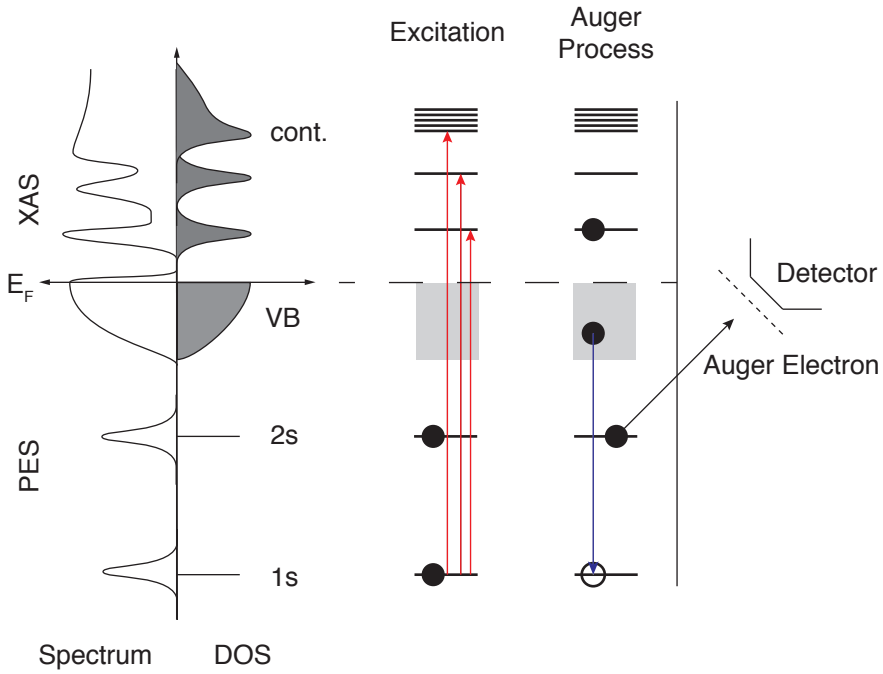

Figure 4.5. – **Left:** Energy diagram for the occupied and unoccupied density of states and sketches of corresponding spectra. The DOS consists of localized core level states (e.g. 1*s*) and the valence band (VB). The unoccupied states may consist of localized electronic or band states and the continuum states above the ionization potential. **Right:** Two-step diagram of a specific Auger process. The excitation of an 1*s* electron into an unoccupied state (labeled transitions in red) creates an electron-hole pair, which may be filled by a valence band electron (blue labeled transition). The energy released by this relaxation emits an electron of an intermediate state, e.g. a 2*s* electron. The electrons are detected by an electron detector.

periodic table. The respective transitions are very sensitive to changes of the chemical and electronic environment of the probed material. Different chemical species may have different resonance energies, which can be detected. As an example related to this work, reference [119] may serve, where Parent *et al.* describe the x-ray absorption ranges of different azide compounds and ammonia. Each individual compound is detected at a specific resonance energy. Chemical interactions may arise as new or vanishing states due to electron (charge) transfer and hence changes in the population of certain states which can be observed in NEXAFS. Wernet *et al.* [120] for example have reported on the example of water/ice transitions, the appearance of new states, depending on the interaction (electron donation) of the water molecules when going from amorphous water to ice.

An important feature of NEXAFS is the direct correlation of the geometry of the incident light and the geometry of the probed states [121]. The interaction of the electric field vector has to fulfil special geometric requirements. Changing the experimental ge-

ometry gives information about the orientation and geometrical distribution of adsorbed molecules or surfaces, such as graphene.

From eq. 4.34 the intensity of a transition is proportional to the transition matrix element

$$I_{if} \propto |\langle f|\vec{e}\cdot\vec{r}|i\rangle|^2 \propto |\vec{e}\cdot\langle f|\vec{r}|i\rangle|^2, \tag{4.35}$$

assuming a linear polarization of the x-rays with direction of the unit vector $\vec{e}$. The dipole matrix element $\langle f|\vec{r}|i\rangle|$ contains only initial and final states and the direction of polarization of the probing light. Since mainly K shell excitations are used for this technique, the initial state can be restricted to a spherical state, given as the $1s$ state $|i\rangle = R_{1s}(r)$. Hence only the final state $\langle f|$ in combination with the direction of the electric field vector of light is of importance. It becomes immediately clear that only if the overlap between the spatial orientation of a final state (the empty orbital) and the electric field vector of light is non-zero, the signal is also not zero. Vice versa, if the field vector and the orbital orientation are collinear, a maximum overlap is achieved.

4.2.3. Instrumentation and Data Analysis

In this work, NEXAFS spectra were acquired using two different experimental setups: one is located at MaxLab in Lund, Sweden and one is located at BESSY II in Berlin, Germany.

At MaxLab, the experimental chamber at beamline D1011 (a bending magnet or dipole beamline) is equipped with an multi-channel plate (MCP) electron detector. It collects electrons emitted from the sample, photoemission as well as secondary or Auger electrons; only fast electrons due to a retarding potential of -100-150 V on a mesh in front of the MCP entrance are collected. Hence, this system is a high pass filter. This means that the detector is surface sensitive, since slow electrons usually originate from scattering events inside the bulk material. In this setup, the photoemission lines which are always present under photon irradiation, result in a constant background.

The BESSY II endstation is equipped with a hemispherical analyzer, allowing to selectively collect electrons of a specific kinetic energy in a defined energy window, determined by the pass energy. This is, in contrast to the MCP detector, a band pass filter. Here, also slow electrons are neglected. However, photoemission lines may result in extra features or artefacts in the spectrum. Figure 4.6 shows a two dimensional plot of photon energy versus electron kinetic energy. Vertical lines of constant kinetic energy are Auger electron emission lines, whereas diagonal lines are photoemission lines of constant $E = \hbar\omega - E_{kin}$. In this experimental setup, the photoemission lines do not result in a constant background signal but may cross the region of interest, hence, the kinetic energy has to be chosen accordingly. The kinetic energy range has to be selected such that no photoemission line crosses the region of interest. In case of graphene on Ir(111), a kinetic energy of

$E_{kin} = 260\,\text{eV}$ is suitable. Only the pre-edge energy range is crossed by a weak PE line, so that the spectrum itself is not affected.

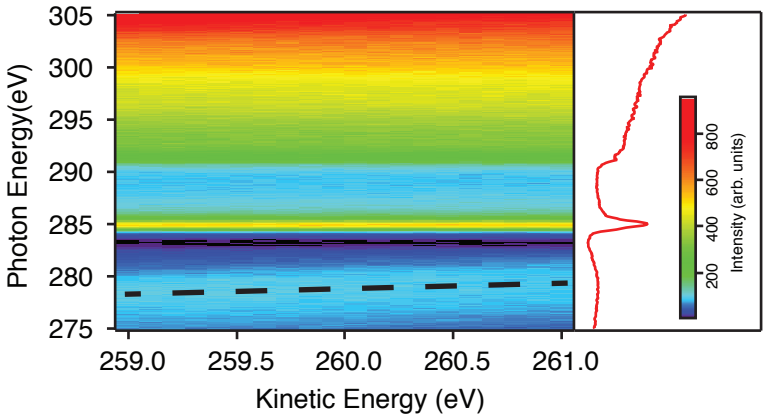

Figure 4.6. – Intensity map of photoelectron spectra for Auger emission lines: photon energy vs. kinetic energy of the photoelectrons. The vertical line on the right represents a NEXAFS spectrum at a fixed kinetic energy. Diagonal lines represent PE spectral lines which scale with the excitation and kinetic energy. The presented excitation energy corresponds to the carbon K absorption edge, typically starting around 285 eV photon energy. In the energy range of 275-280, a diagonal photoemission line crosses the map (dashed black line). The energy spectrum (uncorrected) on the right hand side reveals an artefact from this PE line, resulting in a broad feature. The map however shows that this feature is not crossing the Auger emission lines, which makes this energy range suitable for NEXAFS spectroscopy

The NEXAFS spectra evaluation requires a specific data treatment. Since the light is interacting with the optical elements in the beamline, the intensity of the incident light on the sample is not constant, but may suffer from absorption on the optical elements. This is most critical for the carbon K absorption edge. The beamline optics are contaminated with carbon, which leads to an intensity reduction in the respective energy range of carbon K transitions on the order of a factor of 10 or more. Hence a normalization spectrum has to be acquired and the spectrum has to be corrected accordingly. The normalization spectra are basically spectra of the same photon energy region, without the sample. They can be acquired on a clean or different sample, or with a diode, measuring the beamline flux. The spectra are further corrected by subtracting the pre-edge background and normalizing on the last point of the spectrum. The corrected spectrum S_c is given as

$$S_c = \frac{\frac{S}{S_0} - S_N(start)}{S_N(end)}, \tag{4.36}$$

where S is the acquired spectrum, S_0 is the reference spectrum and $S(x)$ are the start

and end value of the normalized spectra. It may be necessary that the spectrum has to be corrected for a linear background. This does not affect the resulting energy but accounts for comparable intensities. The linear background is typically fitted to the pre-edge area, where the sample influence is negligible.

4.3. Scanning Tunneling Microscopy

4.3.1. The Tunneling Effect

The method of scanning tunneling microscopy is a surface science technique, able to image a conducting surface down to the atomic scale without contact of the probe to the sample. The method is based on the physical phenomenon of *quantum mechanical tunneling*. In this method, an atomically sharp apex of a metallic tip is approached towards the probed surface until *quantum mechanical tunneling* appears. The tip is moved along the surface and the response of the tip to the surface is acquired while a potential is applied between the sample and the tip (see Figure 4.7 right). The resulting current is a function of the local density of states (LDOS), the voltage applied and the position of the tip position in three dimensions. The method was developed by Gerd Binning and Heinrich Rohrer in 1981 [122]; they were awarded the Nobel prize in physics in 1986. In this section, a basic understanding of the tunneling effect and the method will be provided, containing the basic theory, the instrumentation and the data analysis procedures.

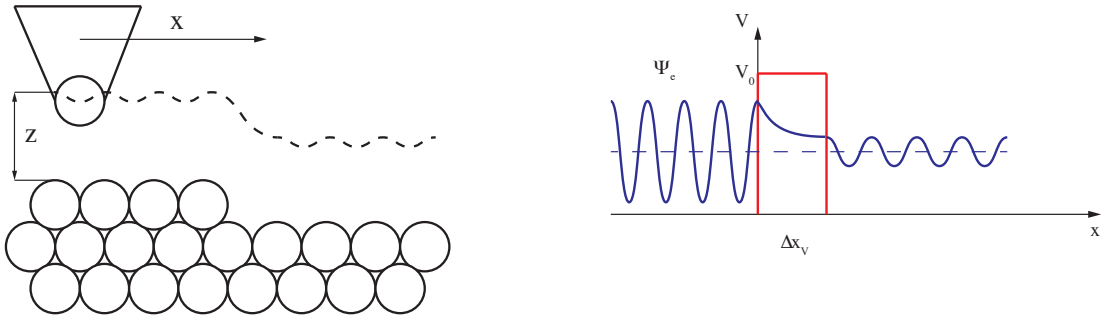

Figure 4.7. – **Left:** Schematic diagram of a tunneling microscopy experiment (constant current). The tip is approached to the surface until tunneling appears. Moving the tip along the surface images the surface by the response of the probe to the measured tunneling current. **Right:** Schematic energy diagram of the quantum tunneling effect. A particle displayed as a wave hits a potential barrier, whose potential V_0 is larger than the kinetic energy E of the particle. The solution of the Schrödinger equation to this problem implies an exponential decay function for the particle-wave within the barrier. The thickness of the potential barrier determines the energy which is remaining on the particle after Δx_V. This energy is proportional to the probability that the particle can exist on the other side of the potential barrier.

Quantum tunneling describes the effect of a particle's ability to penetrate a (finite) potential barrier without overcoming the specific potential energy of the barrier. In classical mechanics, this is impossible. In a classical hill picture, a ball cannot overcome the hill if

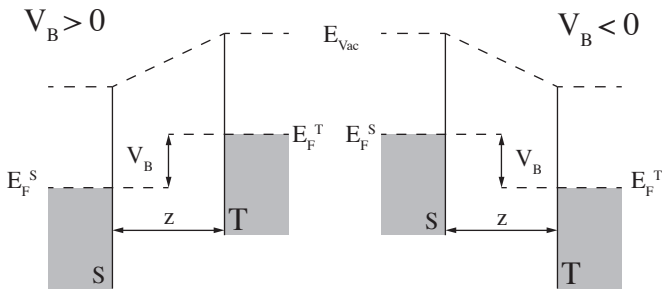

Figure 4.8. – Schematic energy diagram of a tunneling situation with a bias voltage applied. **Left:** The Bias voltage is positive on the tip. **Right:** The bias voltage is positive on the sample.

the kinetic energy of the wall is lower than the potential energy at the top of the hill. The particle-wave dualism of quantum mechanics, however, permits under specific conditions, that the particle penetrates the barrier. Figure 4.7 illustrates the tunneling effect with a simple model. A particle, displayed as a wave with energy $E < V_0$ hits the potential barrier with energy V_0. Since the potential is finite, the wave can be described within the potential by an exponentially decaying wave function, similar to the solution of the particle in a box with walls of a finite potential. The thickness of the barrier determines the suppression of the wave function amplitude by the exponential function used to describe the electron in the barrier. The difference in the amplitude of the particle wave function at the end of the barrier (after Δx_V) determines the probability for the particle to continue as a wave after the potential barrier. The remaining part of the wave is reflected from the wall. This has two interesting consequences. First, particles may penetrate every wall with a probability that is non-zero (however, it becomes very improbable for even microscopic length scales). Secondly, the thinner the wall, the more particles can penetrate the barrier. In an STM experiment, this directly determines the scale of the tunneling current with respect to the distance of a tip to a surface. The particle is here the electron that moved from the tip into the surface (or vice versa), when a bias voltage (representing the kinetic energy of the classical example) is applied at the finite barrier (vacuum). The overall tunneling current I_T can be expressed as

$$I_T = \int_0^{eV_B} \rho_S(E)\rho_T(E - eV_B) \cdot T(E, eV_B)dE. \tag{4.37}$$

Here eV_B (also commonly called U_T) is the applied bias potential. The terms $\rho_{S,T}$ represent the local density of states at the energy E of the sample and the tip, respectively. $T(E, eV_B)$ is the tunneling probability for electrons of energy E and applied potential eV_B:

$$T(E, eV_B) = \exp\left(-\frac{2z\sqrt{2m}}{\hbar}\right)\sqrt{\frac{\phi_S + \phi_T}{2} + \frac{eV_B}{2} - E} \tag{4.38}$$

z is the distance between the tip and the sample, $\phi_{S,T}$ are the work functions of the sample and tip, respectively and m is the mass of the electron. Looking at equation 4.38, it becomes obvious that the current depends on two main quantities: The tip distance z, and the local density of states of the sample and the tip. The distance exponentially influences the strength of the tunneling current: the closer the tip, the higher the tunneling current. The local density of states, on the other hand, is often mistakenly believed to measure the atom positions in an STM experiment. In one of the first STM images presented by Binnig [123], spherical shapes were observed which were interpreted as the atom positions of the Si atoms on the Si(111) surface. This interpretation is correct (the atomic ordering of the surface) under the condition that the image displays the electron density distribution around the atom positions and not the atom itself. In some cases the intensity modulation in an STM picture is not directly related to the real-space topology. A special example is found in graphene/Ir(111). The moiré structure can be observed in direct and inverse contrast, depending on the bias voltage. Under special conditions the electron rich positions of the *fcc* and *hcp* adsorption sites appear brighter (indicating a higher tunneling current) than the atop sites (see Figure 2.9). However the structure is exactly opposite as described in Section 2.2.3.

4.3.2. Instrumentation and Data Analysis

Figure 4.9 shows a schematic representation of the Aarhus STM head as developed by Besenbacher and coworkers [124] and manufactured by SPECS GmbH, Berlin. The probing unit and the approach system are combined within a small tube, located inside an aluminium block. This block is vibrationally decoupled from the UHV system by three springs. It can be fixed for cooling or transfer and released for measurement. The STM head itself is a combined approach and scanning part. The labels in Figure 4.9 show the main parts. The tip (4) is spot-welded on a small metal plate (5) which sits on the x-y piezo table (6). The centre rod (7) is clamped inside the "inchworm" approach motor (9). The wiring is not presented in the drawing. The whole probe head (4-6) is insulated from ground and connected to the pre-amplifier of the electronics.

The STM can be operated in two different modes: *constant height* and *constant current*. In a *constant current* experiment, the feedback loop always adjusts the tip-sample distance in a way that the tunneling current is constant. Changes in the tunneling current are corrected by changing the potential on the z-piezo. The modulation of height is then read out from each measured position of the tip relative to a chosen setpoint. This mode is mainly used in the present work. A benefit of this technique is the safety and stability of

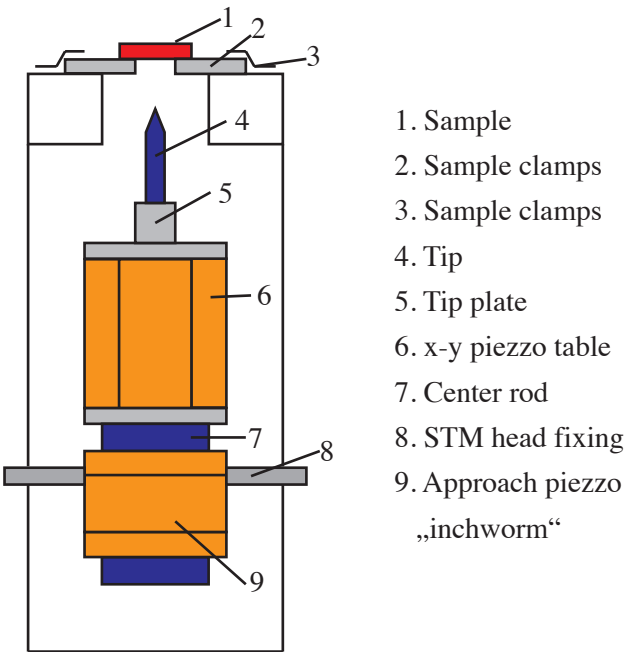

Figure 4.9. – Schematic drawing of the Aarhus STM head. The drawing is adopted from the publication of Besenbacher *et al.* [124].

the tip. Large steps on the surface are recognized by the feedback loop and the position of the tip is adjusted in order to avoid crashes. The second mode is the *constant height* mode. Here the distance between the sample and the tip is fixed and the measured quantity is the tunneling current. Modulations in the surface electron density cause a change in the transition probability and hence in a different tunneling current.

The images acquired have to be corrected in order to extract the physically correct representation of the surface. First, the images have to be plane-corrected since a small deviation from perfect planar mounting of the sample always appears. If step edges appear in the image it is possible to post-correct the slope in order to have a flat step like appearance. The probably most powerful correction is the fast Fourier transformation (FFT). In a FFT correction, the image is transferred from real space into reciprocal space. The result is a picture which is comparable to a LEED image. Periodic structures appear as diffraction like spots. With this method it is possible to obtain information about periodicities and structures. Removal of structures in the FFT and back-transformation into real space can lead to a smoothing or to a removal of periodic distortions, e.g. vibrations or electrical oscillations.

5. Sample Preparation and Experimental Stations

5.1. The BESSY-II Endstation and Beamline

The experimental station at BESSY II is a mobile endstation for variable operation at different beamlines. It consists of three individual linked chambers. The analysis chamber (enhanced red in Figure 5.1) is equipped with a hemispherical PHOIBOS electron energy analyzer 100 (enhanced yellow) manufactured by SPECS GmbH. For details of the analyzer, see Section 4.1.4. The angle between the analyzer and the incoming beam is 50 °. The sample geometry is controlled with a 5+1 axis manipulator, able to adjust the sample in Cartesian coordinates x, y and z, as well as the rotation of the sample surface normal in the plane of the analyzer (θ) and the out-of-plane tilting (β); these axes are controlled via stepped motors. The rotation around the sample azimuth (ϕ) is achieved by a manual rotational feedthrough. The manipulator head is also equipped with a 0.25 mm Ta-filament for radiation heating of the sample up to 550 °C, a gold-film for spectroscopic rough alignment of the experimental chamber at the beamline and a quartz microbalance. The manipulator can be cooled down to below 100 K with liquid nitrogen. A liquid nitrogen vessel is connected with the cryostat through an isolated pumping line, delivering the liquid nitrogen down to the bottom of the manipulator rod, just above the sample holder. The liquid nitrogen is pumped through the system with a vacuum pump. Pointing to the centre of the chamber (and therefore to the sample in measurement position), two evaporator ports are installed, allowing the collection of real time spectra during deposition of materials. The two evaporator ports are equipped with gate valves separating the UHV from the evaporator. This allows service and exchange of the evaporators without breaking the vacuum in the analysis chamber. The chamber also contains a LEED and a QMS residual gas detector. At the connection to the beamline, a photodiode is installed, which can be moved into the beam, to collect flux curves for the flux normalization of the acquired NEXAFS data. The base pressure achieved in this chamber is better than $7 \cdot 10^{-11}$ mbar. The preparation chamber is equipped with a manipulator head that is electrically insulated from ground for electron beam heating with positive potential on the target. The electron source is a 0.25 mm tantalum filament on a linear motion device

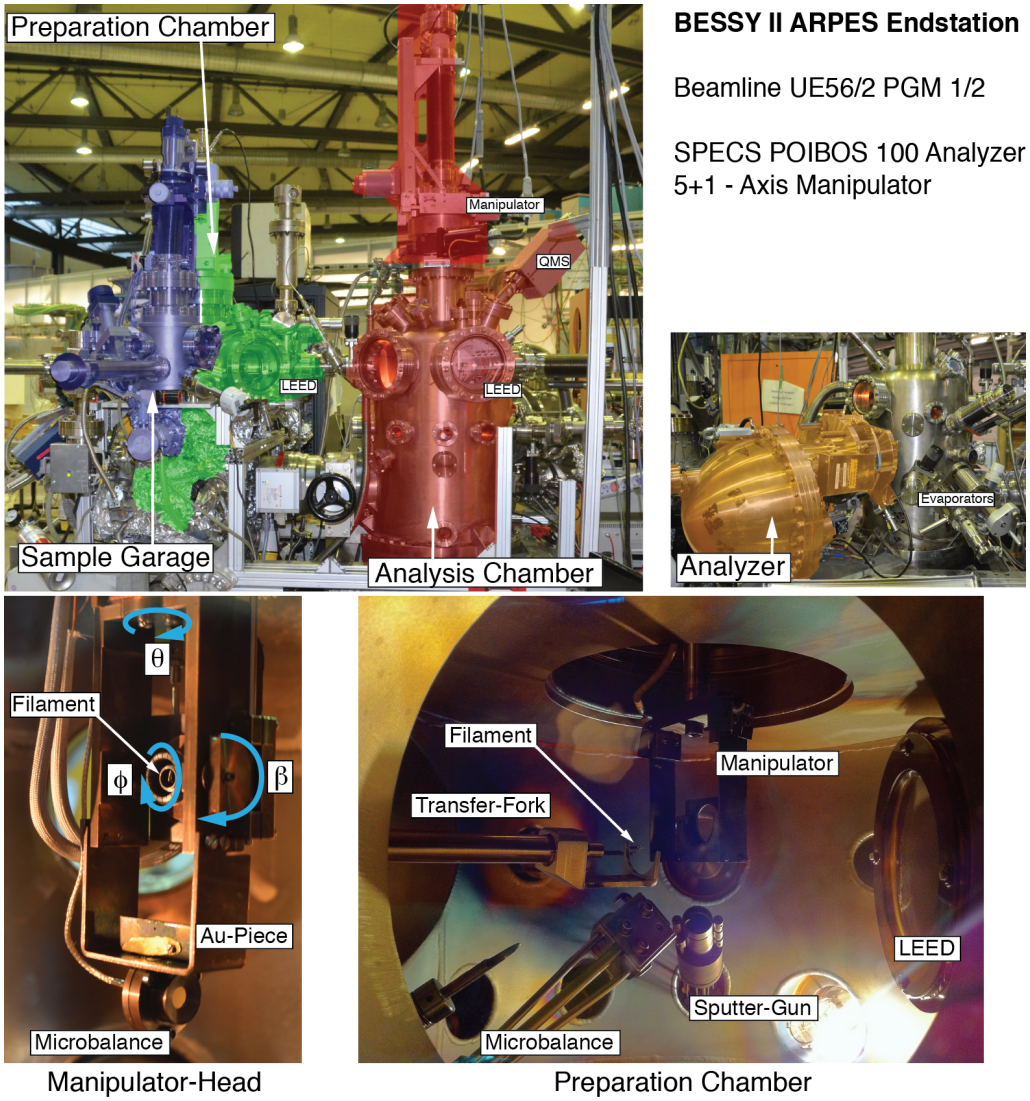

Figure 5.1. – Photographs of the BESSY II end-station, showing the analysis chamber (red), preparation chamber (green) and the sample garage (blue). The analyzer is highlighted in yellow. The manipulator head consist of three rotational axes, tilting β, rotation θ and azimuth ϕ.

in order to reach the back of the sample in the manipulator. The chamber further consist of an analog QMS, a LEED, a quartz microbalance, two evaporator ports and a sputter gun. The base pressure in the preparation chamber is better than $4 \cdot 10^{-11}$ mbar.

The sample garage with the load lock is a small chamber with 12 sample holders under high vacuum conditions of $5 \cdot 10^{-8}$ mbar.

In this work, the machine was used only on the UE56/2 undulator beamline at BESSY II in Berlin-Adlershof at its two branches PGM-1 and -2 [125]. These beamlines are equipped with two undulators and a plane grating monochromator [126]. The photon

energies reachable at this beamline are in the range of 60-1300 eV. The photon flux is about 10^{14} photons/s on a spot size of 10×10 and $10 \times 100\,\mu$m, for PGM-1 and PGM-2, respectively. In the particular case of the PGM-1 beamline, this corresponds to a photon flux density of about $3.3 \cdot 10^{19}$ photons/cm^2·s at 450 eV photon energy [127]. The corresponding flux curves for the UE56/2 beamline are given in the appendix in Figure A.1.1.

5.2. The-MaxLab Endstation

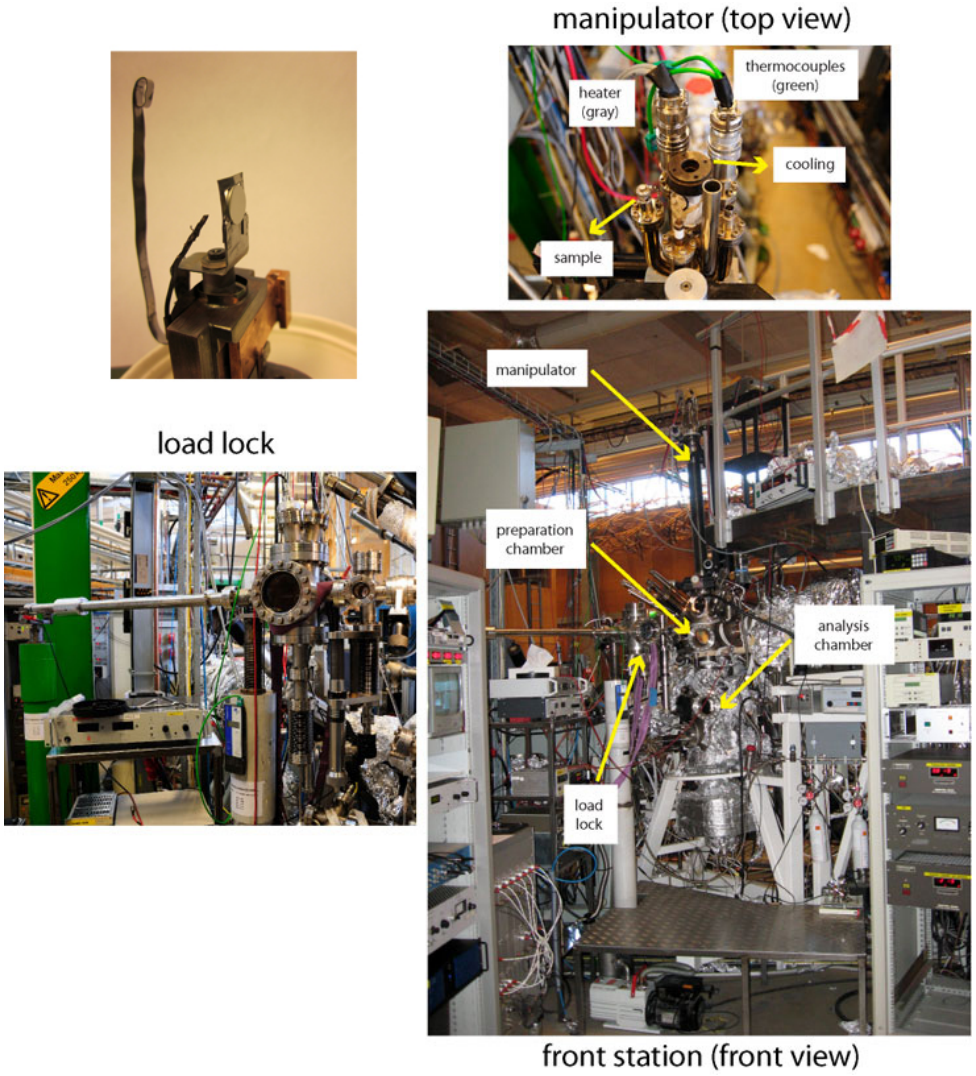

Figure 5.2. – Photographs of the D1011 beamline at MaxLab, Lund, Sweden. The images are kindly provided and printed with permission from Alexei Preobarjenski.

The experimental station of the D1011 dipole beamline at MaxLab, Lund, Sweden is a two chamber design. It consists of a preparation chamber above the analysis chamber

and a four-axis manipulator with linear motion in x, y and z, as well as rotation of θ. The sample holder is a homemade design, where the crystals are spot welded onto a small molybdenum plate in the rotational axis of the manipulator, insulated to ground. In this way it is possible to prepare the sample inside the manipulator by e-beam heating with the methods described below. It also allows to collect the total electron yield within the x-ray absorption spectra in addition to the partial electron yield.

The preparation chamber is equipped with an OMICRON LEED optics, two evaporator ports, a quartz balance and a 0.25 mm tantalum filament on a linear motion device for e-beam heating. The analysis chamber is equipped with a SCIENTA SES200 hemispherical analyzer for photoemission measurements and a multi channel plate (MCP) for the partial yield measurements of the x-ray absorption experiments. At the connection to the beamline a gold-grid and a photodiode is installed, which can be moved into the beam for recording flux curves for the normalization of the NEXAFS spectra. The base pressure in both chambers is better than $1 \cdot 10^{-10}$ mbar. D1011 is a dipole beamline with photon energies reachable from 40-1400 eV. The photon flux is about 10^{10}-10^{11} photons/s on a spot size of 1×3 mm ($v \times h$).

5.3. The Variable Temperature STM

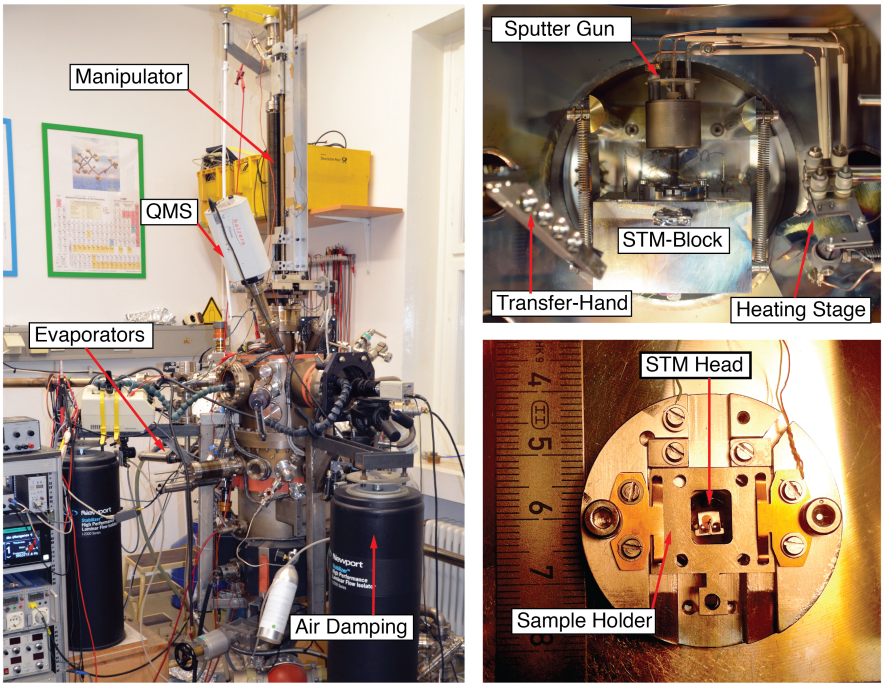

Figure 5.3. – Photographs of the STM chamber (left), the interior of the chamber (right top) and the STM head with sample holder (right bottom).

The variable temperature STM Aarhus 150 by SPECS (for details see Section 4.3) is installed in a single chamber manufactured by Riber. This chamber consists of the STM, a manipulator for sample transfer between analysis and preparation stage, a heating stage for e-beam heating, two evaporator ports in the lower preparation stage of the camber, a quartz microbalance balance, and a residual gas detector. It further consists of a load lock and a "mechanical hand" for sample transfer. An air damping system from Newport Inc. is installed in this chamber to reduce the vibration coupling to the environment of the experimental chamber. The base pressure in the laboratory STM chamber is better than $3 \cdot 10^{-11}$ mbar. An argon sputter gun is installed on top of the STM head in order to clean the tip before performing an experiment. This procedure is found to significantly increase the tip quality and reproducibility of the experiments. The sputter gun is adopted from a SPECS IQE 11/35 sputter-gun with a homemade mounting inside the vacuum. For the sputtering process, a special sample-holder with a 1 mm hole is used through which the tip of the STM has to be driven. This shield protected the piezo drive from damage during sputtering. For sputtering the tip, an argon pressure of $p_{Ar} \approx 1 \cdot 10^{-5}$ mbar, a potential of 2000 V and a current of 1 μA for 15 min is applied.

5.4. Sample Preparation

5.4.1. Graphene/Ni(111)

For graphene preparation on Ni(111) a single crystalline Ni(111) film with a thickness higher than 100 Å on a W(110) crystal was used. Graphene was grown by thermal decomposition of propylene according to the recipe described in refs. [34, 35, 128]. Nickel grows pseudomorphically in the (111) orientation on the pseudo-hexagonal (110) surface of tungsten. After several layers, the existence of a W(110) substrate has no more influence on the newly formed nickel bulk. W(110) was cleaned by cycles of annealing in oxygen atmosphere ($p_{O_2} = 1 \times 10^{-6}$ mbar) for 30 min followed by thermal flashing above 2000 °C for 15 s. The heating of the crystal was achieved by electron beam heating. For this, the sample was set on a potential of +1000 V and a 0.25 mm tantalum filament, as the electron source, was approached from the back to a distance of 1-2 mm. The power applied via electron beam was 40-70 W for oxygen treatment and 250 W for thermal flashing. The temperature control of the surface was performed with a pyrometer. The purity of the W(110) surface was ascertained via LEED by the absence of carbide diffraction spots, and for the presence of pseudo-hexagonal diffraction spots of the W(110) surface [129]. The Ni(111) layer was prepared by metal beam evaporation from a highly pure Ni source, a small piece or rod of nickel heated via electron beam heating. The nickel target was set to a potential of +1000 V and a filament next to the target was used for electron emission. The sources were partly self designed evaporators (small nickel piece), but also commercial single metal source evaporators from Focus GmbH (2 mm nickel rod). After the deposition with a rate of approx. 1-2 Å/min, the surface was heated just below 500 °C in order to supply enough energy to the surface atoms to form an ordered (111) surface (not exceeding the temperature for the decomposition of propylene, see below). After 5 min recovery time for the Ni(111) surface, graphene/Ni(111) was prepared by thermal cracking of propylene on the Ni(111)/W(110) surface at a partial pressure of $p_{C_3H_6} = 1 \times 10^{-6}$ mbar and $T = 500$ °C. The surface was pre-heated for 2 min to ensure a homogeneous temperature on the surface, followed by an exposure of propylene on the hot crystal surface for 15 min. The quality of the graphene/Ni(111) sample was verified by means of LEED and core-level as well as valence-band photoelectron spectroscopy (CL-PES and ARPES) (see for example Figures 2.6 and 6.6).

5.4.2. Graphene/Ir(111)

Graphene/Ir(111) was prepared on a single crystal Ir(111) surface. The cleaning process of Ir(111) was similar to the method of cleaning tungsten just described; however, the parameters were slightly different. The cleaning process consisted of subsequent cycles of flashing up to 1800° C (200 W) for 20 s followed by annealing at an oxygen partial

pressure of 1×10^{-6} mbar at 1400° C (40-70 W) for 30 min. The surface quality of the Ir(111) surface was confirmed via LEED measurements. Carbon contaminations were observed to segregate from the bulk material to the surface, forming an overlayer that is similar, if not identical to graphene, however not well ordered [130]. Clean Ir(111) only exhibits a pure (1x1) structure in LEED. Graphene on Ir(111) was then prepared by thermal decomposition of ethylene or propylene at 1300° C at a partial pressure of 5×10^{-7} mbar for 30 minutes; for this, the sample was heated via electron beam heating to the aimed temperature, controlled via pyrometry. The quality of the graphene/Ir(111) sample was verified by means of low energy electron diffraction (LEED) and core-level as well as valence-band photoelectron spectroscopy (see for example Figures 2.10,7.2 and 7.3).

5.4.3. Adsorption Experiments

All adsorption experiments were performed at a sample temperature of 100 K or lower. The molecule sources were high purity sources of the individual gases. "Ultrapure" water from Merck GmbH dosed was from the vapour pressure over the liquid phase at room temperature. The cleaning process consists of several freeze-pump-thaw cycles, where the gas phase above the frozen ice was pumped until the residual gas detector in the UHV chamber only showed pure water from the gas phase above the water in the reservoir upon dosing. Ammonia 99.9 %, and SO_2 99.9 % were obtained from Sigma Aldrich and NO_2 98.0 % from Linde Gases in lecture bottles. PF_3 was kindly provided by the workgroup of Prof. Seppelt at the Freie Universität Berlin in a lecture bottle. The purity of each gas was verified by residual gas analysis with a QMS. Dosing of each gas was performed from a small reservoir attached to the UHV system via a dosing valve, allowing to adjust the pressure with an accuracy of at least $5 \cdot 10^{-10}$ mbar. The dosing in all spectroscopic experiments at BESSY and MaxLab was controlled via real time deposition (water and ammonia) or cycles of a defined dose with subsequent XPS characterization of the adsorbed amount (NO_2, SO_2 and PF_3). For the TPD experiments, the surface coverage was defined by the dose, where 1 L=$1.33 \cdot 10^{-6}$ mbar·s, for exposures from 0.3 L up to 20 L. These experiments were performed in the variable temperature STM chamber, with a SRS QMS residual gas detector for the collection of the specific mass signal and a EUROTHERM 2408 PID controller for the temperature ramping by a Delta ES 10-30 power supply. The mounting of the sample was shown in Figure 5.4. The crystal was contacted between two Cu rods and is additionally contacted with a type K thermo couple for temperature readout. The Cu rods have two tasks. First, they are the electric contact between the sample and the power supply. Secondly, the rods are connected to the liquid nitrogen reservoir (isolated to the wall by teflon tubes) and therefore also act as cooling rods. The rods are fed through ceramic feedthroughs at the bottom of the manipulator

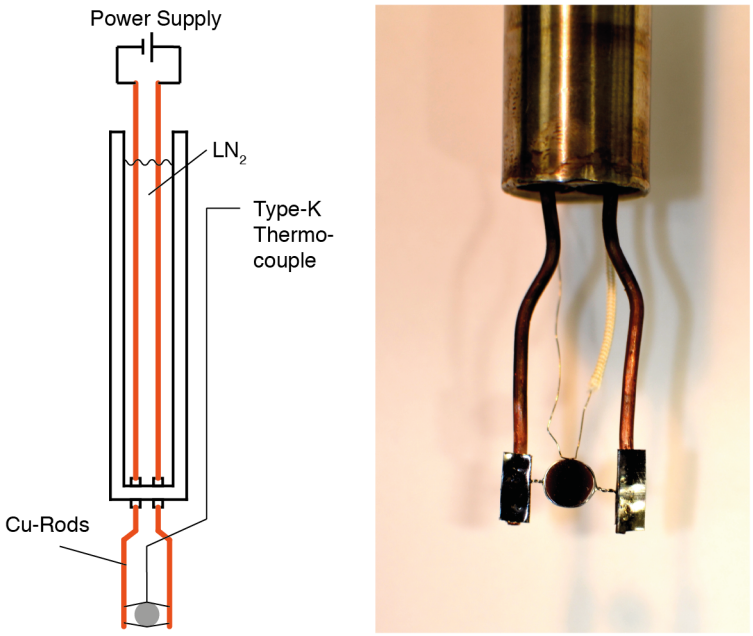

Figure 5.4. – Setup for TPD measurements. The sample is contact via two Cu-rods, that are both, electric contact to the power supply and cooling rods. The rods are guided through the liquid nitrogen reservoir. The sample is contacted via two wires to the electric circuit and via a thermo-element type K to the PID controller.

head in order to isolate them from ground (see Figure 5.4). In this way the sample was contacted almost directly to the liquid nitrogen reservoir and the heating current only heated the sample but not the rods. This ensured specific heating of the sample and prevent the TDP measurements to be affected by other desorption processes.

5.4.4. Deposition of Manganese

Manganese was deposited from a home-built electron beam evaporator. The evaporator consisted of a small crucible filled with manganese. For the STM experiments, the crucible was closed with a cap with a 0.5 mm hole to prevent manganese dropping out of the crucible because the evaporator was mounted horizontally. A rate of 0.1-0.2 Å/min was achieved by a heating power of 11.5 to 12.5 W via electron beam heating (target at 1000 V). The rate was calibrated with a quartz microbalance and XPS, where possible.

Part III.

Results and Discussion

6. Weakly Interacting Molecules - Beyond Physisorption

6.1. Introduction

This chapter deals with the interaction of small molecules, namely water and ammonia, and their interaction with graphene on Ni(111) and Ir(111). For reasons that will become clear later, molecules have been chosen that do not contain carbon atoms. The idea behind using water and ammonia for adsorption experiments is the fact that these two gases represent some of the simplest heteroatomic molecules. Water is also one of the most important gases present in the atmosphere. Early experiments by the Geim group have utilized graphene specifically as a gas sensor for these molecules [131]. It is hence of interest to study the interaction of such atmospheric gases with graphene, when technological applications of graphene become reality. The vast literature available on adsorption of water [132] and ammonia (see for example [96]) makes them well-understood adsorbate systems, and their handling under UHV experimental conditions is straightforward.

Water and ammonia are found to show an unusual interaction with graphene. They appear physisorbed at first, but exhibit a considerable chemical interaction when brought in contact with graphene/Ni(111) and Ir(111). It will be shown that water and ammonia adsorbed on graphene induce the appearance of new substrate electronic states, which I interpret as a fingerprint of the adsorbate-derived electronic structure of the substrate. I assign this to orbital mixing of the substrate and adsorbate valence states. The fingerprint signal is observed in NEXAFS spectroscopy on both the substrate and the adsorbate. This is, to my knowledge, the first time that such experiments are carried out in this fashion, since adsorbates are usually not studied by NEXAFS from the substrate side. The problem is that usually the substrates are not two-dimensional, which results in a superimposed signal between the bulk and surface. Graphene however provides a substrate that has only a surface with no bulk material, combined with a well defined electronic structure, that allows such fingerprint signals to be detected. This method required molecules that have no carbon atoms, however. When comparing graphene/Ni(111) to Ir(111), the interactions strength of both adsorbates is found to be different.

This section starts with a discussion of the coverage calibration using the example of water, studied by valence band photoemission spectroscopy, followed by the presentation of the temperature programmed desorption measurements. Then the influence of the adsorbates on the electronic structure of the graphene substrate is discussed and compared between Ni(111) and Ir(111) by means of NEXAFS on the substrate absorption edge. A model derived from these data is further investigated by adsorbate NEXAFS and XPS measurements. Finally, the influence of the substrate on the adsorption strength will be discussed within a simple model and further extended to a more general consideration of graphene/substrate interaction.

The spectroscopic measurements of water and ammonia on graphene/Ni(111) were performed during my master's thesis and are published in the thesis [20], and parts of it in [133]. The models and conclusions that are described in the present work, i.e. the growth and interaction model, the analysis of the adsorbate NEXAFS spectra, the TPD measurements and all experiments concerning water and ammonia adsorbed on graphene/Ir(111), the data analysis and interpretation are entirely part of this thesis.

6.2. H_2O and NH_3 on Graphene/Ir(111) and Ni(111)

6.2.1. Coverage Calibration and Thermal Desorption Experiments

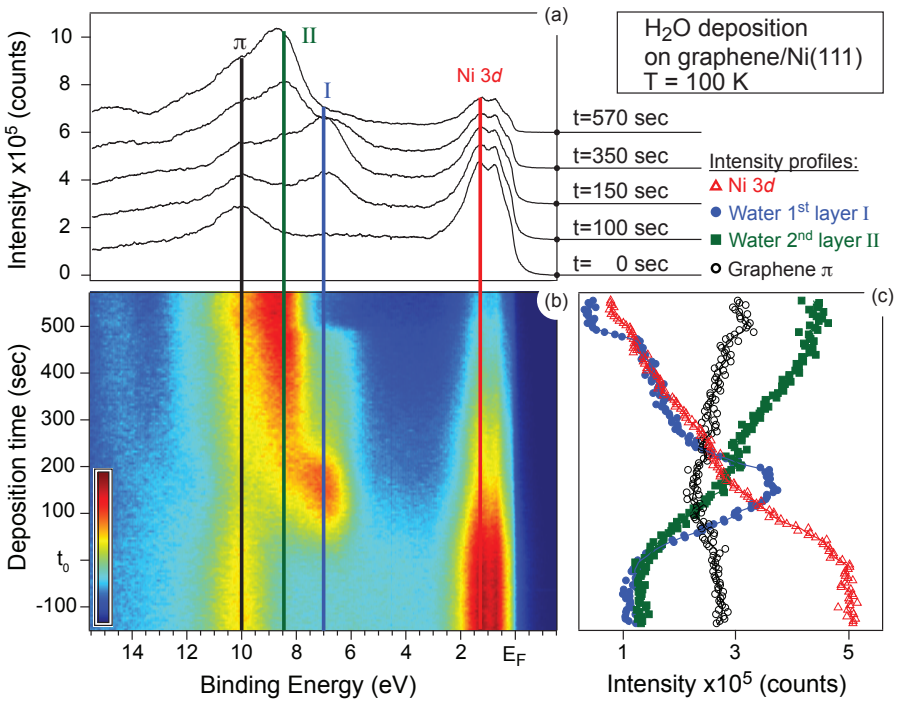

Figure 6.1. – Real time spectra of the deposition of water: (A) Time sequence of ARPES spectra collected around the Γ point. (B) Photoemission spectra for several time steps showing the main features, graphene-π and Ni-3d bands as well as the water-related states **I** and **II**. (C) Photoemission intensity distribution vs. deposition time for water states I (7 eV) and II (8.3 eV) and for the graphene π- (10 eV) signal. The solid lines obtained from gaussian smoothing of the extracted profiles and may serve as a guide to the eye.

In order to control the amount of adsorbed molecules on the surface, valence-band photoemission spectra for the calibration of the water deposition were collected. Figure 6.1 shows a time sequence of ARPES spectra collected in normal emission (around the Γ-point of the hexagonal Brillouin zone) during water deposition. (a) presents the intensity profiles for a few steps, showing the bottom of the graphene π- (10 eV binding energy) and the Ni 3d- bands (0-2 eV binding energy), as well as the water-related signals from the $3a_1$ molecular orbital (**I** at 7 eV binding energy and **II** at 8.3 eV binding energy), (b) shows the evolution of the valence band spectra upon water deposition as a false colour plot. (c) presents the development of the intensity distribution of the graphene π-, Ni 3d- and the water states **I** and **II** during deposition versus time. The water state **I** corresponds to emission from the $3a_1$ molecular orbital for the first layer of water molecules on the surface. In the present example, this state appears at t_0 after the partial pressure of water

reached 5×10^{-8} mbar. The signal rises upon exposure and the graphene π- and Ni $3d$-states decrease in intensity. When the water deposition starts, another signal around 8 eV binding energy appears which is assigned to the $3a_1$ signal of the second layer of water molecules (**II**). This assignment is based on the energy shift of the two signals relative to the Fermi energy, a screening effect of the photoemission hole of the first adsorbate layer on the surface. For the second layer, such screening effect is not observed. Another influence may be that the first layer of water molecules is less strongly bonded to graphene than to another water layer [134]. Evidence for this assumption will also be presented within the TPD discussion given below. The second layer appears at higher binding energies. The slope of this signal is lower compared to signal **I**, showing a slower deposition of the second layer. Upon higher dosage of water, signal **I** reaches its maximum at $t \approx 150$ s. The first layer signal is suppressed by the second layer of water molecules, which grows simultaneously until t=200 s. Here a plateau is observed for signal **II**, coming with a change of a slope of the first layer signal and a new signal around 14 eV binding energy. This very broad signal can be assigned to another water related state whose intensity was too low to be observed earlier. I assign the behaviour of the photoemission intensities at t=350 s to the completion of the first layer of water molecules. The intensity profiles are interpreted by water growing in a modified Volmer-Weber (VM, island growth) mode, with similarities to a Stranski-Krastanov (SK) mode. The simultaneous growth of both layers with different slopes is interpreted such that the n^{th}-layer starts to grow before the $(n-1)^{th}$ layer is completed [102]. In addition, the change of the slope after the first layer is completed is a characteristic of the SK growth type [102]. Hence, I assign the growth to an intermediate type between VM and SK growth type, where the first layer of water molecules is growing fast and the islands on top of this wetting layer grow more slowly. The growth of the second layer starts as soon as there is enough first layer surface. I have fitted the curves according to a growth model, where I assume that the photoemission intensities follow eq. 6.1 and eq. 6.2 for growth and suppression, respectively:

$$I_{grow} = I_{end} \cdot \left(1 - e^{-\frac{t-t_0}{\tau}}\right) \tag{6.1}$$

$$I_{cover} = I_0 \cdot e^{-\frac{t-t_0}{\tau}}, \tag{6.2}$$

where I_{grow} and I_{end} are the initial/final photoemission intensities, respectively, and I_{cover} is the suppressed signal of an existing layer, upon adsorption of the next layer, starting from its initial intensity I_0. The exponential expression is given as $\frac{t}{\tau} = \frac{d}{\lambda}$ where τ is the characteristic time to grow a layer of thickness d with an electron mean-free-path λ in time t. These two formulae are used to set up a growth model. The suppression of the Ni $3d$- and graphene π-states is the sum of the two water layers.

$$I^{Ni3d} = I_0 \cdot e^{-\frac{t-t_0}{\tau_1}} + I_0 \cdot e^{-\frac{t-t_0}{\tau_2}} \tag{6.3}$$

The first layer's signal intensity of the water molecules increases according to

$$I^{1ML} = I[t] \cdot \left(1 - e^{-\frac{t-t_0}{\tau_1}}\right), \tag{6.4}$$

where I[t] is a functional, depending on the suppression by the second layer. The suppression itself is a function of the growth of the second layer, since the second layer can only grow, where a first layer was formed:

$$I[t] = e^{-\frac{t-t_0}{\tau*} \cdot \left(1 - e^{-\frac{t-t_0}{\tau_2}}\right)} \tag{6.5}$$

At last the intensity of the second layer signal is given as:

$$I^{2ML} = I_{end} \cdot \left(1 - e^{-\frac{t-t_0}{\tau_2}}\right) \tag{6.6}$$

Due to limitations of these functions it is hardly possible to describe those signals that appear after the first layer is completed, such as the new signal around 14 eV binding energy. Hence such signals will not be discussed in this context. The fit of the extracted intensity profiles of Figure 6.1 (c) was performed over all four signals using the same set of three parameters τ_i. The characteristic value τ_1 for the first layer growth is obtained from which it is possible to calculate the average thickness d after time t. With $\tau_1 = 200\,\text{s}$ and $\lambda \approx 7\,\text{Å}$ the first layer is completed after 200 s. This is based on the assumption that one layer of water on graphene has a thickness of 4 Å (based on the lattice constant of ice [135]). In this case, after 100 s half a monolayer is deposited on graphene when the intensity ratio of the graphene π-band and the water state **I** is ≈1. This calibration has been chosen for all following experiments, leading to a accuracy in thickness of $\frac{1}{3}$ to $\frac{1}{2}$ of a monolayer. A more precise calibration is not trivial, since the limited pumping speed induces a further deposition, after the dosing valve is already closed. However, the absence of the second layer signal **II** in all following experiments ensures the existence of one water species only with submonolayer coverage. The adsorption of water and ammonia for both substrates, graphene/Ni(111) and Ir(111), was monitored. Since the adsorption behaviour was similar in all cases, I assumed the same growth conditions and the same assignment for the coverage for all discussed experiments. The intensity of the oxygen 1s and nitrogen 1s core levels has been monitored with XPS after deposition. The intensity in relation to the carbon 1s core level is equal for both water and ammonia experiments, respectively. The uncertainty of the coverage observed from the core level spectra is below 15% of the respective core level signal.

In order to discuss the adsorption of water and ammonia with graphene/Ni(111) and graphene/Ir(111), information about the interaction strength can be acquired using x-ray absorption and photoemission spectroscopy as it will be presented below. However, the

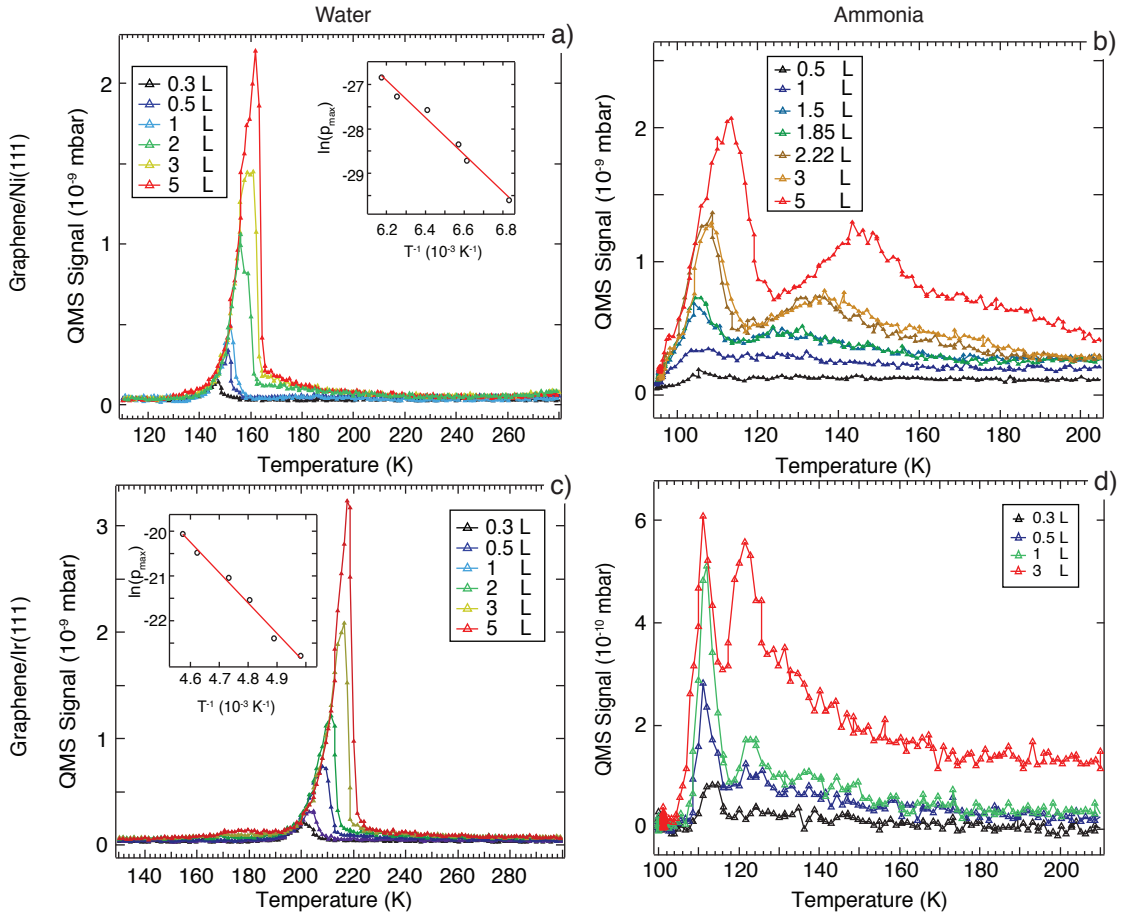

Figure 6.2. – Temperature programmed desorption spectra for water and ammonia on graphene/Ni(111) (a and b) and graphene/Ir(111) (c and d), respectively. All spectra are recorded for different exposures of water or ammonia to the surface. The insets in a) and c) present the Arrhenius plot of $ln(p_{max})$ vs. $1/T$. Water desorption exhibit a pseudo 0^{th}-order desorption, where ammonia shows first order desorption kinetics.

first approach to quantify an adsorbate system is to measure the desorption enthalpy of the adsorbed molecules, accessible via thermal programmed desorption (TPD) spectroscopy. Figure 6.2 presents the TPD spectra for water and ammonia adsorbed on graphene/Ni(111) and Ir(111). The spectra are recorded as a function of the gas exposure, given in Langmuir ($1L = 1.33 \cdot 10^{-6}$ mbar·s). The analysis of the TPD spectra is described in Section 3.3.

Figure 6.2 a) and c) show TPD spectra for water adsorbed on graphene/Ni(111) and Ir(111) respectively. Judged by the shape, a 0^{th} order mechanism can be assumed for the desorption of water, which is consistent with TPD experiments of water on graphite [104]. It is reasonable to assume a pseudo-0^{th} order desorption: this type represents stronger lateral interaction between the adsorbed molecules compared to the adsorption energy to the substrate. The inset is the Arrhenius plot of $ln(p_{max})$ vs. $1/T$. From the slope of the inset

a desorption enthalpy of 356 ± 23 meV (34.4 ± 2.2 kJ/mol) for H_2O/graphene/Ni(111) and 585 ± 31 meV (56.4 ± 2.9 kJ/mol) for H_2O/graphene/Ir(111) is calculated. These values are in the range of the sublimation enthalpy of ice (490 meV) [136] and are characteristic for physisorbed species. It is worth noting that the desorption enthalpy is much higher for water on graphene/Ir(111) compared to Ni(111), which I interpret as stronger lateral interactions on graphene/Ir(111). On graphene/Ni(111) the submonolayer coverage may yield weaker lateral interactions due to the flatter surface and greater possible intermolecular distances of the water layer. Due to the corrugated structure of graphene/Ir(111), the water molecules may be packed more densely in the *fcc* and/or *hcp* valleys. Spectra b) and d) of Figure 6.2 present the desorption spectra of ammonia on graphene/Ni(111) and Ir(111), respectively. The desorption order of ammonia from both graphene surfaces can be interpreted as a first order mechanism, since the position of the first signal does not vary with the dosage of ammonia and hence with the surface coverage. The desorption spectra for ammonia on graphene/Ni(111) exhibit two signals: the first one around 111 ± 4 K represents desorption from the first layer. The calculated desorption enthalpy according to the Redhead method is 281 ± 11 meV (27.1 ± 1.0 kJ/mol). For dosages above 1.85 L the peak shifts to higher temperatures. However, since the shape of the peak does not change, a 0^{th} order can be excluded. The spectrum is most probably broadened due to the second layer signal which is too close to the first layer signal to be resolved here. From the 5 L spectrum ($T_{max} = 113 \pm 4$ K) the desorption enthalpy of the second layer can be estimated to be 303 ± 11 meV (29.2 ± 1.1 kJ/mol). The second signal in the spectrum located between 130 and 160 K and is probably an artefact of desorption from different surfaces such as the crystal back side or the sample holder.

The spectra for ammonia desorption from graphene/Ir(111) are similar to the desorption spectra from graphene/Ni(111). Again, a first order desorption is observed. In contrast to graphene/Ni(111) the signals which are assigned to be first and second layer desorption are clearly separated. An additional desorption signal from other surfaces is observed as an enhanced background signal after the desorption edge. The temperature of the first layer signal is located at 111 ± 4 K and corresponds to a desorption enthalpy of 296 ± 9 meV (28.6 ± 1.1 kJ/mol). This value is slightly higher than for graphene/Ni(111), however within a larger error. The second layer signal is located at 120 ± 4 K and corresponds to a desorption enthalpy of 322 ± 12 meV (31.1 ± 1.1 kJ/mol). The low desorption enthalpies for water and ammonia suggest that both adsorbates are physisorbed on graphene. However, in the next section it will be shown that a considerable chemical interaction occurs between both adsorbates and the substrates.

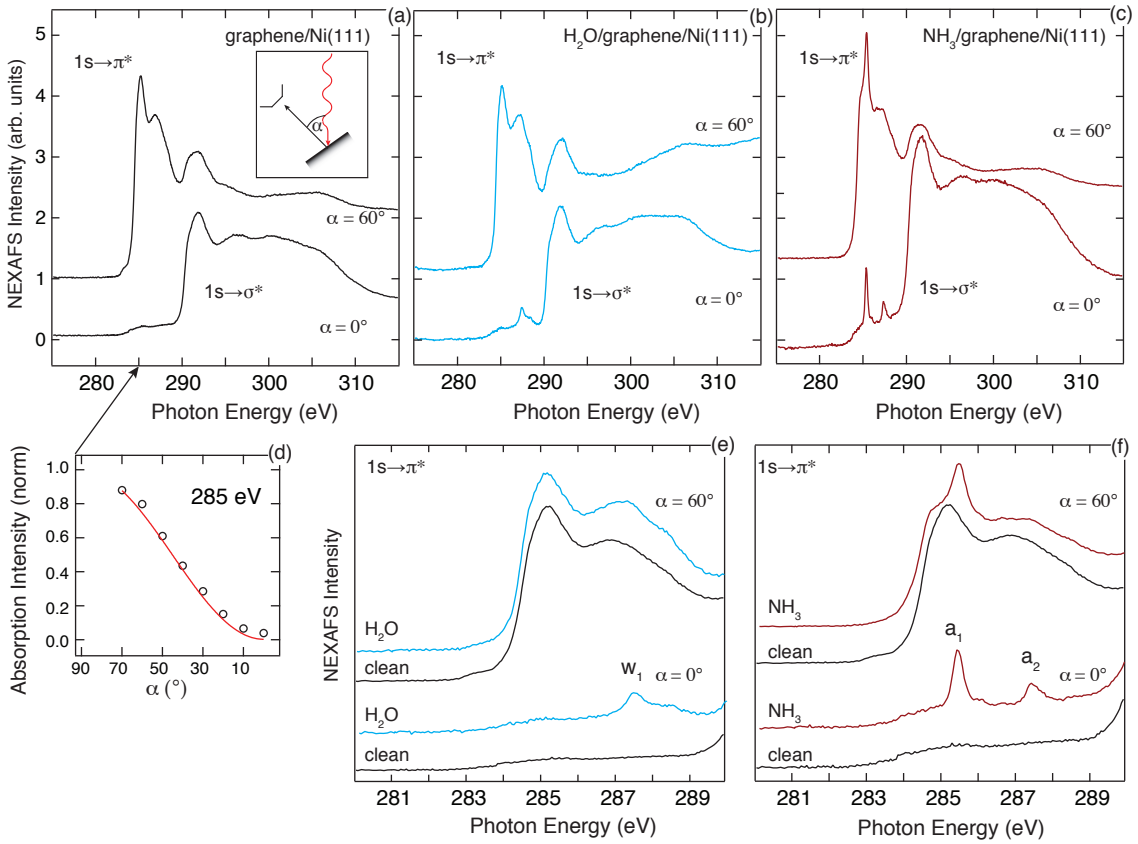

Figure 6.3. – NEXAFS spectra of the carbon K absorption edge. All spectra are collected as a function of the incident light. (a) clean graphene/Ni(111), (b) water adsorbed on graphene/Ni(111) and (c) ammonia adsorbed on graphene/Ni(111). (e) and (f) represent enhanced areas of the C $1s\rightarrow$ π^* transition area. The coverage for ammonia and water is assigned to be $\frac{1}{3}$ to $\frac{1}{2}$ of a molecular layer. d) shows a plot of the absorption intensity distribution under variation of the incident light.

6.2.2. Substrate NEXAFS - The Adsorbate Fingerprint

The big difference between the vast majority of NEXAFS data from adsorbates and the present experiments is that one can examine the unoccupied electronic structure not only of the adsorbate but also its effect on the substrate unoccupied states. In Figure 6.3 the NEXAFS spectra obtained at the carbon K edge for clean graphene/Ni(111) (a), and for adsorbed water (b,e) and ammonia (c,f), are presented. The spectra are recorded at different angles of incidence of the light. Here, α is the angle between the direction of the impinging light and the surface normal (i.e. $\alpha = 0\,^\circ$ is normal incidence and $\alpha = 60\,^\circ$ is grazing incidence). The reference spectra for clean graphene/Ni(111) clearly demonstrate the orbital mixing of the valence and conduction band states of graphene and the underlying substrate, Ni(111), resulting in two main regions for the absorption at the carbon K edge. According to the analysis in refs. [65, 128] the two structures belong to transitions from the C $1s$ core level into the unoccupied graphene π^*- (285-290 eV of photon energy)

and σ^*-states (from 290 eV of photon energy). The first sharp feature (at 285.5 eV of photon energy) of the C $1s\rightarrow \pi^*$ transition corresponds to an excitation into an electronic state just above the Fermi level, located around the K-point of the hexagonal Brillouin zone. Following the nomenclature of Voloshina *et al.* [78] these states are named as *hybrid* states after and will further be called I_j, according to Table 2.3, where the present state is I_4. (I_1 to I_3 are located in the occupied states.) This hybrid state originates from C $2p_z$-Ni$3d$ hybridization and results in an antibonding orbital between the C^1 carbon atom and the first layer nickel atom (see Figure 2.5). The second feature at 287.1 eV originates from a C $1s\rightarrow \pi^*$ transition into a hybrid state located at the M-point of the hexagonal Brillouin zone, and is attributed to a bonding orbital of the C $2p_z$-Nip_x,p_y,$3d$ hybridization between both carbon atoms C^1 and C^2 and the interface nickel atom (see Figure 2.5). This hybrid state will be called I_5. In case of light incident perpendicular to the surface, the electric field vector of light lies in plane with the graphene σ-bonds, yielding a higher intensity due to the overlap of the electric-field vector with the orientation of these states. Hence the cross section for the graphene π^*-states is near zero for this setting. Upon varying the angle of the incident light with respect to the surface, the cross section for probing the graphene π-states increases, whereas it decreases for the graphene σ-states. On the example of the transition at 285 eV photon energy, panel d) presents the angular dependence plot of the absorption intensity. Using the fitting functions of Stöhr [121] it is possible to extract the orientation of graphene adsorbed on Ni(111). An angle of $5\pm9\,^\circ$ has been obtained from a full set of spectra for every $10\,^\circ$ between $\alpha = 0\,^\circ$ and $\alpha = 60\,^\circ$, which means that an almost perfect flat adsorption of graphene on Ni(111) can be safely assumed.

In the case of water adsorbed on graphene/Ni(111) [see Figure 6.3 (b) and the enhanced C $1s\rightarrow \pi^*$ range in (e)] a new spectral feature (w_1) appears at the C $1s\rightarrow \pi^*$ transition (285-290 eV photon energy). It is located in the energy range corresponding to the hybrid state I_5. Since NEXAFS represents approximately the carbon projected DOS (except for cross section and transition matrix element effects), this new spectral feature has to originate from an electronic state on the carbon atom which has been formed through the interaction with water. Such a substrate fingerprint signal for a charge exchange between the adsorbate and the substrate has to the best of my knowledge, not yet been reported. Ammonia adsorbed on graphene/Ni(111) [see Figure 6.3 (c) and the enhanced C $1s\rightarrow \pi^*$ range in (f)] shows two new signals (a_1 and a_2) near the C K absorption threshold. Both are located in the C $1s\rightarrow \pi^*$ transition range but they are distributed over both peaks of the double structure [cp. Figure 6.3 (a)]. The first signal is found in the range of a transition into the interface state I_4. The second feature is, similar to the H_2O case, located in the energy range corresponding to the interface state I_5. Interestingly, the new features are extraordinarily sharp, compared to the resonances of the pristine graphene layer. It is also remarkable that for ammonia the intensity of the new resonances is much higher

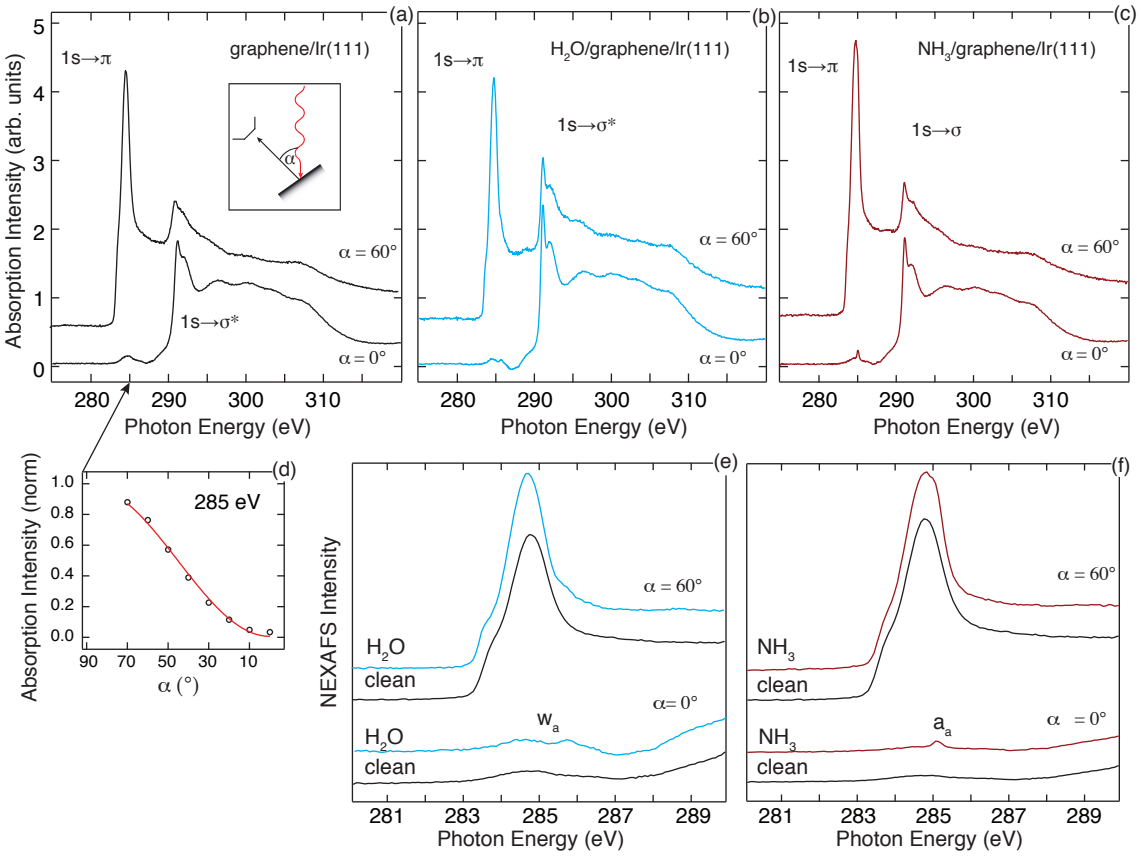

Figure 6.4. – NEXAFS spectra of the carbon K absorption edge of graphene/Ir(111). All spectra are collected as a function of the incident light. (a) clean graphene/Ir(111), (b) water adsorbed on graphene/Ir(111) and (c) ammonia adsorbed on graphene/Ir(111). (e) and (f) represent enhanced areas of the C $1s\rightarrow$ π^* transition area. The coverage for ammonia and water is assigned to be $\frac{1}{3}$ to $\frac{1}{2}$ of a molecular layer. d) shows a plot of the absorption intensity distribution under variation of the incident light.

than for water. I interpret these states to reflect a "chemical" (i.e. charge exchange) interaction between graphene/Ni(111) and the adsorbates, despite the fact that our TPD spectra put the bonding strength into the "physisorption" regime. The experimental results presented in this section will provide evidence for such a chemical interaction of the weakly bonded water and ammonia molecules, using substrate and adsorbate NEXAFS and core level spectroscopy. For this purpose, a comparison between graphene/Ni(111) and graphene/Ir(111) and the adsorption of water and ammonia will be given.

Figure 6.4 shows NEXAFS spectra recorded on the carbon K edge for clean graphene/Ir(111) (a) water (b) and ammonia (c) adsorbed on graphene/Ir(111) for different angles of the incident light. Again, the spectra for clean graphene/Ir(111) show transitions into the unoccupied π^*- and σ^*- states of graphene. The overall appear-

ance of these spectra is similar to those of bulk graphite [128]. The first sharp feature at 284.8 eV reflects a transition into the unoccupied π^*-state. The small shoulder before and just after this main peak arises from a small hybridization of graphene with the Ir(111) surface, as reported by [137], which most probably takes place at the *fcc* and *hcp* positions of graphene supercell on Ir(111) [44, 84]. At photon energies larger than 291.1 eV the transitions into the σ^*-states are detected. The angular dependence of the π^*- and σ^*-states indicates the flat adsorption of graphene on Ir(111). A small signal around 285 eV photon energy for α=0° results from the corrugation of the graphene layer [87]. The graphene layer is not perfectly flat, there is a small amount of π^*-states whose orientation differs from the direction of the surface normal (see section 2.2.3). As a result, there is a small remaining interaction of the light with those π^*-states which are not oriented along the surface normal. Similar to graphene/Ni(111), the angular dependence can be fitted using the formalism of Stöhr [121]. An average adsorption angle of $7 \pm 4°$ is obtained for graphene/Ir(111), which is slightly higher compared to graphene/Ni(111). On adsorbing water and ammonia on graphene/Ir(111), again new features arise in the energetic range of the π^*-states. These new features appear at photon energies of 285.7 eV in case of water (w_a) and 285.1 eV in case of ammonia (a_a). This energy range reflects the region where signals due to hybridization are observed for clean graphene/Ir(111) [137]. It can be concluded that water and ammonia have to be adsorbed in the areas which allow such hybridization. Such areas on the graphene/Ir(111) surface are the *top-hcp* and *top-fcc hollow* sites of the supercell (see Figure 2.8) which are assumed to be the more strongly bound areas of graphene to the substrate. This behaviour has already been observed for cluster formation of graphene/Ir(111) [84]. The explanation is the chemical modulation of graphene on Ir(111) [44]. The *fcc* and *hcp hollow* sites are active areas, where an enhanced orbital mixing of the graphene and metal states forms hybrid states that are chemically more active. Recent AFM/STM studies support this finding: Voloshina *et al.* [74] have found a shift of the tip frequency when probing these areas with an AFM tip. The chemical forces, responsible for the tip frequency change, are stronger in these areas. The water- and ammonia-induced states do not show the same angular dependence as the graphene states but they are observed under all shown angles of the incident light, as already found for the graphene/Ni(111) case. Compared to graphene/Ni(111), shown in Figure 6.4, the overall intensity of these new resonances is much smaller, a fact which will be evaluated later. However, the relative intensity of the water-induced features is smaller than the ammonia-induced signal. This relation is again consistent with the observations from the graphene/Ni(111) surface, where the water-induced features are lower in intensity than the ammonia-induced ones.

As proposed by Li *et al.* [75] the bonding of an adsorbate is enhanced when graphene strongly interacts with the substrate. The intensities of the new resonance features may

reflect the *interaction strength* of the surface bond, e.g. the formation of a new hybridized state between the graphene states and the adsorbate frontier orbitals. A possible influence on the intensity by the concentration of the adsorbates on the surface as well as possible multilayer islands can be excluded since a similar submonolayer coverage of water and ammonia was observed for graphene on Ni(111) and on Ir(111). The new resonance features imply a considerable chemical interaction. This is somewhat surprising, since graphene is reported to be a very inert system [34]. A consistent way of describing the bond would be a molecular orbital-based picture, taking into account the frontier orbitals of water and ammonia, respectively, and the substrate states. To this purpose, NEXAFS from the adsorbates is performed in order to get a complete picture of the bonding situation in an MO scheme.

6.2.3. Adsorbate NEXAFS

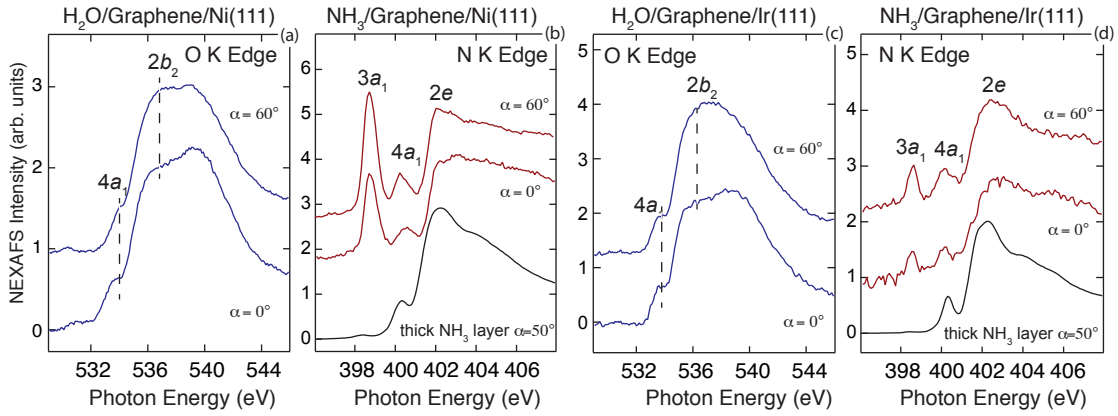

Figure 6.5. – Adsorbate K edge NEXAFS spectra for water and ammonia adsorption, respectively. (a) shows the O K edge for H_2O/graphene/Ni(111), (b) shows the N K edge for NH_3/graphene/Ni(111), (c) shows the O K edge for H_2O/graphene/Ir(111) and (d) shows the N K edge for NH_3/graphene/Ir(111). All spectra are recorded for different experimental geometries.

This section shows complementary NEXAFS spectra for the oxygen K and nitrogen K edge for water and ammonia, respectively, adsorbed on graphene/Ni(111) and graphene/Ir(111), to provide a complete picture of the electronic structure of the adsorption complex. Figure 6.5 a) shows the oxygen K edge for water adsorbed on graphene/Ni(111). Following similar spectra from literature [120, 138–143] three adsorption ranges are identified: (i) the pre-edge area around 534 eV, (ii) the main-edge area around 536 eV and (iii) the post-edge area starting from 539 eV. The pre- and main-absorption edges are transitions into the unoccupied $4a_1$ and $2b_2$ molecular states of water, respectively, and belong mainly to the OH bonds [120]. The spectra reveal water to be adsorbed in an amorphous

manner on the surface: The pre-edge feature $4a_1$ points towards a local order of water and the formation of hydrogen bonds [143]. This observation can explain the high desorption enthalpy of water in the TPD spectra. However, the features are not as pronounced as in solid ice [143]. The N K edge spectra for ammonia adsorbed on graphene/Ni(111) are presented in Figure 6.5 b). They consist of three main signals, located in the pre-edge (around 399 eV photon energy) and the main-edge area (around 400 eV photon energy). The NEXAFS spectra show signals which are mainly associated with transitions into unoccupied states related to the NH-bonds, namely the $4a_1$ (400 eV photon energy) and the $2e$ (402 eV photon energy) state. The overall appearance of these two signals is in perfect agreement with ammonia adsorbed on other substrates, as for example Cu(110) [144]. At energies beyond 402 eV the Rydberg states appear. The pre-edge area at 399 eV is usually assigned to transitions into a partially empty $3a_1$ (HOMO) state [144,145], as for example in C=N bonds [146, 147] or to decomposition products (NH_x species) [119]. The spectra reveal exactly this signal at 399 eV photon energy; however, since graphene/Ni(111) is an inert system [34] a decomposition of NH_3 can be ruled out. One possible mechanism could be a decomposition at the uncovered step edges of the substrate since the flat Ni(111) surface is perfectly covered by graphene [35]. However, such a reaction would be slow since the actual reactive area is very low compared to the remaining graphene surface. This is in contrast to the observations presented here, where a large signal at 399 eV photon energy is observed. I interpret the pre-edge signal as evidence for a noticeable chemical interaction originating from a partially empty $3a_1$ state and (as a consequence) a C=N type interaction between the graphene surface and the ammonia molecule. The double-bond character of the energy of the signal [146, 147] might be explained as a π-backbonding mechanism (a similar case has been observed for NH_3 on ZnO [145] and also for NH_3 on Cu(110) [144]). The unoccupied interface state I_4 interacts with the occupied $3a_1$ orbital (the lone pair and HOMO) of the ammonia molecule, whereas the occupied interface state I_3 interacts with the unoccupied $4a_1$ orbital (LUMO) of ammonia. The absence of such an enhanced feature in the oxygen K edge spectra for water on graphene/Ni(111) concludes that water does not bond via such a donation-backdonation mechanism.

Figure 6.5 c) shows the oxygen K edge NEXAFS spectra for water adsorbed on graphene/Ir(111). The appearance of the resonances is similar to those of water on graphene/Ni(111). The pre-, main- and post-edges can be identified according to the description of Figure 6.5 a) for water on graphene/Ni(111). However, the spectra still indicate an amorphous water layer. Figure 6.5 d) shows the nitrogen K edge NEXAFS spectra for ammonia adsorbed on graphene/Ir(111). The appearance of the spectra is similar to the N K absorption spectra of ammonia on graphene/Ni(111). The main- and post-absorption edge can be clearly identified and again a pre-edge feature at 399 eV photon energy is observed. I assign this again to the emptied $3a_1$ HOMO orbital of

ammonia. However, the ratio between the pre-edge feature and the main-edge features is much smaller compared to ammonia on graphene/Ni(111). From this information I can conclude that the electron transfer from the $3a_1$ orbital into the graphene layer on Ir(111) (and therefore the back-bonding character) is much weaker compared to graphene on Ni(111). This is consistent with the observations from the C K NEXAFS spectra, where the induced signal is also weaker and gives rise to the assumption that the bonding strength on graphene/Ir(111) is much weaker compared to graphene/Ni(111), however still detectable. A detailed analysis of the relative intensities will be given below.

6.2.4. Core level spectroscopy

Further understanding of the bonding situation can be obtained from the chemical shift information from the carbon 1s photoemission core level spectra. The influence of the different proposed interactions of water and ammonia should be reflected in a different behaviour of the C 1s core level line. Since I will show below that ammonia is assumed to bond via a donation-backdonation mechanism, an almost electron-neutral situation should be observed in the chemical shift, which should be different in water.

Figure 6.6 shows the carbon C 1s core level spectra for graphene/Ni(111) (a) with water (b) and ammonia (c) adsorbed, as well as for graphene/Ir(111) (d) with water (e) and ammonia (f) adsorbed. The C 1s peak for graphene/Ni(111) is located at 284.6 eV binding energy with a full width at half maximum (FWHM) of 570 meV. This is in good agreement with earlier published data [27, 128, 148] and reflects the charge transfer from the Ni substrate by a shift of 1 eV to higher binding energy compared to graphite [27]. Upon adsorption of water on graphene/Ni(111), the C 1s core level shows a shift to higher binding energies by about 300 meV, to 284.9 eV under conservation of its FWHM. This shift can be explained by a change of the chemical environment upon adsorption of water. I assume the water molecules to localize valence electrons of the graphene layer around the adsorption site, forming an induced dipole due to the strong electro-negative character of the oxygen atom. This interaction is still weak, in order to explain the physisorption behaviour, but it is apparently strong enough to change the carbon projected DOS, as observed from the C K NEXAFS spectra. In the case of adsorbed ammonia on graphene/Ni(111) only a minor shift for the C 1s core level state is observed. It is localized at 284.7 eV binding energy (shift $<$ 100 meV) with a FWHM of approx. 500 meV. This observation is most interesting, because the nitrogen atom of ammonia is also more electronegative than carbon and a stronger shift should be expected, when assuming a similar adsorption mechanism as for water. However, the core level does not shift and the FWHM is lower ($\Delta E \approx 70$ meV). This observation can be explained within the model proposed above: The donation-backdonation mechanism almost compensates a charge transfer since electrons are shared in both directions, towards the adsorbate and towards

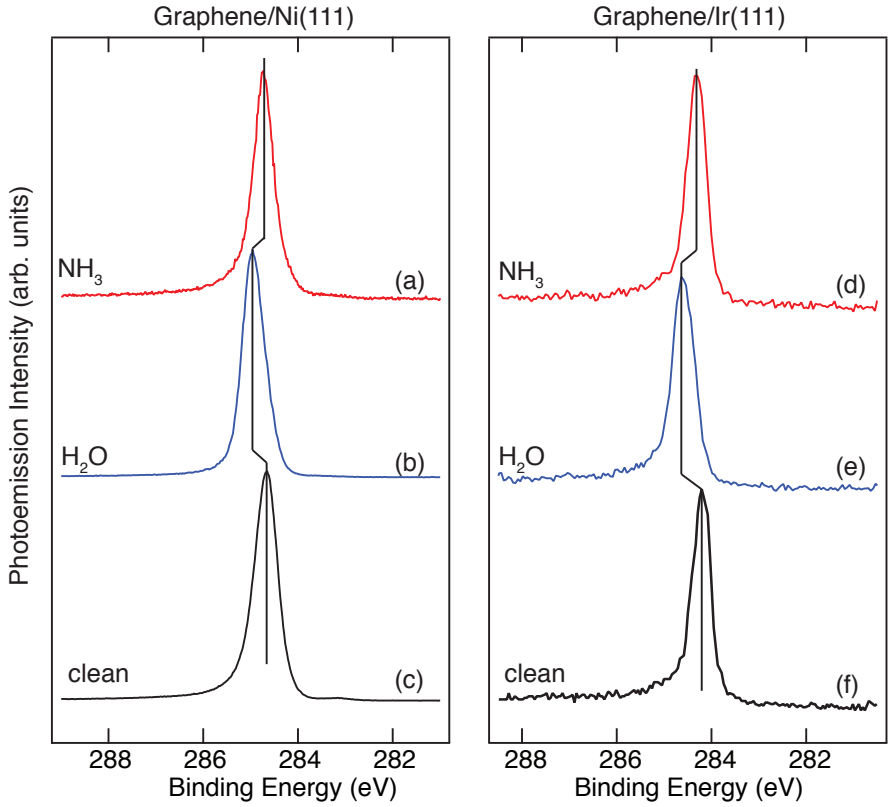

Figure 6.6. – C 1*s* core level spectra obtained for graphene/Ni(111) (left panel) with water and ammonia adsorbed, as well as for graphene/Ir(111) (right panel) with water and ammonia adsorbed. The C 1*s* core level state shifts upon adsorption of water to higher binding energies (ΔE_B=300 meV). In case of adsorbed ammonia this shift is almost negligible ($\Delta E_B < 100$ meV).

the substrate. This model is further illustrated below.

Figure 6.6 also shows the C 1*s* core level spectra for graphene/Ir(111) (d) with water (e) and ammonia (f) adsorbed. The C 1*s* core level for graphene on Ir(111) is located at 284.2 eV binding energy with a FWHM of 410 meV. The binding energy is smaller compared to graphene/Ni(111) and closer to the value of bulk graphite [27]. This indicates the weaker bonding interaction of the graphene layer to the Ir(111) surface. The adsorption of water and ammonia on the graphene/Ir(111) surface yields comparable results to the graphene/Ni(111) case by looking at the C 1*s* core level component. The C 1*s* core level spectra for water adsorbed on graphene/Ir(111) is shifted by 400 meV to higher binding energy compared to the pristine graphene/Ir(111) case. The FWHM is about 80 meV higher, indicating a variation of the chemical environment for the C 1*s* core level. Again I assume an induced dipole interaction for the adsorption of water on the graphene/Ir(111) surface. When adsorbing ammonia on the graphene/Ir(111) surface, the C 1*s* core level component is shifted by 100 meV to higher binding energies to 284.3 eV. The FWHM is almost conserved with a value of 430 meV. These values indicate that the situation for

water graphene/Ni(111) and graphene/Ir(111) is similar. Again, the adsorbate nitrogen K absorption edge for NH_3 on graphene/Ir(111) reveals also a partially emptied HOMO orbital. The same mechanism as discussed for ammonia on graphene/Ni(111) is also active here, however, electron donation from the ammonia molecule to the graphene/Ir(111) substrate is less compared to graphene/Ni(111). These observations underline the possibility to conclude a different strength of the bonding according the predictions by Li *et al.* [75].

6.2.5. Interaction Scheme

In summary, water and ammonia reveal an interaction to the graphene/Ni(111) substrate that exhibits aspects of both physisorption and chemisorption. The low temperatures required for the adsorption and the low desorption enthalpies point to a simple physisorption picture. Despite this general finding, both adsorbates show a behaviour which can be seen as the evidence for chemisorption: Both molecules exhibit new spectroscopic features in the carbon K absorption edge. The new structures are clearly carbon states, since x-ray absorption is element-specific. The formation of new *hybrid* electronic states is a signature of a chemical bond. At this point, both adsorbate differ from each other: whereas water shows only a small signal in the C K NEXAFS, ammonia reveals two very strong and extraordinarily sharp new spectroscopic features. NEXAFS on the adsorbate K edge shows that water behaves as an amorphous water layer whereas ammonia exhibits a chemical component from a partially empty HOMO orbital. This observation is indeed a clear signature of charge transfer from the molecule to the substrate. XPS data of the carbon $1s$ core level show that upon water adsorption a shift of the C $1s$ occurs. Upon adsorption of ammonia, the C $1s$ core level shows only a small shift, which indicates an almost electron-neutral binding situation. Such a mechanism may be explained by a π-backdonation mechanism, as proposed by Blyholder for the adsorption of CO on nickel [149]. In a very simple molecular orbital scheme, presented in Figure 6.7, the electronic states of the frontier orbitals of the ammonia molecules and graphene are mixed and form two new occupied and two new unoccupied states. The new states in the substrate NEXAFS, e.g. a_1 and a_2 in NH_3/graphene/Ni(111), and the fact that the first two spectral features in the adsorbate NEXAFS exhibit the same energy separation as a_1 and a_2, suggest that these features represent indeed the expected electronic states from the simple MO model.

On graphene/Ir(111) in principle the same effects are observed. Water and ammonia induce new spectroscopic features in the carbon K absorption edge, and the adsorbate K edges exhibit again amorphous water and a partially empty HOMO orbital for NH_3. However, the intensity of the fingerprint signals, as well as the pre-edge feature in the nitrogen K edge are much smaller. A possible explanation for this might be that the interaction

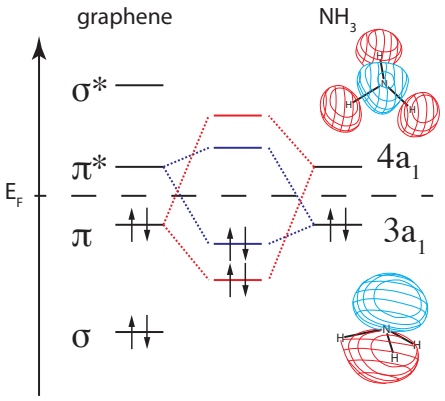

Figure 6.7. – A simple representation of the frontier orbital mixing between graphene and ammonia. The electronic states of the substrate (hybrid or localized interface states) and the frontier orbitals of ammonia are hybridized and form two new occupied and unoccupied states. The orbital pictures are drawn after [150].

of graphene to Ir(111) is weaker compared to Ni(111). Note that this statement is currently under debate, since state-of-the-art DFT calculation are not able to reproduce the expected binding energies, due to the problem of treating dispersion interactions within in these calculations (see refs. [32] and [33] and references therein). So far, DFT calculations are post-corrected for Van-der-Waals interactions, using for example the Grimme Method [70, 71]. Therefore the calculated electron binding energies are in the range of 50-150 meV, with the largest value for the "strongly" interacting graphene/Ni(111) [32]. In the following, the *interaction strength* of ammonia to graphene will be evaluated and a picture will be shown, where this interaction strength may be used to characterize also the interaction strength of graphene to the substrate.

The different intensity of the pre-edge feature in the adsorbate K edge NEXAFS data [Figure 6.5 b) and d)] and the intensity of the fingerprint signal in the carbon K edge NEXAFS data [Figure 6.3 c) and 6.4 c)], gives the possibility to probe the binding energy of ammonia to the graphene layer on Ir(111) relative to Ni(111). Li *et al.* [75] have proposed that the adsorption strength of water to the substrate scales with the amount of orbital mixing of the graphene layer to the metal substrate. In their study, the adsorption of water on graphene/Ni(111) and graphene/Cu(111) was calculated with the result that the copper states do not form the same type of orbital mixing with graphene as found for graphene/Ni(111) (see chap. 2.2.3). The adsorption on graphene/Ir(111) may serve as a comparable example to graphene/Cu(111). The preservation of the Dirac cone, the small electron doping and the large distance of graphene to the metal surface (as obtained by x-ray standing wave experiments by Busse *et al.* [44]) indicate a weak bonding of graphene to the substrate. However, in contrast to copper, graphene/Ir(111) exhibits areas of similar

chemical environments as graphene/Ni(111), namely the *top-fcc* and *top-hcp* adsorption sites (see Figure 2.8). The intensity of the fingerprint signals and pre-edge signals can now be used to estimate the relative bonding interaction of the molecule to the graphene layer.

Adsorbate NEXAFS Signal

In the following, the intensity of the pre-edge signal intensities in Figures 6.5 b) and d) as well as the induced signals in Figure 6.3 c) and Figure 6.4 c) will be used to estimate the relative bonding strength of ammonia to the substrate. The NEXAFS signal intensity of the unoccupied states can be used to estimate the interaction strength. However, it requires the consideration of some parameters, such as the relative amount of interacting molecules with the surface. This will be discussed within two possible models:

Model A considers all ammonia molecules to be interacting with the substrate. This means that the pre-edge signal intensity I_{NK} in Figure 6.5 b) and d) is a quantity that depends on the amount of the electron depletion from the HOMO orbital of ammonia, and is hence proportional to the bonding strength (here assumed to correlate with the adsorption energy E_B)

$$I_{NK} \propto E_B. \tag{6.7}$$

The ratio between the two signals χ_{NK} will then be the ratio of the binding energies for ammonia on graphene/Ni(111) (E_B^{Ni}) and Ir(111) (E_B^{Ir}):

$$\chi_{NK} = \frac{I_{NK}^{Ir}}{I_{NK}^{Ni}} \propto \frac{E_B^{Ir}}{E_B^{Ni}}. \tag{6.8}$$

The intensity of the pre-edge features from Figures 6.5 b) and d) have been fitted and χ_{NK} has been found to be equal to 0.18 ± 0.02. In the present model, that means that the electron transfer in NH_3/graphene/Ni(111) is five times larger than found for NH_3/graphene/Ir(111).

Model B is a generalization of model A and assumes that only a fraction of ammonia molecules on graphene/Ir(111) chemically interact with the surface. The intensity scales with both, the number of interacting molecules and the strength interaction. In this case, eq. 6.7 transforms into

$$I_{NK} \propto \frac{N_{chem}}{N_{tot}} \cdot E_B, \tag{6.9}$$

leading to an expression for χ_{NK} as

$$\chi_{NK} = \frac{I_{NK}^{Ir}}{I_{NK}^{Ni}} \propto \frac{\left[\frac{N_{chem}}{N_{tot}}\right]^{Ir}}{\left[\frac{N_{chem}}{N_{tot}}\right]^{Ni}} \cdot \frac{E_B^{Ir}}{E_B^{Ni}}. \tag{6.10}$$

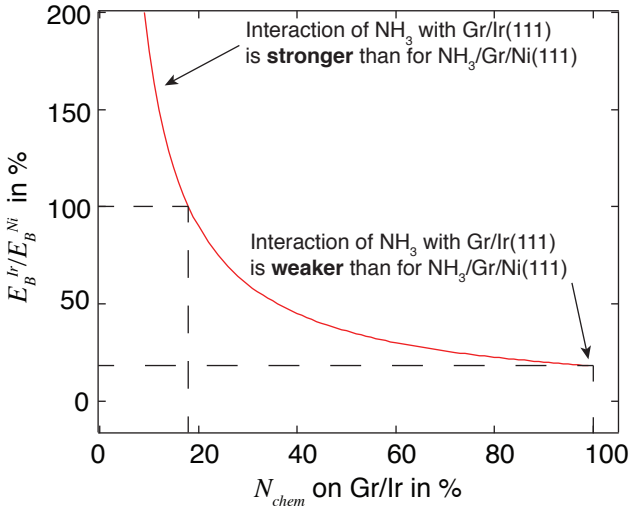

Figure 6.8. – Binding energy fraction $\frac{E_B^{Ir}}{E_B^{Ni}}$ vs the number of chemisorbed ammonia molecules on Graphene/Ir(111), based on the interaction model B.

At this point, two assumption have to be made in order to evaluate the relative interaction in this parametrized model. First, the experiments were performed with the same amount of molecules on graphene/Ni(111) and Ir(111). The amount of molecules on the surface was controlled by ARPES and XPS measurements on the nitrogen related signals and the coverage was obtained to be half a monolayer in both cases. N_{tot} is hence known and is supposed to be equal for graphene/Ni(111) and Ir(111). Second, the amount of interacting ammonia molecules on graphene/Ni(111) is the reference and it is assumed that all molecules on the surface interact. The physical reason for this assumption is the fact that graphene/Ir(111) is chemically modulated [44]. Only the *top-fcc*, *top-hcp* and possibly the *bridge* positions interact with the adsorbates due to the enhanced orbital mixing. On graphene/Ni(111), the entire surface is covered with such "chemically activated" graphene. Therefore $[N_{chem}/N_{tot}]^{Ni}$ is normalized to the total number of molecules N_{tot} and is hence 1. Then, χ_{NK} simplifies to

$$\chi_{NK} \propto N_{chem}^{Ir} \cdot \frac{E_B^{Ir}}{E_B^{Ni}}. \tag{6.11}$$

Figure 6.8 presents the relative interaction strength of ammonia on graphene/Ir(111) vs. Ni(111) as a function of the fraction of interacting molecules; the lower the number of chemisorbed molecules on the surface, the stronger the bonding of ammonia to graphene/Ir(111). Three special cases may be discussed: (I): In the case of only 18% interacting molecules on graphene/Ir(111), the bonding strength on both substrates would be equal. (II): A lower number of interacting molecules than 18% would mean that the signal is dominated by the low number of interacting molecules, leading to a lower overall NEXAFS signal. (III): The higher the number of interacting molecules, the lower the ac-

tual electron transfer has to be, within this model. In case of 100% interacting molecules, model B becomes model A.

Substrate Fingerprint Signal

The induced signal in the substrate fingerprint signal can be evaluated in the same way as the adsorbate signal. For the substrate the number of surface atoms is not a proper quantity in order to evaluate the interaction, since not all carbon atoms can be situated close to an adsorbate molecule; the number of possible sites has to be taken into account. Hence, the area of active graphene may be used instead of the total number of molecules. The number of interacting molecules N_{chem} is normalized to this active area σ:

$$I_{CK} \propto \frac{N_{chem}}{\sigma} \cdot E_B. \tag{6.12}$$

The fraction of the interaction strength of ammonia on graphene/Ir(111) to Ni(111) is then

$$\chi_{CK} = \frac{I^{Ir}}{I^{Ni}} \propto \frac{\frac{N^{Ir}_{chem}}{\sigma^{Ir}} \cdot E^{Ir}_B}{\frac{N^{Ni}_{chem}}{\sigma^{Ni}} \cdot E^{Ni}_B}. \tag{6.13}$$

This expression can be simplified using the initial assumptions: the number of molecules on graphene/Ir(111) and Ni(111) is the same, e.g. $N^{Ir}_{chem} = N^{Ni}_{chem}$. The active area on graphene/Ni(111) is the complete surface and the normalization factor is hence $\sigma^{Ni} = 1$. The active area on graphene/Ir(111) is assumed to be 50%, e.g. $\sigma^{Ir} = 0.5$. We obtain for χ_{CK}

$$\chi_{CK} \propto 2 \cdot \frac{E^{Ir}_B}{E^{Ni}_B}. \tag{6.14}$$

From the NEXAFS data, χ_{CK} is calculated to be 0.30 ± 0.03. Hence the fraction $\frac{E^{Ir}_B}{E^{Ni}_B} = 0.15 \pm 0.02$, assuming $\sigma^{Ir} = 0.5$. This value is comparable to χ_{NK} obtained from model A or model B assuming a large number of interacting ammonia molecules on graphene/Ir(111).

Graphene/Substrate Interaction

Observing a ratio of 5:1 for the electron donation from ammonia on graphene/Ni(111) to Ir(111) suggests a difference in the interaction behaviour of graphene to Ir(111) and Ni(111). Besides the widely accepted characterization of strong and weak interaction, there may be a possibility to characterize the interaction in a picture of strong and weak orbital mixing, rather than net adsorption energies. A recent study of Voloshina and Dedkov [151] suggests a general view of the orbital mixing of graphene to the substrate, based on the instantaneous doping and interaction of the graphene and metal electronic states. The doping by the metal contact determines the shift of the π-band and Dirac cone and the bare appearance of electronic bands leads to avoided crossings if the energy and

geometry of the electronic bands match. This has several consequences: Since most metals that exhibit the appropriate bands for avoided crossing also strongly n-dope the graphene band, a large energy range of many avoided crossings appear below E_F. These numerous little gaps appear as a large band gap and indicate a large interaction of graphene to the substrate. However, most of the new states (including the bonding and antibonding gap part) are filled in systems like graphene/Ni(111) [27,65]. Hence, the overall attractive electronic bonding part is small. The majority of the interaction originates from dispersion interactions. Comparing graphene/Ni(111) to graphene/Ir(111), only a few states may be able to interact between graphene and Ir(111) since the graphene π-band does not cross any Ir(111) bands close to the Dirac point. Further, the area of orbital mixing is limited to the active sites of the graphene/Ir(111) supercell. The amount of orbital mixing observable and reported for graphene/Ir(111) is small [137]. Using ammonia adsorbed on graphene on Ni(111) and Ir(111) can be interpreted as a probe to the amount of orbital mixing of graphene/Ni(111) and Ir(111).

6.3. Conclusions

The sub-monolayer adsorption of water and ammonia on graphene/Ni(111) and Ir(111) has been studied in terms of TPD, photoemission and NEXAFS spectroscopy. Due to the sharp electronic structure of the one-atom thick graphene substrate, an influence of the adsorbate on the substrate is observed in substrate carbon K edge NEXAFS spectra. Water and ammonia induce new electronic states, appearing as new and sharp spectroscopic features at the C K edge NEXAFS spectra of the graphene/Ni(111) substrate. This observation is a novel finding: the well defined and sharp electronic structure of graphene allows the observation of small changes in the unoccupied states of graphene. Complementary observations for ammonia were made in the adsorbate N K edge NEXAFS spectra, where a partially emptied HOMO orbital for ammonia could be observed. Hence, I interpret the nature of the new electronic state in the substrate electronic structure and the partially empty HOMO in the adsorbate to be a chemical interaction between the *hybrid state* of the graphene layer and the nickel substrate and the frontier orbitals of ammonia. The evidence for a chemical interaction is somewhat surprising, since the TPD measurements exhibit extremely low desorption enthalpies for both water and ammonia, and therefore a low upper limit for the adsorption energy. Furthermore, ammonia, which shows the strongest fingerprint signals in the C K NEXAFS spectra, shows the lowest desorption enthalpy, typically ascribed to physisorbed systems. The observation of a charge transfer from the HOMO orbital of the NH_3 molecule into the unoccupied states of the substrate, paired with such a weak adsorption energy, contradicts the accepted scheme of physisorption and chemisorption. I interpret these findings within a bonding model that

allows charge transfer in both directions (donation-backdonation), which leads in sum to an almost electron-neutral bonding situation.

Repeating the experiment with graphene/Ir(111) also shows fingerprinting effects in the graphene substrate carbon K edge NEXAFS spectra, however slightly different in their appearance. Water and ammonia induce new spectroscopic features that are weaker in intensity compared to graphene/Ni(111). In the case of ammonia, also the electron donation from the lone-pair to the graphene substrate is weaker, deduced from a weaker pre-edge feature in adsorbate N K NEXAFS. I believe that the amount of charge transfer, and therefore the *interaction strength* (not the adsorption energy, which still cancels out in this case) scales with the amount of graphene/metal hybridization, as suggested by Li *et al.* [75].

I have set up a model to quantitatively analyze the electron donation on the basis of the assumed interaction and found that the amount of electron donation from ammonia to graphene/Ni(111) is five times larger than in graphene/Ir(111). I have also assumed that the amount of electron donation is proportional to the amount of *hybrid state* formation between graphene and the substrate and that the electrons can only be donated into these states. In this case the strength of *hybrid state* formation between graphene and nickel is five times larger than for graphene/Ir(111).

A model has been proposed in the literature, that intends to explain the *interaction strength* of graphene with the metal substrate not in terms of binding energy per atom (which is almost equally low for all known metals, see Section 2.2.3) but in terms of the amount of *hybrid state* formation between graphene and the metal substrate [33]. Since I have interpreted the observations to be quantitatively dependent on the formation of such *hybrid states*, the results presented here can be seen as a quantitative probe of hybrid state formation between graphene and the metal substrate.

7. Strongly Interacting Molecules - Chemisorption on Graphene

7.1. Introduction

Water and ammonia adsorb non-dissociatively on graphene. The chemical interaction is, while clearly observable, weak and the adsorption process is reversible. This observation need not be true for other adsorbates. In the present section, three adsorbates have been chosen that exhibit similar requirements to adsorbates as water and ammonia: They do not contain carbon in order to use the C K edge NEXAFS spectra for the detection of possible of fingerprinting signals. The geometry of the molecules should be as simple as possible, in order to assign possible electronic origins of interactions. In addition, molecules should be chosen that show a larger reactivity with its environment in order to show an enhanced chemical interaction. The adsorbates used here are nitrogen dioxide (NO_2), sulfur dioxide (SO_2) and phosphorus trifluoride (PF_3). These molecules are highly reactive. NO_2 and SO_2 are the basis for nitric acid and sulfuric and sulfurous acid, respectively. Both gases are toxic and corrosive, which is a direct consequence of their reactivity. A special interest lies in NO_2, since graphene was early shown to have gas detecting capabilities [152], presented for the examples of H_2O, NH_3, CO and NO_2. PF_3, on the other hand, is a molecule with a very similar shape as ammonia: C_{3v}. Its toxicity also points to a high reactivity with its environment and its large dipole moment of 1.03 D [153] may enable it to interact with graphene in a similar fashion as ammonia. Due to their overall larger reactivity, these adsorbates were intended to chemically interact more strongly with graphene than water and ammonia.

We will see that all these molecules adsorb dissociatively under photon irradiation, which provides a pathway to another chemical interaction: the interaction of fragments, either incorporated into the graphene lattice, or strongly interacting with the remaining graphene backbone via adsorption. Both cases will be discussed in the following chapter starting with the oxidation of graphene from NO_2, followed by the oxidation and fragment adsorption from SO_2 and finally the almost pure fragment adsorption of PF_3.

The present section has partly been published in

S. Böttcher, H. Vita, and K. Horn, Reversible Photon-Induced Oxidation of Graphene by NO_2 Adsorption, *Surface Science* **621**, 117 (2014) doi:10.1016/j.susc.2013.11.010,

where I am the principal investigator, with assistance by Hendrik Vita and under the supervision of Karsten Horn.

7.2. Photooxidation from Adsorption of NO_2

7.2.1. Adsorption and Photolysis of NO_2 on Graphene/Ir(111)

The reactivity of NO_2 opens a possible way to a chemical functionalization of graphene. NO_2 is supposed to be strongly bonded to graphene, as judged from experimental data for adsorption on carbon nanotubes [154]. In contrast to water and ammonia which adsorb non-dissociatively, NO_2 is known to undergo photolysis under UV light [155–157]. I will show that photolysis opens a pathway to incorporate oxygen atoms into the graphene lattice, i.e. to form oxidized graphene layers or graphene oxide (GrO). This observation is interesting because the oxidation of graphene has so far been achieved by either dispersion of graphite oxide in basic solutions, yielding what is expected to be a precursor to graphene preparation [158], or a strong chemical or physical treatment such as oxygen atom bombardment [159].

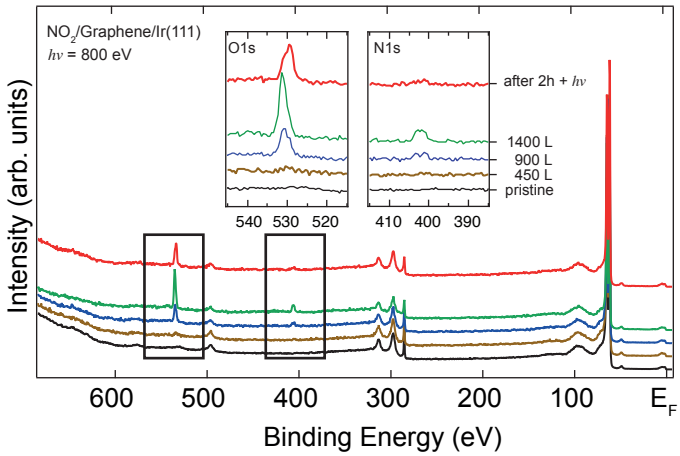

Figure 7.1. – PE overview spectra for the NO_2 deposition on graphene/Ir(111). Each spectrum represents a specific dose starting from pristine graphene. The insets shows a zoom on the O 1*s* N 1*s* core level components. Upon irradiation, the N 1*s* line vanishes and the O 1*s* core level line is shifted to lower binding energy, implying a change of the chemical environment of the oxygen atoms.

In order to study the adsorption behaviour of NO_2 on graphene/Ir(111), core level photoelectron spectroscopy was performed to identify adsorbed species on the surface. This method provides the possibility to distinguish between adsorbed NO_2 molecules and possible reaction products of photolyzed NO_2 molecules by the appearance of chemically shifted core level photoemission lines. Figure 7.1 shows a set of photoemission (PE) survey spectra of graphene/Ir(111), starting with the pristine graphene surface and stepwise exposure of NO_2 up to 1400 Langmuir, recorded at 800 eV photon energy and an average photon density of $3 \cdot 10^{19}$ photons/cm^2·s The flux and flux densities presented in the following are calculated according to the beamline characteristics from ref. [127]. These values are given because the photon flux has a massive influence on the outcome of the experiment. The fifth spectrum from the bottom shows the spectrum after approximately two hours further irradiation at 450 and 800 eV photon energy. All features in the black spectrum at the bottom can be ascribed to either iridium or carbon and are in agreement with the literature [44, 159, 160]; in addition around 410 and 530 eV binding energy, the N 1s and O 1s core level lines appear in the spectra upon dosage of NO_2. The dose of NO_2, required for the adsorption is very high. An exposure of 1400 L was required in the present experiment to adsorb an amount of NO_2 of about two monolayers. I ascribe this to photon-induced desorption, commented on later. However, the core level lines reflect the increase of the amount of adsorbed NO_2 as expected. The oxygen 1s and nitrogen 1s levels show a ratio of approx. 4:1, which corresponds to a ratio of two oxygen atoms per nitrogen atom, taking into account the photoemission cross sections for the nitrogen and oxygen 1s states excited by 800 eV photons [161]. After exposure of the sample to light of photon energies between 450 and 800 eV (last spectrum in the row after a total dose of approx. 10^{15} photons) the N 1s core level component almost completely vanishes, while the O 1s core level is shifted to lower binding energies. I interpret this as a breakup of the adsorbed molecule, with concomitant nitrogen desorption. The shift of the O 1s core level line between the fourth and fifth spectrum implies a change of the chemical environment of the oxygen atom from adsorbed NO_2. I interpret this as a decomposition of NO_2, leaving atomic oxygen as a reactant on the surface. This decomposition is apparently induced by the soft x-rays, not unexpectedly since the decomposition of NO_2 in the gas phase starts already at 400 nm (3 eV photon energy) [155, 156] and adsorbed on surfaces at 193 nm or 6.5 eV photon energy [162], but may be also induced by secondary electron-induced decomposition.

7.2.2. Oxidation of Graphene

Evidence for a chemical reaction of graphene with the oxygen atoms present on the surface can be found in the photoemission data from the graphene/Ir(111) substrate. Consider the C 1s core level line in Figure 7.2 and the Ir 4$f_{7/2}$ core level line in Figure 7.3. In Figure 7.2

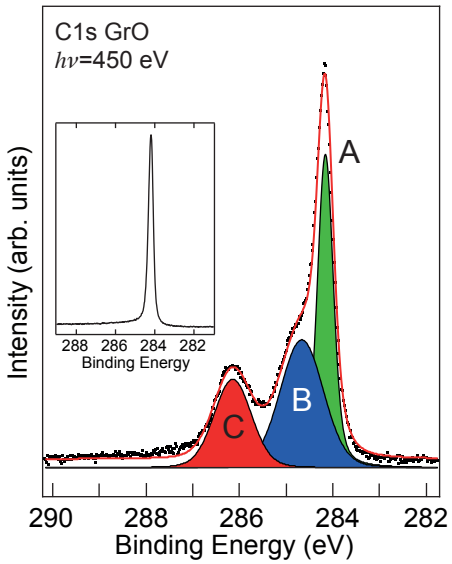

Figure 7.2. – C 1*s* core level photoemission spectrum for graphene oxide. The components of the fit are (A) sp^2-bonded carbon from graphene, (B) sp^3 rehybridized carbon neighbouring the epoxidic carbon atoms and (C) epoxidic carbon atoms. The inset shows the pristine graphene/Ir(111) C 1*s* core level line.

the formerly sharp C 1*s* core level line (see the inset) exhibits an additional shoulder approx. 500 meV towards higher binding energy, and a new feature at 286.2 eV binding energy upon NO_2 adsorption. The signal for the sp^2 component at 284.1 eV binding energy with a FWHM of 390 meV is almost identical to the pristine graphene C 1*s* of the inset at 284.1 eV binding energy with a FWHM of 350 meV. The component at $E_B = 286.2$ eV is usually ascribed to graphene oxide [159, 163–165], an assignment that is based on the observation of different oxygen species in bulk graphite oxide: Hydroxyl groups (C-OH), ketones (C=O), ethers (C-O-C without a C-C bond), epoxidic oxygen (C-O-C with a C-C bond), or acid/ester (COOX) groups are found in such compounds [158,166]. In principle, these functional groups also appear in graphene oxide sheets [164,165]. In a recent study of oxidized graphene prepared by atomic oxygen exposure, Vinogradov *et al.* interpreted their findings in terms of mostly epoxidic oxygen formation on graphene/Ir(111) [159]. The observation of two new C 1*s* line components, one at 286.2 eV binding energy and a shoulder around 500 meV higher binding energy apart from the main graphene C 1*s* peak, matches perfectly with their analysis of the formation of an epoxidic oxygen moiety on graphene. The shoulder at 284.6 eV binding energy is assigned to the carbon atoms adjacent to the epoxidic carbon atoms. Due to rehybridization, these neighbouring atoms are now able to bind more strongly to the Ir(111) substrate, e.g. they are "pinned" (following the nomenclature of Feibelman in ref. [86]) to the surface iridium atoms [86,159]. From the best fit of the C 1*s* core level line, using a polynomial background and Voigt profiles with restricted Lorenzian weights, it is possible to quantify the amount of oxidized

carbon atoms on the surface. The intensity of the pristine C 1s line is split into roughly 38% remaining sp^2 carbon, 23% epoxidic carbon and 39% sp^3 hybridized carbon atoms in the oxidized spectrum. The FWHM for components B and C are equal but differ from the sp^2 component. This may be caused by structural distortions related to the oxidation and rehybridization. The ratio between the oxidized carbon atoms and the distorted sp^3-carbon atoms represents the stochiometric composition of an epoxidic group: If one C=C double bond is oxidized, the two affected carbon atoms are surrounded by four neighbouring carbon atoms whose environment is distorted. Such a stochiometric 2:1 ratio is close to the ratio of 1.7:1 observed in the presented spectrum. It can be concluded that NO_2 adsorption with subsequent dissociation leads to an oxidized graphene surface in which the oxygen atoms form an epoxidic structure. A small deviation of the fit from the experimental data of 2% of the carbon $1s$ intensity between the fit and the GrO C 1s line is found around 287.5 eV binding energy. This difference may occur from the fitting procedure, i.e. using insufficient background functions, but may also be related to a missing component. However, an extra component may also result from small contaminations at defects, which would in this case not affect the interpretation of the epoxidic component.

The bonding of the sp^3-distorted carbon atoms also leads to a change in the appearance of the Ir $4f$ core level component, as shown in Figure 7.3 for the $4f_{7/2}$ core level lines of the pristine graphene/Ir(111) case and the oxidized graphene overlayer. The fit was performed over the full Ir $4f$ core level line, by using a linear background and spin-orbit split and Doniach-Sunjic corrected Voigt profiles [167]. The Ir $4f$ bulk (60.8 eV E_B) and surface (60.35 eV E_B) components are clearly visible. The ratio of these two spectral components results from the probing depth at a photon energy of 450 eV and represents an unperturbed Ir(111) surface [159, 160]. Upon oxidation, the Ir $4f$ surface component is suppressed and partly replaced by an Ir-carbon (Ir-C) component. This Ir-carbon line reflects the interaction of the sp^3 distorted carbon atoms with the iridium substrate [159].

These observations in general agree with the data from graphene oxide prepared at room temperature by oxygen atom deposition. However, they may be interpreted, especially from the C $1s$ core level line, as a high selectivity to epoxidic groups in the prepared GrO sheet upon irradiation of pre-adsorbed NO_2 on graphene/Ir(111), as well as fewer defects on the graphene surface. NO_2 probably adsorbs on *top-fcc* or *top-hcp* sites of the graphene/Ir(111) moiré structure due to the chemical activity of these sites [44]. The *top-fcc* and/or *top-hcp* sites are preferred for several adsorbates on other graphene moiré structures, on Ru [41] and Rh [37, 38]. With the loss of nitrogen upon photodissociation of NO_2, active oxygen atoms are formed on the surface where NO_2 is adsorbed, leading to an oxidation specifically located in these *hollow* sites of graphene/Ir(111).

Complementary to the substrate lines, the adsorbate core level spectra give insight into the bonding situation. Figure 7.3 shows a PE spectrum of the oxygen $1s$ core level

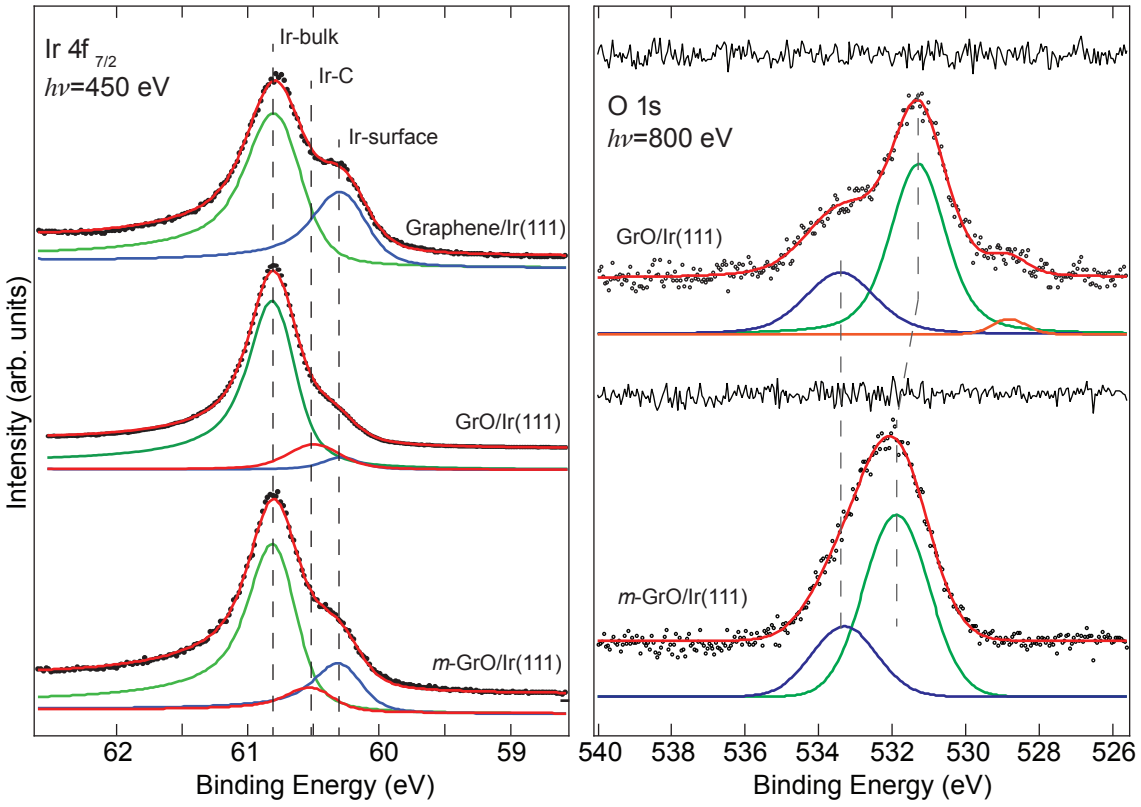

Figure 7.3. – **Left:** PE spectra from the Ir $4f_{7/2}$ core level as observed for pristine graphene/Ir(111), completely oxidized graphene oxide (GrO) and metastable graphene/Ir(111) (*m*-GrO). The fitted spectral lines are the Ir $4f$ bulk component (green), the surface component (blue) and the Ir-carbon signal (red). **Right:** PE spectra from the O1*s* core for the fully oxidized graphene oxide (GrO) and metastable graphene oxide (*m*-GrO). The fitted spectral lines correspond to epoxidic oxygen (green) intercalated oxygen (orange) and remaining NO_2 (blue). The epoxidic line is shifted by approx. 600 meV to higher BE for m-GrO.

line taken at 800 eV photon energy. The line can be fitted by one main component at 531.3 eV binding energy, i.e. one chemical environment of the oxygen atoms, and two small peaks on either side: one at 528.8 eV binding energy is assigned to intercalated oxygen as found in graphene oxide [159] and oxygen intercalation studies [47, 168, 169]. Oxygen intercalation is likely to take place at defect sites where the active oxygen species can penetrate the graphene layer, as in other intercalation systems. The second minor component is probably due to remaining NO_2, located at 533.4 eV binding energy. At room temperature, this component vanishes. These spectra agree with the observation of Vinogradov *et al.* [159].

Complementary data for the influence of oxygen on the electronic structure of graphene/Ir(111) are derived from the unoccupied valence band states, determined from

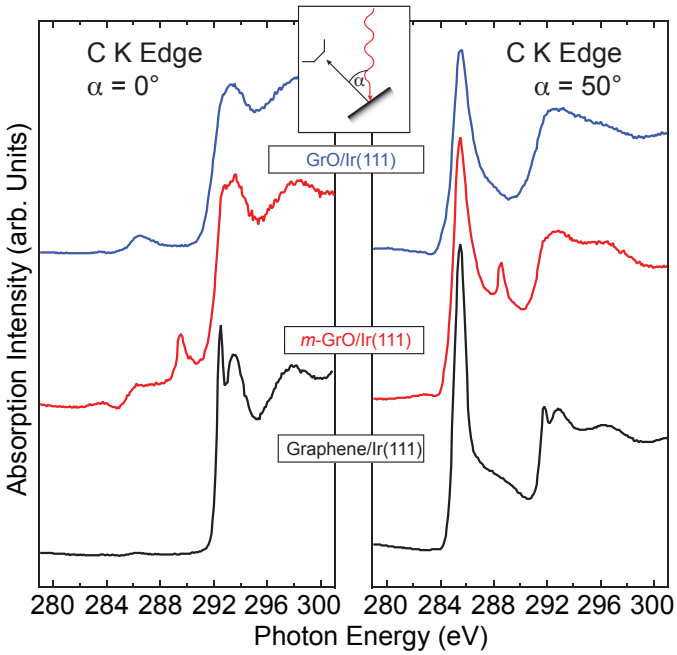

Figure 7.4. – NEXAFS spectra for graphene oxide (blue), metastable graphene oxide (red) and pristine graphene/Ir(111) (black), taken at the carbon K absorption edge. The spectra are collected for normal incident and partially grazing incident light. All spectra are aligned with respect to their C1$s \rightarrow \pi^*$ transition.

NEXAFS data on graphene oxidation shown in Figure 7.4. The spectra for the pristine graphene/Ir(111) consist of two main absorption regions, showing the C1$s \rightarrow \pi^*$ transitions starting at 285 eV photon energy and the C1$s \rightarrow \sigma^*$ transitions, starting from 290 eV photon energy, as discussed in detail in Section 6.2.2. All spectra are recorded for two different experimental geometries for the incident light beam (light with normal incidence at $\alpha = 0°$ and for moderate grazing incidence at $\alpha = 50°$, see inset of Figure 7.4) in order to assign possible changes in the corrugation of graphene, through a change in the absorption cross section under the given angles of incidence of light. Due to the nearly perfectly flat graphene layer on Ir(111) (a height modulation of about 0.3 Å was determined by N'Diaye and coworkers from scanning tunneling microscopy experiments [84]), its π^*-states are almost totally suppressed when the light beam impinges at normal incidence, because the electric field vector of the light in this geometry is perpendicular to the orientation of the π^*-states, while the cross section for the σ^*-states is at its maximum in this configuration [59, 133, 170, 171] (see also Section 6.2.2). Changing the experimental geometry from normal to grazing incidence reverses the effect. The NEXAFS data in Figure 7.4 show that when NO_2 is adsorbed and irradiated by UV light, the C1$s \rightarrow \pi^*$ transition is broadened, and the intensity is weaker compared to the pristine case. The C1$s \rightarrow \sigma^*$ regime is broadened as well; the intensity is almost the same as for the clean surface. This can be explained by rehybridization and the resulting rearrangement of the probed

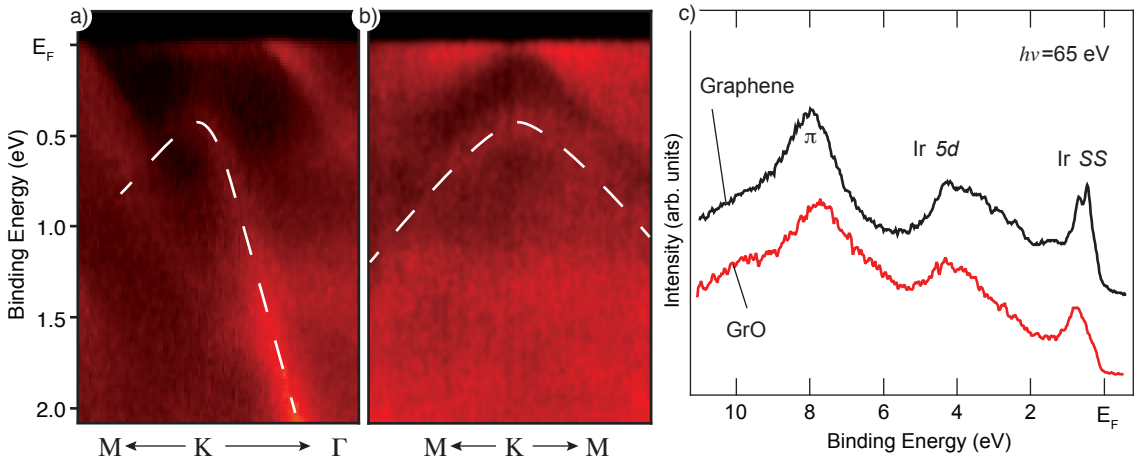

Figure 7.5. – Valence band spectra for graphene (black) and graphene oxide (GrO) from adsorption and Irradiation of NO_2. a) and b) present photoemission intensity maps of $I(E_B, k_x)$ along $\Gamma \rightarrow$ K $\rightarrow$ M and $I(E_B, k_y)$ perpendicular to $\Gamma \rightarrow$ K. The dashed line is a guide to the eye based on a fit of the momentum distribution curves for each energy below $E_B = 1\,\text{eV}$. c) presents PES spectra, taken at the Γ-Point of the hexagonal Brillouin zone. The main features are labeled. Upon oxidation, the graphene π band is suppressed and the Ir surface state (Ir *SS*) is partly destroyed.

carbon states. When changing the corrugation or the hybridization state of the carbon atoms, the distribution of the π^*-states will differ from the initial upright orientation; by going from sp^2 to sp^3, the former planar arrangement of the carbon atoms is partially converted into a distorted tetrahedral structure. This leads to a smaller variation of the resonance intensity as a function of angle of incidence [121]. As a consequence, at angles close to normal incidence, C1$s \rightarrow \pi^*$ absorption intensity should now also occur and is indeed observed. The intensity of the rehybridization feature at 285 eV photon energy is enhanced by a factor of 10, when comparing the NEXAFS spectrum of GrO to pristine graphene. Furthermore, the intensity for the C1$s \rightarrow \pi^*$ transition in grazing incidence should be weaker, as found in our spectra. Although the areas unperturbed by adsorbed oxygen atoms mask these effects to some extent, they are, however, clearly detectable.

The results presented above show that, upon oxidation of graphene, the electronic structure changes significantly in the range of the low energy unoccupied electronic states. The PE data discussed above imply a change of the graphene surface towards epoxidic structures by chemisorption of oxygen atoms. In addition, NEXAFS shows evidence for a rehybridization of the carbon atoms in the vicinity of the chemisorbed oxygen atoms. This is bound to have an influence on the long range order of graphene. Evidence for this assumption is found in the occupied valence band states of graphene.

Figure 7.5 presents a valence band map at the K point of the hexagonal Brillouin zone

in the direction of $\Gamma \rightarrow K \rightarrow M$ (a), perpendicular to $\Gamma \rightarrow K$ (b) with a dashed line as a guide to the eye for the graphene π-band dispersion (based on the fit described below) and single line spectra (c) of graphene/Ir(111) (black) and GrO/Ir(111) (red), taken at the Γ-point. After oxidation, a band gap has been formed at the position of the former Dirac cone. In the present example an amount of 23 at.% oxygen on graphene leads to a band gap of approx. 580 meV. However, just a fraction of the gap is visible in the occupied band structure. The size of the band gap can be estimated according to the assumption that it forms symmetrically around to Dirac point, splitting up and down in energy. The Dirac point is of course not easily visible in the measurement of the electronic structure since only the lower part of the band structure is observed. The energy of the former Dirac point can, however, be extrapolated from the remaining part of the linear dispersing graphene π-band. This is already a necessary assumption for the method described here: the effect on the electronic structure of graphene (e.g. the flattening of the band around the gap) has to be restricted to a small energy range around the energy maximum of the graphene π-band. If this is the case, a large part of the linear dispersion has to survive. This part can be fitted and the former Dirac energy can be extrapolated.

The maximum of the π-band dispersion is found to be at 420 meV binding energy. The band dispersion in the energy range of 1 to 2 eV binding energy appears still linear and was fitted. The position of the former Dirac point has been extrapolated to be at a binding energy of 130 meV. The fitting procedure[1] used a Lorentz profile fit of the momentum distribution curves (MDC) at every binding energy value between 1 and 2 eV. A momentum distribution curve is a composition of photoemission intensities I vs. one in plane momentum, i.e. k_x (instead of I vs. E_B). The shape of an electronic band in an MDC is best described by a Lorentz profile. The fitting routine locates hence the maximum of the π-band intensity for every binding energy slice. The result is a plot of binding energy vs. k dispersion, that follows exactly the maximum photoemission intensity along the electronic band. This dispersion was fitted by a linear function and an energy value of 130 meV at $k = 1.71\,\text{Å}^{-1}$ was obtained. The band gap is then calculated to be twice the difference of the former Dirac energy value and the top of the remaining graphene π-band.

The single line valence band photoemission spectra for graphene/Ir(111) (black) and graphene oxide/Ir(111) (red) are presented in Figure 7.5 c), extracted from the Γ point. The clean graphene/Ir(111) spectra show the Rashba-split iridium surface state near the Fermi energy [172] as well as the intense iridium $5d$ states around 2-4 eV binding energy and the graphene π-band around 8 eV binding energy. When graphene is oxidized by irradiation of pre-adsorbed NO_2, the intensity of the graphene π-band is drastically reduced. I ascribe this to the fact that upon chemisorption and rehybridization towards

[1] The fitting routine used is courtesy of Aaron Bostwick from the Lawrence Berkeley Laboratory, Berkeley

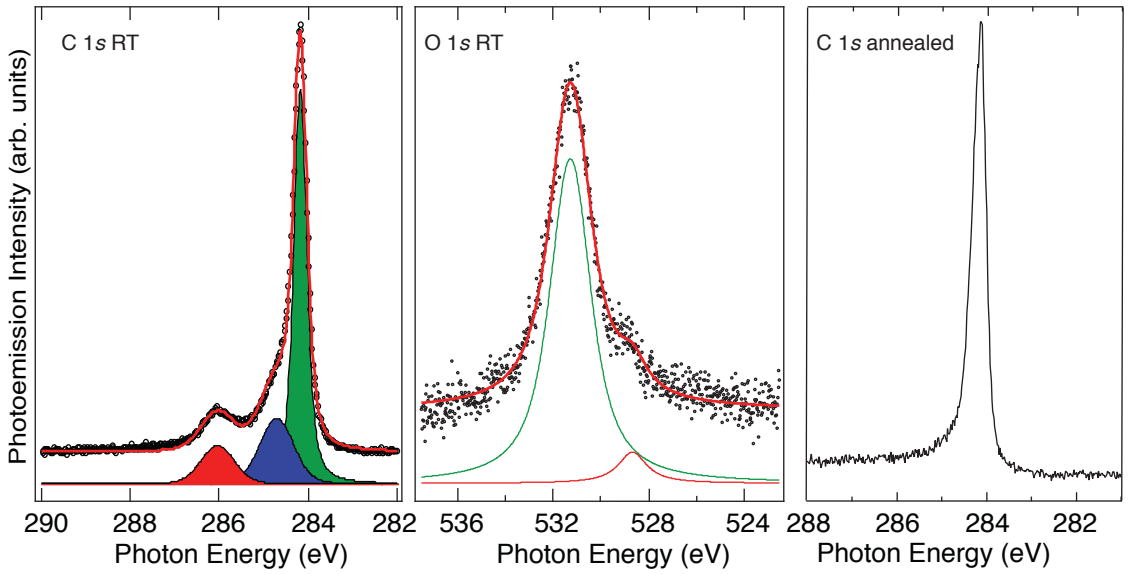

Figure 7.6. – a) C 1*s* core level line of GrO/Ir(111), as obtained from photon induced oxidation at room temperature. All spectroscopic features of epoxidic GrO are observed at the identical energy positions as in Figure 7.2. The sp^2 carbon component is higher because of the vanished adsorbate layer. b) O 1*s* core level line. Two components are observed: epoxidic oxygen (green) and intercalated oxygen (red). The third component, assumed to be adsorbed NO_2, is vanished at room temperature. c) Graphene/Ir(111) C 1*s* core level line obtained after annealing GrO at 500-600° C. A minor shoulder remains after the reduction at higher BE, resulting from defects after the oxidation.

sp^3, the extended electronic structure of graphene is disrupted. In addition, the Ir surface state loses its well-defined shape and the splitting. This is another indicator for the enhanced bonding of the carbon atoms adjacent to the epoxidic oxygen adsorbates in the graphene layer, as also revealed by the changes in the Ir 4*f* core level states. A broadening is also found in the angular resolved photoemission data in Figure 7.5 a) and b). This observation is consistent with a recent study on band gap formation upon oxidation of graphene/Ir(111) by oxygen atom impact [173]. The authors report a broadening of the graphene π-band around the K point prior to the opening of a band gap at the Dirac point. The LEED image of the oxidized sample also suffers from the distortion of the long range order of the surface and the diffraction spots become less sharp (not shown). However, the moiré superstructure stays intact in the LEED and shows essentially the same pattern as clean graphene/Ir(111).

The formation of graphene oxide from dissociated NO_2 is stable at room temperature (Figure 7.6); the C 1*s* core level, upon warming up to room temperature, shows the same feature at 286.2 eV and 284.6 eV binding energy as for low temperatures, and the Ir 4*f* core level lines lack their surface components (not shown). The O 1*s* core level only shows the epoxidic and intercalated species at room temperature. If the sample is annealed to

around 500-600° C, graphene is almost completely restored. A small shoulder remains at the C 1*s* core level at slightly higher binding energies. This was reported to originate from oxygen-induced defects, formed during the reduction process [159], as already described in the literature [163]. However, compared to other methods, the preparation method for graphene oxide presented here shows fewer defects after annealing of graphene, as judged from a lower concentration of intercalated oxygen and by the C 1*s* core level line at room temperature that exhibits a much smaller shoulder after annealing compared to the study where the atomic oxygen source was used [159]. The method of NO_2 adsorption and photon-induced dissociation is likely to be "milder" than the deposition of oxygen atoms through an atom source which dissociates oxygen molecules by heating up to 1650° C. This method has been reported to lead to the creation of a high concentration of defects [159]. The fact that NO_2 is adsorbed mainly in the *fcc* and/or *hcp* positions, not only results in a high selectivity for the oxidation in these areas, but also in a saturation oxidation, lower than obtainable from other methods.

7.2.3. Oxidation Kinetics and Intermediate Species

Changing the flux density leads to another pathway of the adsorption/reaction, which then contains one or more intermediate species, as it will be shown now. This intermediate step is more difficult to characterize. In this section, results for two different flux densities are compared and the effect of a lower dissociation rate, determined from the number of photons per surface area, will be discussed. There are several possibilities to tune the photon flux density in a synchrotron experiment. The most obvious is to change from an undulator beamline to a dipole beamline, which is not an easy thing to do within an experimental run. Another possibility is to sacrifice intensity by aligning the monochromator energy to a value that is not exactly at the same value as the photon energy that is mainly produced by the undulator. Using the monochromator not at the maximum of the undulator harmonic but on its flank reduces the flux density as well. However, the technical issues are big. The alignment of the monochromator/undulator energy is precisely defined. Systematically changes of the monochromator energy to a value just beside the harmonic maximum requires an intensive calibration. For single photon energies, this may be applicable but it is impractical for photon energy scans, such as x-ray absorption experiments. Another pathway to reduce the photon flux density will be described below.

In the experiments presented below, the flux density was reduced by changing the so-called c_{ff} parameter of the x-ray monochromator, which increases the spectral resolution of a plane grating monochromator at the expense of flux [126]. In the present case, the value for the monochromator *fixed focus distance* (c_{ff}) was chosen to change between 2.25

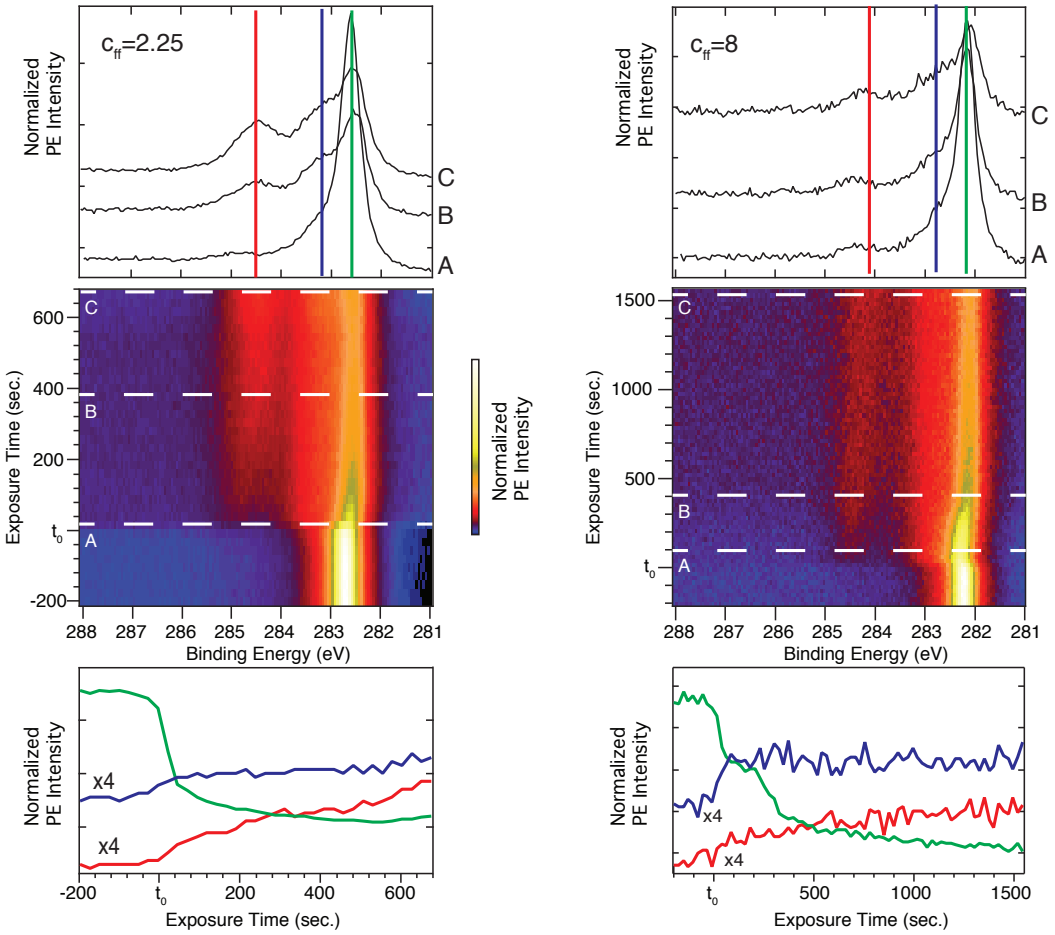

Figure 7.7. – Real time spectra of the photooxidation of graphene/Ir(111) under constant pressure of $5 \cdot 10^{-8}$ mbar NO_2 for different photon flux densities. The left panel shows the high photon flux with a c_{ff} value of 2.25, the right panel shows the same experiment with a c_{ff} value of 8. The centre graphs show exposure time vs. electron binding energy. The extracted photoemission spectra show the beginning of the gas exposure (A), after 200 s of exposure (B) and close to the end of the oxidation experiment (C).

(optimized default value) and 8, resulting in a flux density reduction of about one order of magnitude for the latter value. The influence of this reduction on the dissociation rate is presented in Figure 7.7. The left and right schemes present the development of the carbon 1s core level line under constant exposure of $5 \cdot 10^{-8}$ mbar NO_2 and light of 450 eV photon energy, representing a flux density of $3 \cdot 10^{19}$ photons$/s \cdot cm^2$ for $c_{\mathrm{ff}} = 2.25$ and $3 \cdot 10^{18}$ photons$/s \cdot cm^2$ for $c_{\mathrm{ff}} = 8$, respectively. The centre panels present a map of the C 1s PE line vs. exposure time, the upper panels show the extracted PE spectra at the beginning of the exposure at t_0 (A), after $t \approx 200$ s of exposure (B) and at the end of the exposure (C), and the lower panels exhibit the extracted intensity profiles of the carbon sp^2- (green), sp^3- (blue) and epoxide component (red). The sp^3 and epoxide

intensity profiles are multiplied by a factor of 4 for clarity. All recorded spectra vs. time are normalized to the area under each line. The extracted spectra are aligned relative to their sp^2 component.

When the gas exposure starts at t_0, a drop in the intensity is observed. This behaviour is due to the instantaneous coverage of NO_2 on the cold surface and the resulting suppression of the photoemission signal by the adsorbed layer. Furthermore, a small shift of 100 meV for the sp^2 peak of the C $1s$ occurs during exposure. This may be caused by an overall electron doping of the system. The corresponding high resolution C $1s$ spectra show no shift after being corrected to the Fermi level.

The reaction is driven by the photon flux density. From Figure 7.7 it is obvious that after identical exposure times, the amount of epoxidic carbon atoms is lower for a reduced photon flux density (compare curves B under different photon flux densities). Comparing the photoemission profile of line B ($t \approx 400s$) from $c_{\mathrm{ff}} = 2.25$ and C from $c_{\mathrm{ff}} = 8$ ($t \approx 1600s$), gives a comparable amount of C-sp^2 suppression and epoxide formation. The time necessary to achieve the same oxidation level is around four times longer for the reduced photon flux density. The two experiments offer the possibility to estimate a value for a photo oxidation cross section for this specific experiment, from a very simple approach. The cross section σ_x may be defined as the occurrence of an oxidation event[2], divided by the fraction of incident photons per time and area and the number of NO_2 molecules hitting the crystal (Z_W) per time and area.

$$\sigma_x = \frac{\mathrm{Oxidation - Event}}{Z_{Photons}/Z_W} = \frac{\Delta k_{rel}}{\Delta \varrho_{\mathrm{ph}}}, \tag{7.1}$$

The experiments alone allow no access to the absolute number of oxidation events, but to the relative reaction rates $k_{2.25}$ and k_8 instead. The reaction rate was observed to scale with the photon flux density. Hence, under constant gas pressure, the cross section can be determined from both experiments using the relative reaction rate, which is assumed to be proportional to the amount of oxidation events. $Z_{Photons}$ is the photon flux density calculated from the beam-line characteristics at the given c_{ff} values of 2.25 and 8. The number of NO_2 molecules hitting the crystal is a simple textbook expression [174].

$$Z_W(5 \cdot 10^{-8}\mathrm{mbar}) = 1.5 \cdot 10^{13} \frac{1}{\mathrm{s} \cdot \mathrm{cm}^2}. \tag{7.2}$$

Assuming the reaction to depend linearly on the photon flux density (at least within the available values for the photon density at the given c_{ff} values), σ_x can be determined as the slope between the relative reaction rates and the number of photons per molecule ϱ_{ph} from both photon exposures:

[2] An oxidation event in this approach is the photodissociation of an NO_2 molecule adsorbed on the surface and hit by a photon, forming, e.g. an oxygen radical.

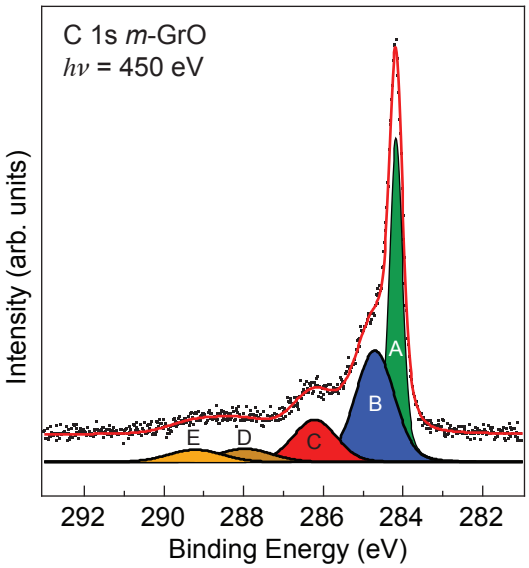

Figure 7.8. – C 1*s* core level photoemission spectrum for metastable graphene oxide. The components of the fit are (A) sp^2-carbon from graphene, (B) sp^3 rehybridized carbon neighbouring the epoxidic carbon atoms and (C) epoxidic carbon atoms. The new features (D) and (E) correspond to carbonyl carbon atoms, probably located at the *atop* and *hollow* sites of graphene/Ir(111)

$$\sigma_x = \frac{k_{2.25} - k_8}{\varrho_{2.25} - \varrho_8} = \frac{4-1}{2 \cdot 10^6 - 2 \cdot 10^5} = 6 \cdot 10^{-5} \tag{7.3}$$

This value may be interpreted as a simple approximation to the photo oxidation cross section for the present experiment, containing the photo-dissociation cross section of NO_2 at $\hbar\omega = 450\,\text{eV}$ and the sticking coefficient of NO_2 on graphene/Ir(111) with the gas at room temperature and the sample temperature of 100 K.

The reduced reaction rate has a significant influence on the formation of the oxide of graphene/Ir(111). The lower reaction rate opens the possibility to obtain intermediate (kinetic) products, containing different oxygen subspecies. Figure 7.8 presents the PE C 1*s* spectrum recorded from adsorbed NO_2 taken at c_{ff}=8. The carbon 1*s* core level component has now split into multiple components and the fit reveals two new spectral features (D and E) as compared to the spectrum in Figure 7.2 which appear at binding energies of 288 eV and 289 eV. These belong to new carbon-oxygen species, probably C=O [164, 165]. The interpretation on the basis of the energies alone is difficult. Two scenarios are possible: The new oxides can be carbonyl groups on both high symmetry areas (the *hollow* and *atop* sites) of graphene/Ir(111), or different functional groups containing carbonyl groups, e.g. esters or acid groups [165], are formed. Since NO_2 is most probably adsorbed only in the *fcc/hcp* hollow sites of the graphene/Ir(111) moiré, the second possibility is

more favourable. However, the results presented here do not allow to decide among the possibilities. The new phase, containing other oxide groups, will be denoted as *m*-GrO, where *m* stands for metastable. I use this term, since its concentration can be reduced under further irradiation and NO_2 exposure as I will show later. From the NEXAFS spectra I assign this phase to a carbonyl (or ketone) oxide phase. The NEXAFS spectra in Figure 7.4 for the metastable phase shows a new, sharp transition feature around 288.5 eV photon energy, found for C=O species in graphene oxide [175] or adsorbed carbon monoxide on metal-oxide surfaces [176]. In addition, a strong disturbance in the sp^2 character can be observed, especially for normal incidence, visible as a strong background in the energy range of 285-290 eV. This effect can be interpreted in terms of the formation a C=O double bond. Upon formation of epoxides, the former C=C double bond still exists as a single bond. In order to introduce a C=O double bond into the graphene lattice, a C=C double bond has to be broken, which leads to a strong disturbance in the lattice. In both cases an Ir-C bond may be formed, but the strain within the graphene lattice, consisting of C=O double bonds, might be much stronger due to steric considerations: The carbonyl group has to be in the plane of the sp^2 bonds due to the hybridization state of the carbonyl group. This means that the oxygen lies within the vacancy which was the C=C bond before. Such an atom environment is heavily distorted since the atoms have to move away from each other. This can explain the strong (and compared to GrO even stronger) rehybridization, observed in *m*-GrO NEXAFS and the larger ratio between peaks B and C in Figure 7.8 compared to pure GrO from Figure 7.2. The corresponding Ir $4f$ core level is shown in Figure 7.3. It shows, apart from the bulk signal, a weakened Ir $4f$ surface component and a weak Ir-carbon signal. The Ir surface component is not as strongly reduced as for the GrO case above. This means that the Ir-C signature has also not yet developed as strongly as for the fully oxidized case. However, the effect is clearly observed and supports our interpretation of the formation of a different oxide formation in *m*-GrO. The oxygen $1s$ core level for *m*-GrO is presented in Figure 7.3 b). The main component is located at 531.9 eV binding energy and is shifted by about 600 meV to higher binding energy compared to GrO. The second component, probably NO_2, is located close to the value observed for GrO. Although this system has to contain carbonyl species in principle, as shown from the C $1s$ and NEXAFS data, they are not clearly resolved in the O $1s$ spectrum, because of its broad lineshape. Carbonyl groups are expected at lower BE than the epoxide oxygen atoms on graphene oxide [177], however, CO adsorbed on Ir(111) is found to show a core level line at 532.4 eV [178], which is close to the value for the broad O $1s$ component, observed here. The strong rehybridization may lead to a large shift of the oxygen $1s$ level for the different species. The main component (green) of *m*-GrO has a larger FWHM than the corresponding GrO line. This may cover different structures of oxidized carbon atoms inside the oxygen $1s$ line.

There are other possibilities to explain the observations shown above, such as physi-

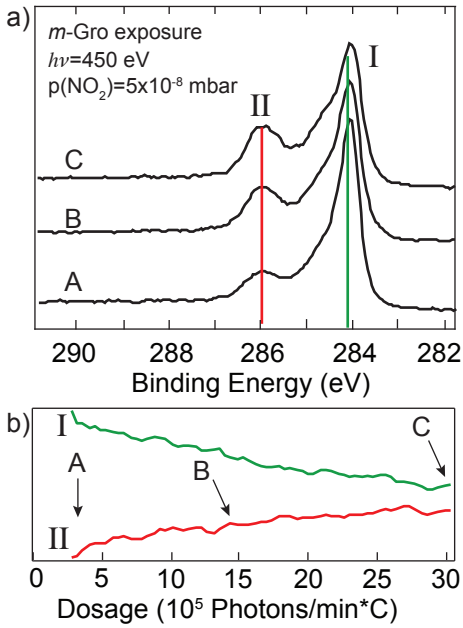

Figure 7.9. – Transitions from the carbon 1s core level line to GrO: Intensity versus exposure of approx. $1cdot10^5$ photons/ (min·carbon-atom), with equilibrium pressure of $5{\cdot}10^{-8}$mbar NO_2, starting with *m*-GrO. The upper panel a) shows representative extracted spectra at the beginning of the exposure (A at 5 min) in the middle (B at 15 min) and at the end in saturation (C at 30 min). The lower panel b) shows the evolution of the sp^2 carbon component (green line, label I) and the epoxidic carbon component (red line, label II), during the oxidation from *m*-GrO towards GrO.

sorbed C=O on GrO/Ir and/or graphene/Ir(111) instead of C=O groups incorporated into the graphene overlayer. Adsorbed C=O would be a simpler explanation and would also lead to the new spectral feature in NEXAFS and might also not be resolved in the O 1*s* beside an epoxide, due to the low coverage. An argument for this interpretation is the fact that the C=O signature is lost at room temperature. However, I believe that the C=O groups are incorporated in the graphene overlayer for the following reasons: The NEXAFS data show a much stronger disturbance in the sp^2/sp^3 region in the proposed *m*-GrO, which cannot be explained if incorporated C=O is absent. Also, the new feature shows no strong angular dependence as expected for an upright oriented CO molecule; a CO signal should be absent under normal incidence light [179]. Also, the ratio between peaks B and C in Figure 7.8 is larger compared to fully oxidized GrO, which is here interpreted as a larger amount of sp^3 hybridized carbon atoms compared to the existing epoxidic species. Although C=O is still an sp^2 carbon species, the lattice strain of C=O in the graphene lattice distorts more surrounding carbon atoms than an epoxide. I may speculate that both cases can occur: C=O is incorporated into the graphene lattice by the photodissociation of NO_2, which leads to a strongly disturbed graphene lattice that is, hence, more active and CO adsorption could take place as a consequence of the C=O

incorporation.

The results show that by reducing the photon flux towards NO_2 photodissociation, the outcome of the adsorption process can lead to different species being present on the surface. The metastable character of this phase should be emphasized. Apart from the fact that the carbonyl phase is not stable up to room temperature (in contrast to the epoxidic case), it is also possible to drive the reaction towards the stable GrO-phase. Upon irradiation of the *m*-GrO-sample with light of 450 eV photon energy under an equilibrium pressure of NO_2 of $5 \cdot 10^{-8}$ mbar and an average flux-density of roughly $3 \cdot 10^{18}$ photons/$s{\cdot}cm^2$ (Figure 7.9), the ratio between the sp^3 signal and the epoxidic signal decreases. It ends up in the already observed saturated case, which I believe to be the oxidation of the *hollow* sites with epoxidic graphene oxide sites as seen in the experiments described at the beginning of this section. I attribute the loss of the metastable components to a photon-induced reduction of graphene. Such mechanisms are proposed in the literature, in order to obtain graphene from GrO [180–182]. Epoxides are stable as judged by the high reproducibility and long-time stability of the sample. However, other species, such as ketons or acidic/esteric groups, may be damaged by photon impact and allow a reduction pathway. The fact that *m*-GrO can be transformed into GrO by further irradiation (under NO_2 presence) may be explained by this possibility. At room temperature, the reduction of the energetically unfavored (because sterical stressed) oxides may be even more efficient due to the larger amount of energy present in the system containing carbonyl groups at room temperature. If the carbonyl groups are stable at room temperature, they may just vanish directly after exposing the sample to the synchrotron radiation due to a photo-reduction process [180–182].

7.2.4. Summary

Graphene adsorbed on Ir(111) can be transformed into a graphene oxide layer on Ir(111) by low temperature adsorption of NO_2 and successive irradiation with soft-x-ray radiation. The oxidation leads to a phase that contains almost exclusively epoxidic carbon groups within the graphene-layer. Since the adsorbed molecules are most likely adsorbed in the *fcc* and/or *hcp* sites of the graphene/Ir(111) supercell [44], the oxidation only takes place at these sites and the overall amount of oxygen on the surface is limited. This finding is supported by the fact that only one epoxidic carbon $1s$ component is found in the spectra, contrary to other studies [159]. Apart from the oxidation, a strong rehybridization of the former sp^2 lattice is observed. This is due to the fact that the epoxidic groups are sp^3 hybridized and the distortion affects the adjacent carbon atoms. The electronic structure of graphene oxide differs in important points from the electronic structure of graphene. At the K point of the hexagonal Brillouin zone, a band gap is formed, destroying the linear dispersion and crossing of the bands. The band gap opening observed for GrO

oxidized by photolysis of NO_2 is 580 meV. Graphene oxide thus formed is stable up to room temperature. Graphene can be retrieved by annealing GrO to 500-600 °C, and the recovered graphene layer is of high quality. Epoxides are shown to be removable by annealing without introducing defects by etching [183]. Another reason for the high quality of the reduced graphene is the fact, that the preparation method is likely to be milder, compared to other methods as for example oxygen atom bombardment. This observation is judged by the extremely low number of intercalated oxygen atoms: oxygen atoms can only intercalate at defects in graphene [47], which are present after the preparation of graphene itself or due to the oxidation procedure.

Oxidation by photolysis of NO_2 depends strongly on the photon flux density. Varying the number of photons per time and area, changes the reaction speed and gives access to intermediate species. Here it is observed that reducing the photon density by one order of magnitude reduces the reaction rate by a factor of four. The reduced reaction rate offers a pathway to the formation of other oxygen species on graphene, as judged by the carbon 1*s* core level spectrum. These new oxygen species are probably carbonyl or acidic groups and are not stable under ambient condition and irradiation, and are therefore denoted as metastable. It is further possible to transform the intermediate graphene oxide into the pure epoxidic phase.

The oxidation of graphene by the adsorption and photolysis of oxygen containing gas molecules may be a general observation. The next section will deal with the adsorption and reaction of sulfur dioxide on graphene.

7.3. Photooxidation of Graphene from SO_2

7.3.1. Photolysis of SO_2 and Oxidation of Graphene

In the previous section, the formation of graphene oxide from adsorption and irradiation of NO_2 on graphene/Ir(111) was observed. The photolysis of adsorbed molecules forms oxygen atoms that can then react with the graphene layers, where graphene is chemically activated by graphene/metal interaction.

In principle this observation should not be restricted to NO_2, but it may be possible for every molecule that contains oxygen, shows a similar reactivity to NO_2 and undergoes photolysis under UV irradiation. Sulfur dioxide is also known to undergo fragmentation on surfaces [184, 185] and photolysis has been reported from irradiation with light of 184 nm (6.7 eV photon energy) [186]. Hence, it can be expected to form atomic oxygen on the graphene/Ir(111) surface, providing an oxidation reaction. In this section, I will show that SO_2 can indeed be used to oxidize graphene from photolysis of adsorbed SO_2. However, in contrast to NO_2, the fragments of sulfur dioxide do not desorb but tend to stay on the surface, affecting the oxidation efficiency and the lattice distortion due to a

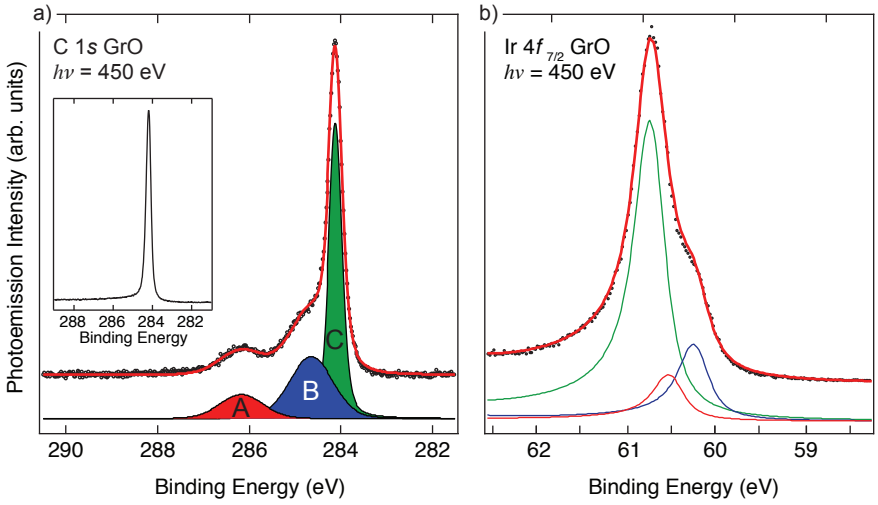

Figure 7.10. – XPS core level spectra of GrO/Ir(111) from submonolayer SO_2 adsorption and additional subsequent dosage and irradiation. a) shows the carbon 1*s* core level line spectrum with the spectral components of epoxidic carbon (A), distorted sp^3 carbon (B) and remaining pristine graphene (C). The inset shows clean graphene/Ir(111). b) presents the Ir $4f_{7/2}$ core level with the spectral components of bulk Ir (green) Ir-C (red) and surface-Ir (blue).

chemical interaction with the graphene backbone.

As in the case of NO_2 adsorption, the core levels reveal details of adsorption and reaction of SO_2 on graphene, and its photo-dissociation on graphene/Ir(111) is reflected in the carbon 1*s* photoemission line as shown in Figure 7.10 a), acquired at an excitation energy of 450 eV. The C 1*s* PE line shows new spectral features compared to the clean graphene/Ir(111) spectrum (inset). Besides the remaining graphene (sp^2) component, located at 284.1 eV binding energy and a FWHM of 390 meV (cp. to the pristine graphene C 1s at $E_B = 284.1$ eV and a FWHM of 350 meV), new lines at 286.2 eV binding energy and a shoulder at 284.6 eV binding energy appear. The new spectral line at 286.2 eV binding energy can be assigned to epoxidic carbon atoms, in agreement with GrO formed by NO_2 [187] and other studies of the oxidation of graphene/Ir(111) [159, 163]; see also Figure 7.2. The carbon atoms involved in the epoxide group have changed their electron configuration from sp^2 to sp^3. This distortion of the perfect two dimensional graphene lattice extends further into the graphene lattice. The carbon atoms adjacent to the epoxidic groups also experience an (albeit much smaller) distortion, which leads to a spectral line appearing as a shoulder to the pristine graphene signal at 284.6 eV binding energy. This observation is again in agreement with the oxidation by NO_2 [187] and other experiments [159, 163]. GrO obtained from photolysis of SO_2, however, differs from the results presented in Section 7.2. Fitting the C 1*s* core level line using Voigt profiles with

restricted Lorenzian and open Gaussian weights (the width are the same for line B and C), identical to Figure 7.2, the ratio between lines B and C is found to be 2.5:1. This ratio is relatively large, and much larger than the ratio of 1.7:1 obtained from oxidation by NO_2 [187]. Consider the following model: every epoxy group contains two carbon atoms and is surrounded by four distorted carbon atoms, assuming the epoxide group is isolated on the surface. This purely geometrical assumption would lead to an upper limit for the ratio of 2:1 for peak B and C. The observed ratio is thus 25% larger than expected, an observation that may be caused by the possibility of a less effective and/or more defective oxidation of graphene/Ir(111). The epoxidic component represents 13 at.% of the integrated C $1s$ peak intensity after exposure of $5 \cdot 10^{-8}$ mbar SO_2 and a photon dose of approx. $3 \cdot 10^{18}$ photons/s·cm^2 (c_{ff}=8) for 30 min, while for NO_2 an amount of 23 at.% is obtained under comparable conditions [187]. Beside the weaker oxidation, another possible explanation for the strong(er) rehybridization shoulder B may be that the graphene lattice is much more distorted than expected from the oxidation alone: it is possible that the remaining decomposition products, such as SO, have a strong influence on the graphene backbone as well, leading to a stronger rehybrization of graphene's carbon atoms.

A sign that the oxidation of graphene is indeed not as effective as observed for GrO from NO_2 photolysis is given in Figure 7.10 b), which presents the Ir $4f_{7/2}$ core level line of GrO/Ir(111) after SO_2 adsorption and photolysis, taken at a photon energy of 450 eV. The spectrum is aligned towards the Ir $4f$ bulk photoemission line (green) in comparison with Figure 7.3 for the NO_2 case. The Ir $4f$ surface component (blue) and the Ir-C related line (red) match perfectly with GrO/Ir(111) obtained from NO_2 adsorption and photolysis. The intensity distribution of the three components is comparable to the intermediate graphene oxide sample presented in Figure 7.3 b) (m-GrO). In principle, the amount of epoxidic oxygen on the surface should scale with the reduction of the Ir $4f$ surface component and the formation of the Ir-C component (see Figure 7.3). Since this is the case, it can be concluded that the increase of sp^3 carbon, observed in Figure 7.10, is not due to a stronger interaction of graphene (-oxide) to the Ir(111) substrate. The possibility of decomposition products and their influence on the graphene backbone is actually revealed by XPS and NEXAFS spectroscopy on the adsorbate core level lines, i.e. the existence of SO_x fragments.

Figure 7.11 (a) presents the oxygen $1s$ core level and (b) the sulfur $2p$ core level spectrum after SO_2 adsorption and photolysis. The oxygen $1s$ peak is fitted using a third order polynomial background (subtracted here) and a Voigt profile for each core level feature. The sulfur $2p$ photoemission line is fitted using spin-orbit split Voigt profiles and a third order polynomial background (subtracted here as well). For consistency and to decrease the number of free parameters, the fit has been performed over the spectra presented in Figures 7.11 and 7.12 together.

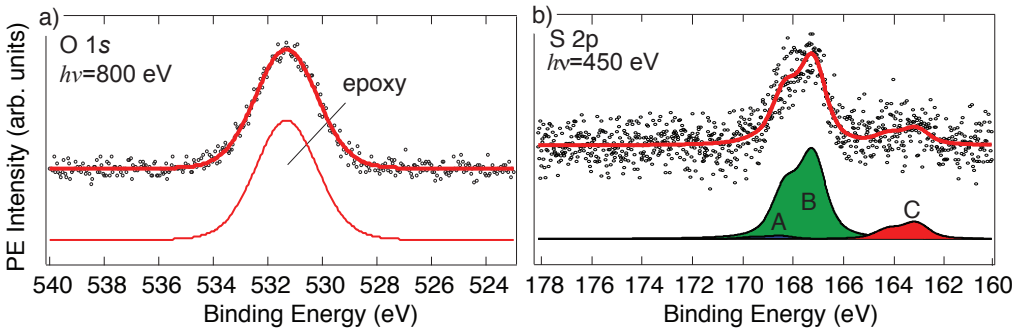

Figure 7.11. – Adsorbates core level spectra: Oxygen 1*s* (a) and sulfur 2*p* (b) corresponding to the substrate core levels presented in Figure 7.10. all spectra are background subtracted (third order polynom) and fitted by Voigt (a) or Doniac-Sunnjic corrected Voigt profiles (b), respectively. The spectra are fitted within the set of spectra containing Figure 7.12.

The oxygen core level spectrum in Figure 7.11 (a) consists of one component only, located at 531.3 eV binding energy, whose large FWHM of 2.9 eV (cp. Figure 7.3) and tiny shoulder around 529.5 eV suggest that more than one species of oxygen atoms is present, but cannot be resolved in this spectrum. From the C 1*s* core level line shape, only one epoxide species is assumed. The adsorption and oxidation on different high symmetry sites, like the *atop* and *hollow* regions of graphene/Ir(111), is ruled out for the same reasons as for NO_2. The chemical activity on the *hollow* sites suggests adsorption and irradiation only to take place at these [44].

Three components in the sulfur 2*p* core level line of GrO obtained from SO_2 adsorption and irradiation are found in the spectra of Figure 7.11 and 7.12: Component A is assigned to adsorbed SO_2 ($E_B = 168.5$ eV), B is adsorbed SO ($E_B = 167.2$ eV) from photolysis of SO_2, and component C is assigned to elemental sulfur adsorbed on GrO ($E_B = 163.2$ eV), in agreement with other experiments on adsorbed and photolysed SO_2 [184, 185]. Line A is small but appears in the spectra in Figure 7.12, hence it is taken into account. Lines B and C represent decomposition products of photolysis of SO_2. In contrast to NO fragments, these fragments are able to remain on the surface after fragmentation of SO_2. The overall amount of sulfur on the surface is about 5 at.% w.r.t. the carbon 1*s* core level line.

Figure 7.12 a) shows the outcome of an experiment with a larger initial coverage of SO_2, where the O 1*s*:C 1*s* intensity ratio is calculated to be 1.75:1 after cross section correction. The upper spectrum in Figure 7.12 a) shows the oxygen 1*s* core level line directly after adsorption of SO_2, the lower spectrum after subsequent irradiation. The total photon dose is comparable to the experiment in Figures 7.10 and 7.11. The epoxidic O 1*s* component (red) is found in both spectra. The binding energy is obtained from a fit

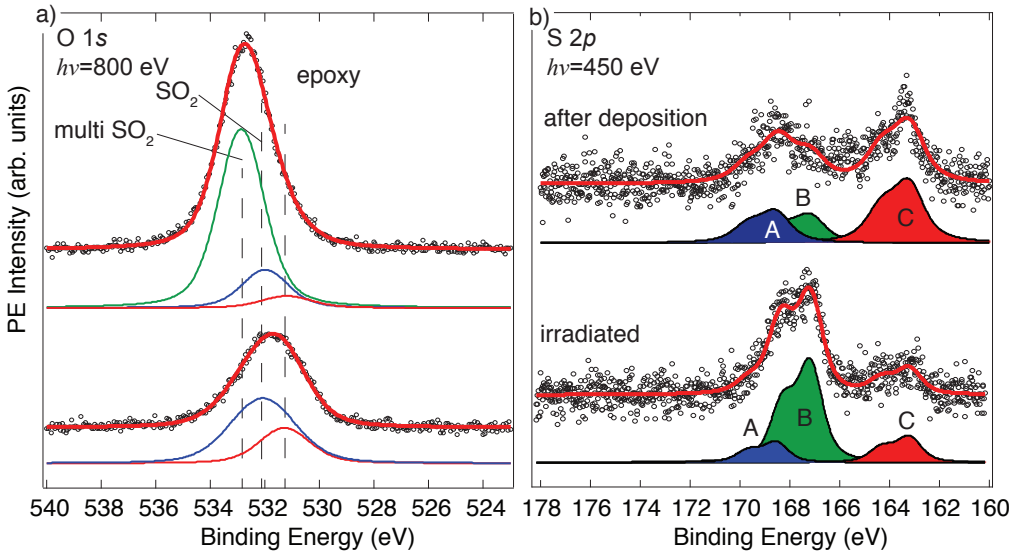

Figure 7.12. – Adsorbates core level spectra for higher initial SO_2 coverage: Oxygen 1*s* (a) and sulfur 2*p* (b) corresponding to the substrate core levels presented in Figure 7.10. all spectra are background subtracted (third order polynomial) and fitted by Voigt (a) or Doniac-Sunnjic corrected Voigt profiles (b), respectively. The upper spectra present the adsorbate core level lines directly after adsorption. The lower spectra present the same set of spectra after a longer measurement period and subsequent irradiation.

together with Figure 7.11. With subsequent irradiation, the amount of epoxidic oxygen is found to grow. The blue and green components are probably SO_2 and multilayers of SO_2, respectively. Their energies are 523.0 eV (SO_2) and 523.7 eV, respectively. Note that the shift between what is assumed to be the single and multilayer of SO_2 is comparable to what is observed from single and multilayer water in Figure 6.1. Another indicator for the multilayer assignment is the loss over time and irradiation of the multilayer SO_2 component. The upper spectrum of Figure 7.12 a) is acquired during the preparation step and may incorporate uncertainties from the ongoing chemical photoreaction during every acquisition cycle. However, this uncertainty should only affect the intensities of the individual components but not the energies.

Figure 7.12 b) shows the sulfur 2*p* photoemission lines for the larger initial coverage. The decomposition products of SO_2 during irradiation are clearly visible. This time, also a considerable amount of SO_2 is observed. The two spectra are acquired directly after adsorption (upper spectrum with a dose of approx. $3.3 \cdot 10^{18}$ photons/cm^2·s for about 30 min) and after irradiation (lower spectrum). These spectra illustrate the decomposition with photon dose. With SO_2 adsorbed on graphene/Ir(111), all fragments (SO and S) are present shortly after the irradiation has started. The amount of elemental sulfur ($E_B = 163.21$ eV) is largest after the adsorption process. This can be interpreted as sulfur

being formed by fast photolysis as soon as SO_2 is adsorbed. With subsequent photon dose, SO_2 and S components vanish, leaving mostly the SO line in the spectrum, whose intensity is here about 9 at.% of the C 1*s* intensity. This trend shows that the amount of fragments scales with the initial amount of adsorbed SO_2. These fragments may be adsorbed on graphene in those areas which are rehybridized towards sp^3, and may also explain the larger ratio of peaks B and C in Figure 7.10. If SO fragments are chemisorbed on graphene, they may further distort the graphene backbone, inducing more sp^3 rehybridized carbon atoms. Furthermore, if a large amount of SO is chemisorbed during the oxidation procedure, this would inhibit graphene from being further oxidized, since SO fragments would block the active areas of graphene. Both finding together may result in the larger hybridization peak B/C ratio in Figure 7.10.

The appearance of these fragments and their varying relative concentration during light exposure also suggests an activated adsorption. NO_2 as well as SO_2 require a high dose of the corresponding gas and more than one cycle of deposition. An adsorption signal has never been observed after the first deposition. Since graphene is inert [34] and a sample can be carried through air, it is reasonable to assume that molecules such as NO_2 and SO_2 are weakly bonded to graphene, probably driven by dispersion forces. Photon-induced desorption or a very low sticking coefficient could prevent adsorbates from being detected under synchrotron conditions. An activated adsorption, in this framework, is the key to explain the required high dose of a pre-adsorption experiment: Only if NO_2 or SO_2 are adsorbed and photolysed on the sample, an activated site that enhances the interaction possibility of graphene is formed. Such activated sites can be an sp^3 distorted carbon atoms or the epoxide itself. The contact can be achieved by either irradiation under constant partial pressure (see Section 7.2.3) or oxidation of a small amount of remaining adsorbate after deposition (prior to a possible photo-desorption, as discussed above).

A perturbation of the graphene backbone should be visible in the substrate NEXAFS at the carbon K edge, resulting from the oxidation and possibly scaling with the amount of SO_2 on the surface. Figure 7.13 shows the NEXAFS spectra obtained for clean graphene/Ir(111) (black), graphene oxide obtained from a small (blue) and graphene from a large initial coverage of SO_2 (red). The small initial coverage (blue) corresponds to the XPS data from Figure 7.10 and Figure 7.11, while the large initial one corresponds to Figure 7.12. α is the angle between the incident light and the surface normal. The NEXAFS spectrum for clean graphene/Ir(111) shows the transitions into the π^*- (285 eV photon energy) and the σ^*-states (290 eV photon energy), in agreement with the NEXAFS data presented in the previous section. The general observation of the oxidation of graphene is qualitatively similar to the NO_2 case. The spectrum for the small initial

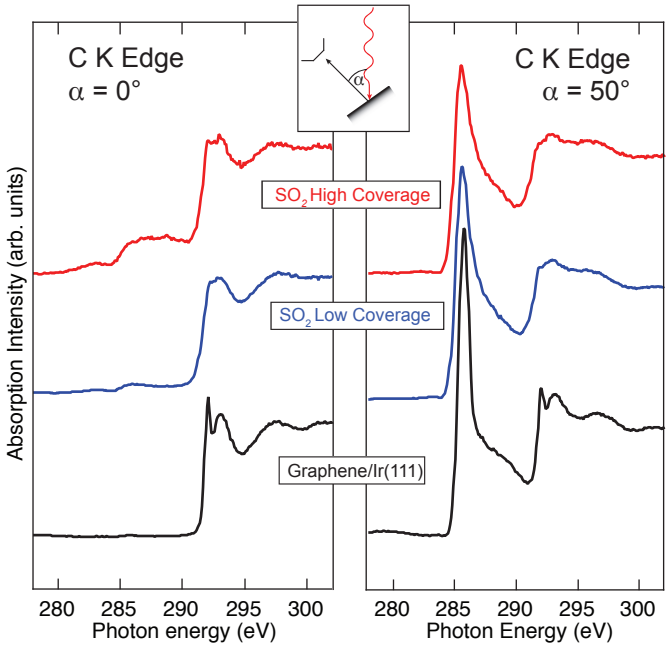

Figure 7.13. – Near Edge X-Ray Absorption Fine Structure Spectra for the carbon K absorption edge of Graphene/Ir(111) (black), GrO/Ir(111) obtained by a low initial coverage and further subsequent SO_2 dose and irradiation and GrO obtained from a large initial coverage (>1 ML) of SO_2.

coverage shows the same broadening of the π^*- and σ^*-transitions as already observed for the NO_2 case in Figure 7.4. Due to the rehybridization from sp^2 (pristine graphene) to sp^3 (epoxidic carbon atoms and adjacent distorted carbon atoms) the formerly sharp and well-defined transitions are broadened because the affected carbon atoms change their electronic configuration. With light impinging at normal incidence, an enhanced π^*-transition is observed, showing that in this experimental geometry several electronic states of the affected carbon atoms differ from the initial planar configuration. This enhancement leads to an intensity of the C $1s \rightarrow \pi^*$ transition, which is six times larger for $\alpha = 0\,^\circ$ than for pristine graphene. However, in direct comparison to NO_2-derived GrO from Figure 7.4 (blue) and SO_2 derived GrO in Figure 7.13 (blue), the signal intensity differs. The amount of epoxidic oxygen is lower, which results in a lower rehybridization signal. While the C $1s \rightarrow \pi^*$ transition for normal incidence is enhanced by a factor of 10 for oxyidation from NO_2, here the enhancement of the C $1s \rightarrow \pi^*$ transition is by a factor of 6.

The red spectra of Figure 7.13 correspond to a high initial coverage of SO_2. The oxidation effects are observed, similar to the low initial coverage. However, besides the broadening of the transition around 285 eV photon energy, the spectrum is also much broader in the energy range between the C $1s \rightarrow \pi^*$ and the C $1s \rightarrow \sigma^*$ transitions, around 288 eV. The major difference between these two experiments is the amount of SO fragments

on the surface. The strong broadening in the energy range between 285 and 290 eV photon energy reflects a strong influence on the graphene backbone, apart from the oxidation and its related rehybridization. One explanation may be the fact that the SO species is the majority of remaining fragments on the surface, and is the reason for the distortion. Such fragments would be adsorbed in the *fcc* or *hcp* hollow sites of graphene/Ir(111) as already suggested for adsorbates in general [44]. Comparing to the GrO NEXAFS spectra from Figure 7.13 for a low and high amount of adsorbed SO_2 (blue and red) implies a correlation between the amount of SO fragments and rehybridization. This correlation may be interpreted as follows: The SO fragments are adsorbed close to the oxdized carbon atoms, an environment that contains a considerable amount of sp^3 hybridized carbon atoms that may enhance the adsorption of SO. On the other hand, an enhanced adsorption of SO may cause a stronger distortion because the bond of the carbon atoms to SO may be relatively strong, possibly already in the range of a weak chemisorption. Such a chemical interaction is most dominant in the unoccupied states by the electronic rearrangement of the affected carbon atoms.

In comparison to the results from Section 6.2.2, no sharp lines as observed for water and ammonia are present in the substrate carbon K edge NEXAFS spectra of oxidized graphene/Ir(111). One explanation for this circumstance may be that the hybridization of the affected carbon atoms has changed. The sharp and well-defined structure of pristine graphene is changed towards an electronic structure originating from multiple electronic configurations. The strong background, especially for the normal incidence spectra, is likely to inhibit the formation and/or detection of a small, but sharp feature from chemisorbed SO_x.

The formation of a band gap after oxidation of graphene has been shown in the case of NO_2 in Figure 7.5. Since the core level and NEXAFS spectroscopy reveals the formation of graphene oxide, a band gap should be expected. It can further be expected that the size of the band gap may be different due to the lower amount of oxygen in the graphene lattice. Figure 7.14 shows a valence band photoemission spectrum taken at the K point of the hexagonal Brillouin zone at room temperature. The extracted photoemission maps of energy vs. $k_{||}$ are presented along directions $\Gamma \rightarrow$ K and perpendicular to $\Gamma \rightarrow$ K as energy vs. k_x and k_y, respectively. Upon oxidation, a band gap of about 330 meV is formed at the K point. The band gap is evaluated according to the procedure described for Figure 7.5. The energy dispersion of E_B vs. k was fitted below the band gap by fitting a Lorentz function to every MDC between 0.5 and 1.5 eV binding energy. The thus-obtained maximum photoemission intensity of the graphene π-band fit in E_B vs. k was then fitted by a linear function. From this function, the energy position of the former Dirac cone was extrapolated (energy value of the linear fit at $k_x = 1.71\text{Å}^{-1}$). The band gap is assumed to be twice the difference between the former Dirac point and the maximum band dispersion of GrO. With 330 meV, the band gap is smaller compared to

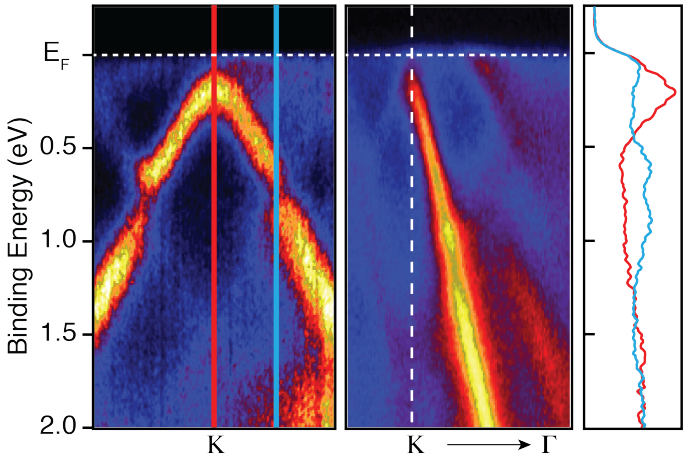

Figure 7.14. – Valence band map of GrO/Ir(111) from adsorption and irradiation of SO_2: Photoemission intensity $I(E_B, k_x, k_y)$ in false colour. The spectrum is acquired at room temperature. The panels show (from left to right) the energy vs. k dispersion, perp. to $\Gamma - \mathrm{K}$, the dispersion along $\Gamma - \mathrm{K}$ and extracted profiles directly at the K point (red) and inside the mini gap (blue).

the value obtained from oxidation by NO_2 with 580 meV (Figure 7.5). Hence, the band gap scales with the amount of oxygen on the graphene/Ir(111) surface, as observed in the literature [173].

7.3.2. Summary

In summary, SO_2 adsorbs dissociatively under synchrotron radiation conditions on graphene/Ir(111), forming graphene oxide as found for NO_2 as well as fragment adsorption on graphene/graphene oxide. From XPS on the substrate, the formation of graphene oxide upon adsorption and irradiation of SO_2 is observed, similar to the observations from NO_2. The reaction is limited to a lower oxygen amount than observed from NO_2 adsorption and irradiation. XPS on the adsorbate core level lines, reveals the existence of SO_x fragments from adsorbed SO_2. SO and elemental sulfur are detectable after the oxidation. I believe that these fragments block the surface due to a strong adsorption on the graphene/Ir(111) hollow sites. Evidence for this interpretation is found in the substrate carbon K edge NEXAFS spectra. Upon higher dosages of SO_2 on the surface, a noticeable broadening of the $C\,1s \rightarrow \pi^*$ transition range is detected, which I assign to be a strong distortion of the graphene backbone due to chemical interaction of the SO fragments.

At room temperature, the formation of a band gap has been observed after the oxidation. The width of the band gap is smaller compared to the oxidation from NO_2 photolysis and scales with the amount of incorporated oxygen within the graphene lattice.

7.4. Phosphorus-Trifluoride on Graphene

7.4.1. Introduction

Apart from oxidation described in the present chapter, several other attempts have been made to covalently attach atoms to graphene in order to form a band gap needed for possible electronic switching applications [3]. Among these, hydrogenated graphene, called graphane in analogy to the alkanes, was predicted to exhibit a large band gap of up to 3.7 eV [188,189]. However, the structure of graphane suffers from thermal instability [190]. Another possibility is to introduce fluorine, leading to a structure that has been called the two-dimensional teflon: fluorographene [191–194]. Completely fluorinated graphene ($[CF]_n$) can be obtained from wet chemical exfoliation of graphite-fluorite [195], but also from decomposition of XeF_2 on graphene [191, 196] or laser induced decomposition of a fluoropolymer [193]. Recently, half fluorinated graphene ($[C_2F]_n$) has been obtained on graphene/H-SiC by decomposition of XeF_2 [194]. Fluorinated graphene also exhibits a band gap in the order of $\sim$3 eV.

Using PF_3 may open another path to obtain such functionalized graphene, accessible via a similar mechanism as I have described for the oxidation of graphene above, using x-rays from the synchrotron light source. The fragmentation, and hence the release of fluorine, is expected from other experiments of PF_3 adsorption on Ru(0001) [197,198]. Apart from its uses described above, PF_3 was also chosen because of its similarities to ammonia. It has the same symmetry as ammonia, which should give it the possibility to adsorb in a similar way to graphene/Ir(111), possibly showing the same fingerprinting behaviour in the NEXAFS data. Furthermore, a large dipole moment of 1.05 D [153] and the fact that it does not contain carbon atoms, makes PF_3 a possible candidate for identifying its interaction with graphene through carbon K edge NEXAFS fingerprint, such as observed for water and ammonia, in Chapter 6. However, not only is PF_3 unstable under irradiation with synchrotron radiation, it turns out that PF_3 undergoes fragmentation on the surface. This behaviour is indeed similar to NO_2 and SO_2 under synchrotron irradiation conditions.

In the following, the dissociation under photon flux will be characterized using substrate and adsorbate core level spectroscopy. Additional spectral components from the carbon atoms are found which are assigned to an interaction of the PF_3 fragments with graphene. A quantitative analysis of the adsorbate core level lines is performed in order to reveal the nature of the fragments. Finally an analysis of the carbon K edge NEXAFS confirms the existence of chemically interacting PF_x fragments with the graphene/Ir(111) substrate.

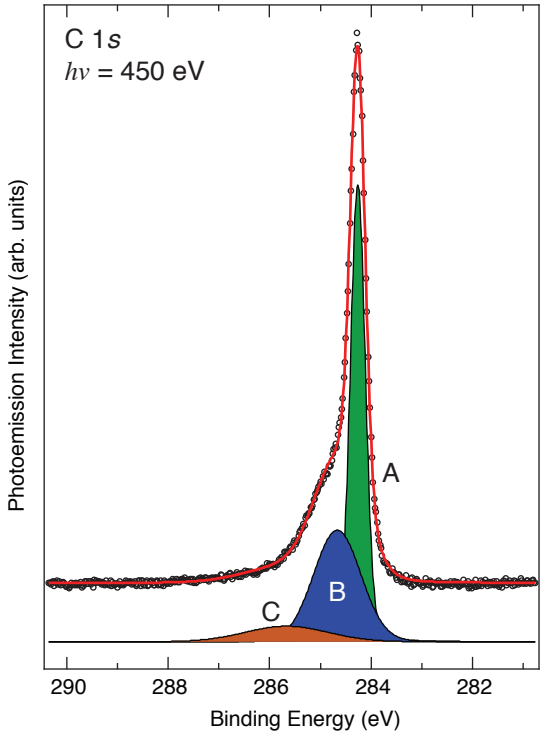

Figure 7.15. – Carbon 1*s* core level line for PF_3/graphene/Ir(111), after a total photon dose of $\approx 1 \cdot 10^{23}$ photons/cm^2. A is the pristine graphene sp^2 component, B is the rehybridized sp^3 component and C is a new component attributed to the interaction of graphene to PF_x fragments.

7.4.2. Adsorption and Fragmentation of PF_3 on Graphene

Possible influences of adsorbates are well detectable in the carbon 1*s* core level line, as observed in the experiments presented in Section 7.2 and 7.3. Hence, the C 1*s* core level line should provide the first insight into the interaction of PF_3 with graphene. Figure 7.15 shows the carbon 1*s* core level line after adsorption of PF_3 on graphene/Ir(111) at T=100 K and subsequent irradiation with a total amount of $\approx 1 \cdot 10^{23}$ photons/cm^2 (flux density of $3 \cdot 10^{19}$ photons/cm^2·s). The core level line has been fitted as usual, using Voigt profiles with open Gaussian width for all peaks and a fourth order polynomial background (subtracted here). The parameters for the sp^2 and sp^3 components agree with the previously obtained values from the GrO experiments. The adsorption required high doses as in the case of NO_2 and SO_2 before observing spectroscopic evidence for the presence of PF_3. This behaviour points to a possible activated adsorption. In case of SO_2 I have interpreted a similar behaviour as the necessity to form some epoxides, in order to have a reaction centre to start the adsorption of SO_2. However, no oxygen incorporation is possible with PF_3 we will see that a similar activation is present, when discussing the adsorbate core level spectra.

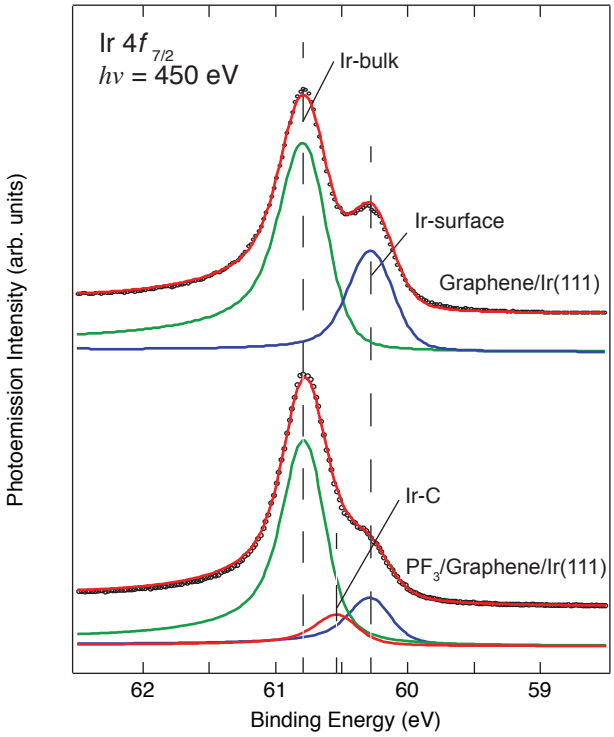

Figure 7.16. – Core level spectra for the Ir $4f_{7/2}$ line, presented for clean graphene/Ir(111) and after adsorption and irradiation of PF_3. The individual components are the Ir-bulk (green), the Ir-surface (blue) and Ir-C (red) component.

When a considerable amount of PF_3 was observed on the surface, a change in the carbon $1s$ core level could be observed. Similar to the graphene oxide studies presented above, the sp^2 component with 52% (A) of the integrated signal intensity, and an sp^3 component (B) with 38% of the integrated signal intensity can be identified at binding energies of 284.2 eV and 284.7 eV, respectively. This observation already suggests a distortion in the graphene layer. A third component (C) is located around 285.7 eV binding energy, with an intensity of 10% of the integrated signal intensity. The binding energy alone is not sufficient to derive its origin, e.g. wether it is a possible C-P-component, a C-F-component or a chemically shifted graphene signal due to noncovalently bonded adsorbates. Fluorination may be expected, but the new feature is at binding energies too low to be a C-F bond, according to fluorographene studies [196, 199]. Phosphorus doped graphene, obtained from reduced GrO is also reported to show C-P bonds at higher binding energies [200]. However, only in compounds such as triphenylphosphine derivates, a binding energy of a C-P component in the C $1s$ was found in a comparable range as observed here [201]. To assign a possible origin of this new core level component, the fragmentation pattern of PF_3 on graphene/Ir(111) has to be evaluated.

The formation of sp^3 rehybridized carbon atoms was found to correlate with a reduction of the Ir $4f$ surface components (see Figures 7.3 and 7.10). The presented fit was per-

formed using spin-orbit split Doniac-Sunjic [167] corrected Voigt profiles over the whole Ir $4f$ core level range with a linear background. Three components can be identified in agreement with Ir $4f_{7/2}$ core level spectra of the graphene oxide studies presented above: An Ir $4f_{7/2}$ bulk component at 60.7 eV binding energy (green), the Ir $4f_{7/2}$ surface component at 60.2 eV binding energy (blue) and an Ir-C component at 60.5 eV binding energy (red). The intensity depletion of the Ir-surface component and the rise of the Ir-C component illustrates the rehybridization of the sp^2 carbon atoms to a distorted sp^3 phase of the graphene layer with the concomitant enhanced interaction to the Ir(111) substrate upon adsorption of PF_3. The formerly unperturbed Ir(111) surface atoms are now affected by the rehybridized carbon atoms. The spectrum presented here is comparable to weakly oxidized graphene oxide from NO_2 as presented in Figure 7.3.

In order to obtain information about the origin of the strong rehybridization of the graphene lattice and the new core level component in the C $1s$ line after adsorption of PF_3, core level spectra of the adsorbate photoemission lines F $1s$ and P $2p$ were recorded. Figure 7.17 shows the F $1s$ (a) and P $2p$ (b) core level spectra for two different stages of the experiment. The upper spectra present the core level lines after deposition whereas the lower spectra show the core level lines after longer exposure to x-ray radiation of $\approx 1 \cdot 10^{23}$ photons/cm^2. F $1s$ and P $2p$ core level lines were fitted with the same parameters for both stages of the experiments, respectively. The F $1s$ core level line was fitted using two Voigt profiles, with restricted FWHM and a fourth order polynomial background (subtracted here). For the P $2p$ core level line, three spin-orbit split Voigt profiles were used with restricted FWHM and spin-orbit splitting. The background correction was achieved by recording a background spectrum on the clean sample. However, for the corrected spectrum a third order polynomial background was used.

The F $1s$ core level line in Figure 7.17 a) consists of two individual components at 685.1 eV (blue) and 682.2 eV (green) binding energy. The ratio of the two signals, calculated from the fit, is 45%:55%, respectively. The overall intensity corresponds to an amount of C $1s$:F $1s$ of 1.5:1 (66% w.r.t. the C $1s$ intensity), including a correction of the PE cross sections for the fluorine and carbon $1s$ core level lines at 1000 eV [161]. After irradiation, the intensity of the F $1s$ core level line is reduced to ≈40% of its initial value, to a ratio of C $1s$:F $1s$ of 3.3:1. The component at 682.2 eV binding energy is here more strongly reduced than the component at higher binding energy. The ratio between both components is now 67%:33% (blue and green curves). An assignment of the individual components is not trivial since neither the C $1s$ nor the P $2p$ line (see next paragraph) support an obvious interpretation of the two components. Two scenarios may be considered: One is that the two components of the F $1s$ core level show fragments of PF_3. Hence a possible explanation could be two different chemical environments, e.g. two bonding situation or oxidation states of phosphorus. This can, for example, be PF_3+PF_2 and PF, or PF_3 and PF_2+PF, i.e. assuming that two out of the three fragments exhibit the

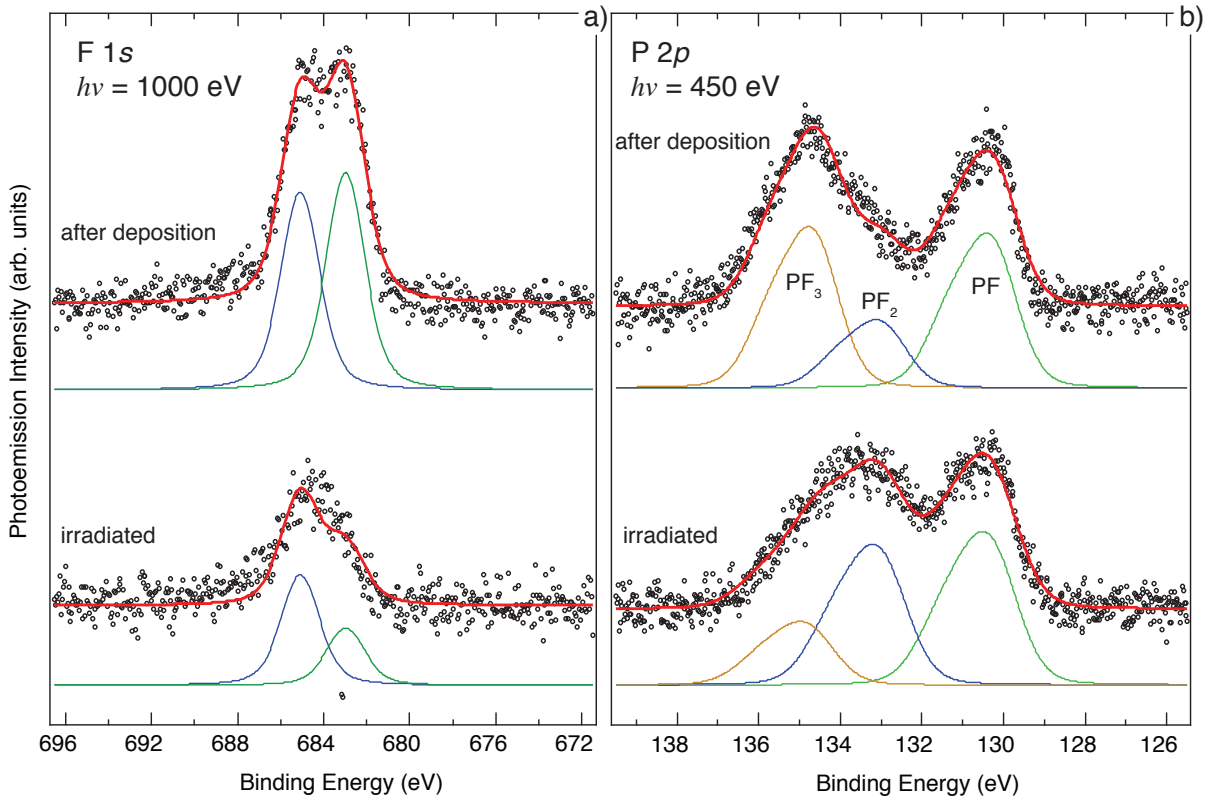

Figure 7.17. – Core level spectra for the adsorbate F 1*s* and P 2*p* line, directly after adsorption (upper spectra) and after a total dose of $\approx 1 \cdot 10^{23}$ photons/cm^2 (lower spectra).

same chemical environment to the fluorine atom. Another possibility is that one component shows the fluorine signal from all PF_x fragments, whereas the other component is a fluorine species not connected to PF_x, maybe molecular (F_2) or atomic fluorine on the surface. Either possibility has to be consistent with the amount of phosphorus and fluorine obtained from the intensity of the core level signals. For this reason a quantitative analysis of the P 2*p* core level line will be given below.

The phosphorus 2*p* photoemission line is presented in Figure 7.17 b). The P 2*p* core level shows three spin-orbit split components, located at 134.8 eV, 133.0 eV and 130.3 eV eV binding energy. I assign these lines to the break-up of PF_3 under irradiation and the formation of PF_x fragments on the surface. A similar fragmentation of PF_3 has been reported on Ru(0001) in the literature [197, 198]. Hence, I assign the three components to be PF_3, PF_2 and PF, respectively. In the literature an energy difference between the fragments of 1.7 eV is observed for PF_3 on Ru(0001) [198]. Between the PF_3 (134.8 eV) and PF_2 (133.3 eV) an energy difference of 1.8 eV is observed here, which matches with the reported separation of PF_3 fragments on Ru(0001). However, what I assign to be the PF component is shifted by around 1 eV to lower binding energies, as expected, by a total of 2.7 eV. Comparing the two exposures it becomes also clear that exactly this line (PF)

is present directly after the adsorption. The upper spectrum in Figure 7.17 is collected approx. 30 min after adsorption exposed to a flux density of $3.3 \cdot 10^{19}$ photons/cm^2·s. The total amount of phosphorus on the surface is extracted from the core level spectra presented here, corrected by the photoemission cross section [161], showing a ratio of C 1s:P 2p of 9:1.

In order to assign the two components of the fluorine 1s core level line, the expected amount of fluorine on the surface can be calculated, by summing up over the intensity of the individual PF_x components and calculating the ratio of F 1s intensity w.r.t. the C 1s core level line, in the following referred as to %(w.r.t. C 1s). Then it may be estimated wether one of the interpretations for the F 1s core level components is correct. The quantitative analysis given below is summarized in Table 7.1

Directly after irradiation, the P 2p core level line consists of individual fragments whose intensities of the core level line are 42% PF_3, 18% PF_2 and 40% PF. This would correspond to a net amount of fluorine of $\approx PF_2$. The expected amount of fluorine can now be evaluated by calculating the intensity ratio of the fluorine 1s core level line to the C 1s line. The P 2p line has about 11% w.r.t. the C 1s line intensity, which then corresponds to roughly an expected amount of 22%(w.r.t. C 1s) for the fluorine 1s core level line. The amount of fluorine obtained is 66%(w.r.t. C 1s) which means that an intensity of 44%(w.r.t. C 1s), cannot be related to PF_x. If the two components of the F 1s line would correspond to PF_x and elemental fluorine, then another ratio should be observed. Both individual components should in this case have a ratio of 33:67. However, from Figure 7.17 a), a ratio of the two components of 45:55 is obtained. There is a simple explanation why the analysis fails for the two upper spectra: the F 1s and P 2p do not show the same reaction stage, because in between these two measurements, the sample is exposed to a dose of $3.3 \cdot 10^{19}$ photons/cm^2·s for about 30 minutes. For this reason, no conclusion can be made if one of the two possible explanations, suggested for the appearance of two F 1s components above, is correct.

The situation is different for the late stage of the experiment, where the reaction has reached its saturation or is very close to this point. The same analysis for the ratio of the F 1s core level line intensity w.r.t. the C 1s line was performed, on the basis of the P 2p line. The different distribution of the individual components intensity leads to another relative amount of fluorine on the surface, calculated on the basis of the P 2p core level. Here the amount of the individual components is found to be 18% PF_3, 39% PF_2 and 43% PF. This corresponds to a net fluorine amount of $\approx PF_{1.75}$. The intensity of the P 2p line is also at this late stage on the order of 11%(w.r.t. C 1s). Therefore, no phosphorus has desorbed from the surface. The estimated F 1s core level intensity on the basis of the P 2p core level intensity should be 19%(w.r.t. C 1s). The observed intensity of the F 1s is 27%(w.r.t. C 1s). A remaining intensity of 8%(w.r.t. C 1s) should be observed in

stage	C 1s:F 1s (%C1s fit)	C 1s:P 2p (%C1s fit)	PF_x (net)	C 1s:F 1s (%C1s calc)	residual (%C1s)	F 1s ratio calc (obs)
deposited	1.5:1 (66%)	9:1 (11%)	2.02	(22%)	(46%)	33:67 (45:55)
irradiated	3.3:1 (27%)	9:1 (11%)	1.75	(19%)	(8%)	70:30 (65:35)

Table 7.1. – Summary of the quantitative analysis of the expected fluorine amount based on the P 2p core level line. All percentages are relative intensities to the corresponding carbon 1s core level line. PF_x refers to the net amount of fluorine normalized to all PF_x components. The F 1s ratio is the ratio ob the two components of Figure 7.17 (blue:green) as expected from the analysis (calc) and observed (obs)

the F 1s core level line, which then corresponds to a ratio of both lines on the order of of 70%:30% (≈2:1). Indeed, almost these values (65%:35%) are found in the fit of the F 1s line in Figure 7.17.

This finding leaves only one conclusion open to the nature of the two F 1s components. The component at $E_B = 685\,\text{eV}$ can be assigned to PF_x, assuming fluorine always has the same chemical shift, and the second component at 683 eV binding energy is elemental fluorine that desorbs under irradiation. Note that graphene has been reported to be inert to elemental fluorine [202]. The possibility to observe two different PF_x related signals can be ruled out for another reason. If the two components are assigned to two types of fragments, such as $PF_{x=2,3}$ and PF, the relative amount of fluorine calculated from the lower P 2p spectrum in Figure 7.17 (57% $PF_{2.3}$ and 43% PF), would also lead to a ratio of ≈2:1. However, the overall intensity of the F 1s line does in this case not agree with this explanation, since too much fluorine is observed in the F 1s core level line. Furthermore, in the P 2p line, the PF component does not change over time, whereas the two individual components of the F 1s line do. Assuming one component, such as that at 683 eV, to be due to PF, it should not change over time. However, since such a change is observed, this assignment can be ruled out.

In summary, the quantitative analysis of the individual F 1s and P 2p components suggests that only one chemical environment for fluorine from PF_x can be resolved. A second component is highly unstable under irradiation. This is surprising since the chemical shift of the PF component, which is almost 1 eV larger than expected, may suggest that more F 1s components may be observed (yet another oxidation state of fluorine or an additional chemical shift). However, this analysis leaves a possibility to explain the carbon 1s component at 285.7 eV. It may be that the PF fragments interact strongly with graphene. Since carbon is more electronegative than phosphorus, it may induce a charge transfer

from the PF fragment towards graphene, which would explain the larger shift of 2.7 eV (see Figure 7.17). If this is the case, a distortion of the graphene backbone in NEXAFS has to be observed, such as in the case of the SO_2 fragments.

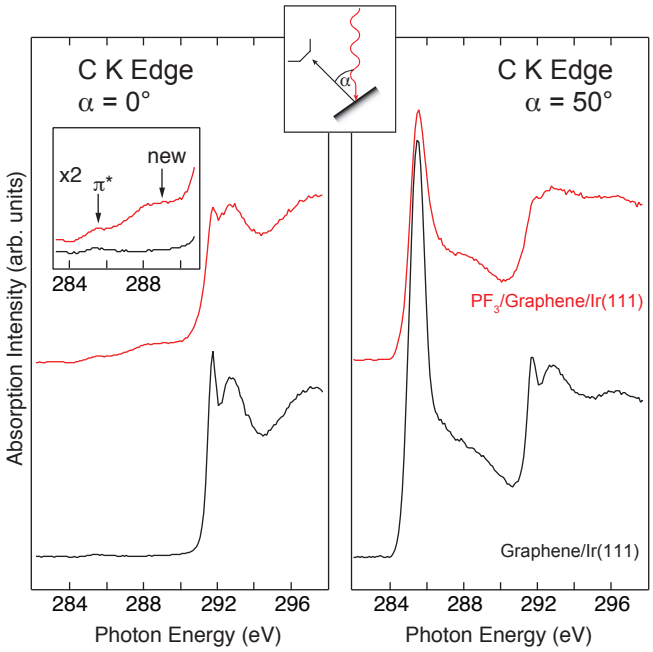

Figure 7.18. – NEXAFS spectra at the carbon K absorption edge for clean graphene/Ir(111) (black) and PF_3 adsorbed and irradiated. The spectra are presented for light impinging at normal incidence ($\alpha = 0\,°$) and moderate grazing incidence ($\alpha = 50\,°$). The inset presents a zoom on the π^* transition range, enhanced by a factor of 2.

Figure 7.18 presents two NEXAFS spectra for graphene/Ir(111) and PF_3/graphene/Ir(111). The light impinges at normal incidence for $\alpha = 0°$ and moderate grazing incidence for $\alpha = 50°$. The inset presents a closeup on the $C\,1s \rightarrow \pi^*$-transition of the NEXAFS spectrum. The NEXAFS spectra for pristine graphene/Ir(111) exhibit the same features as already described for Figures 7.4 and 7.13. After adsorption and irradiation of PF_3, the NEXAFS spectra show a decrease of the sp^2 hybridization by a broadening of the π^*- (258 eV) and σ^*-transition (290 eV) regions. The sharp features of graphene are broadened and weaker in intensity for $\alpha = 50\,°$. However, for $\alpha = 0\,°$ the π^*-transition intensity is increased. These observations are similar to the interpretation of the oxidation of graphene, which was attributed to the rehybridization from sp^2 to sp^3. This is also consistent with the observations from the carbon $1s$ core level line in Figure 7.15. The inset shows a closeup on the $C\,1s \rightarrow \pi^*$-transition from 284 to 290 eV photon energy, enhanced by a factor 2. The increase of the π^*-feature is shown by the arrow pointing at the spectral feature at 285 eV. Similar to the adsorption of SO_2 fragments on graphene (see Figure 7.13), the broadening of the region between 285 and 290 eV is clearly visible. Indeed it is even sharper since the formation of graphene oxide,

that also induces a broadening, does not happen here. The new spectral feature in the C K edge spectra is located around 289 eV photon energy.

At this point I would like to revisit my initial intention, to study the adsorption of molecules and their possible fingerprinting in the carbon K edge NEXAFS spectra, such as I observed it for water and ammonia on graphene/Ir(111) (see Chapter 6). I hence interpret this feature at 289 eV photon energy is a fingerprint signal of the PF fragment on graphene/Ir(111). PF fulfils (like initially intended for PF_3) several conditions for a fingerprinting: It does not contain carbon, which would affect the analysis. Neutral PF would have the oxidation state 1 for phosphorus which then includes lone pairs that could interact in a similar fashion as the lone pair of ammonia. Finally, due to the presence of fluorine, a large dipole moment, as it is also present for water and ammonia, can be expected for PF, since PF_3 already has a large dipole moment of 1.03 D [153].

7.4.3. Summary

The adsorption of PF_3 on graphene/Ir(111) under synchrotron radiation results in a photon induced dissociative adsorption. All fragments of PF_3, containing fluorine, are present. However, the adsorption may be activated by the PF fragments, that chemically interact with the graphene surface and rehybridize the graphene backbone. Evidence for this conclusion is found in the carbon 1*s* core level line that exhibits a novel component at higher binding energies than the sp^2 and sp^3 components, and in a strong differential chemical shift of the PF fragment compared to PF_3 and PF_2. The chemical interaction of PF with the graphene layer can also be found in the NEXAFS spectra of PF_3/graphene/Ir(111), which exhibit a new, broad spectral feature. This new feature appears besides the characteristic change of the spectra due to rehybridization and are clearly separated. The formation of a possible C-P bond between graphene/Ir(111) and the PF fragments also makes clear that no fluorination is observed.

7.5. Conclusions

The adsorption and photolysis of NO_2, SO_2 and PF_3 on graphene/Ir(111) was studied, and all molecules were found to dissociate under synchrotron radiation. In contrast to Chapter 6, where water and ammonia were adsorbed non-dissociatively, the formation of fragments of the adsorbed NO_2, SO_2 and PF_3 open a path to a covalent functionalization of graphene.

The photolysis of NO_2 and SO_2 results in the formation of active oxygen atoms on the surface that are able to oxidize graphene. The oxidation reaction probably takes place only where molecules are adsorbed. Since the *hollow* sites of the graphene/Ir(111) moiré are preferred adsorption sites, due to their enhanced chemical activity [44], the oxidation is selective and limited to these areas. The active oxygen atoms, formed under irradiation, very selectively produce epoxidic oxygen atoms when irradiated with high intensity light. Only if the reaction rate is lowered for the photolysis of NO_2 adsorbed on graphene/Ir(111), intermediate carbonyl species are observed. However, these kinetic products are metastable and can be transformed into epoxides under further irradiation and oxidation. The oxidation from photolyzed NO_2 and SO_2 molecules is likely to be less intrusive compared to other methods. This is judged from the fact that the thus formed graphene oxide can be reduced into graphene with a negligible amount of defects and no loss of carbon from the surface after the reduction. This finding has two main reasons. Epoxides which are exclusively formed here, are found to be easily removable without introducing major defects into graphene [183]. On the other hand, the oxidation by locally selective photolysis of the adsorbed molecules also does not introduce defects during the oxidation, as it was reported from other oxidation methods, such as oxygen atom bombardment [159]. Finally, the oxidized graphene layer exhibits a band gap whose energy splitting is, as expected [203], dependent on the amount of oxygen on the surface.

The pure adsorption of all molecules without dissociation of the molecules on graphene is likely to be inhibited by an activation barrier. This is not surprising, since graphene was reported to be very inert [34]. I observed that no adsorption is achieved by simply exposing the molecules to the surface. However, the molecules are detectable on the surface as soon as fragments have formed under irradiation. This happens after irradiation of a weak amount of molecules on the surface after a long exposure. In case of SO_2, SO and elemental sulfur are found besides SO_2 only if epoxides are formed and the graphene is activated by the incorporated oxygen atoms. In this case, the adsorption of SO is likely to further increase the reactivity of graphene by inducing an additional distortion into the formerly sp^2 hybridized graphene layer, as judged from NEXAFS experiments. The appearance of fragments, on the other hand, limits the amount of oxidation. The fragments block the active sites that are necessary to adsorb SO_2 for photolysis. In case

of PF_3, its adsorption appears with the concomitant appearance of PF. This fragment probably binds to graphene and induces a distortion into the graphene lattice, that is then activated and able to adsorb PF_3.

The photolysis of PF_3 did not lead to a fluorination under fragmentation. Instead, the formation of a chemical interaction between the PF fragment of PF_3 with graphene is present, under loss of F_2. Evidence for this interpretation is found in the large chemical shift of PF component of the P $2p$ line, compared to the other fragment components, and by new spectral features in the carbon $1s$ core level line and the carbon K edge NEXAFS spectra. For the latter, the new features exhibits similarities to the fingerprint signals of water and ammonia in chapter 6.

8. Functionalizing Graphene by Substrate Modification- Graphene on Intercalated Manganese

8.1. Scanning Tunneling Microscopy from Manganese Intercalation on Graphene/Ir(111)

8.1.1. Introduction

In Chapters 6 and 7 the adsorption and reaction of molecules on graphene was studied. The adsorption of molecules could successfully observed by utilizing graphene's abilities to reflect the influence of water and ammonia adsorption, in its clear electronic structure. A chemical functionalization of graphene could be achieved by oxidation. The photolysis of adsorbed molecules such as NO_2 and SO_2 leads to the formation of graphene-oxide. Another pathway to functionalization is to change the chemical environment of graphene by modifying its support or the graphene back-side, as named by Schumacher *et al.* [204]. Bringing a new metal layer into the space between graphene and the substrate provides the possibility to systematically tune the electronic and crystallographic structure of the entire graphene layer, instead of punctual functionalization, such as by local oxidation. As already summarized in Section 2.2.3, many intercalation studies are present in the literature. The influence of intercalation can range from a complete electronic decoupling of graphene from the substrate by hydrogen [64] or gold [49], towards an introduction of special properties, such as magnetism [57] or the transformation of graphene from a semimetallic to a semiconducting phase by forming a band gap [56].

In this section, the intercalation of manganese is studied by means on scanning tunneling microscopy and core level and valence band photoemission spectroscopy. First, the deposition and the intercalation process will be discussed. Then, the formation of a close-packed intercalated manganese layer will be presented, supported by photoemission spectroscopy of the valence band of graphene/Mn/Ir(111). Finally, a classification within the interaction strength terminology will be provided.

The experiments presented here were performed in a joint study by the present author and Hendrik Vita. The investigation and interpretation of the electronic structure and the interaction of graphene to the pseudomorphic manganese layer is partly based on the doctoral thesis of Hendrik Vita [205], while I concentrate on the morphological aspects of this system.

8.1.2. Intercalation Process

The process of intercalation of foreign materials into bulk graphite has been studied extensively and is reviewed in detail by Dresselhaus and Dresselhaus [45]. The intercalation process on graphene, especially graphene/Ir(111), has been shown for various materials, such as gold [50], nickel [58], cobalt [57], and cesium [61]. All these intercalating metals grow pseudomorphically with respect to the metal substrate, meaning they adapt to the Ir(111) lattice, with the Ir(111) lattice constant. The only exception in this comparison is cesium, because its lattice constant is larger than that of Ir(111) [61]. Manganese has so far not been used for intercalation on graphene/Ir(111), but for graphene on SiC [206]. The mechanism of intercalation can be studied if a low amount of the deposited metal is present in a specific area of the surface. For example, Sicot *et al.* studied the intercalation of nickel between graphene/Rh(111) at small intercalated island, so-called nanoislands, using STM [38]. These graphene intercalation structures cover only a small number of moiré cells. They offer a direct comparison to the adjacent unaffected substrate if they are well isolated from each other. Another example of intercalation growth is cobalt intercalation between graphene/Ir(111), by Decker *et al.* [57]. The authors presented structural data on the intercalation of cobalt, detected on some nanoislands but mostly starting from step edges of the substrate. The edges of the intercalated areas are often found to follow the underlying substrate, especially following the moiré pattern of graphene [38, 57, 58]. Leicht *et al.* report that the intercalating metal thereby occupies the *top-fcc* and *top-hcp* sites of the graphene/substrate positions first. The *atop* positions of the unit cells are only filled when the areas with *top-fcc/hcp* are already occupied [207].

Figure 8.1 presents an STM image after room temperature deposition of manganese on graphene/Ir(111). As I will discuss below, panels a) and b) show nanoislands of manganese intercalated between graphene and Ir(111). Panel c) is a schematic drawing of the nanoislands in the centre of panels a) and b), showing the crystallographic assignment of the *atop* sites. The height profile in panel c) is acquired from the green line in the inset of panel b), also shown on the schematic drawing in c). These images were recorded in constant height mode and are presented in false colour. The image is observed directly after deposition of $\approx$1 ML of manganese on graphene/Ir(111) at room temperature, without annealing the sample afterwards. Let us consider the structure of graphene/Mn/Ir(111).

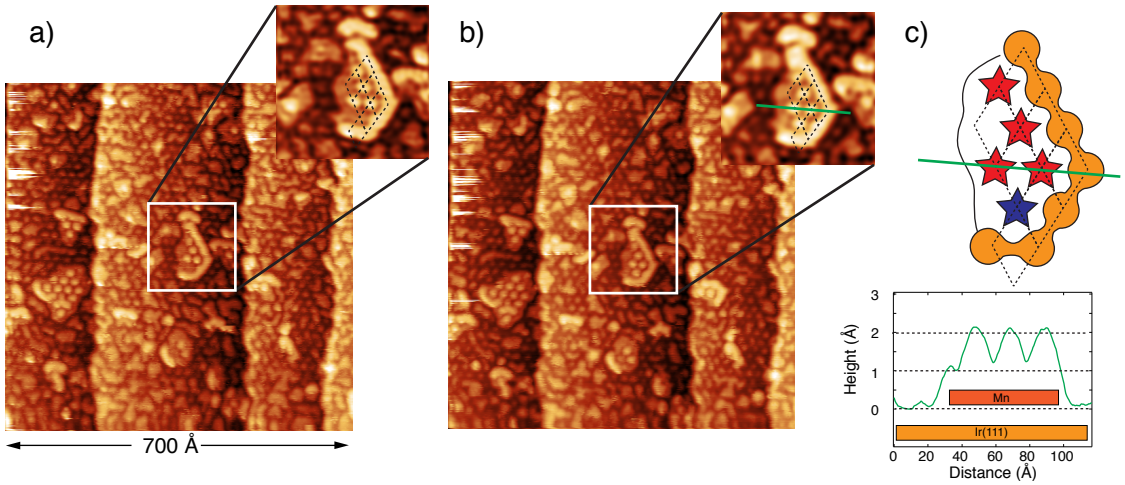

Figure 8.1. – STM images after room temperature deposition of ∼1 ML manganese on graphene/Ir(111). Several nanoislands of intercalated graphene/Mn/Ir(111) appear, one beeing shown in the white square. Both images are acquired at $U_T = -0.6$ V and $I_T = -2$ nA. Between the images a) and b), a time period of approx. 60 seconds passed for each scan. c) is a schematic representation of the nanoisland in the inset of panel a) and b). The orange border represents the wall of the nanoisland, the red stars represent the *atop* sites present on both images and the blue star marks the spontaneously filled *atop* site. The spontaneously occupation of this *atop* site reflects the diffusion and growth of the intercalated Mn monolayer. The green height profile is obtained from the green line in the inset of panel b).

I assign the structure in the white square to be a nanoisland of manganese intercalated between graphene/Ir(111). It is surrounded by the remaining graphene/Ir(111) moiré at the centre of the image, visible by the *atop* sites imaged in direct contrast, surrounded by other nanoislands and by clusters of manganese. The coverage of manganese on the surface is not homogeneous but areas with larger and smaller clusters are found. The graphene/Mn nanoisland in the centre and in the inset shows an open side on the left flank, where the step height between the base plane of the graphene/Ir(111) moiré and the base of the nanoisland plane, without the corrugation, is roughly 1 Å [see height profile in panel c)]. I interpret this as an intercalated manganese layer leading to a shorter distance between graphene and the substrate, because the step height of graphene/Ir(111) is around 2 Å. The right-hand side of the nanoisland is confined by a wall-like structure, whose height is about 2 Å, measured from the plane of the graphene/Ir(111) moiré. In the centre of the nanoisland, on the image in panel a) four moiré *atop* sites are occupied, but five on the image in panel b). The corrugation of the moiré *atop* sites after manganese intercalation is enhanced compared to graphene/Ir(111); it is found to be on the order of 1 Å. The wall structure shows hence the height of the step plus the enhanced corrugation size.

The only difference between these two images is the time needed to image this area with the STM tip, which is about 60 seconds. Within this time lapse, an additional hill has formed which I assign to a spontaneously occupied *atop* site of the moiré supercell; this position is marked by the blue star in panel c). I interpret this behaviour as manganese occupying the crystallographic *atop* site of the moiré pattern underneath the graphene layer at room temperature, forming the intercalated pseudomorphic layer of manganese on Ir(111) and under graphene. The two STM images directly show the Mn intercalation process at room temperature, leading to a pseudomorphic layer in between graphene and Ir(111). As suggested by Leicht *et al.* [207], the *atop* site is occupied last. The interpretation by Leicht *et al.* is that the intercalating atoms seek first the locations of the highest chemical potential, which are the *hollow* sites of the moiré supercell.

The formation of the nanoisland takes place far away from step edges of the Ir(111) substrate. In this case the intercalation probably occurs at defects, as also proposed for nickel intercalation on graphene/Rh(111) [38]. This penetration at defects is always assumed to coincide with the penetration at step edges during the actual intercalation experiment by heating the surface of graphene/Ir(111) [57, 58], because the intercalant atoms cannot penetrate the clean graphene layer on the terraces. Such examples for the intercalation of manganese are presented in the next section.

The temperature needed for the intercalation is very low, which is already suggested by the intercalation during deposition, i.e. it happens already at room temperature. Apparently that the kinetic energy of the evaporated atoms is sufficient to intercalate at defects, forming the nanoislands such as presented in the centre of Figure 8.1.

The intercalation process is examined by core level spectroscopy in Figure 8.2, where the carbon $1s$ core level spectra, acquired at 400 eV photon energy, are presented. The three steps of the intercalation are the pristine graphene layer, manganese deposited on top and manganese intercalated in the space between graphene and Ir(111) by heating the surface to $\approx 300\,^{\circ}\mathrm{C}$. The actual temperature determination is difficult since it is performed by pyrometry, whose lower limit is $245\,^{\circ}\mathrm{C}$ with our equipment. A systematic error has to be assumed that is not easy to determine. However, the temperature for intercalation was found to be consistent between the STM and photoemission experiments.

The pristine graphene/Ir(111) C $1s$ core level line exhibits a single component at 284.2 eV binding energy with a FWHM of 240 meV. The fit was performed using a Voigt profile corrected with an asymmetry factor in order to take into account the asymmetry of the C $1s$ core level line, due to its multiple components in the supercell [208], arising from a large number of carbon atoms in different chemical environments [44]. Including an asymmetry correction is a sufficient approximation to take into account the observed deviation to the perfect Voigt profile. Upon deposition of manganese at room temperature, the carbon $1s$

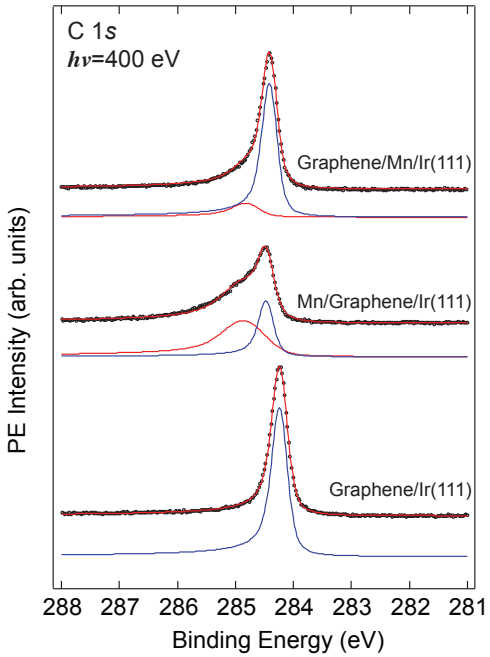

Figure 8.2. – Carbon 1*s* core level spectra acquired at $h\nu = 400\,\text{eV}$ for pristine graphene/Ir(111), manganese deposited ontop and intercalated by annealing at around 300 °C. The blue curve represents the graphene sp^2 component, the red line represents the sp^3 rehybridization component, that appears upon deposition of manganese. The shift of the sp^2 component is 300 meV to higher BE after deposition and 200 meV to higher BE after intercalation.

core level line shifts to a binding energy of 284.5 eV and exhibits a new shoulder, located around 284.8 eV. The shift can be attributed to the doping by the deposited manganese. The shoulder is very broad; from the fit a FWHM of 540 meV is observed. The appearance of such a shoulder is a consequence of the rehybridization that appears when clusters are deposited on graphene/Ir(111). Such a deposition of metal clusters often results in a "pinning" of the graphene layer to the substrate, i.e. the clusters force a rehybridization of the graphene layers at the location where they are adsorbed. This was theoretically predicted by Feibelmann *et al.* [86, 208], and such cluster formation in the *hollow* sites of the supercell was also observed experimentally by STM measurements, verifying the rehybridization process [41, 84]. In addition, it is observed that a small amount of Mn already intercalates during deposition. The large FWHM is hence interpreted as a superposition from signals of manganese clusters deposited on top and partly intercalated manganese.

The top spectrum in Figure 8.2 is acquired after annealing the sample at around 300 °C for 5 min. The rehybridization shoulder has almost completely vanished, leaving only a weak component at 284.8 eV binding energy. This reduction of the rehybridization shoulder is a sign that the intercalation is complete. In the next section I will present structural data that confirm this assumption. The main C 1*s* line has shifted slightly

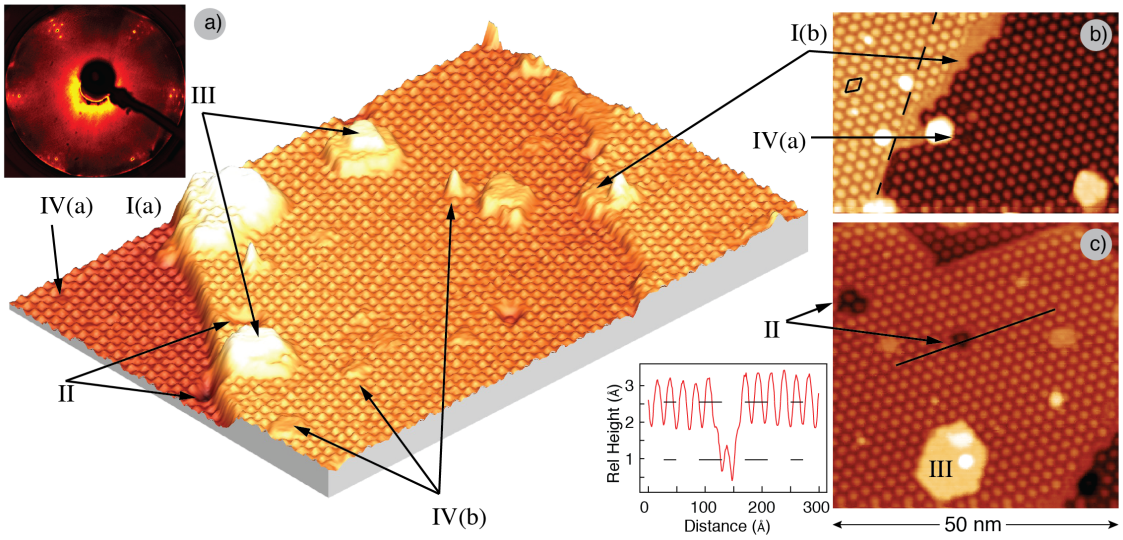

Figure 8.3. – Morphology of graphene/Mn/Ir(111) obtained by STM measurements. a) is a 3D representation of a large area of graphene/Mn/Ir(111) with 1500×900 Å, acquired at $U_T = 0.65\,\mathrm{V}$ and $I_T = 0.36\,\mathrm{nA}$. b) shows a closeup of 500×350 Å, acquired at $U_T = -0.3\,\mathrm{V}$ and $I_T = -1.3\,\mathrm{nA}$. c) is a closeup with 500×500 Å, acquired at $U_T = -0.3\,\mathrm{V}$ and $I_T = -1.15\,\mathrm{nA}$, together with a height profile corresponding to the black line. The labels are double [I(a)], single atomic step edges [I(b)], non-intercalated areas appearing as small holes (II), multilayer intercalated islands (III), and defects, such as non occupied *atop* sites [IV(a)] or, for example manganese clusters and structural defects [IV(b)]. The LEED image ($E = 120\,\mathrm{eV}$) in the inset of panel a) is obtained from an ARPES experiment of the corresponding structure.

to 284.4 eV binding energy, which is a total shift of 200 meV to higher binding energy compared to clean graphene.

8.1.3. Structure of Graphene/Mn/Ir(111)

The islands shown in the previous section form during deposition of manganese intercalation and due to the kinetic energy of the evaporated metals atoms, probably at defects. Complete intercalation can then be achieved by annealing the sample up to $\approx 300\,^{\circ}\mathrm{C}$. The result of this procedure is presented in Figure 8.3: a) shows a 3D representation of a large area of graphene/Mn/Ir(111), with one monolayer of manganese intercalated, and including a LEED image obtained from a corresponding ARPES experiment. b) and c) show details in smaller areas on the surface.

In Figure 8.3 a)-c), several structures appear that illustrate the existence and morphology of the intercalation, and its mechanism presented above. According to the labels in Figure 8.3, I(a) is a double and I(b) is a single atomic step edge. Other structures are

non-intercalated areas appearing as small holes (II), multilayer intercalated islands (III), and defects, such as unoccupied *atop* sites [IV(a)] or, for example manganese clusters and structural defects [IV(b)].

I(a) in panel a) is a step edge of 4 Å, which corresponds to a double atomic step of the Ir(111) substrate. The surface is covered with graphene/Mn/Ir(111) on both sides of the step. Evidence for this interpretation are the two hole defects (II) on both sides of the double atomic step. As shown in panel c), these defects appear randomly on the surface and are $\sim 1.5-1.6$ Å deep [see the hight profile next to panel c)]. These areas mark places where the intercalation process of manganese, growing underneath graphene, is stopped by a lack of material or is inhibited, e.g. by substrate defects. These defects are mostly trigonal, but the edges always follow the moiré structure.

The double atomic step [I(a)] exhibits another feature of the intercalation process. These step edges appear relatively straight, comparable to the step edges presented in Figure 2.9 for clean graphene/Ir(111). The intercalation structure of graphene/Mn/Ir(111), with its moiré structure, forms until it reaches the border of the step edge. Compare this step edge to the single atomic step edge I(b). This step edge is not as straight and ordered as I(a), but exhibits an irregular edge that exclusively follows the moiré pattern of graphene/Mn/Ir(111). A similar structure is also presented in panel b), marked by the dashed line, representing a potential Ir(111) substrate step edge. At some positions the intercalation does not stop at a single atomic step edge but continues above the already formed first intercalated layer of Mn. On the right-hand side of the dashed line in panel b), but close to the edge, several positions remain open without the typical hills that correspond to the *atop* sites. Finally it can be concluded that indeed both sides of the step are intercalated areas, as judged by the appearance of cluster defects on the surface [IV(b)] and open *atop* sites [IV(a)]. The formation of double layer intercalation is not restricted to the step edges, but also found in small islands on the terrace (III). Here one or several layers of manganese accumulate and form islands with heights of up to 6 Å and more. Some of the islands with double layer intercalation still exhibit a moiré structure. No atomic resolution could be observed on the intercalated moiré structures. The tip conditions cannot be responsible for this effects since I will later present structural data with atomic resolution directly next to the enhanced moiré areas. Hence it is likely that the local DOS inhibits the imaging of the surface down to the atomic scale.

Comparing this structure to clean graphene/Ir(111), several aspects are worth mentioning. First, the corrugation of ~ 1 Å is much higher compared to graphene/Ir(111) (0.3 Å). This effect is often found for $3d$ transition metals intercalated between graphene and Ir(111), such as cobalt [57] or nickel [58], where the enhanced corrugation is explained by the "strong" interaction that graphene shows when it is adsorbed on these $3d$ metals (see

Section 2.2.3). Secondly, there is no contrast inversion present on graphene/Mn/Ir(111), such as in graphene/Ir(111). The contrast inversion was assigned to hybrid states that form between graphene and the Ir(111) substrate at the *hollow* sites of the moiré supercell [44, 74]. The absence of such a contrast inversion, i.e. the missing enhancement of the tunneling current in the low lying regions, suggests that a weaker hybridization appears between graphene and the manganese layer, as recently found for intercalated copper [56]. These two findings are somewhat contradictory: The corrugation is found for strong interaction and the loss of the contrast inversion may be a hint for a weak interaction. In Section 2.2.3, several criteria for the interaction strength have been discussed, such as the appearance of the carbon 1s core level line presented in Figure 8.2. Its shift after the intercalation to higher binding energy may be interpreted as a stronger interaction between graphene and the substrate, but it is much smaller than other shifts, e.g. for example, for nickel intercalation [58]. Hence, the STM and core level spectroscopy have to be complemented by angle resolved photoemission data, to study the valence band properties of this system and possibly gain information about the interaction strength of graphene to the manganese intercalation layer.

8.1.4. Valence Band Properties of Graphene/Mn/Ir(111)

A comparison of the valence band electronic structure as revealed by photoemission is presented in Figure 8.4, showing graphene/Ir(111) (a), manganese deposited on graphene/Ir(111) (b) and intercalated graphene/Mn/Ir(111) (c). Every set of images presents a valence band map of photoemission intensity $I(E_B, k_x, k_y)$. The upper panel of each column is a constant energy map $I(k_x, k_y)$, at $E_B = 400\,\mathrm{meV}$. The lower left panels are photoemission band maps of binding energy vs. k_x along the K $\rightarrow$ Γ direction and the right panels are perpendicular to $\Gamma \rightarrow$ K. These observation planes in the Brillouin zone are schematically shown at the bottom in the left column for graphene/Ir(111). The dashed lines are guides to the eye for different structures in the valence band: The open circles mark the replica bands around the K points, the horizontally dashed line marks the Fermi level and the diagonal dashed lines mark the graphene π-band intensity maxima in E_B vs k.

Upon deposition of 1 ML of manganese on graphene/Ir(111) a doping of the graphene π-band is observed that shifts the Dirac point by 400 meV down into the occupied band region. This doping affects the complete electronic structure, including the replica bands of graphene and the carbon 1s core level line. It is hence a shift of the Fermi level relative to the electronic structure of graphene by electron doping. The shift of the graphene π-band is slightly higher than that for the carbon 1s core level. This suggests an addi-

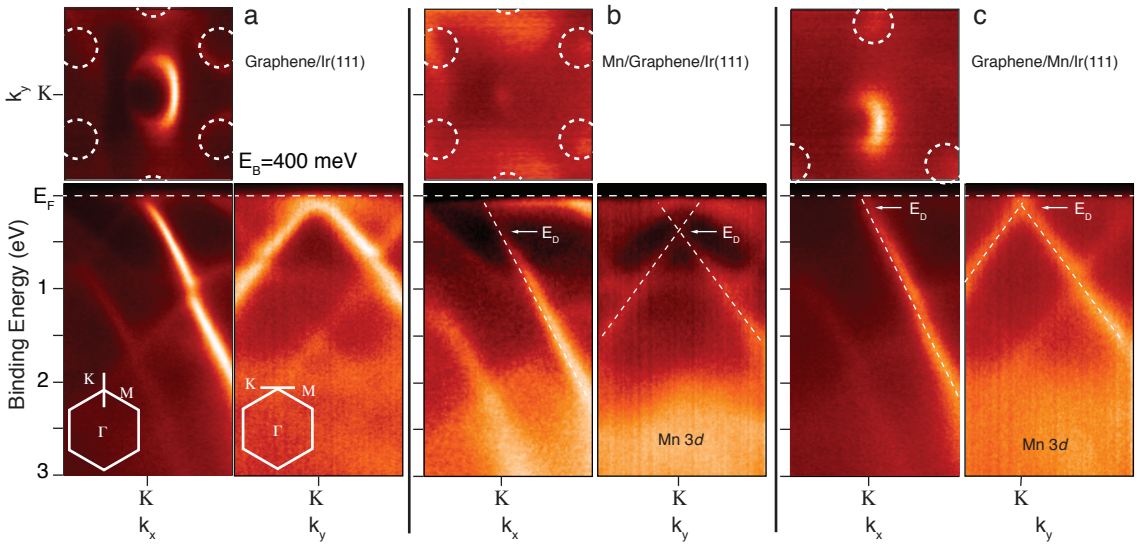

Figure 8.4. – Valence band map of graphene/Ir(111) (a), manganese deposited on graphene/Ir(111) (b) and intercalated graphene/Mn/Ir(111) (c) around the K point of the Brillouin zone. The photoemission intensity $I(E_{kin}, k_x, k_y)$ is given in false colour. The upper panels are constant energy maps at $E_B = 400\,\text{meV}$. The dashed circles are a guide to the eye for the position and appearance of the replica bands of graphene/Ir(111) at the K point. The dashed lines in the lower panels are a guide to the eye for the Fermi level and the dispersion of the π-bands around the Dirac cone. Manganese deposited ontop of graphene/Ir(111) shifts the Dirac cone due to n-doping to $E_B \approx 400\,\text{meV}$. After intercalation the Dirac cone is located around $E_B \approx 100\,\text{meV}$ and every second replica cone is suppressed.

tional chemical influence of the deposited clusters on the graphene π-states. The clusters are not ordered as judged from the STM data presented above. Hence, no symmetry breaking is observed in the electronic structure due to cluster growth. Such a symmetry breaking has been observed for Ir clusters deposited on graphene/Ir(111), which leads to suppression of every second replica band of the K point [209]. In contrast to Mn, these clusters exclusively grow in the *top-fcc* sites of the graphene/Ir(111) moiré. The resulting rehybridization beneath the Ir clusters suppresses those replica bands that are formed due to the superpotential of the *top-fcc* sites in the graphene/Ir(111) supercell. From this I conclude that the disordered growth of manganese on graphene/Ir(111) is reflected in both the STM and APRES experiment.

After intercalation, the electronic structure of graphene/Mn/Ir(111) has changed significantly. Although the Dirac cone is preserved, the Dirac point is now located at around $E_B \approx 100\,\text{meV}$. Compared to the situation before deposition of manganese, this is a shift of the Dirac point of about 200 meV, again consistent with the shift of the carbon $1s$ core level line. The replica bands of the Dirac cone exhibit a strong anisotropy; only three out of the six replica cones are now visible. A very weak intensity remains at the

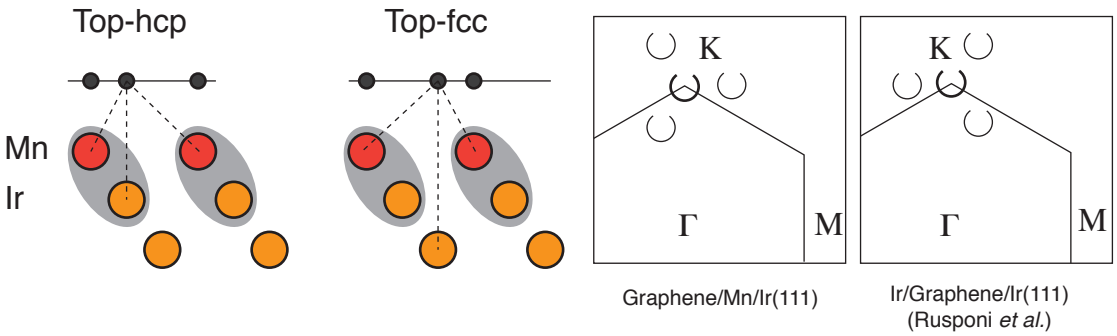

Figure 8.5. – **Left:** Schematic representation of then newly formed graphene/Mn/Ir(111) structure with a focus on the *top-hcp* and *top-fcc* sites. The red balls are manganese, the orange balls are iridium. The black dots are the carbon atoms sitting on top of a surface manganese atom and on top of the *hcp* or *fcc* hollow site, respectively. The grey shadow represents a hypothetical bond between manganese and iridium, that could influence the *top-hcp* carbon atoms stronger than those of the *top-fcc* site of the graphene/Mn/Ir(111) moiré. **Right:** Comparison of the replica band suppression of graphene/Mn/Ir(111) (the *top-hcp* replicas are suppressed) and Ir/graphene/Ir(111) (the *top-fcc* replicas are suppressed). The latter case is adopted from [209].

k values for the other three *top-hcp* replica cones. However, this is probably due to an imperfectly homogeneous coverage of manganese and remaining pristine graphene areas. In the constant energy map of graphene/Mn/Ir(111), the three remaining Dirac cones are highlighted by the open dashed circles. A systematic suppression was reported for the deposition of periodically arranged clusters on graphene/Ir(111) by Rusponi *et al.* [209]. The authors argue that the selective deposition of Ir(111) clusters breaks one of the two threefold superpotentials of the moiré unit cell, namely that of the *top-fcc* adsorption sites, such that those replica bands vanish that appear due to the superpotential of the *top-fcc* areas. Since manganese is almost completely intercalated, and the STM experiments do not show any ordering of Mn-clusters after heating the surface of graphene, the effect on the band structure presented here cannot originate from clusters breaking the symmetry.

Again, two observations are made that contradict each other to some extent. The preservation of the Dirac cone is a sign for a weak interaction, whereas the symmetry breaking and the vanishing replica bands point to a strong interaction between graphene and the substrate. Rusponi *et al.* [209], assign this anisotropy to the enhancement of the chemical interaction, achieved by a variation of the chemical potential of graphene to the Ir(111) substrate on the *top-fcc* or *top-hcp* sites, by forming a periodic cluster lattice selectively in the *top-fcc hollow* sites of graphene Ir(111). Comparing their results to the anisotropy observed for intercalated graphene/Mn/Ir(111) sample it becomes clear that

exactly those replica bands are present in our experiment which have been suppressed by the cluster lattice [209]. A possible interpretation is presented in Figure 8.5. Manganese intercalated between graphene/Ir(111) can be expected to form a metallic bond to the Ir(111) substrate due to the fact that Mn is assumed to grow pseudomorphically on Ir(111). This interaction is symbolized by the grey shadow under the schematic atomic structure of Figure 8.5. By this, I imply the chemical interaction of graphene to the Mn layer to be slightly stronger than to the Ir(111) substrate. Indeed, graphene adsorbed on such a manganese layer is found to have a shorter bonding distance to the manganese layer than to Ir(111) (see Figure 8.1). In order to induce the required local symmetry breaking in the *top-hcp* sites, the carbon atoms in these areas need to have a considerably stronger chemical interaction to the manganese layer than those carbon atoms in the *top-fcc* areas. A possible source for this broken symmetry could be the nearest neighbour interaction of the carbon atoms that are located above *fcc* and *hcp hollow* sites, as present in the corresponding *top-fcc* and *top-hcp* areas, respectively. Consider the schematic drawing of the *top-hcp* and *top-fcc* sites with intercalated and pseudomorphically grown manganese in Figure 8.5. The carbon atoms on the local *hcp hollow* sites of the *top-hcp* areas are affected by the bond that is formed between Ir(111) and the manganese layer, represented by the grey shadow. The observed symmetry breaking could thus be explained by the fact that the carbon atoms on the crystallographic *top-hcp* site are closer to the Ir(111) surface atoms that are bonded to the manganese atoms, and are hence more strongly affected than the carbon atoms on the *top-fcc* areas.

This difference could be weak; however, it may be sufficiently strong enough to induce the required symmetry breaking and explain the fact that exactly those replica bands are suppressed that survive when the superpotential of the graphene moiré is disturbed by cluster adsorption on the *top-fcc* sites.

8.1.5. High Temperature Intercalation Phase

The preparation of the graphene/Mn/Ir(111) system is difficult because the temperature window available for intercalation is narrow and the temperature is very low. By heating the surface to higher temperatures during the intercalation process or afterwards, changes in the morphologic and electronic structure are observed. These are found to destroy the properties described above and lead to a new phase of graphene/Mn/Ir(111) as shown in Figure 8.6, in a set of STM images for graphene/Mn/Ir(111) after heating a sample of 1 ML Mn/graphene/Ir(111) up to 500 °C.

This surface shows a new morphologic structure. Some areas are probably atomic steps of a second layer of intercalated manganese, originating from large clusters that have not been imaged in the STM experiments or manganese from formerly multilayered intercala-

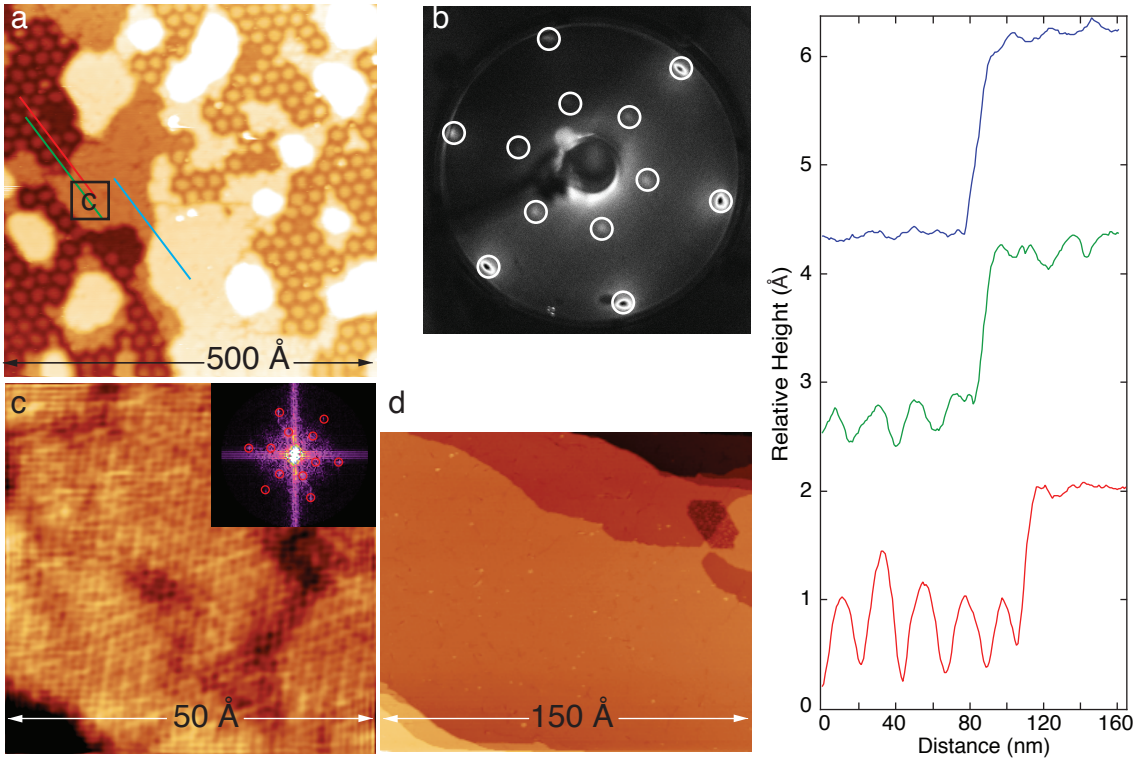

Figure 8.6. – STM data from annealed graphene/Mn/Ir(111). a) presents an overview image over 500 Å, acquired at $U_T = 1.25\,\mathrm{V}$ and $I_T = 1\,\mathrm{nA}$. The coloured lines are extracted height profiles, presented in panel e). The inset, labeled c) shows the area where panel c) is acquired. This image c) is measured at $U_T = 0.3\,\mathrm{V}$ and $I_T = 1.86\,\mathrm{nA}$. d) is an overview image over 150Å for the pure (2×2) surface, obtained at $U_T = 2.35\,\mathrm{V}$ and $I_T = 0.27\,\mathrm{nA}$. b) is LEED image, corresponding to the APRES measurement from Figure 8.7 with the same structure as panel d).

tion areas, e.g. defect type III from Figure 8.3. Such steps are almost 2 Å high as revealed by the blue profile in panel e). Other areas, formed under such conditions, are also flat and are on the same terrace as the graphene/Mn/Ir(111) moiré structure. A closeup of these structures with atomic resolution is presented in Figure 8.6 c). This area exhibits approximately a (2×2) pattern in the corresponding FFT plots of the acquired image (inset). This is not a perfect (2×2), however, I will refer to it as a (2×2) for simplicity. Annealing destroys the previous moiré structure of graphene/Mn/Ir(111) and replaces the moiré structure by the (2×2) structure. Further annealing leads to the formation of more such structural transformations until the surface is finally entirely covered by this new phase [panel d)]. The height difference between the newly formed, flat (2×2) step and the adjacent graphene/Mn/Ir(111) moiré can be determined from the height profiles in Figure 8.6 e). The green line shows a height profile starting between the *atop* hills of the lower step, whereas the red line shows a profile along the *atop* hills of the moiré pattern. This one-step height is on the order of 1.6-1.8 Å. It is hence an intermediate step height

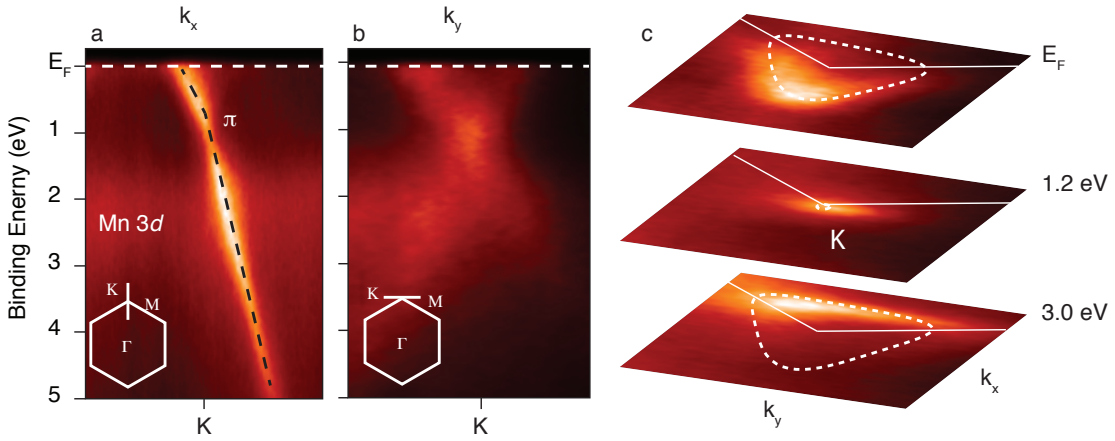

Figure 8.7. – Valence band photoemission map of (2×2)-graphene/Mn/Ir(111) photoemission intensity $I(E_B, k_x, k_y)$. The panels present the photoemission maps along the high symmetry directions $\Gamma \rightarrow$ K (a), perpendicular to $\Gamma \rightarrow$ K (b) and for three constant energy maps at the Fermi level, at $E_B = 1.2\,\text{eV}$ and $E_B = 3\,\text{eV}$ binding energy (c). The white dashed line is a guide to the eye to the Fermi level, the black dashed line corresponds to a fit of the carbon π-band dispersion intensity maximum. The white dashed line are a guide to the eye for the Dirac cone shape in panel c).

compared to the single atomic steps observed in Figure 8.3 ($\sim 2\,\text{Å}$). This means that the underlying substrate is still a manganese layer, but it also suggests a change in the adsorption distance of the carbon layer to the substrate compared to the graphene/Mn/Ir(111) moiré structure. Such a (2×2) structure is not only observed on the terraces as shown in panel c), but also on the higher steps, such as under the blue profile. The underlying structure can hardly be determined from such measurements since only its effect on the variation of the local DOS of the carbon layer is visible. The formation of a (2×2) structure can originate from a different interaction of the carbon layer with the new substrate structure or by a change of the substrate superpotential affecting the carbon layer, e.g. surface alloying.

Panel b) of Figure 8.6 presents a LEED image of similarly prepared graphene/Mn/Ir(111) sample. In this experiment, a slightly larger amount of manganese than one monolayer was deposited and annealed above 650 °C for 10 minutes. The larger amount was necessary because the high temperature treatment was found to result in the loss of manganese during annealing. The resulting structure of such an experiment is the (2×2) structure on the terraces, in agreement with the STM data. Here, change in the crystallographic order were observed to have a significant effect on the electronic structure of the (2×2) graphene/Mn/Ir(111) system. Figure 8.7 presents an ARPES bandmap of photoemission intensity $I(E_B, k_x.k_x)$. The figure shows the same cuts along the high

symmetry directions as Figure 8.4: a) shows the carbon π-band dispersion along $\Gamma \rightarrow$ K, b) perpendicular to $\Gamma \rightarrow$ K and c) shows a set of constant energy maps at the Fermi level, at $E_B = 1.2\,\text{eV}$ and $E_B = 3\,\text{eV}$ binding energy. The electronic structure of the (2×2) phase is heavily doped. Since it is not clear if this phase can still be called graphene, I will restrict myself to use the term carbon π-band. The Dirac point is shifted by 1.2 eV to higher binding energy. The upper dispersion of the σ-bands is shifted to higher BE by 1.6 eV and the bottom of the π-band is shifted by 2 eV to higher BE. Around the energy of the Dirac point, a depletion of the photoemission intensity is observed which hints on the formation of band gap that is, however, difficult to resolve here. Approximately 300-400 meV below the Fermi level a kink in the carbon π-band dispersion is observed that changes the slope of the electronic band. The electronic structure is heavily changed after the phase transformation. The electronic behaviour of the π-band exhibits similarities to the structure of graphene/Ni(111), excluding the strong band splittings. The electronic bands of the manganese layer do not seem to fulfil the symmetry requirements to interact with the carbon π-band by avoided crossings. A further discussion of the formation of this structural phase and its electronic structure will be part of the doctoral thesis of Hendrik Vita [205].

In summary, a drastic change in the electronic structure is observed, which shows that the formation of a graphene layer on intercalated manganese is highly sensible to higher temperatures. The formation of a clean intercalation layer hence depends strongly on the correct temperature window, chosen for the intercalation.

8.2. Conclusions

I have observed the formation of a pseudomorphic manganese layer in the space between graphene and Ir(111) upon deposition and subsequent annealing. The intercalation appears already at room temperature during the evaporation of the metal atoms, which I ascribe to the kinetic energy of the metal atoms during evaporation. On the thus formed graphene/Mn/Ir(111) nanoisland, the intercalation process could be observed. After heating the sample to 300 °C, a pseudomorphic manganese layer between graphene and Ir(111) is observed that preserves the Dirac cone of the graphene π-band. However, the structure exhibits a strong corrugation, similar to intercalated cobalt [57] or nickel [58], and a strong anisotropy of the electronic structure around the K point. For the latter, the enhanced chemical interaction leads to a symmetry breaking by affecting the carbon atoms in the *top-hcp* adsorption sites of the graphene/Mn/Ir(111) moiré structure, resulting in the suppression of three of the six Dirac cone replica bands. The formation of this intercalated structure is very sensitive to the annealing temperature of the intercalation process. Higher temperatures lead to a phase transition of the graphene/Mn/Ir(111) structure, forming a different (2×2) carbon structure with respect to the graphene unit cell, probably due to surface alloying.

Part IV.

Conclusions

9. Summary and Conclusions

The adsorption of molecules and the chemical functionalization of graphene adsorbed on Ni(111) and Ir(111) was performed by adsorption of the polar molecules water and ammonia, by photolysis and subsequent oxidation from the precursor molecules NO_2 and SO_2 on graphene/Ir(111), and by the interaction of the photolysis fragments of PF_3 on graphene/Ir(111). Graphene could also be functionalized by introducing a new metal layer of manganese into the space between graphene and the substrate by the method of intercalation. The kind of functionalization thereby depends on the kind of interaction between graphene and its adsorbate or substrate, respectively.

The term functionalization, as initially addressed, can be discussed in several ways. In the case of adsorption of water and ammonia, functionalization of graphene can be seen by its sensing abilities to detect adsorbates and their interaction to the surface from the substrate side. To this purpose, carbon K edge NEXAFS was used to specifically detect the adsorbate/graphene interaction by the appearance of new spectroscopic features in the x-ray absorption spectra. The unique properties of graphene, its two-dimensional nature, its clear electronic structure and its sharp spectroscopic features, enable the detection of the interaction of the adsorbate and the substrate in the electronic structure of both the graphene layer and the adsorbate with the same spectroscopic technique. Furthermore, this technique provides us with the ability to quantify the effect of functionalization with respect to the graphene/metal system, which was found to be different for graphene/Ni(111) and graphene/Ir(111). NEXAFS is hence not only a tool to detect molecules and their interaction strength to graphene, but it provides also the possibility to measure the interaction strength of graphene to the metal substrate.

A more chemical way of functionalization, namely the incorporation of additional chemical groups into the graphene backbone, is achieved by the oxidation of graphene due to photolysis of NO_2 and SO_2 at low temperatures. These molecules undergo decomposition when irradiated with intense x-ray radiation. The result is the formation of a graphene-oxide layer on Ir(111). The oxidation is very selective to epoxide groups, which is a benefit if the reduction of graphene-oxide to graphene is required [183]. Oxidation is furthermore specific to the adsorption site of the precursor molecule. Since adsorption mainly takes place at the chemically more active *hollow* sites of the graphene/Ir(111) moiré, oxidation is likely to be specific but also restricted to these sites. Finally, due to the fact that

oxidation is achieved at low temperature and with *in-situ* formed oxygen on the surface, the graphene-oxide layer is found to have only minor defects. This is judged by the fact that graphene can be recovered from such formed graphene-oxide, to a very high quality, compared to other methods that are less specific, i.e. wet chemical methods, or intrusive, such as oxygen atom bombardment.

The method of oxidation presented here depends strongly on the photon flux density, which can be seen as the driving force for the reaction rate. Lowering the reaction rate provides access to intermediate oxygen species, such as carbonyl groups, that can be seen as the kinetic products of the reaction. However, these groups are metastable with respect to temperature and probably irradiation, but metastable especially to further oxidation under precursor exposure and irradiation.

The fragmentation of the molecules also leads to adsorption of the fragments on graphene if they are adsorbed in a stable manner. While this is not observed for NO, the fragments of SO_2, SO and elemental sulfur, and the fragments of PF_3, PF_2 and PF, are found after the photolysis. The appearance of these fragments coincides with the adsorption of their precursor molecules, which is here interpreted as an activated adsorption mechanism. The activation is in this case the adsorption of strongly interacting fragments, i.e. SO (besides the epoxide) and PF, respectively, that induces a further distortion within the graphene layer. This distortion breaks the inertness of the sp^2 configuration of graphene and allows the precursor molecules to adsorb more easily than possible on pure graphene. A drawback of this observation is, however, that the fragments occupy the same sites on graphene that are believed to be populated by the oxidation precursor molecules. Hence, these fragments inhibit the oxidation in the case of SO_2 to some extent.

The adsorption of PF_3 and its fragments is also interesting in this discussion. However, no chemical functionalization, e.g. by fluorination, is observed, the PF fragments of PF_3 are found to interact relatively strongly with graphene/Ir(111) and produce an interaction that is similar to the fingerprint interaction of water and ammonia.

Functionalization of graphene can also be achieved by affecting the "other surface of graphene", its back-side [204], in the space between the graphene layer and its substrate. The formation of an intercalated metal layer changes the electronic structure of graphene, and may induce functionalities in graphene by varying its electronic and morphologic properties. The intercalation of, cobalt [57] or nickel [58] for example,, but also the intercalation of copper [56], change the appearance of the electronic structure by inducing band gaps, electron doping and changes of the morphologic structure. These changes are permanent and the surface of graphene stays almost intact. Manganese intercalated between graphene and Ir(111) has been found to preserve the Dirac cone and the magnitude of doping. On the other hand, it is found to enhance the surface roughness by a

stronger corrugation and breaks local symmetry in the graphene layer, yielding a strong anisotropy in the electronic structure of graphene on intercalated manganese. The three examples discussed above present three cases of functionalization of graphene, starting with a rather weak adsorption of molecules in order to use graphenes properties of sensing and its clear electronic structure for observing the effects induced by the adsorbates. Then, the chemical reactions of locally produced oxygen atoms by photolysis of adsorbed molecules and the formation of graphene-oxide was studied. This example represents a chemically much stronger functionalization of graphene than the pure sensing abilities by a weak reversible adsorption. Finally, graphene's properties were changed by forming a new, artificial manganese substrate, that intends to complete the row of the $3d$ transition metal interactions to graphene [33]. The intercalated metal, i.e. manganese, can be used to tune the properties of graphene towards a designated utilization. However, the important aspects of graphene, i.e. the Dirac cone, the sp^2 hybridization and possibly the properties that originate from these [22], are preserved.

10. Outlook

The results presented and discussed in this work shed light on two extremes of the adsorption of molecules and the functionalization, that was achieved. Water and ammonia were weakly and non-dissociatively bonded, however, revealing the presence of a chemical bond component. On the other hand, adsorption of NO_2 and SO_2 with subsequent dissociation of the adsorbed molecules and with concomitant covalent modification of graphene occurs. In both cases, further work is clearly necessary to fully understand the mechanisms and driving forces in detail.

On the example of water and ammonia, the interpretation of the experimental data will benefit from future theoretical considerations. The studies of water and ammonia on graphene/Ni(111) and graphene/Ir(111) have so far not been supported by theoretical considerations. The reasons for this are the limitations of theoretical methods available and of the computational capability. I have already attempted to calculate the adsorption of water and ammonia within my master's thesis [20]; however, the current DFT functionals were insufficient to describe the bonding situation of weakly adsorbed molecules on graphene, especially the fingerprinting effect. It is questionable wether the new dispersion-corrected DFT functionals are able to characterize this interaction today. The application of hybrid functionals in DFT calculations on surfaces may change this in the future.

The understanding of the chemical modification of graphene by incorporation of new chemical groups, from photolysis of precursors, will benefit from investigations that do not yield the photolysis of the precursors. The large doses that were needed to adsorb the molecules imply an activated adsorption, whose initial steps are still unknown. The photon-based methods presented here suffer from the fact that photolysis competes with the adsorption of the intact molecules; use of vibrational spectroscopy, such as for example IR or RAMAN spectroscopy may provide experiments, that allow to study the non-dissociative adsorption of NO_2 and SO_2. If these reveal the conditions and reaction mechanism of the adsorption, photolysis and oxidation, this method may be used in the future to lithographically produce oxidized graphene patterns on graphene surfaces. Beside the oxidation of graphene, adsorption and reactions on graphene will continue to be interesting, i.e. doping of graphene with foreign atoms, e.g. by nitrogen or boron.

With respect to examine the influence of the substrate on graphene's adsorption properties, an important step has been made in this thesis by the comparison of graphene/Ni(111) and graphene/Ir(111). Future studies on other graphene systems, such

as graphene/Cu(111) or graphene on semiconductors, such as SiC(0001), will be of great interest for applications, in order to systematically change the properties of graphene at will.

Intercalation of foreign metals between graphene and the substrate in general, will continue to attract interest. The studies presented here have shown that beyond the formation of a pseudomorphic arrangement of the intercalated metal layer, surface alloying may occur, which opens a path to a large variety of new surface structures, covered and protected by graphene. Thus, the interest in this subfield of graphene research will continue to be active.

Part V.

Appendix

A. Supplementary Figures

A.1. BESSY beamline UE56/2 Flux Curves

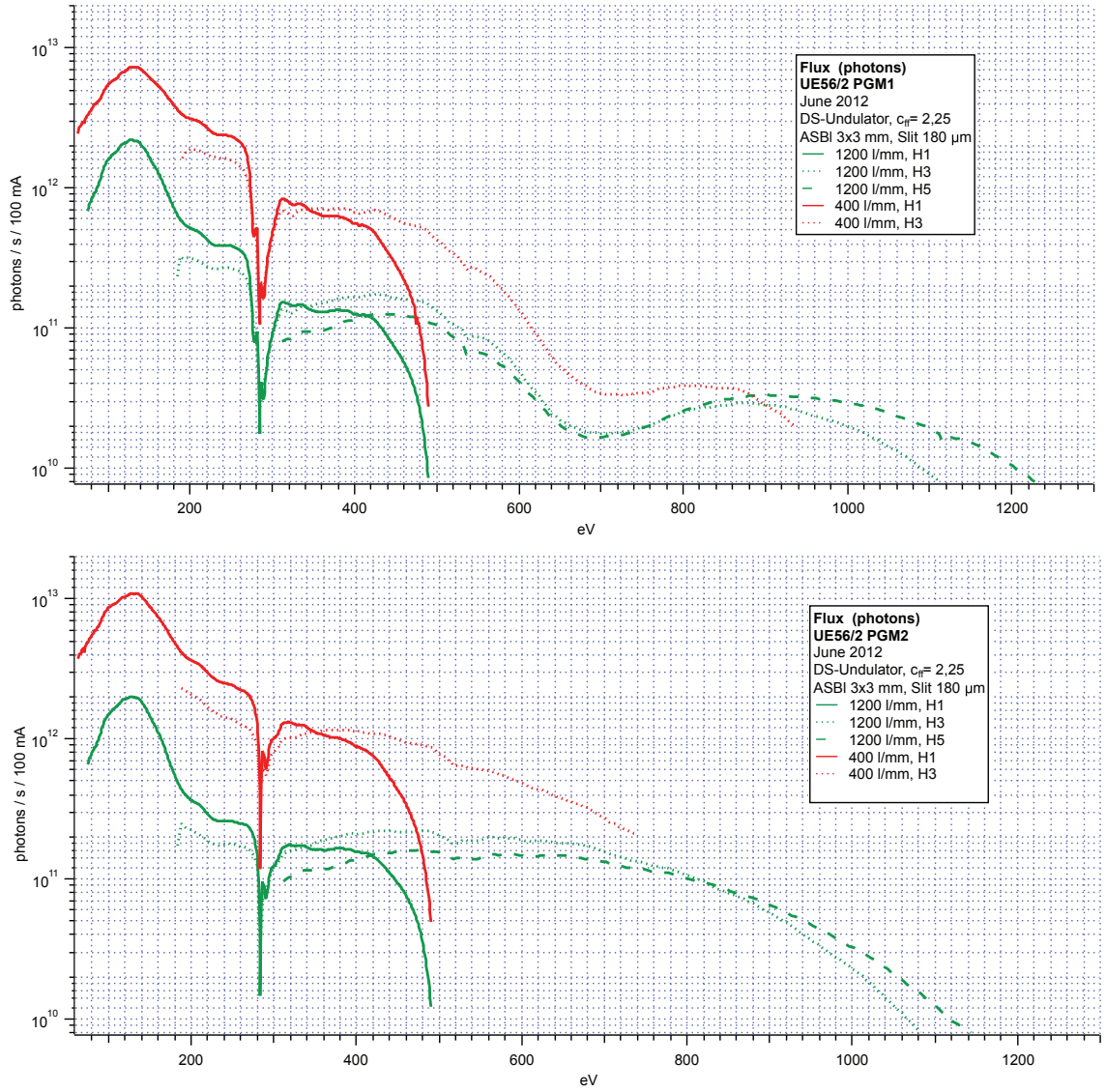

Figure 1.1. – Photon-flux curves of the BESSY II UE56/2 PGM-1 and -2 beamlines. The figures are kindly provided and printed with permission by Willy Mahler [127].

B. Lists

B.1. List of Abbreviations

AFM	Atomic Force Miscroscopy
ARPES	Angle Resolved Photoemission Spectroscopy
at %	atomic percent
CB	Conduction Band
CCD	Charge Couples Device
CL	Core Level
DFT	Density Functional Theory
DNA	Deoxyribonucleic Acid
DOS	Density of States
E_B	Binding Energy
E_D	Dirac Energy
EDC	Energy Distribution Curve
EF	Fermi Energy
eV	Electron-Volt
fcc	Face Centered Cubic
FFT	Fast Fourier Transformation
FM	Frank-Van-der-Meerve
FWHM	Full Width at Half Maximum
GGA	Generalized Gradient Approximation
GrO	Graphene-Oxide
hcp	hexagonal closed-packed
HOMO	Highest Occupied Molecular Orbital
IR	Infrared
IUPAC	International Union of Pure and Applied Chemistry
L	Langmuir
LDA	Local Density Approximation
LDOS	Local Density of States
LEED	Low Energy Electron Diffraction
LUMO	Lowest Unoccupied Molecular Orbital
m-GrO	metastable Graphene-Oxide
mBZ	mini Brillouin Zone
MCP	Multi Channel Plate
MDC	Momentum Distribution Curve
NEXAFS	Near Edge X-Ray Absorption Fine Structure

PE	Photoemission
PES	Photoemission Spectroscopy
PGM	Plane Grating Monochromator
PID	Partial-Integral-Differential
QMS	Quadrupole Mass Spectrometer
RT	Room Temperature
SEQ	Schrödinger Equation
SK	Stranski-Krastanov
SPM	Scanning Probe Microscopy
STM	Scanning Tunneling Microscopy
TDS	Thermal Desorption Spectroscopy
TPD	Temperature Programmed Desorption
UHV	Ultra High Vacuum
UV	Ultra-Violet
VASP	Vienna Ab Initio Simulation Package
VB	Valence Band
VdW	Van-der-Waals or Van-der-Vaals
VM	Vollmer-Weber
w.r.t.	with respect to
XAS	X-Ray Absorption Spectroscopy
XPS	X-Ray Photoelectron Spectroscopy

B.2. List of Publications

- H. Vita, S. Böttcher, P. Leicht, K. Horn, A. B. Shick, and F. Máca Electronic structure and magnetic properties of cobalt intercalated in graphene on Ir(111), (submitted 2014)
- H. Vita, S. Böttcher, K. Horn, E. Voloshina, R.E. Ovcharenko, T. Kampen, A. Thissen, and Y.S. Dedkov, Understanding the origin of band gap formation in graphene on metals: graphene on Cu/Ir(111) *Scientific Reports* **4**, (2014).
- S. Böttcher, H. Vita, and K. Horn, Reversible Photon-Induced Oxidation of Graphene by NO2 Adsorption, *Surface Science*, **621**, 117 (2014)
- Markus Ostler, Felix Fromm, Roland J. Koch, Peter Wehrfritz, Florian Speck, Hendrik Vita, Stefan Böttcher, Karsten Horn, Thomas Seyller, Buffer layer free graphene on SiC(0001) via interface oxidation in water vapor, *Carbon*, **70**, 258-265 (2014)
- E. Voloshina, A. Generalov, M. Weser, S. Böttcher, K. Horn, and Y.S. Dedkov, Structural and electronic properties of the graphene/Al/Ni(111) intercalation system, *New Journal of Physics* **13**, 113028 (2011)
- S. Böttcher, M. Weser, Yu. S. Dedkov, K. Horn, E. N. Voloshina and B. Paulus, Graphene on ferromagnetic surfaces and its functionalization with water and ammonia, *Nanoscale Research Letters* **6**, 214 (2011)

B.3. List of Presentations

- S. Böttcher, H. Vita, and K. Horn, *Graphene Oxide Formation by Adsorption and Photolysis of NO_2 and SO_2 on Graphene/Ir(111)* (Frühjahrstagung der Deutschen Physikalischen Gesellschaft, Dresden, Germany, 2014)
- S. Böttcher, H. Vita, and K. Horn,*Photooxidation of Graphene: Adsorption and Dissociation of NO_2 on Graphene/Ir(111)* (HZB Users Meeting, Berlin, Germany 2013)
- Stefan Böttcher, Hendrik Vita, Karsten Horn, *Reversible Photooxidation of Graphene*, (Frühjahrstagung der Deutschen Physikalischen Gesellschaft, Regensburg, Germany, 2013)
- S. Böttcher, M. Weser, H. Vita, Y. Dedkov and K. Horn, *Molecules on Graphene: The Fingerprint oft the Adsorbate in Substrate NEXAFS*, (HZB Users Meeting, Berlin, Adlershof, 2012)
- S. Böttcher, M. Weser, H. Vita, F. Bisti, Y. Dedkov and K. Horn, *Polar Molecules Adsorbed on Graphene: Influence of the Metal Substrate*, (CMD-24,ECOSS-29,CMMP-12,ECSCD-11, Edinburgh, United Kindom, 2012)
- S. Böttcher , M. Weser, H. Vita, Y. Dedkov, K. Horn,*Adsorption of polar molecules on graphene/Ni(111) by substrate sensitive NEXAFS spectroscopy*, (Frühjahrstagung der Deutschen Physikalischen Gesellschaft, Berlin, Germany, 2012)

- S. Böttcher , M. Weser , K. Horn, Y. Dedkov, E. Voloshina, and B. Paulus *Adsorption of Water on Graphene/Ni(111): Experiment vs. Theory*, (75 Frühjahrtagung der Deutschen Physikalischen Gesellschaft, Dresden, Germany, 2012)

- S. Böttcher, M. Weser, K. Horn, Y. Dedkov, E. Voloshnia, and B. Paulus, *Functionalization of Graphene: Water Adsorbed on Graphene/Ni(111)*, (HZB Users Meeting 2011, Berlin, Germany)

- S. Böttcher, M. Weser, Yu. S. Dedkov, K. Horn, E. Voloshina and B. Paulus, *Combined photoelectron spectroscopy and* ab initio *studies of water adsorbed on graphene/Ni(111)*, (Ψ_k-2010 Conference 2010, Berlin, Germany, 2010)

- S. Böttcher, M. Weser, Yu. S. Dedkov, K. Horn, E. Voloshina and B. Paulus, *Water on graphene/Ni(111): photoemission experiments and DFT calculations*, (The 27$^{\text{th}}$ European Conference on Surface Science, Groningen, The Netherlands, 2010)

B.4. Curiculum Vitae

For reasons of data protection,
the curriculum vitae is not included in the online version

C. Danksagung

Ich möchte die Gelegenheit nutzen um mich bei all denjenigen zu bedanken, welche mich durch diese wertvolle und wichtige Phase meines Lebens begleitet haben.

Zunächst möchte ich meinem Doktorvater, Prof. Dr. Karsten Horn, für all die Ratschläge und Lebenshilfen danken, die er mir hat zu Teil werden lassen; nicht nur im wissenschaftlichen, sondern auch im privaten Leben. Ich habe seinen Rat und seine Kritik jederzeit geschätzt und sie war für mich eine wertvolle Bereicherung. Ich danke Prof. Dr. Thomas Risse für die freundliche Unterstützung und Begutachtung meiner Doktorarbeit. Die Diskussionen zu meinen Themen und seine Vorschläge haben einen wichtigen Beitrag zu der hier verfassten Arbeit beigetragen.

Daneben möchte ich mich bei den Leuten bedanken, die mich durch meine bisherige Laufbahn begleitet haben, sei es mit guten Diskussionen oder durch das Teilen einer Strahlzeit (Messschulden sind Ehrenschulden): Yuriy Dedkov und Elena Voloshina, Martin Weser, Hendrik Vita, Chris Nicholson, Philipp Leicht, Roland Koch, Federico Bisti, Birgit Zada, Willy Mahler, Alexander Generalov, Sergey Peredkov, Nicolai Vinogradov, Alexei Preobarjenski und Christian Doye. Fehlen dürfen natürlich auch nicht all die Kollegen aus der Abteilung MP und PC, die in den letzten Jahren eine großartige Arbeitsatmosphäre geschaffen haben. Im speziellen möchte ich den MPlifiers, Petrik Bischoff, Dirk Jannik, Andreas Liedtke, Georg Hammer und (natürlich) Inga von Dölln danken.

Zwei Personen und Mentoren aus meiner Jugend dürfen an dieser Stelle nicht unerwähnt bleiben: Detlev Wolf für den Mut, die Unterstützung und den Glauben an mich, und Wolfgang Porsch für die ersten wissenschaftlichen Schritte, welche ich in eine größere Welt getan habe.

Eine solch lange Zeit voller Entbehrungen wäre nicht möglich ohne den Rückhalt meiner Famile, meiner Eltern und meiner Schwester, meiner Freunde (Pascal, Tobi und Vanessa und Rubina, Marcel und Sandra und Liam, John, Andre, Dirk Nora und Adrian, Locke, Baum, Ben, Olli, Olli, Marcus, Pascal, Tomasz, Jan und noch eine ganze Menge mehr Leute).

Zuletzt, und damit am wohl wichtigsten Platz dieser Danksagung, bleibt noch der Dank an die wohl wichtigste Person: meine Frau, Kati. Danke! Ohne Dich hätte ich weder den Mut, noch die Kraft gehabt diesen Weg zu gehen! Du hast all den Anstrengungen, die ich auf mich genommen habe, ein Ziel gegeben.

Ich danke Euch/Ihnen allen!

D. Literaturverzeichnis

[1] Novoselov, K., Geim, A., Morozov, S., Jiang, D., Zhang, Y., Dubonos, S., Grigorieva, I., and Firsov, A. *Science* **306**(5696), 666–669 (2004).

[2] Geim, A. K. and Novoselov, K. S. *Nature Materials* **6**(3), 183–191 (2007).

[3] Novoselov, K. S., Fal, V. I., Colombo, L., Gellert, P. R., and Fabian, J. *Nature* **490**(7419), 192–200 (2012).

[4] Landau, L. D. *Physikalische Zeitschrift der Sowjetunion* **11**, 26–35 (1937).

[5] Wallace, P. R. *Physical Review* **71**(9), 622 (1947).

[6] Kroto, H., Heath, J., O'Brien, S., Curl, R., and Smalley, R. *Nature* **318**(6042), 162–163 (1985).

[7] Iijima, S. *Nature* **354**(6348), 56–58 (1991).

[8] Novoselov, K., Geim, A., Morozov, S., and Jiang, D. *Nature* **48**(10), 197 (2005).

[9] Lee, C., Wei, X., Kysar, J. W., and Hone, J. *Science* **321**(5887), 385–388 (2008).

[10] Bunch, J. S., Verbridge, S. S., Alden, J. S., van der Zande, A. M., Parpia, J. M., Craighead, H. G., and McEuen, P. L. *Nano Letters* **8**(8), 2458–2462 (2008).

[11] Ataca, C., Aktürk, E., Ciraci, S., and Ustunel, H. *Applied Physics Letters* **93**(4), 043123 (2008).

[12] Subrahmanyam, K. S., Kumar, P., Maitra, U., Govindaraj, A., Hembram, K., Waghmare, U. V., and Rao, C. *Proceedings of the National Academy of Sciences of the United States of America* **108**(7), 2674–2677 (2011).

[13] Balandin, A. A. *Nature Materials* **10**(8), 569–581 (2011).

[14] Morozov, S. V., Novoselov, K. S., Katsnelson, M. I., Schedin, F., Elias, D. C., Jaszczak, J. A., and Geim, A. K. *Physical Review Letters* **100**(1), 016602 (2008).

[15] Winzer, T. and Malic, E. *Physical Review B* **85**(24), 241404 (2012).

[16] Ashcroft, N. and Mermin, N. *Festkörperphysik*. Oldenbourg, (2007).

[17] Hoffmann, R. *Reviews of Modern Physics* **60**(3), 601–628 (1988).

[18] Hoffmann, R. *Angewandte Chemie* **99**(9), 871 (1987).

[19] Hoffmann, R. *Solids and surfaces: a chemist's view of bonding in extended structures*. Wiley-VCH, (1988).

[20] Böttcher, S. *Functionalization of Graphene: A Theoretical and Experimental Study of Water and Ammonia Adsorbed on graphene/Ni(111).* Master-thesis, Free University of Berlin, (2010).

[21] Bostwick, A., Ohta, T., Seyller, T., Horn, K., and Rotenberg, E. *Nature Physics* **3**(1), 36–40 (2006).

[22] Castro Neto, A. H., Peres, N. M. R., Novoselov, K. S., and Geim, A. K. *Reviews of Modern Physics* **81**(1), 109–162 (2009).

[23] DiVincenzo, D. P. and Mele, E. J. *Physical Review B* **29**(4), 1685 (1984).

[24] Wintterlin, J. and Bocquet, M. L. *Surface Science* **603**(10-12), 1841–1852 (2009).

[25] Dedkov, Y. S., Horn, K., and Preobrajenski, A. In *Graphene Nanoelectronics,* Raza, H., editor, 189–234. Springer (2012).

[26] Rosei, R., De Crescenzi, M., Sette, F., and Quaresima, C. *Physical Review B* **28**(2), 1161 (1983).

[27] Nagashima, A., Tejima, N., and Oshima, C. *Physical Review B* **50**(23), 17487–17495 (1994).

[28] Gamo, Y., Nagashima, A., Wakabayashi, M., Terai, M., and Oshima, C. *Surface Science* **374**(1-3), 61–64 (1997).

[29] Hagstrom, S., Lyon, H. B., and Somorjai, G. A. *Physical Review Letters* **15**(11), 491 (1965).

[30] Lyon, H. B. and Somorjai, G. A. *The Journal of Chemical Physics* **46**, 2539 (1967).

[31] Grant, J. T. and Haas, T. W. *Surface Science* **21**(1), 76–85 (1970).

[32] Voloshina, E. and Dedkov, Y. *Physical Chemistry Chemical Physics* **14**(39), 13502–13514 (2012).

[33] Voloshina, E. and Dedkov, Y. S. *Materials Research Express* **1**, 035603 (2014).

[34] Dedkov, Y. S., Fonin, M., and Laubschat, C. *Applied Physics Letters* **92**, 052506 (2008).

[35] Dedkov, Y. S., Fonin, M., Rüdiger, U., and Laubschat, C. *Physical Review Letters* **100**, 107602 (2008).

[36] Varykhalov, A. and Rader, O. *Physical Review B* **80**(3), 035437 (2009).

[37] Voloshina, E., Dedkov, Y. S., Torbrügge, S., Thissen, A., and Fonin, M. *Applied Physics Letters* **100**(24), 241606 (2012).

[38] Sicot, M., Bouvron, S., Zander, O., Rüdiger, U., Dedkov, Y. S., and Fonin, M. *Applied Physics Letters* **96**(9), 093115 (2010).

[39] Marchini, S., Günther, S., and Wintterlin, J. *Physical Review B* **76**(7), 075429 (2007).

[40] Brugger, T., Günther, S., Wang, B., Dil, J. H., Bocquet, M.-L., Osterwalder, J., Wintterlin, J., and Greber, T. *Physical Review B* **79**(4), 045407 (2009).

[41] Zhou, Z., Gao, F., and Goodman, D. W. *Surface Science* **604**(13-14), L31–L38 (2010).

[42] Aizawa, T., Hwang, Y., Hayami, W., Souda, R., and Otani, S. *Surface Science* **260**, 311–318 (1992).

[43] Pletikosić, I., Kralj, M., Pervan, P., Brako, R., Coraux, J., N'diaye, A., Busse, C., and Michely, T. *Physical Review Letters* **102**(5), 056808 (2009).

[44] Busse, C., Lazić, P., Djemour, R., Coraux, J., Gerber, T., Atodiresei, N., Caciuc, V., Brako, R., N'Diaye, A. T., Blügel, S., Zegenhagen, J., and Michely, T. *Physical Review Letters* **107**(3), 036101 (2011).

[45] Dresselhaus, M. S. and Dresselhaus, G. *Advances in Physics* **30**(2), 139–326 (1981).

[46] Gierz, I., Suzuki, T., Weitz, R. T., Lee, D. S., Krauss, B., Riedl, C., Starke, U., Höchst, H., Smet, J. H., Ast, C. R., and Kern, K. *Physical Review B* **81**(23), 235408 (2010).

[47] Grånäs, E., Knudsen, J., Schröder, U. A., Gerber, T., Busse, C., Arman, M. A., Schulte, K., Andersen, J. N., and Michely, T. *ACS Nano* **6**(11), 9951–9963 (2012).

[48] Shikin, A., Prudnikova, G., Adamchuk, V., Moresco, F., and Rieder, K. *Physical Review B* **62**(19), 13202 (2000).

[49] Varykhalov, A., Sánchez-Barriga, J., Shikin, A., Biswas, C., Vescovo, E., Rybkin, A., Marchenko, D., and Rader, O. *Physical Review Letters* **101**(15), 157601 (2008).

[50] Leicht, P., Zielke, L., Bouvron, S., Moroni, R., Voloshina, E., Hammerschmidt, L., Dedkov, Y. S., and Fonin, M. *ACS Nano* **8**(4), 3735–3742 (2014).

[51] Varykhalov, A., Marchenko, D., Scholz, M., and Rader, O. *Physical Review B* **85**(20), 201413 (2012).

[52] Bae, S., Kim, H., Lee, Y., Xu, X., Park, J., Zheng, Y., Balakrishnan, J., Lei, T., Kim, H., and Song, Y. *Nature Nanotechnology* **5**, 574 (2010).

[53] Li, X., Cai, W., An, J., Kim, S., Nah, J., Yang, D., Piner, R., Velamakanni, A., Jung, I., Tutuc, E., Banerjee, S. K., Colombo, L., and Ruoff, R. S. *Science* **324**(5932), 1312–1314 (2009).

[54] Zhao, L., Rim, K. T., Zhou, H., He, R., Heinz, T. F., Pinczuk, A., Flynn, G. W., and Pasupathy, A. N. *Solid State Communications* **151**(7), 509–513 (2011).

[55] Dedkov, Y. S., Shikin, A., Adamchuk, V., Molodtsov, S., Laubschat, C., Bauer, A., and Kaindl, G. *Physical Review B* **64**(3), 35405 (2001).

[56] Vita, H., Böttcher, S., Horn, K., Voloshina, E., Ovcharenko, R. E., Kampen, T., Thissen, A., and Dedkov, Y. S. *Scientific Reports* **4**, 5704 (2014).

[57] Decker, R., Brede, J., Atodiresei, N., Caciuc, V., Blügel, S., and Wiesendanger, R. *Physical Review B* **87**(4), 041403 (2013).

[58] Pacilé, D., Leicht, P., Papagno, M., Sheverdyaeva, P. M., Moras, P., Carbone, C., Krausert, K., Zielke, L., Fonin, M., and Dedkov, Y. S. *Physical Review B* **87**(3), 035420 (2013).

[59] Weser, M., Voloshina, E., Horn, K., and Dedkov, Y. S. *Physical Chemistry Chemical Physics* **13**, 7534 (2011).

[60] Sicot, M., Leicht, P., Zusan, A., Bouvron, S., Zander, O., Weser, M., Dedkov, Y. S., Horn, K., and Fonin, M. *ACS Nano* **6**(1), 151–158 (2012).

[61] Petrović, M., Šrut Rakić, I., Runte, S., Busse, C., Sadowski, J. T., Lazić, P., Pletikosić, I., Pan, Z. H., Milun, M., Pervan, P., Atodiresei, N., Brako, R., Šokčević, D., Valla, T., Michely, T., and Kralj, M. *Nature Communications* **4**, 2772 (2013).

[62] Larciprete, R., Ulstrup, S., Lacovig, P., Dalmiglio, M., Bianchi, M., Mazzola, F., Hornekær, L., Orlando, F., Baraldi, A., and Hofmann, P. *ACS Nano* **6**(11), 9551–9558 (2012).

[63] Walter, A. L., Bostwick, A., Jeon, K.-J., Speck, F., Ostler, M., Seyller, T., Moreschini, L., Chang, Y. J., Polini, M., Asgari, R., MacDonald, A. H., Horn, K., and Rotenberg, E. *Physical Review B* **84**(8), 085410 (2011).

[64] Riedl, C., Coletti, C., Iwasaki, T., Zakharov, A. A., and Starke, U. *Physical Review Letters* **103**(24), 246804 (2009).

[65] Bertoni, G., Calmels, L., Altibelli, A., and Serin, V. *Physical Review B* **71**, 075402 (2005).

[66] Karpan, V. M., Giovannetti, G., Khomyakov, P. A., Talanana, M., Starikov, A. A., Zwierzycki, M., Van Den Brink, J., Brocks, G., and Kelly, P. J. *Physical Review Letters* **99**(17), 176602 (2007).

[67] Karpan, V. M., Khomyakov, P. A., Starikov, A. A., Giovannetti, G., Zwierzycki, M., Talanana, M., Brocks, G., Van Den Brink, J., and Kelly, P. J. *Physical Review B* **78**(19), 195419 (2008).

[68] Giovannetti, G., Khomyakov, P., Brocks, G., Karpan, V., Van Den Brink, J., and Kelly, P. *Physical Review Letters* **101**(2), 026803 (2008).

[69] Fuentes-Cabrera, M., Baskes, M., Melechko, A., and Simpson, M. *Physical Review B* **77**(3), 035405 (2008).

[70] Grimme, S. *Journal Of Computational Chemistry* **25**, 1463 (2004).

[71] Grimme, S. *Journal Of Computational Chemistry* **27**, 1787 (2006).

[72] Bianchini, F., Patera, L. L., Peressi, M., Africh, C., and Comelli, G. *The Journal of Physical Chemistry Letters* **5**(3), 467–473 (2014).

[73] Zhao, W., Kozlov, S. M., Höfert, O., Gotterbarm, K., Lorenz, M. P. A., Viñes, F., Papp, C., Görling, A., and Steinrück, H.-P. *The Journal of Physical Chemistry Letters* **2**(7), 759–764 (2011).

[74] Voloshina, E., Fertitta, E., Garhofer, A., Mittendorfer, F., Fonin, M., Thissen, A., and Dedkov, Y. S. *Scientific Reports* **3**, 1072 (2013).

[75] Li, X., Feng, J., Wang, E., Meng, S., Klimeš, J., and Michaelides, A. *Physical Review B* **85**(8), 085425 (2012).

[76] Saeedi, K., Simmons, S., Salvail, J. Z., Dluhy, P., Riemann, H., Abrosimov, N. V., Becker, P., Pohl, H. J., Morton, J. J. L., and Thewalt, M. L. W. *Science* **342**(6160), 830–833 (2013).

[77] Weser, M. *Electronic and Magnetic Properties of Graphene-Based Systems*. Dissertation, Freie Universität Berlin, (2013).

[78] Voloshina, E. and Dedkov, Y. *Electronic and Magnetic Properties of the Graphene-Ferromagnet Interfaces: Theory vs. Experiment in Physics and Applications of Graphene - Experiments*. InTech, (2011).

[79] Kawanowa, H., Ozawa, H., Yazaki, T., and Gotoh, Y. *Japanese Journal of Applied Physics* **41**, 6149 (2002).

[80] Voloshina, E., Generalov, A., Weser, M., Boettcher, S., Horn, K., and Dedkov, Y. S. *New Journal of Physics* **13**(11), 113028 (2011).

[81] Mittendorfer, F., Garhofer, A., Redinger, J., Harl, J., and Kresse, G. *Physical Review B* **84**(20), 201401 (2011).

[82] Varykhalov, A., Marchenko, D., Sánchez-Barriga, J., Scholz, M. R., Verberck, B., Trauzettel, B., Wehling, T. O., Carbone, C., and Rader, O. *Physical Review X* **2**(4), 041017 (2012).

[83] Bostwick, A., Ohta, T., McChesney, J. L., Emtsev, K. V., Speck, F., Seyller, T., Horn, K., Kevan, S. D., and Rotenberg, E. *New Journal of Physics* **12**(12), 125014 (2010).

[84] N'diaye, A., Bleikamp, S., Feibelman, P., and Michely, T. *Physical Review Letters* **97**(21), 215501 (2006).

[85] Kang, M. H., Jung, S. C., and Park, J. W. *Physical Review B* **82**(8), 085409 (2010).

[86] Feibelman, P. *Physical Review B* **77**, 165419 (2008).

[87] Coraux, J., Plasa, T., Busse, C., and Michely, T. *New Journal of Physics* **10**, 043033 (2008).

[88] Perdew, J., Burke, K., and Ernzerhof, M. *Physical Review Letters* **77**(18), 3865 (1996).

[89] Blöchl, P. *Physical Review B* **50**(24), 17953 (1994).

[90] Kresse, G. and Hafner, J. *Physical Review B* **48**(17), 13115 (1993).

[91] Gierz, I., Henk, J., Höchst, H., Ast, C. R., and Kern, K. *Physical Review B* **83**(12), 121408 (2011).

[92] Chorkendorff, I. and Niemantsverdriet, J. W. *Concepts of Modern Catalysis and Kinetics*. Wiley, (2006).

[93] Somorjai, G. A. and Li, Y. *Introduction to Surface Chemistry and Catalysis*. John Wiley & Sons, (2010).

[94] Hofmann, P. *Surface Physics: An Introduction*. Philip Hofmann, (2013).

[95] Jones, J. E. *Proceedings of the Royal Society A: Mathematical, Physical and Engineering Sciences* **106**(738), 463–477 (1924).

[96] Ertl, G. *Reactions at Solid Surfaces*. Baker Lecture Series. Wiley, (2010).

[97] Nilsson, A., Weinelt, M., Wiell, T., Bennich, P., Karis, O., Wassdahl, N., Stöhr, J., and Samant, M. G. *Physical Review Letters* **78**(14), 2847–2850 (1997).

[98] Nilsson, A., Wassdahl, N., Weinelt, M., Karis, O., Wiell, T., Bennich, P., Hasselström, J., Föhlisch, A., Stöhr, J., and Samant, M. *Applied Physics A: Materials Science & Processing* **65**(2), 147–154 (1997).

[99] King, D. A. and Wells, M. G. *Proceedings of the Royal Society A: Mathematical, Physical and Engineering Sciences* **339**(1617), 245–269 (1974).

[100] Venables, J., Spiller, G., and Hanbucken, M. *Reports On Progress In Physics* (1984).

[101] Reichelt, K. *Vacuum* **38**(12), 1083–1099 (1988).

[102] Rhead, G., Barthes, M., and Argile, C. *Thin Solid Films* **82**(2), 201–211 (1981).

[103] Jackson, D., Gallon, T., and Chambers, A. *Surface Science* **36**(2), 381–394 (1973).

[104] Chakarov, D., Österlund, L., and Kasemo, B. *Vacuum* **46**(8-10), 1109–1112 (1995).

[105] Redhead, P. A. *Vacuum* **12**(4), 203–211 (1962).

[106] Hertz, H. *Annalen der Physik und Chemie* **267**(8), 983 (1887).

[107] Einstein, A. *Annalen der Physik* **332**(6), 132 (1905).

[108] Monney, C. *Exciton condensation in 1T-$TiSe_2$: A photoemission study and its theoretical model*. Dissertation, Université de Neuchâtel, (2009).

[109] Pendry, J. B. *Surface Science* **57**(2), 679–705 (1976).

[110] Feibelman, P. and Eastman, D. *Physical Review B* **10**(12), 4932–4947 (1974).

[111] Caroli, C., Lederer-Rozenblatt, D., Roulet, B., and Saint-James, D. *Physical Review B* **8**(10), 4552–4569 (1973).

[112] Randeria, M., Ding, H., Campuzano, J. C., Bellman, A., Jennings, G., Yokoya, T., Takahashi, T., Katayama-Yoshida, H., Mochiku, T., and Kadowaki, K. *Physical Review Letters* **74**(24), 4951 (1995).

[113] Hüfner, S. *Photoelectron Spectroscopy: Principles and Applications*. Springer, (2003).

[114] Ibach, H. and Carette, J. *Electron spectroscopy for surface analysis*. Topics in current physics. Springer, (1977).

[115] Kevan, S. *Angle-Resolved Photoemission: Theory and Current Applications*. Studies in Surface Science and Catalysis. Elsevier Science, (1992).

[116] Gaebel, T., Popa, I., Gruber, A., Domhan, M., Jelezko, F., and Wrachtrup, J. *New Journal of Physics* **6**, 98–98 (2004).

[117] Kordyuk, A., Borisenko, S., Koitzsch, A., Fink, J., Knupfer, M., and Berger, H. *Physical Review B* **71**(21), 214513 (2005).

[118] Stöhr, J. *NEXAFS spectroscopy*. Springer, (1992).

[119] Parent, P., Bournel, F., Lasne, J., Lacombe, S., Strazzulla, G., Gardonio, S., Lizzit, S., Kappler, J.-P., Joly, L., and Laffon, C. *The Journal of Chemical Physics* **131**(15), 154308 (2009).

[120] Wernet, P., Nordlund, D., Bergmann, U., Cavalleri, M., Odelius, M., Ogasawara, H., Näslund, L. Å., Hirsch, T. K., Ojamäe, L., and Glatzel, P. *Science* **304**(5673), 995–999 (2004).

[121] Stöhr, J. and Outka, D. A. *Physical Review B* **36**(15), 7891–7905 (1987).

[122] Binnig, G., Rohrer, H., Gerber, C., and Weibel, E. *Physical Review Letters* **49**(1), 57–61 (1982).

[123] Binnig, G., Rohrer, H., Gerber, C., and Weibel, E. *Physical Review Letters* **50**(2), 120–123 (1983).

[124] Besenbacher, F. *Reports on Progress in Physics* **59**(12), 1737 (1996).

[125] Sawhney, K., Senf, F., Scheer, M., Schäfers, F., Bahrdt, J., Gaupp, A., and Gudat, W. *Nuclear Instruments and Methods in Physics Research Section A* **390**(3), 395–402 (1997).

[126] Petersen, H., Jung, C., Hellwig, C., Peatman, W. B., and Gudat, W. *Review of Scientific Instruments* **66**(1), 1 (1995).

[127] Mahler, W. unpublished, (2012).

[128] Weser, M., Horn, K., Sicot, M., Fonin, M., Preobrajenski, A. B., Voloshina, E., Goering, E., and Dedkov, Y. S. *Applied Physics Letters* **96**(1), 012504 (2010).

[129] Weinberg, W. H. *The Journal of Chemical Physics* **56**(6), 2893 (1972).

[130] Nie, S., Walter, A. L., Bartelt, N. C., Starodub, E., Bostwick, A., Rotenberg, E., and McCarty, K. F. *ACS Nano* **5**(3), 2298–2306 (2011).

[131] Geim, A. K., Morozov, S. V., Hill, E. W., Katsnelson, M. I., and Novoselov, K. S. *Nature Materials* **6**(9), 652–655 (2007).

[132] Henderson, M. *Surface Science Reports* **46**, 1–308 (2002).

[133] Böttcher, S., Weser, M., Dedkov, Y. S., Horn, K., Voloshina, E., and Paulus, B. *Nanoscale Research Letters* **6**(1), 214 (2011).

[134] Sexton, B. and Hughes, A. *Surface Science* **140**(1), 227–248 (1984).

[135] Rottger, K., Endriss, A., Ihringer, J., Doyle, S., and Kuhs, W. F. *Acta Crystallographica Section B: Structural Science* **50**(6), 644–648 (1994).

[136] Eisenberg, D. S. and Kauzmann, W. *The structure and properties of water*. Oxford University Press, (1969).

[137] Preobrajenski, A., Ng, M., Vinogradov, N. A., and Mårtensson, N. *Physical Review B* **78**(7), 073401 (2008).

[138] Cavalleri, M., Ogasawara, H., Pettersson, L., and Nilsson, A. *Chemical Physics Letters* **364**(3-4), 363–370 (2002).

[139] Parent, P., Laffon, C., Mangeney, C., Bournel, F., and Tronc, M. *The Journal of Chemical Physics* **117**(23), 10842–10851 (2002).

[140] Ogasawara, H., Nordlund, D., Nyberg, M., Pelmenschikov, A., Pettersson, L., and Nilsson, A. *Physical Review Letters* **89**(27), 276102 (2002).

[141] Hinch, B. J. and Dubois, L. H. *The Journal of Chemical Physics* **96**, 3262 (1992).

[142] Ito, M. and Yamazaki, M. *Physical Chemistry Chemical Physics* **8**(31), 3623 (2006).

[143] Myneni, S., Luo, Y., and Näslund, L. *Journal Of Physics Condensed Matter* (2002).

[144] Hasselström, J., Föhlisch, A., Karis, O., Wassdahl, N., Weinelt, M., Nilsson, A., Nyberg, M., Pettersson, L., and Stöhr, J. *The Journal of Chemical Physics* **110**, 4880 (1999).

[145] Ozawa, K., Hasegawa, T., Edamoto, K., Takahashi, K., and Kamada, M. *Journal Of Physical Chemistry B* **106**, 9380–9386 (2002).

[146] Polzonetti, G., Carravetta, V., Iucci, G., Ferri, A., Paolucci, G., Goldoni, A., Parent, P., Laffon, C., and Russo, M. V. *Chemical Physics* **296**(1), 87–100 (2004).

[147] Zhu, Q., Money, S., Russell, A., and Thomas, K. *Langmuir* **13**(7), 2149–2157 (1997).

[148] Dedkov, Y. S., Fonin, M., Rüdiger, U., and Laubschat, C. *Applied Physics Letters* **93**, 022509 (2008).

[149] Blyholder, G. *The Journal of Physical Chemistry* **68**(10), 2772–2777 (1964).

[150] Jorgensen, W. *The Organic Chemist's Book of Orbitals*. Elsevier Science, (2012).

[151] Voloshina, E., Usvyat, D., Schuetz, M., Dedkov, Y., and Paulus, B. *arXiv:1103.1978 [cond-mat.mtrl-sci]* (2011).

[152] Geim, A. K., Morozov, S. V., Hill, E. W., Katsnelson, M. I., and Novoselov, K. S. *Nature Materials* **6**(9), 652–655 (2007).

[153] Nitschké, F. *The Journal of Chemical Physics* **74**(10), 5911–5921 (1981).

[154] Burghard, M. *Surface Science Reports* **58**, 1 (2005).

[155] Jones, I. T. N. *The Journal of Chemical Physics* **59**(9), 4836–4844 (1973).

[156] Gardner, E. P., Sperry, P. D., and Calvert, J. G. *Journal of Geophysical Research* **92**(D6), 6642–6652 (1987).

[157] Crowley, J. N. and Carl, S. A. *The Journal of Physical Chemistry A* **101**(23), 4178–4184 (1997).

[158] Zhu, Y., Murali, S., Cai, W., Li, X., Suk, J. W., Potts, J. R., and Ruoff, R. S. *Advanced Materials* **22**(35), 3906–3924 (2010).

[159] Vinogradov, N. A., Schulte, K., Ng, M. L., Mikkelsen, A., Lundgren, E., Mårtensson, N., and Preobrajenski, A. B. *Journal Of Physical Chemistry C* **115**(19), 9568–9577 (2011).

[160] Van der Veen, J. F., Himpsel, F. J., and Eastman, D. E. *Physical Review Letters* **44**(3), 189 (1980).

[161] Yeh, J. J. and Lindau, I. *Atomic data and nuclear data tables* **32**(1), 1–155 (1985).

[162] Sawabe, K. and Matsumoto, Y. *Chemical Physics Letters* **194**(1), 45–50 (1992).

[163] Hossain, M. Z., Johns, J. E., Bevan, K. H., Karmel, H. J., Liang, Y. T., Yoshimoto, S., Mukai, K., Koitaya, T., Yoshinobu, J., Kawai, M., Lear, A. M., Kesmodel, L. L., Tait, S. L., and Hersam, M. C. *Nature Chemistry* **4**, 305–309 (2012).

[164] Liu, J., Fu, S., Yuan, B., Li, Y., and Deng, Z. *Journal Of The American Chemical Society* **132**(21), 7279–7281 (2010).

[165] Xu, L. Q., Yang, W. J., Neoh, K.-G., Kang, E.-T., and Fu, G. D. *Macromolecules* **43**(20), 8336–8339 (2010).

[166] Mkhoyan, K. A., Contryman, A. W., Silcox, J., Stewart, D. A., Eda, G., Mattevi, C., Miller, S., and Chhowalla, M. *Nano Letters* **9**(3), 1058–1063 (2009).

[167] Doniach, S. and Sunjic, M. *Journal of Physics C: Solid State Physics* **3**(2), 285 (1970).

[168] Zhang, H., Fu, Q., Cui, Y., Tan, D., and Bao, X. *The Journal of Physical Chemistry C* **113**(19), 8296–8301 (2009).

[169] Ostler, M., Koch, R. J., Speck, F., Fromm, F., Vita, H., Hundhausen, M., Horn, K., and Seyller, T. *Materials Science Forum* **717-720**, 649–652 (2012).

[170] Dedkov, Y. S. and Fonin, M. *New Journal of Physics* **12**, 125004 (2010).

[171] Dedkov, Y. S., Sicot, M., and Fonin, M. *Journal Of Applied Physics* **107**(9), 09E121–09E121–3 (2010).

[172] Varykhalov, A., Marchenko, D., and Scholz, M. *Physical Review Letters* **108**(6), 066804 (2012).

[173] Schulte, K., Vinogradov, N. A., Ng, M. L., Mårtensson, N., and Preobrajenski, A. B. *Applied Surface Science* **267**, 74–76 (2013).

[174] Wedler, G. *Lehrbuch der Physikalischen Chemie*. Wiley, (2005).

[175] Dubin, S., Gilje, S., Wang, K., Tung, V. C., Cha, K., Hall, A. S., Farrar, J., Varshneya, R., Yang, Y., and Kaner, R. B. *ACS Nano* **4**(7), 3845–3852 (2010).

[176] Lindsay, R., Gutierrez-Sosa, A., Thornton, G., Ludviksson, A., Parker, S., and Campbell, C. T. *Surface Science* **439**, 131–138 (1999).

[177] Barinov, A., Malcioğlu, O. B., Fabris, S., Sun, T., Gregoratti, L., Dalmiglio, M., and Kiskinova, M. *Journal Of Physical Chemistry C* **113**(21), 9009–9013 (2009).

[178] Fujitani, T., Nakamura, I., Kobayashi, Y., Takahashi, A., Haneda, M., and Hamada, H. *Journal Of Physical Chemistry B* **109**(37), 17603–17607 (2005).

[179] Stöhr, J., Baberschke, K., Jaeger, R., Treichler, R., and Brennan, S. *Physical Review Letters* **47**(5), 381–384 (1981).

[180] Xiang, F., Zhong, J., Gu, N., Mukherjee, R., Oh, I.-K., Koratkar, N., and Yang, Z. *Carbon* **75**(C), 201–208 (2014).

[181] Ji, T., Hua, Y., Sun, M., and Ma, N. *Carbon* **54**(C), 412–418 (2013).

[182] Trusovas, R., Ratautas, K., Račiukaitis, G., Barkauskas, J., Stankevičienė, I., Niaura, G., and Mažeikienė, R. *Carbon* **52**(C), 574–582 (2013).

[183] Larciprete, R., Fabris, S., Sun, T., Lacovig, P., Baraldi, A., and Lizzit, S. *Journal Of The American Chemical Society* **133**(43), 17315–17321 (2011).

[184] Polcik, M., Wilde, L., Haase, J., Brena, B., Comelli, G., and Paolucci, G. *Surface Science* **381**(1), L568–L572 (1997).

[185] Polcik, M., Wilde, L., Haase, J., Brena, B., Cocco, D., Comelli, G., and Paolucci, G. *Physical Review B* **53**(20), 13720 (1996).

[186] Driscoll, J. N. and Warneck, P. *The Journal of Physical Chemistry* **72**(11), 3736–3740 (1968).

[187] Böttcher, S., Vita, H., and Horn, K. *Surface Science* **621**, 117–122 (2014).

[188] Sofo, J., Chaudhari, A., and Barber, G. *Physical Review B* **75**(15), 153401 (2007).

[189] Boukhvalov, D., Katsnelson, M., and Lichtenstein, A. *Physical Review B* **77**(3), 035427 (2008).

[190] Elias, D. C., Nair, R. R., Mohiuddin, T., Morozov, S. V., Blake, P., Halsall, M. P., Ferrari, A. C., Boukhvalov, D. W., Katsnelson, M. I., and Geim, A. K. *Science* **323**(5914), 610–613 (2009).

[191] Nair, R. R., Ren, W., Jalil, R., Riaz, I., Kravets, V. G., Britnell, L., Blake, P., Schedin, F., Mayorov, A. S., Yuan, S., Katsnelson, M. I., Cheng, H.-M., Strupinski, W., Bulusheva, L. G., Okotrub, A. V., Grigorieva, I. V., Grigorenko, A. N., Novoselov, K. S., and Geim, A. K. *Small* **6**(24), 2877–2884 (2010).

[192] Jeon, K.-J., Lee, Z., Pollak, E., Moreschini, L., Bostwick, A., Park, C.-M., Mendelsberg, R., Radmilovic, V., Kostecki, R., Richardson, T. J., and Rotenberg, E. *ACS Nano* **5**(2), 1042–1046 (2011).

[193] Lee, W. H., Suk, J. W., Chou, H., Lee, J., Hao, Y., Wu, Y., Piner, R., Akinwande, D., Kim, K. S., and Ruoff, R. S. *Nano Letters* **12**(5), 2374–2378 (2012).

[194] Walter, A. L., Sahin, H., Jeon, K.-J., Bostwick, A., Horzum, S., Koch, R., Speck, F., Ostler, M., Nagel, P., Merz, M., Schupler, S., Moreschini, L., Chang, Y. J., Seyller, T., Peeters, F. M., Horn, K., and Rotenberg, E. *ACS Nano* (accepted 2014).

[195] Zbořil, R., Karlický, F., Bourlinos, A. B., Steriotis, T. A., Stubos, A. K., Georgakilas, V., Šafářová, K., Jančík, D., Trapalis, C., and Otyepka, M. *Small* **6**(24), 2885–2891 (2010).

[196] Robinson, J. T., Burgess, J. S., Junkermeier, C. E., Badescu, S. C., Reinecke, T. L., Perkins, F. K., Zalalutdniov, M. K., Baldwin, J. W., Culbertson, J. C., Sheehan, P. E., and Snow, E. S. *Nano Letters* **10**(8), 3001–3005 (2010).

[197] Weiss, K. U., Dippel, R., Schindler, K. M., Gardner, P., Fritzsche, V., Bradshaw, A. M., Woodruff, D. P., Asensio, M. C., and González-Elipe, A. R. *Physical Review Letters* **71**(4), 581–584 (1993).

[198] Joyce, S. A., Yarmoff, J. A., and Madey, T. E. *Surface Science* **254**(1-3), 144–152 (1991).

[199] Gong, P., Wang, Z., Wang, J., Wang, H., Li, Z., Fan, Z., Xu, Y., Han, X., and Yang, S. *Journal of Materials Chemistry* **22**(33), 16950 (2012).

[200] Wang, Z., Li, P., Chen, Y., He, J., Liu, J., Zhang, W., and Li, Y. *Journal of Power Sources* **263**(C), 246–251 (2014).

[201] Urzúa-Sánchez, O., Licea-Claveríe, A., González, J., Cota, L., and Castillón, F. *Polymer Bulletin* **49**(1), 39–46 (2002).

[202] Batzill, M. *Surface Science Reports* **67**(3-4), 83–115 (2012).

[203] Loh, K. P., Bao, Q., Eda, G., and Chhowalla, M. *Nature Chemistry* **2**(12), 1015–1024 (2010).

[204] Schumacher, S., Wehling, T. O., Lazić, P., Runte, S., Förster, D. F., Busse, C., Petrović, M., Kralj, M., Blügel, S., Atodiresei, N., Caciuc, V., and Michely, T. *Nano Letters* **13**(11), 5013–5019 (2013).

[205] Vita, H. *Electronic and Magnetic Properties of Graphene-Based Systems*. Dissertation, Humboldt Universität zu Berlin, (in preparation).

[206] Gao, T., Gao, Y., Chang, C., Chen, Y., Liu, M., Xie, S., He, K., Ma, X., Zhang, Y., and Liu, Z. *ACS Nano* **6**(8), 6562–6568 (2012).

[207] Leicht, P. to be published, (2014).

[208] Knudsen, J., Feibelman, P. J., Gerber, T., Grånäs, E., Schulte, K., Stratmann, P., Andersen, J. N., and Michely, T. *Physical Review B* **85**(3), 035407 (2012).

[209] Rusponi, S., Papagno, M., Moras, P., Vlaic, S., Etzkorn, M., Sheverdyaeva, P., Pacilé, D., Brune, H., and Carbone, C. *Physical Review Letters* **105**(24), 246803 (2010).